The Thermal and Fluid Environment of the Cascadia Subduction Zone, Southern Washington State

Marie Suzanne Salmi

A dissertation
submitted in partial fulfillment of the
requirements for the degree of

Doctor of Philosophy

University of Washington

2018

Reading Committee:

H. Paul Johnson, Chair

Robert N. Harris

William S.D. Wilcock

Program Authorized to Offer Degree:
School of Oceanography

University of Washington

Abstract

The Thermal and Fluid Environment
of the Cascadia Subduction Zone,
Southern Washington State

Marie Suzanne Salmi

Chair of the Supervisory Committee:
Professor H. Paul Johnson
School of Oceanography

Subduction zones are areas of tectonic plate collision that produce associated earthquakes and destructive tsunamis and, in addition, provide a link between the atmosphere and ocean. Mapping the thermal and fluid circulation of an active subduction zone can advance our understanding of subduction zone dynamics and fluid budgets, important in understanding global chemical fluxes and the carbon cycle. By exploring the intertwined nature of both the thermal and fluid environment, a more complete picture of the governing processes can be established. The overarching goal of this thesis is to map the thermal and fluid environment within the Cascadia Subduction zone offshore Southern Washington State.

Eleven recently collected multi-channel seismic (MCS) profiles from the 2012 Cascadia Open-Access Seismic Transect (COAST) experiment offshore Washington State were used to characterize the distribution of bottom simulating reflectors (BSRs) from seaward of the deformation front onto the continental shelf of the Cascadia Subduction Zone. From these MCS profiles, we generated a 3-D view of the Cascadia margin thermal structure by interpreting 40,232 individual BSR data points in terms of temperature and heat flow. Localized differences between BSR heat flow and numerical models reflect an estimated regional mean upward fluid flow of 0.53 cm yr^{-1} for the survey area, with localized fluid flow

approaching a maximum of 3.8 cm yr^{-1}. At the deformation front, the incoming oceanic sediment/crust interface temperatures vary between 164°C to 179°C, indicating the up-dip limit of the Cascadia seismogenic zone.

Seafloor heat flow data provides valuable insight into seafloor and subseafloor fluid and geological processes. Thus, understanding the uncertainties associated with heat flow instruments is essential to the interpretation of acquired data. While there have been studies of various instruments ability to accurately capture the necessary elements of a heat flow measurement, a need remains to examine how well individual sensors perform in-situ and to make quantitative comparisons between different instruments and their corresponding methodologies. Four different heat flow instruments were compared: the Violin-bow Probe, Alvin Probe, Thermal Blanket, and a modified Multi-core system, in terms of individual instrument uncertainty and the accuracy of each instrument in estimating the local heat flow. On an east-west profile of the Cascadia accretionary prism, a total of 251 heat flow measurements over water depths from 550 to 2600 meters captured a wide range of seafloor thermal environments. The deployment chronology illuminated large differences in measured temperature profiles due to variable near bottom water temperatures that propagated into the sediment column. While near seafloor water temperature variability generally decreases with water depth, bathymetry and localized oceanic currents are also important because even sites at similar depth may be exposed to vastly different seafloor thermal environments that impact all instrument types.

The collected seafloor heat flow measurements were co-located with the COAST MCS profiles that run perpendicular to the megathrust fault strike, providing additional contextual data in the form of BSR heat flow and internal geological structure. Additional context comes from in-situ thermal conductivity measurements, multibeam derived backscatter, acoustic imaged bubble streams, and ROV video of carbonate deposits and pockmarks. Fluid emission sites differ across-strike from the actively deforming and faulted accretionary toe, with

highly variable and shallow sourced fluid, to long-lived point sources of methane gas from deeper within the accretionary wedge. These surface heat flow measurements throughout the survey proved useful for detecting fluid emissions from the seafloor sediment, especially in the absence of methane gas and carbonate.

TABLE OF CONTENTS

LIST OF FIGURES

LIST OF TABLES

ACKNOWLEDGMENTS

There have been numerous people that have helped me along my journey through graduate school and I can't thank them enough for their support. First and foremost, I'd like to thank my adviser Paul Johnson. He has shown me the value of being a great story teller and to always be thinking outside of the box. I would also like to thank my committee members for helping out in their own unique ways. In particular, Evan Solomon for allowing me to bother him on fluid and methane related questions, Susan for her wonderful support and listening ear throughout my time at the UW, and Rob Harris for his keen eye for detail and for showing me how to think critically.

Throughout my tenure, I have had the joy of participating in a multitude of research cruises, both locally in Puget Sound and out on the Pacific Ocean, and I would like to acknowledge everyone that I worked with on these cruises. This includes but not limited to Evan Solomon, Tor Bjorklund, Casey Hearn, Kira Homola, and the crew of the R/V *Atlantis*, R/V *Thompson*, and ROV *Jason II* who were essential to this experiment.

I would like to thank Tor Bjorklund for help manufactoring the Thermal Blankets and for teaching me the tools of the trade. I have also enjoyed collaborating on numerous projects and papers with Brian Atwater, Susan Hautala, Joan Gomberg, Mike Hutnak, and Ira Leifer.

Graduate school is not complete without the friends made along the way. I would like to thank Emily Eidem and Rick Berg for the occasional beer, hike, run, or bike ride. I would also like to thank Una Miller for being a wonderful companion on cruises and lab trips. Finally I would like to extent a huge thank you to my husband Marcus. Being married to a graduate student is not easy and I thank him for being a constant source of encouragement.

Chapter 1
INTRODUCTION

Subduction zones are areas where tectonic plate collide and the denser plate subducts into the mantle. They are associated with earthquakes and volcanic eruptions and are sites of solid earth processes that link the ocean and atmosphere through an exchange of material and fluids. Interest in subduction zones has been spurred by large, destructive earthquakes and tsunamis with far-reaching socio-economic impacts, such as the recent M_w 9.1 Tohoku-oki earthquake in 2011 and the M_w 9.1 earthquake offshore Sumatra in 2004. Our current understanding of mega-thrust earthquake slip, the primary controller in tsunamigenesis, is that its extent and magnitude is highly dependent on a multitude of parameters including thermal regime, pore fluid pressure, sediment distribution, and the existence and location of prominent splay faults. Exploring these factors can help improve our understanding of the mechanisms of large mega-thrust earthquakes, providing valuable information to help societies understand the risk and thus, respond appropriately.

1.1 Importance of Heat and Fluids within the Accretionary Wedge

Once the incoming plate begins subducting, sediments are compressed, deformed, and accreted against the non-subducting plate, forming the accretionary wedge. Within this accretionary wedge, fluids captured within the incoming sediment and crust exit the system, either by migration along the subducting plates highly permeable layer 2A, or via other permeability pathways such as faults and turbidite layers. Based on models of fluid budgets, it is estimated that the entire ocean volume fluxes through subduction zones every 400 million years, transporting important nutrients and solutes from the sediments and underlying plate

into the overlying oceans (Kastner et al., 2014).

The primary controls on the subduction zone thermal environment include the temperature of the incoming subducting plate, sediment composition, pore pressure, and fluid expulsion rate. This thermal regime is then closely tied to fault mechanics, hydrocarbon production, and geochemical changes within the subduction wedge. Over time, increasing temperature and pressure within the wedge will alter the sediment composition through dehydration reactions that affect frictional properties along the plate boundary. Most notably, the clay mineral conversion from smetite to illite within the temperature range of 60°C to 150°C will cause a drastic increase in the sediment friction coefficient (Saffer and Marone, 2003). This reaction also results in dehydration of the clay minerals that release fluids into the interstitial pore space.

Subduction zones represent an important component to the carbon cycle along continental margins, with their associated methane seeps accounting for 3 to 9% of the global methane budget (Judd et al., 2002). Locations of seafloor methane emission provide habitable environments for chemosynthetic communities and a mechanism for transporting hydrocarbons into the ocean and atmosphere (Kastner et al., 2014). In a suitable temperature and pressure environment, gaseous methane and higher order hydrocarbons are captured within an ice lattice, forming hydrates within the near seafloor accretionary wedge sediments, thus providing a form of carbon storage. The temperature-controlled boundary within the sediment column representing the methane hydrate to gas transition can be mapped within seismic profiles as a Bottom Simulating Reflector (BSR) (Ganguly et al., 2000).

1.2 Location - Cascadia Subduction Zone

The Cascadia subduction zone is formed by the confluence of the North American plate with three micro-plates, the Endeavour, Juan de Fuca, and Gorda, of which the Juan de Fuca is the largest (Figure 1.1). Cascadia is a comparatively small subduction zone that extends roughly 1000 km from Southern British Columbia, Canada to Northern California, USA. The

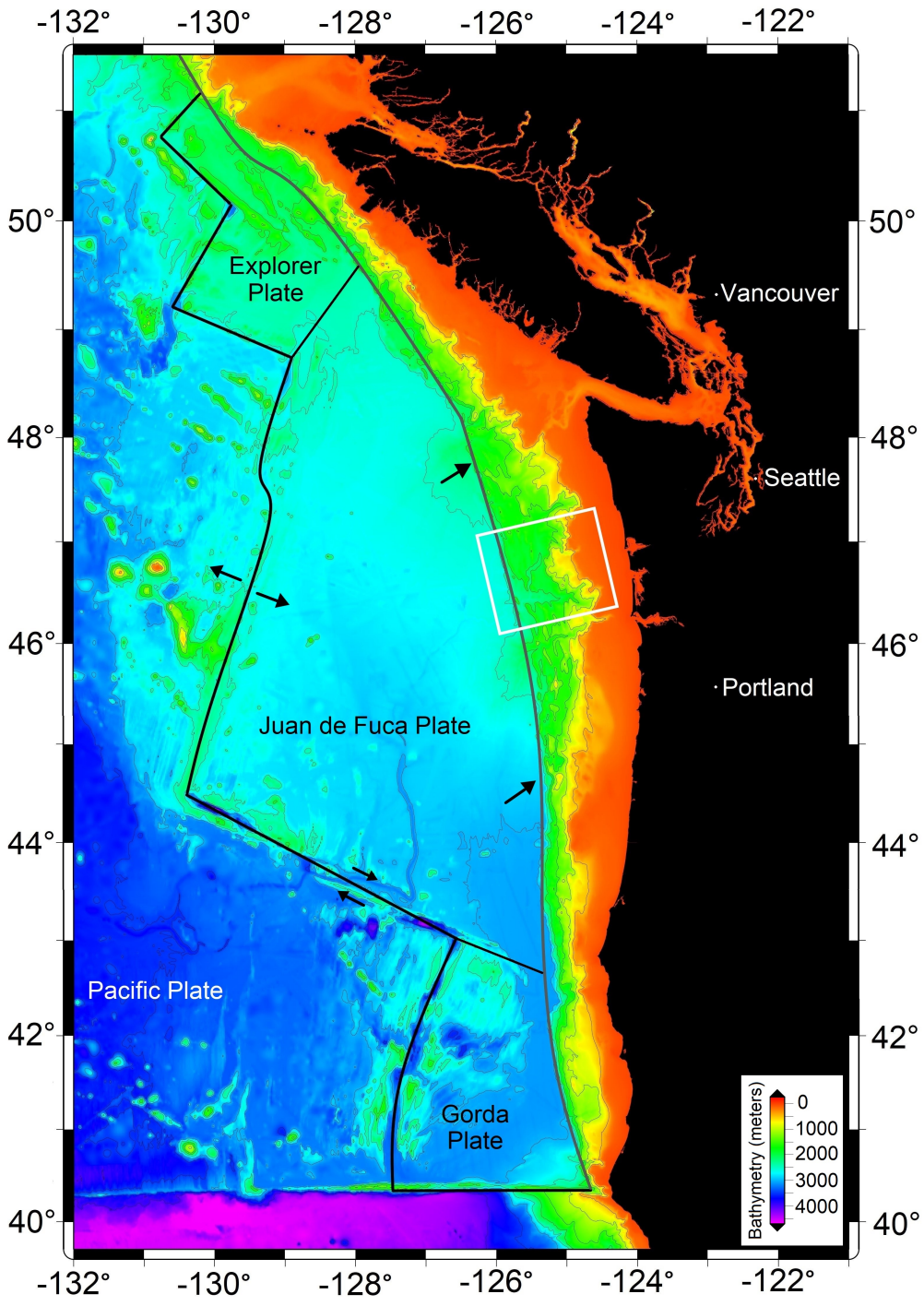

Figure 1.1: Map of the seafloor bathymetry showing the Explorer, Juan de Fuca, and Gorda plates. The deformation front is marked by the gray line tracing the western boundary of the Cascadia Subduction zone. Bathymetry data is derived from the Global Multi-Resolution Topography database (Ryan et al., 2009). The survey location explored within this thesis is outlined by the white box offshore southern Washington State.

subduction zone back-arc basins include several major economic centers and port cities, most notably Vancouver, British Columbia, Seattle, Washington, and Portland, Oregon. Cascadia is characterized as an extremely seismically quiet convergent fault in comparison to other subduction zones. There have been only six major earthquakes (6+ M_w) in the last 120 years and it has yet to produce a large (8+ M_w) earthquake in modern history (Kirby et al., 2002) with the last megathrust earthquake having occurred on January 26th, 1700 (Atwater and Hemphill-Haley, 1997). Previous Cascadia subduction zone thermal modeling suggests that when the next megathrust earthquake occurs, the fault slip will propagate along the decollement fully to the accretionary toe (Hyndman and Wang, 1995; Cozzens and Spinelli, 2012), increasing the risk of a destructive tsunami. The Cascadia region is also characterized by episodic tremor and slip (ETS) downdip of the locked zone, that occurs every 11 to 19 months (Rogers and Dragert, 2003), a phenomenon that has been detected on only a few other subduction zones.

Due to the close proximity of the Cascadia Subduction zone to the Juan de Fuca spreading ridge, the incoming oceanic plate is relatively young and forms a hot incoming sediment-plate interface relative to most other subduction zones. The incoming Juan de Fuca plate age is roughly 6 to 10 Myr old and has 2 to 3.5 km of sediment load at the start of subduction (Han et al., 2016) with a sediment-plate interface of 160° to 250°C (Hyndman and Wang, 1993; Salmi et al., 2017). The accretionary margin is distinguished by distinct along-strike features and by segmented accretionary wedge shape and seismicity (Flueh et al., 1998). One such feature is the change from primarily seaward verging thrust faults offshore Vancouver Island and Southern Oregon/Northern California to landward verging faults within a broad margin offshore Washington state, an indicator of changes in the effective friction along the decollement (Cubas et al., 2016).

1.3 Organization of the Thesis and Research Goals

The goal of this thesis is to explore in detail both the thermal and fluid components of the accretionary wedge offshore Southern Washington State, a portion of the Cascadia subduction zone that is relatively less studied in comparison to offshore Oregon and Vancouver Island. While the primary interest is to investigate across-strike features (West to East), any local along-strike (North to South) variations are also interesting in terms of understanding subduction segmentation. Chapter 2 (Salmi et al., 2017) delves into the large-scale thermal environment of the Cascadia Subduction zone by constructing a finite element model extending from the incoming plate to the back-arc. This model is updated from previous modeling of Cascadia Subduction zone (Hyndman and Wang, 1995) by incorporating general bathymetric trends and more recent estimates of plate sediment thickness and subducting geometry. The model also includes the Siletz, a unique geological accreted terrane that affects the large-scale thermal regime of the subduction zone. BSR derived heat flow measurements determined from the R/V *Langseth* MGL1212 seismic profiles are compared with co-located thermal models and offsets in the heat flow identify large areas of diffuse upward fluid flux and recent mass sediment movement, and provide a framework to explore potential fluid movement up the subducting crust permeable layer 2A.

Accurate measurements of heat flow are critical for studying subduction zone accretionary wedges and can be determined either from BSR or surface measurements. Fully understanding the processes that affect the reliability of heat flow measurements is essential to their interpretation, whether it is fluid flux or variations in the water column temperature near the seafloor. Uncertainty in BSR heat flow measurements is explored in detail within Chapter 2 by isolating and examining the sensitivity of heat flow to the parameters associated with the calculation. Chapter 3 explores uncertainty in heat flow measurements captured at the seafloor, the interface between marine sediments and the overlying ocean. While heat flow measurements taken close to the sediment-ocean interface can be acquired in environments without hydrates, they can be affected by variations in the thermal environment caused

by fluctuating near bottom ocean temperatures. Seafloor temperature records are used to demonstrate that heat flow measurements within shallow sediments are susceptible to bottom water temperature changes, even within relatively deeper portions of the accretionary prism. Four types of heat flow instruments were deployed and tested within numerous wedge environments that include a range of seafloor depths, sites in and around methane vents, and sediments of different compositions. Utilizing multiple instruments throughout the survey area reveals the strengths and weaknesses associated within individual instruments and deployment strategies. This information will be vital for designing future heat flow studies, especially in environments where water temperatures are highly variable.

Chapter 4 evolves from a macroscopic view of the entire subduction zone developed in Chapter 2 to a focused exploration of fluid emissions, with the goal of understanding the processes controlling the changes in the characteristics of fluid emissions across the subduction zone. In order to develop a more complete view of the seafloor environment, heat flow data is combined with video observations of the seafloor, multi-channel seismic profiles, and seafloor backscatter intensity. Heat flow data provides an alternate means of detecting venting locations independent of methane and gas. In combination with observed gas emissions and methane-derived products, such as carbonates, bioherms, and chemosynthetic communities, a more complete map of fluid emissions is established, with an overarching aim of understanding how fluid and methane venting evolves across strike with changing fluid sources and wedge structure.

Chapter 2

THERMAL ENVIRONMENT OF THE SOUTHERN WASHINGTON REGION OF THE CASCADIA SUBDUCTION ZONE

2.1 Introduction

Subduction zones produce some of the largest earthquakes, resulting in damage and loss of life through the generation of tsunamis and destructive ground shaking, and pose the single largest seismic hazard to large population centers (Rogers, 1996). Understanding the thermal environment of a subduction accretionary wedge provides a better comprehension of fault rheology (Hacker et al., 2003; Wada et al., 2008), fluid generation, and elevated sediment pore pressure (Tobin and Saffer, 2009; Daigle and Screaton, 2015), all of which play critical roles in the location of the seismogenic zone (Wang et al., 1993; Wang and Hu, 2006; Harris et al., 2014).

2.1.1 Tectonic Setting

The Cascadia Subduction Zone (CSZ) extends 1100 km along-strike from Mendocino, California, USA to Vancouver Island, Canada and is known to produce infrequent but high magnitude megathrust earthquakes (Atwater and Hemphill-Haley, 1997; Atwater, 2010; Goldfinger et al., 2012). The CSZ subducting plate interface is unusually seismically quiet for an active subduction zone, with only limited numbers of earthquakes observed at the northern and southern terminations and offshore southern Oregon (Tréhu et al., 2008; Morton and Bilek, 2015; Tréhu et al., 2015). This accretionary margin is the result of the Explorer, Gorda, and Juan de Fuca oceanic plates subducting beneath the North American plate. The Juan de Fuca, the largest of these oceanic plates, subducts at a rate of 35 to 41 mm yr^{-1} with

crustal ages ranging between 6 and 10 Ma at the deformation front (Wilson, 1993). There is no distinguishable trench due to Late Pleistocene glacial sediment fill from the adjacent continental margin (Heaton and Hartzell, 1987; Calkins et al., 2011) with sediment thickness seaward of the deformation front varying between 2 and 3 km. The incoming plate has one of the highest known basement temperatures of any subduction zone due to the young age of the plate and the thermal isolation by rapid sediment accumulation rates (Davis et al., 1990; Wilson, 1993).

The Washington State portion of the CSZ comprises an accretionary wedge with distinct lower and upper margins, consisting of landward verging folds and faults (McNeill et al., 1997; Adam et al., 2004) atypical for an active subduction zone. Regions undergoing extension with westward dipping normal and listric faults are present on the middle and upper margin offshore Grays Harbor in areas shallower than 1000 meters water depth (McNeill et al., 1997). The extensional faulting forms a distinctive mid-slope terrace feature within the Grays Harbor area (Figure 2.1) related to fluid over-pressurization at depth (McNeill et al., 1997).

Heat flow data along the CSZ margin is relatively sparse with limited thermal studies offshore Vancouver Island (Davis et al., 1990; Hyndman et al., 1993; Yuan et al., 1996, 1999), Oregon (Tréhu et al., 1995; Zwart et al., 1996), and Washington (Booth-Rea et al., 2008). In this study we analyze Multi-Channel Seismic (MCS) reflection data acquired during the MGL1212 COAST (Cascadia Open-Access Seismic Transects) survey collected on the R/V *Langseth* (Holbrook et al., 2012). This cruise provided seismic imaging of the southern portion of the Washington Margin consisting of nine closely-spaced ($\sim$8 km) lines extending 25 km seaward of the deformation front to the edge of the continental shelf, approximately perpendicular to the margin. Two additional N-S lines provide along-strike data that overlap the nine E-W lines. BSRs imaged within the MCS profiles are interpreted in terms of temperature and provide a high-resolution 3-D view of heat flow variations across the accretionary wedge. The primary goal of this study is to provide an increased

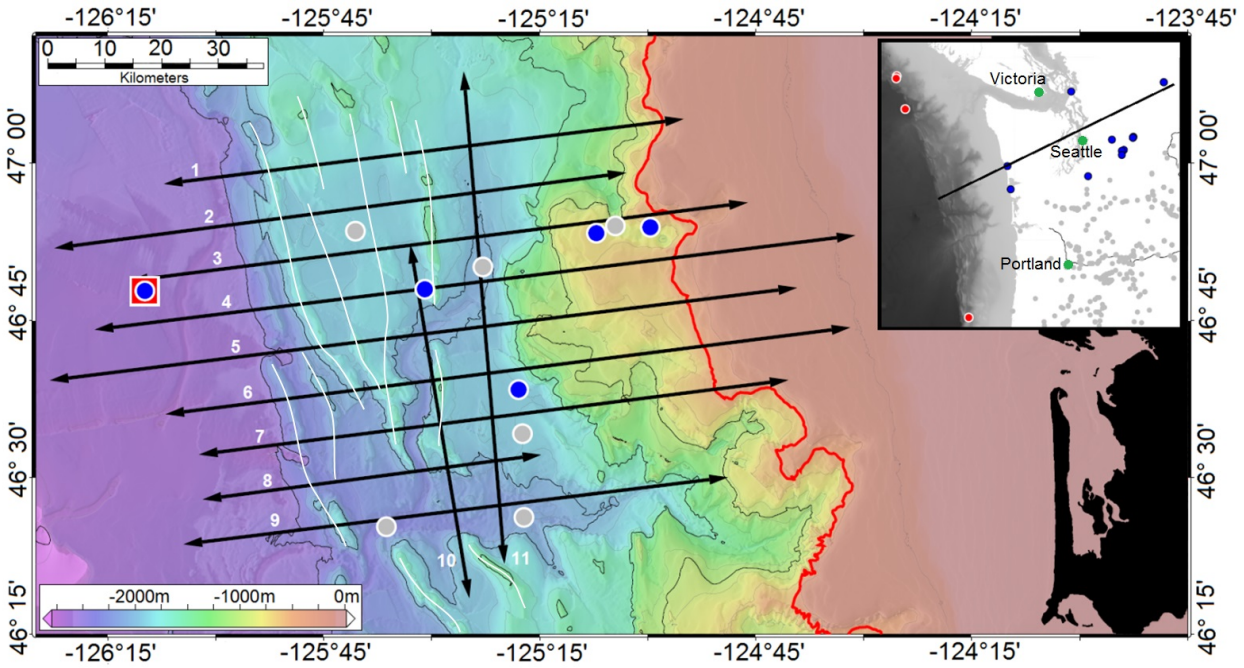

Figure 2.1: Location of COAST 2012 Multi-Channel Seismic profiles (black lines) with their corresponding line numbers (white text). White lines trace prominent anticlinal ridges visible in the MCS. LDEO OBSs (Blue circles) deployed during the 2012-2013 year within the *Langseth* survey area were equipped with thermistors. CTD cast location (red square) was used for BSR seafloor temperature calculations and sediment cores (grey circles) were used for BSR heat flow sedimentation correction. Inset displays IODP/ODP borehole (Red dots) and continental heat flow measurements (grey dots) including those used in the current study (blue dots). Green dots mark major metropolitan cities.

understanding of the thermal environment of a 100 km along-strike portion of the CSZ offshore Southern Washington using analysis of high-resolution BSR data. The BSR heat flow data was corrected for bathymetry and sedimentation accumulation rate, and incorporated MCS derived thermal conductivity values. BSR estimates of heat flow are then compared to a finite element model derived for each of the 9 perpendicular MCS lines to estimate temperatures at the top of the oceanic basement. Areas of misfit between the BSR data and the numerical model are interpreted in terms of fluid discharge.

2.2 BSR Heat Flow

2.2.1 Heat Flow Estimates from Bottom Simulating Reflectors

The COAST MCS profiles (Figure 2.1) were acquired using a single 8 km long streamer deployed at a water depth of 15 meters for all odd numbered lines (1, 3, 5, 7, 9 and 11) and 9 meters depth for all even lines (2, 4, 6, 8, and 10), collecting data at 2 millisecond sample rate. A total of 36 individual airguns were used, resulting in a total of 6600 cubic inches of source volume. All MCS lines were processed shipboard using ProMax seismic software [https://www.landmark.solutions/SeisSpace-ProMAX]. The seismic profiles used to calculate the BSR depths were generated using a two-dimensional velocity structure for each line determined through pre-stack time migration. This study primarily used shipboard processed seismic profiles as the consistently processed data existed for all MCS lines.

Solid hydrate is an ice-like phase with lattice vacancies filled with predominately methane molecules that forms in regions of high pressure and low temperature (Henry and Clennell, 1999; Malinverno et al., 2008). BSRs within the sediment column mark the boundary between solid hydrate above and free gas below, indicating the lower limit of hydrate stability zone (Davis et al., 1990; Kvenvolden, 1993). We identified BSRs using the following criteria: 1) the reflector horizon crosses surrounding sediment stratigraphy, 2) the horizon roughly mimics the seafloor bathymetry; and 3) the acoustic wave forms a negative polarity horizon (Davis et al., 1990). Requirements for BSR formation include upward diffuse fluid flow and relatively high gas concentrations within the sediment pore space (Yuan et al., 1999; Haacke et al., 2008).

Heat flow (Q) is derived from BSRs based on the following equation,

$$Q = K\frac{T_{BSR} - T_{SF}}{Z_{BSR}} \tag{2.1}$$

where T_{BSR} and T_{SF} are the temperatures (°C) at the BSR and seafloor respectively, Z_{BSR} is BSR depth (meters) below seafloor, and K is bulk sediment thermal conductivity. As with

prior studies, we assume that after correcting for the effects of bathymetry and sedimentation, the thermal gradient between the seafloor and BSR is constant and that the accretionary wedge is in a thermal steady state.

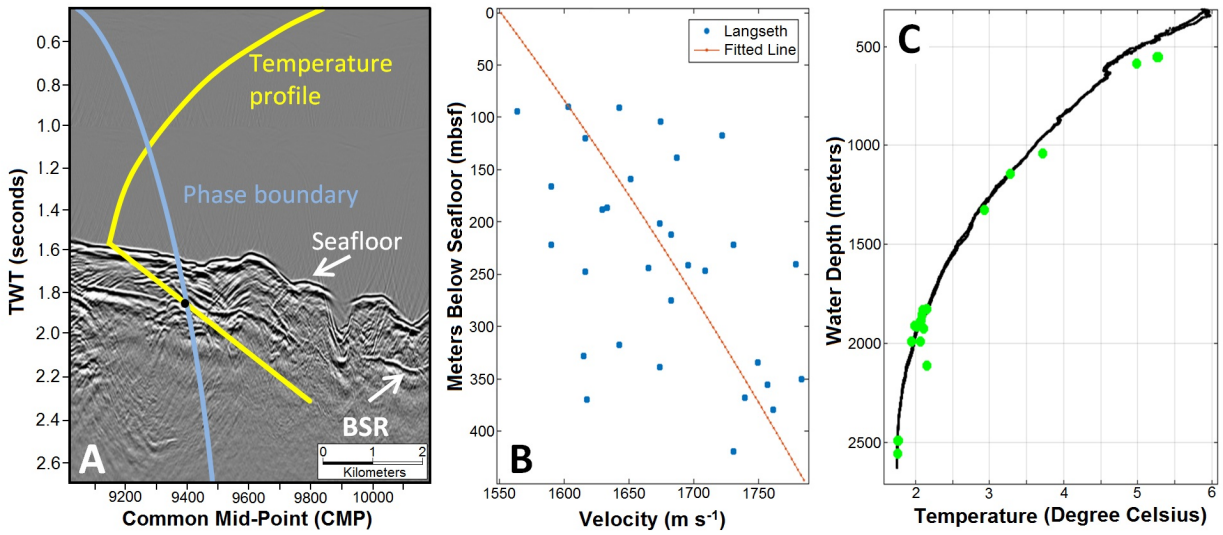

Figure 2.2: Method and parameters used to calculate BSR heat flow. A) BSR temperature is calculated knowing the depth of the seafloor and BSR using the methane hydrate phase stability curve (blue line). B) Seismic velocity (Vp) to meters below seafloor relationship from the *Langseth* pre-stack time migrated velocity profiles. Data points represent velocity picks over anticlinal ridges within the lower accretionary margin. Orange line is the best fit of the data. See text for equation. C) Temperature profile determined by CTD cast (Figure 2.1). Green dots are seafloor temperatures, measured 5 centimeters above the seafloor derived from Thermal Blankets.

To determine Z_{BSR}, the seafloor and BSR two-way travel time (TWT) from the MCS profiles were recorded by the 2-D horizon tracking module within the software program OpendTect [http://www.opendtect.org/]. TWT is recorded for every Common Mid-Point (CMP) within the individual survey profiles. To convert TWT to depth, the velocity profile within the upper 500 meters of the sediment is determined using the method from Hyndman et al., (Hyndman and Wang, 1993) and seismic velocity profiles collected during the 2012 *Langseth* cruise (Figure 2.2) using the relationship,

Table 2.1: Locations and temperature data for Ocean Bottom Seismometers deployed in the COAST survey area. Temperature records were used to determine the uncertainty from seafloor temperature variability. T_{SF} offset is year mean minus summer mean temperature.

OBS	Latitude	Longitude	Depth (meters)	Year Mean	Year 1σ	Summer mean	Summer 1σ	T_{SF} offset
FN12A	46.889	-125.1000	650	5.1693	0.050	NA[a]	NA[a]	NA[a]
FN16A	46.7996	-125.5161	1907	2.5190	0.013	2.554	0.017	-0.035
J50A	46.6402	-125.2991	1909	2.5745	0.040	2.605	0.011	-0.031
J51A	46.7970	-126.1641	2610	2.0176	0.010	2.012	0.004	-0.006
Mean								-0.024

[a] FN12A was retrieved before *Langseth* COAST cruise time period.

$$Z_{BSR} = 0.776\Delta t + 2.33x10^{-4}\Delta t^2 \tag{2.2}$$

where Δt is time difference between the seafloor and the BSR, both in seconds of TWT. Based on the MCS source frequency, the TWT vertical resolution is between ± 3 to ± 5 meters and accounting for uncertainties in the velocity, the depth estimate uncertainty is approximately ± 13 m.

We estimate the average thermal conductivity, K, between seafloor and Z_{BSR} using the relationship provided by Davis et al. (Davis et al., 1990) for the Vancouver Island Margin located 250 km north of our survey area. Comparison of the Z_{BSR} derived K to thermal conductivity measurements from Ocean Drilling Program (ODP) 889/890 boreholes offshore Vancouver Island and Oregon shows a correlation to within $\pm 10\%$ and are assumed to be similarly reliable for the near surface Cascadia margin sediments (Davis et al., 1990; Ganguly et al., 2000). Heat flow is calculated using the average K between seafloor and Z_{BSR} (Ganguly et al., 2000; Riedel and Shankar, 2012).

Seafloor temperatures, T_{SF}, at the seawater/sediment interface are determined using a Conductivity Temperature Depth (CTD) cast taken west of the deformation front (Figure 2.1) by the R/V *Thompson* in 2012, within the same region and time period as the COAST cruise. CTD casts have commonly been used for previous BSR heat flow studies for determining seafloor temperatures (He et al., 2007; Riedel et al., 2010). Based on ocean bottom seismometers (OBS) equipped with temperature sensors deployed for a year prior and during the survey cruise time period (July 12-24, 2012), the mean yearly seafloor temperature had an offset of -0.024°C (Table 2.1) from that estimated by the CTD cast (Toomey et al., 2014).

BSR depth within the sediment column is a function of both pressure and temperature. If the pressure can be estimated, then the phase relationship between gas and hydrate can be used to determine T_{BSR}. Previous studies based on borehole and seismic profiles find that *in-situ* pressures within the sediment column are neither purely lithostatic nor hydrostatic, but fall between these two end members (Hyndman et al., 1993; Screaton et al., 2002; Saffer and Tobin, 2011). Based on these previous BSR heat flow studies, we assume a 50% ratio of hydrostatic to lithostatic pressure at the BSR depth (Hyndman et al., 1993; Saffer, 2015). This assumption differs from previous work on the Cascadia Subduction Zone that applied either fully hydrostatic (Hyndman et al., 1992; Ganguly et al., 2000) or fully lithostatic pressure (Golmshtok et al., 2000), a difference that can account for roughly 3 mW m^{-2} difference in BSR heat flow. For this study, *in-situ* pressure is calculated using the following equation (Haacke et al., 2008),

$$P(Z_{BSR}) = \frac{1}{2}[Lg\phi_o(\rho_f - \rho_s)(1 - e^{-Z_{BSR}/L}) + g\rho_s Z_{BSR} + g\rho_f Z_w + g\rho_f(Z_{BSR} + Z_w)] \quad (2.3)$$

Pressure (P) is based on Z_{BSR} and is calculated assuming a porosity compaction length (L) of 1.2 km (Hyndman et al., 1993), gravity (g) of 9.81 m s^{-2}, grain density (s) of 2.65x10^3 kg m^{-3} (Shi et al., 1988), and seafloor porosity (ϕ_o) of 0.55. Water density (ρ_f) varied based on *in-situ* pore fluid temperature (Sharqawy et al., 2010; Nayar et al., 2016), salinity of 33.5 g

kg^{-1}, and seafloor depth Z_w and Z_{BSR}. We assume a pure methane gas composition (Davis et al., 1990; Kastner et al., 1995) and pore-water salinity at the BSR depth similar to ocean salinity of 33.5 g kg^{-1} (Kastner et al., 1995; Liu and Flemings, 2006; Riedel et al., 2006). BSR pressure and salinity provide a BSR temperature using an empirically derived stability relationship (Tishchenko et al., 2005). Seafloor depths used to estimate water column pressure are determined from swath bathymetry corrected with eXpendable BathyThermograph (XBT) derived sound velocities, collected during the COAST cruise. Estimated overall uncertainty for the pressure was ±0.15 MPa, corresponding to a BSR temperature uncertainty of ±0.06 °C (see Section 2.2.2).

Bathymetric Correction

Seafloor bathymetry variations perturb the geothermal gradient, with local bathymetric highs decreasing the heat flow and depressions increasing the heat flow. To determine the isotherm distribution in the margin sub-surface, we apply a correction to the heat flow measurements (Ganguly et al., 2000; Harris et al., 2010; Li et al., 2013) [Figure 2.3]. Seafloor bathymetry was derived from 50 meter gridded *Langseth* EM122 bathymetry with gaps filled using the 100 meter resolution Global Multi-Resolution Topography [GMRT] (Ryan et al., 2009).

The horizontal dimension of the seafloor area used for the bathymetric correction was determined as 10 times the Z_{BSR} (Figure 2.4). To estimate the thermal gradient correction at the BSR depth due to abrupt changes in bathymetry, a 3-D map of seafloor temperatures was constructed by extracting temperatures corresponding to the seafloor depths from the CTD cast (Figure 2.2). The thermal offsets associated with individual BSR measurements were determined by continuous propagation of the temperature using the discrete Fourier Transform method to account for localized bathymetric variability. The resulting gradient corrections were then applied to the geothermal gradient. The overall average bathymetric correction was +7.5 mW m^{-2} with predominantly large bathymetric corrections concentrated around areas of sharp topographic relief including anticlinal ridges and steep canyon walls.

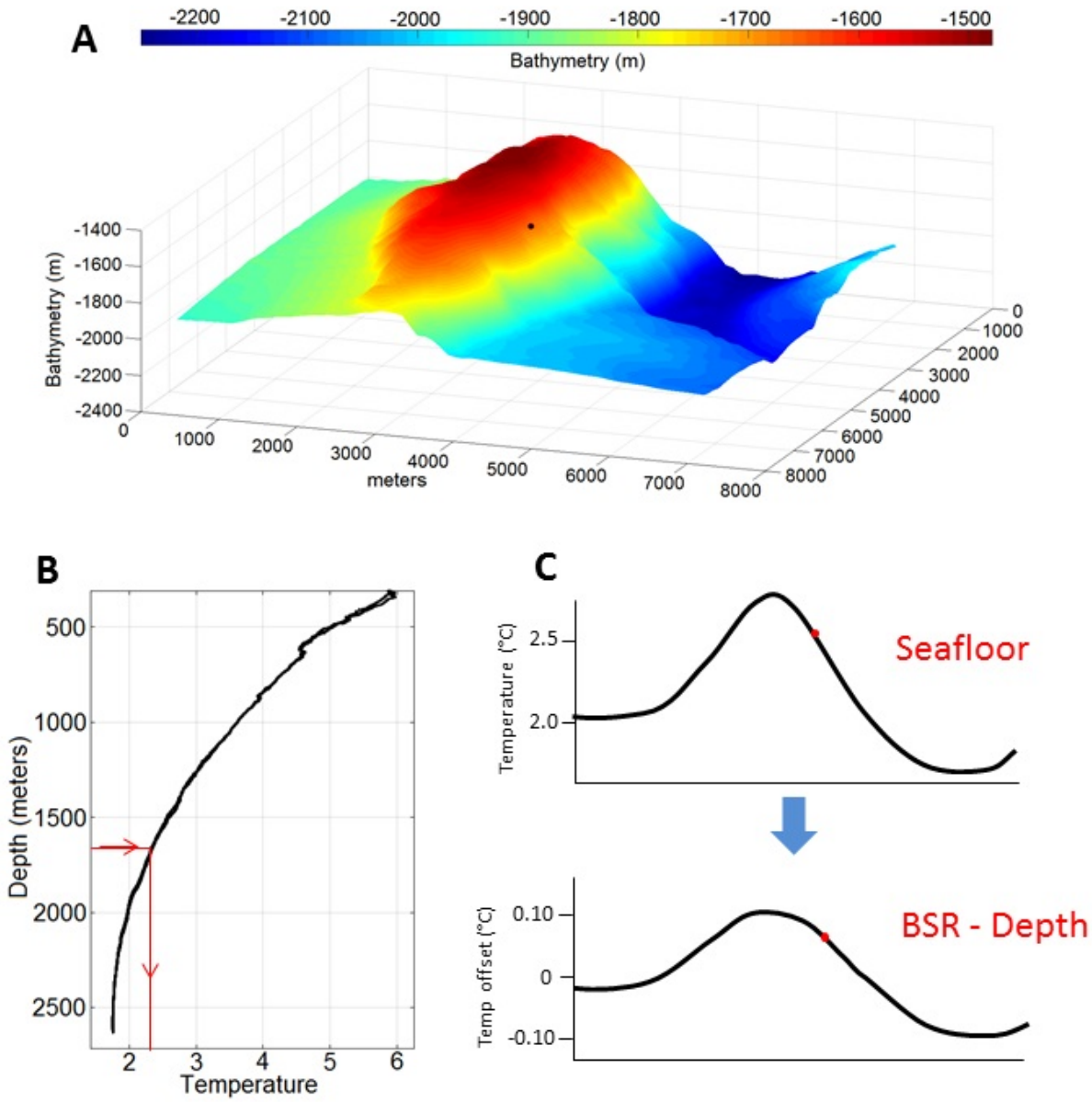

Figure 2.3: Methods to reduce bathymetric impacts on heat flow A) Seafloor depth is extracted for an area that is 10x the BSR depth on all sides of the BSR location (black dot). B) Using the CTD cast, the seafloor temperature for each bathymetric cell is determined. C) Seafloor temperatures are propagated down through the sediment to the BSR depth. The temperature offset at the BSR location (red dot) is then added to the BSR thermal gradient.

Sediment Accumulation Corrections

The rapid sediment accumulation rates present on the Washington margin, ranging up to 44 cm kyr^{-1} (Barnard, 1978), produce a transient decrease in the surface heat flow value (Hutchison, 1985; Kaul et al., 2000). Correcting for recent sedimentation requires both the interval of the deposition and the sediment accumulation rate, which varies widely along a continental margin due to erosive turbidite channels and distance from fluvial inputs. Sediment accumulation rates for the Cascadia accretionary wedge were determined using six age-dated piston cores with lengths ranging from 1.78 to 5.28 meters (Barnard, 1978)[Figure 2.1] applied over an interval of 10,500 years (Table 2.2). The low density of sampling sites required the accumulation rates to be averaged into zones, which included anticlinal ridges, sedimented ponds, and turbidite channels. These corrections were applied to the heat flow values using the solution to the thermal growth model (Martin et al., 2004)[Equation 2.4]:

$$
\begin{aligned}
&Q_{BSR} = \\
&Q_B\Big[1 - \frac{1}{2}\Big[\Big(1 + \frac{v_s t_s}{Z_{BSR}}\Big) erfc\Big(\frac{Z_{BSR} + v_s t_s}{2\sqrt{\kappa_s t_s}}\Big) \\
&- \Big(1 - \frac{v_s t_s}{Z_{BSR}}\Big) e^{(\frac{-v_s Z_{BSR}}{\kappa_s})} erfc\Big(\frac{Z_{BSR} - v_s t_s}{2\sqrt{\kappa_s t_s}}\Big) - 2\Big(\frac{v_s t_s}{Z_{BSR}}\Big)\Big]\Big]
\end{aligned}
\tag{2.4}
$$

The required parameters include the sediment accumulation rate (v_s, in meters year^{-1}), depth of the BSR below seafloor (Z_{BSR}, meters), and sediment accumulation time interval (ts, years). A sediment thermal diffusivity (κ_s) of 1.15x10^{-7} m^2 s^{-1} was determined *in-situ* within the mid-slope terrace of the COAST Line 4 at 1049 meters water depth (Homola et al., 2015). Q_B is the bathymetrically corrected heat flow, resulting in Q_{BSR}, the basal heat flow with effects of sediment accumulation removed. Based on the uncertainties associated with the BSR heat flow calculation (Section 2.2.2), the calculated uncertainty of the BSR heat flow is approximately ±10%, similar to previous estimates (Davis et al., 2003; Marcaillou et al., 2006), with a maximum of ±18% for local areas of rapid bathymetric variations.

Table 2.2: Sediment accumulation rates within the study area used to correct the BSR heat flow estimate

Core Name	Source	Type	Latitude	Longitude	Depth (meters)	Core Length (cm)	Accumulation rate (cm kyr^{-1})
53 -17	Barnard	Piston	N 46° 53.5'	W 125° 40.6'	1829	528 (Main) 131 (Aux)	16
53 -19	Barnard	Piston	N 46° 50.1'	W 125° 22.9'	2003	333 (Main) 52 (Aux)	1.9
53 -22	Barnard	Piston	N 46° 26.2'	W 125° 17.2'	2111	265 (Main) 107 (Aux)	23
63 -08	Barnard	Piston	N 46° 25.3'	W 125° 36.3'	2308	178 (Main) 5 (Aux)	2.5
68-23	Barnard	Piston	N 46° 54.0'	W 125° 4.50'	1156	230 (Main) 86 (Aux)	22
63-10	Barnard	Piston	N 46° 34.2'	W 125° 17.4'	1821	518 (Main) 135 (Aux)	43
# 9	Hedges	Box	N 46° 46.2'	W 127° 00.0'	2600	39.5	5.6 ± 0.3
#19	Hedges	Box	N 46° 45.0'	W 126° 30.0'	2525	43	7.9 ± 0.4

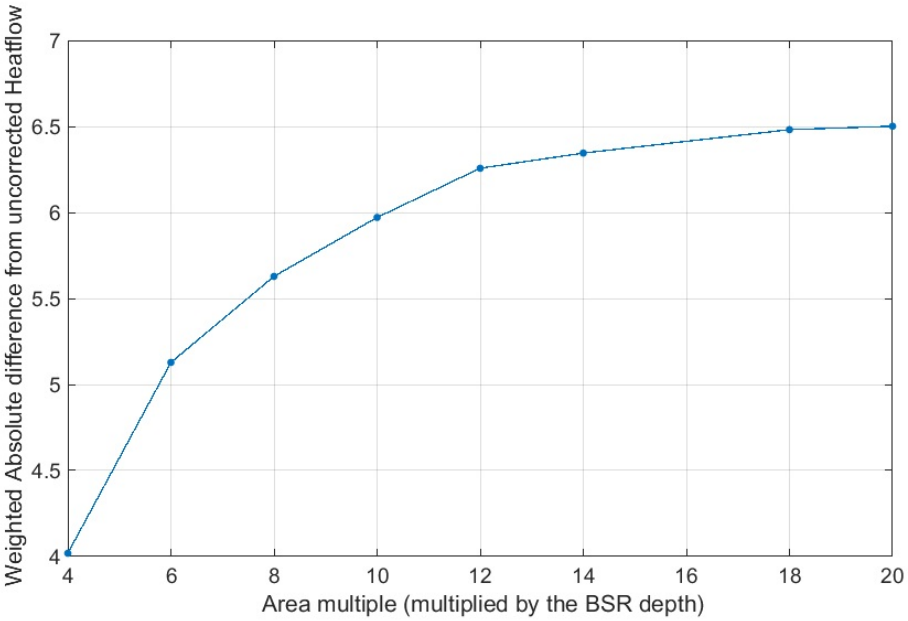

Figure 2.4: Bathymetric scaling test to determine the most appropriate multiple of BSR depth to surface area that best corrects the heat flow within the bathymetric correction. The Y-axis is the average absolute difference between the corrected and non-corrected BSR heat flow using BSR data from Line 1 MCS profile.

2.2.2 BSR Uncertainty Analysis

Accounting for the degree of uncertainty in Bottom Simulating Reflector (BSR) heat flow estimates requires evaluating each parameter included within the BSR heat flow calculation. These uncertainties include: 1) Z_{BSR} depth estimate, both 2) seafloor and 3) BSR temperatures (T_{BSR}), and 4) sediment thermal conductivity. Subsequent internal requirements were also taken into consideration that include seismic velocity, pore fluid pressure, and chemical composition of the hydrate.

BSR Depth Estimate

Estimating the uncertainty associated with BSR depth within the sediment column is a twofold problem as uncertainty due to two-way travel time (TWT) and seismic velocity

(Vp) interact with each other. Davis et al., (Davis et al., 2003) pointed out that variations in Vp have a minimal effect on heat flow, as seismic velocity will affect both the depth and temperature estimates simultaneously and in the inverse direction. For example, a substantial 100 m s^{-1} increase in seismic velocity over the entire depth from the seafloor to the BSR results in a +14 m deepening (6.1% increase) of the BSR, a +0.22°C (1.5%) temperature increase and +0.197 MPa (2.73% increase) pressure increase, which changes the heat flow by -3.34 mW m^{-2} or 5%.

The presence of as little as 15% of hydrates by volume within the sediment pore space will increase the overall sediment density and produce higher seismic velocities (Yuan et al., 1996; Hornbach et al., 2003; Malinverno et al., 2008). This increase in Vp due to the presence of hydrates has been detected only using high resolution downhole logging equipment offshore Vancouver Island margin and was correlated with the presence of $\sim$ 20% hydrate in the pore spaces (Yuan et al., 1999). For the current study, we did not account for any changes in velocity due to hydrate as that would require a consistently high hydrate presence of greater than 20% occupying the pore spaces, distributed uniformly throughout the sediment column. In addition, no abnormal increase in Vp within the top 500 meters was detected in either the shipboard processing or in post-cruise processed Vp profiles. Borehole work offshore Vancouver Island, Canada and Oregon, USA measure hydrate concentrations near the BSR depth as low as 1% to 2%, leading to the conclusion that the BSR is caused more by the presence of free gas below the reflector than by the concentration of solid hydrate in sediment pore spaces above the phase change horizon (Kastner et al., 1995).

Based on the available access to the seismic data, standard estimates of Vp were difficult to determine for all 9 *Langseth* MCS lines. Differences between shipboard and post-processed Vp value estimates within the top 500 m of Lines 3 and Line 5 suggest an uncertainty of $\pm$170 m s^{-1}. This Vp uncertainty is larger than estimates in previous BSR heat flow studies (Yuan et al., 1996; Grevemeyer and Villinger, 2001; Golmshtok et al., 2000), although it is similar to reported differences of >100 m s^{-1} between seismic velocity estimate derived from

MCS and borehole derived Vp (Kastner et al., 1995). Based on the MCS source frequencies of 6 to 40 Hz or 6 to 70 Hz, which varied from line to line in the COAST data, the TWT vertical resolution is roughly ±6 and ±4 milliseconds or ±5 and ±3.3 meters respectively, using the mean Vp of 1663 m s^{-1} for the top 500 meters. Utilizing Monte Carlo analysis, we conclude that a combination of TWT and Vp uncertainties result in an average BSR depth uncertainty of ±13.3 meters, comparable to previous work that derived similar values of ±8 meters computed using the integrated standard deviations (Golmshtok et al., 2000).

Pressure Calculation

Determination of *in-situ* pressure within the sediment column is required to calculate the temperature at the BSR depth and this determination depends on porosity, grain and water density, water depth, and sediment thickness. The two end members are lithostatic and hydrostatic pressure, where true pressure lies somewhere between these values [i.e., for Nankai drilling, see discussion in Saffer and Tobin, (Saffer and Tobin, 2011)]. Heat flow resulting from using the end members of either 100% lithostatic or 100% hydrostatic pressures will have an approximate 3 mW m^{-2} difference. Without drilling at the Grays Harbor margin site, it is not possible to determine the lithostatic/hydrostatic pressure ratio present at the depth of the BSR, and we assumed the pressure is 50% ±10% lithostatic resulting in a heat flow uncertainty of approximately ±0.4 mW m^{-2}.

Porosity values were calculated using Athys law (Athy, 1930) which has been previously shown to agree within ±0.04% porosity for borehole measurements (Grevemeyer and Villinger, 2001). This uncertainty corresponds to a ±0.16 mW m^{-2} variation in the heat flow values. Based on prior MCS work, porosity varies with along-strike distance for the Cascadia margin, as well as between localized areas such as sediment ponds and anticlinal ridges. However, the porosity compaction function roduces only a minimal variation in the heat flow calculation. For example, the change in L from 2500 m to 1500 m that occurs during a transition from the mid-slope terrace to the lower accretionary wedge produces a small change of 0.01 to 0.02 mW m^{-2} in the heat flow. For this reason, only one compaction

length of 1.2 km was used to simplify calculations. Borehole samples from the Cascadia margin show an uncertainty in grain density of ±34 kg m^{-3} (Malinverno et al., 2008) and only very minor (±1.3 kg m^{-3}) changes in the water density arising from temperature and salinity variations for the T_{BSR} and 33.5 psu values used in the heat flow calculation.

In addition to the chemical and physical properties of the sediment, a pressure uncertainty is produced from water depth estimates. Seafloor depths were derived from swath bathymetric data, which were corrected for tides, ocean swells, and water column sound velocity variations. Uncertainties in the measurement of seafloor to the BSR depth are described above and were accounted for in the calculated pressure uncertainty. It should be noted that the BSR depth uncertainty used for both depth and pressure calculations provides an example of how individual uncertainties can compound within the BSR heat flow calculation. Accounting for all uncertainty elements described above produce an overall uncertainty in the pressure measurement of ±0.15 MPa, which represents 0.7% of the calculated pressure. The pressure uncertainty corresponds to a BSR temperature range of ±0.06°C and since most BSR temperature estimates are in the range of 12°C, the temperature variability does not produce a distinguishable change in heat flow.

Temperature Uncertainty

Both seasonal and inter-annual bottom water temperature variations produce non-linear thermal gradients within the near surface sediment temperatures where BSRs are located as water column temperature oscillations propagate into and modulate the geothermal gradient. These variations in seafloor temperatures impact both surface and potentially BSR derived temperatures. A CTD profile collected during the survey cruise time period (July 12-24, 2012) was used to estimate the temperature of near-seafloor water column. These data were supplemented with temperatures from the Cascadia Initiative based Ocean Bottom Seismometers (OBSs) deployed along the Cascadia Margin during years 2011-2012 (Toomey et al., 2014). The Lamont OBS instruments were fitted with Paroscientific quartz temper-

ature sensors attached to their Absolute Pressure Gauge (APGs) that indicated the mean summer seafloor temperatures during the R/V *Langseth* survey time period had a mean offset of +0.024 °C (Table 2.1) when compared to mean annual temperatures. To account for this offset in the BSR calculation, the linear fit to the offset versus depth was applied to the top temperature (T_{SF}).

To support the use of the CTD temperature profiles in this study, a 2013 R/V *Atlantis* GeoPrisms cruise within the same survey area as the *Langseth* survey, deployed 39 thermal blankets (Johnson et al., 2013; Salmi et al., 2014) where each instrument recorded the water column temperature directly at the seafloor for individual periods of 5-6 days. The low thermal conductivity of the thermal blanket foam pad provides a unique situation where bottom water temperature is recorded ∼5 cm above the seafloor. While these records were taken a year later than the 2012 *Langseth* MCS survey, they show good agreement with the CTD cast (Figure 2.2).

To test the sensitivity of the geothermal gradient to seasonal bottom water temperature variability, OBS derived temperatures from summer 2011 to summer 2012 were propagated into the sediment assuming an *in-situ* experimentally derived thermal diffusivity (Homola et al., 2015). A temperature disturbance of 0.001°C was recorded at a sediment depth of 2 - 3.25 meters. Since most BSR depths range from 134 to 486 meters (mean depth of 229 ±35 meters), we assumed that seasonal bottom water temperature variability can be ignored as a significant source of uncertainty. Higher amplitude and lower frequency inter-annual variability due to an El Nino-Southern Oscillation (ENSO) event is harder to evaluate due to a lack of seafloor temperature records on these longer time scales. Geothermal gradients determined at ODP Site 889 on the Vancouver Island Margin appear linear within the borehole (Kastner et al., 1995), corresponding well with measured seafloor temperatures, and indicating a very limited sub-surface influence from bottom water temperature variations.

Radiogenic heating within the sediments can also alter the geothermal gradient. With an assumed radiogenic heating for margin sediments of roughly 0.6 μW m^{-3} (Lewis et al., 1988;

Wang et al., 1995; Oleskevich et al., 1999), radiogenic heating would amplify the present estimated surface heat flow of 60 - 90 mW m^{-2} by an insignificant 0.0002% to 0.0005%, for the typical BSR depth range of 250-500 meters.

The basic assumption of hydrate phase stability can be influenced by pore fluid salinity and the composition of the hydrocarbon component. A change in the pore water salinity of ± 1.5 g kg^{-1}, which is larger than previously reported uncertainty of ± 0.5 g kg^{-1} (Malinverno et al., 2008), would produce a relatively small variation of ± 0.07°C in the estimated BSR temperature, assuming a constant pressure, and would alter the heat flow by less than ± 1 mW m^{-2}.

Considering the above uncertainties in pressure and salinity assumption, the calculated overall BSR temperature uncertainty is ± 0.06°C. ODP boreholes drilled off Vancouver Island and other margins provide an independent check of BSR depth and temperature estimates. As examples, temperatures measured in Cascadia margin drill holes either showed good agreement with BSR-derived temperatures (ODP site 892; on the Oregon margin) or were $\sim$1°C colder than the BSR estimate (ODP site 889, Vancouver Island margin)(Grevemeyer and Villinger, 2001).

Thermal Conductivity

Uncertainty in sediment thermal conductivity represents a substantial unknown and has been previously described as a difficult parameter to quantify (Marcaillou et al., 2006). Scientific drill holes provide the best means of determining thermal conductivity of the sediment column down to BSR depths. Previous studies have used an uncertainty of $\sim$10% based on depth variation of thermal conductivity from ODP Site 889 thermal conductivity measurements (Hyndman et al., 1992). Thermal conductivity determined using the geometric mean of water (K_w) and sediment (K_s) thermal conductivities and Athys standard compaction law had a RMS of 0.12 W $m^{-1}K^{-1}$ with needle probe measurements on Cascadia ODP Sites 889 and 892, which is $\sim$11% of the average thermal conductivity measured value (Grevemeyer

and Villinger, 2001). Thermal conductivity can be empirically estimated from Vp measurements, using traditional velocity-porosity relationships, although these estimates produced larger uncertainties of 5-30% (Grevemeyer and Villinger, 2001). The possible presence of methane hydrate within the sediment pore spaces is believed to have little to no effect on the bulk thermal conductivity (Grevemeyer and Villinger, 2001).

For the present study, an uncertainty estimate for thermal conductivity of ±10% was assumed. Since integrated thermal conductivity values are also dependent on the depth of the BSR, the uncertainty associated with the depth parameter was also included. The overall uncertainty for sediment thermal conductivity in the depth range between the seafloor and the BSR was calculated as ±0.07 W $m^{-1}K^{-1}$, which produces a ±2.4 mW m^{-2} variation in heat flow.

Additional Corrections

Variations in seafloor bathymetry can cause vertical expansion or contraction of the subsurface isotherm distribution and appropriate corrections are required to reduce this effect. Uncertainties in the bathymetric corrections arise directly from the associated uncertainties in seafloor depth and BSR depth. The seafloor depths surrounding each of the BSR picks were determined using swath multi-beam bathymetric data that was corrected for small variations in the water column sound velocity and correlated with the MCS seafloor profiles based on GPS positioning. MCS along-strike profile uncertainty ranged up to ±3 Common Mid-points (CMP) (±30 m) in each direction along the profile and upward to 300 meters perpendicular to the profile, based on comparing the bathymetry from the MCS profiles with the multi-beam bathymetry. Uncertainty is small (∼0.2%) in areas of little bathymetric variation such as sediment ponds. However, the bathymetric uncertainty expands to +2% to +10% in areas of rough bathymetry, where small horizontal changes in the BSR geographic location results in large shoaling or deepening of bathymetry. In addition to seafloor depth uncertainties, the BSR depth uncertainty of ±8 meters produces an average of ±0.35% for

the bathymetrically corrected heat flow.

The rate of sediment accumulation on the Cascadia margin varies substantially, depending on (a) distance from the coastline and (b) the bathymetric features present. Turbidite channels receive the least amount of sediment accumulation due to erosion by turbidites (Fildani et al., 2006) and anticlinal ridge summits and upper flanks only receive sediment from above in the form of hemipelagic sediments. Mid-margin sediment ponds receive sediment both from the surface ocean and in some cases are temporary reservoirs for upper slope turbidites (Hedges et al., 1999; Goldfinger et al., 2012). The accumulation rates assigned to different regional areas were based on distance from the coast and the bathymetric features present (i.e. anticlinal ridge, turbidite channel, mid-slope sediment ponds) that encompass all the heat flow measurements and were applied using the technique described in Martin et al. (Martin et al., 2004). The average Cascadia margin accumulation rate is 12 cm kyr^{-1} across the lower and middle accretionary wedge. Sediment accumulation rate uncertainty was set to $\pm$21 cm kyr^{-1} based on Barnard, (Barnard, 1978) core 53/21 (Table 2.2), which was the piston core with the largest variability. Accounting for the accumulation rate and uncertainty modified the heat flow by 1 ± 0.66 mW m^{-2}. This resulted in a difference of -0.94 to +1.8 mW m^{-2} (from -1.06% to +2%) variation in the applied accumulation correction or a correction range of 0.05 to 2.80 mW m^{-2} (1.23% to 7.21%) to the uncorrected heat flow values.

Total Uncertainty for BSR Heat Flow

The overall uncertainty in the heat flow calculation from this estimate ranges from $\pm$5.9% to $\pm$7.36% ($\pm$1.2 mW m^{-2} to $\pm$8.7 mW m^{-2}) with an average $\sim\pm$6.6% ($\pm$5.2 mW m^{-2}). Uncertainty from the sediment accumulation rate correction is -1.1% to +2% and as high as +10% from the bathymetric correction, mostly due to uncertainty in the three dimensional seafloor depth estimates. An overall BSR uncertainty for a small number of heat flow values ranges as high as 18%, with a mean uncertainty value of $\sim$10% (Table 2.3). This average

compares well to similar estimates of BSR heat flow uncertainties including those that ranged from 1.7% to 17% (Martin et al., 2004), 10% to 20% (Marcaillou et al., 2006), and 10% to 50% (Grevemeyer and Villinger, 2001). In a cross-line comparison where COAST Line 10 overlapped Line 7, the relative uncertainty within the measured and corrected BSR heat flow values at the same location, showed an overall methodological precision of 4.2% to 5.4%.

Table 2.3: Overview of Bottom Simulating Reflector uncertainties

Property	Listed Uncertainty	Magnitude of Accretionary Wedge Heat Flow Uncertainty
BSR: Seismic Velocity	170 m s^{-1}	4%
BSR: TWT resolution	3.3-5 meters	2.5%
BSR: Porosity	±0.04% from Athys Law	0.2%
BSR: Total Pore Pressure	±0.15 MPa	∼0%
Seafloor Temperature	±0.3°C	2%
BSR Temperature	±0.06°C	<1%
Thermal Conductivity	±0.07 W $m^{-1}K^{-1}$	3%
Total BSR uncertainty	±7.7 mW m^{-2}	10%

2.2.3 Localized Heat Flow Behavior

BSRs were identified within 10 of the 11 *Langseth* MCS lines, resulting in a total of 40,232 individual heat flow determinations within the survey area (Figure 2.5). No BSRs were observed within the deformation front or beneath the most seaward anticlinal ridge. The westward limit of detected BSRs was observed along Line 4, beneath the second anticlinal ridge landward of the deformation front. Seafloor depths where BSRs are identified range from 2310 meters within sediment ponds between anticlinal ridges up to 710 meters along

Line 4. No BSRs were observed near the calculated methane hydrate stability water depth of 500 meters at this latitude of the Cascadia margin (Johnson et al., 2015). Of the two *Langseth* MCS lines oriented parallel to the deformation front (Figure 2.1), Line 11 has no detectable BSRs due to poor imaging of the sub-seafloor, although the adjacent Line 10 has better data quality and BSRs are observed along much of the profile. The data gap along Line 10 between Lines 2 and 3 was caused by an air gun shutdown due to the presence of large mammals within the area (Figure 2.5). BSRs are primarily located (51% of total picks) within exposed anticlinal ridges and within the prominent mid-slope terrace (21%) (Figure 2.5), while several buried anticlinal ridges in Lines 1, 2, and 5-7 contain BSRs located above buried structures, such as diapirs. There is a general lack of observable BSRs within the inter-ridge sediment ponds and turbidite channels.

BSR heat flow values show a generally decreasing trend landward from the deformation front, an expected result due to the plate convergence rate and the thickening overlying sediment wedge. Within the lower accretionary wedge, heat flow drops sharply from around 90 mW m^{-2} to 70 mW m^{-2} and then continues to decrease landward at a similar rate as observed in the lower wedge (Figure 2.5B). An abrupt and systematic decrease in heat flow of approximately 12 mW m^{-2} occurs approximately 43 kilometers east of the deformation front, the furthest landward extent of the mid-slope terrace (Figure 2.5B). Another distinct feature within the heat flow profiles is an increase in heat flow exceeding 20 mW m^{-2} over a prominent sharp anticlinal ridge located 30 to 35 km from the deformation front within Lines 1- 5 (Figure 2.5A). Low heat flow values present on the eastern upper margin segment of Line 4 are distinct from other profiles in the same region (Figure 2.5B).

2.3 Subduction Thermal Model

2.3.1 Thermal Model Methodology

A finite element model (FEM) was constructed to represent a 2-D slice of the subduction zone replicating the thermal and geological conditions for each of the 9 across-strike MCS

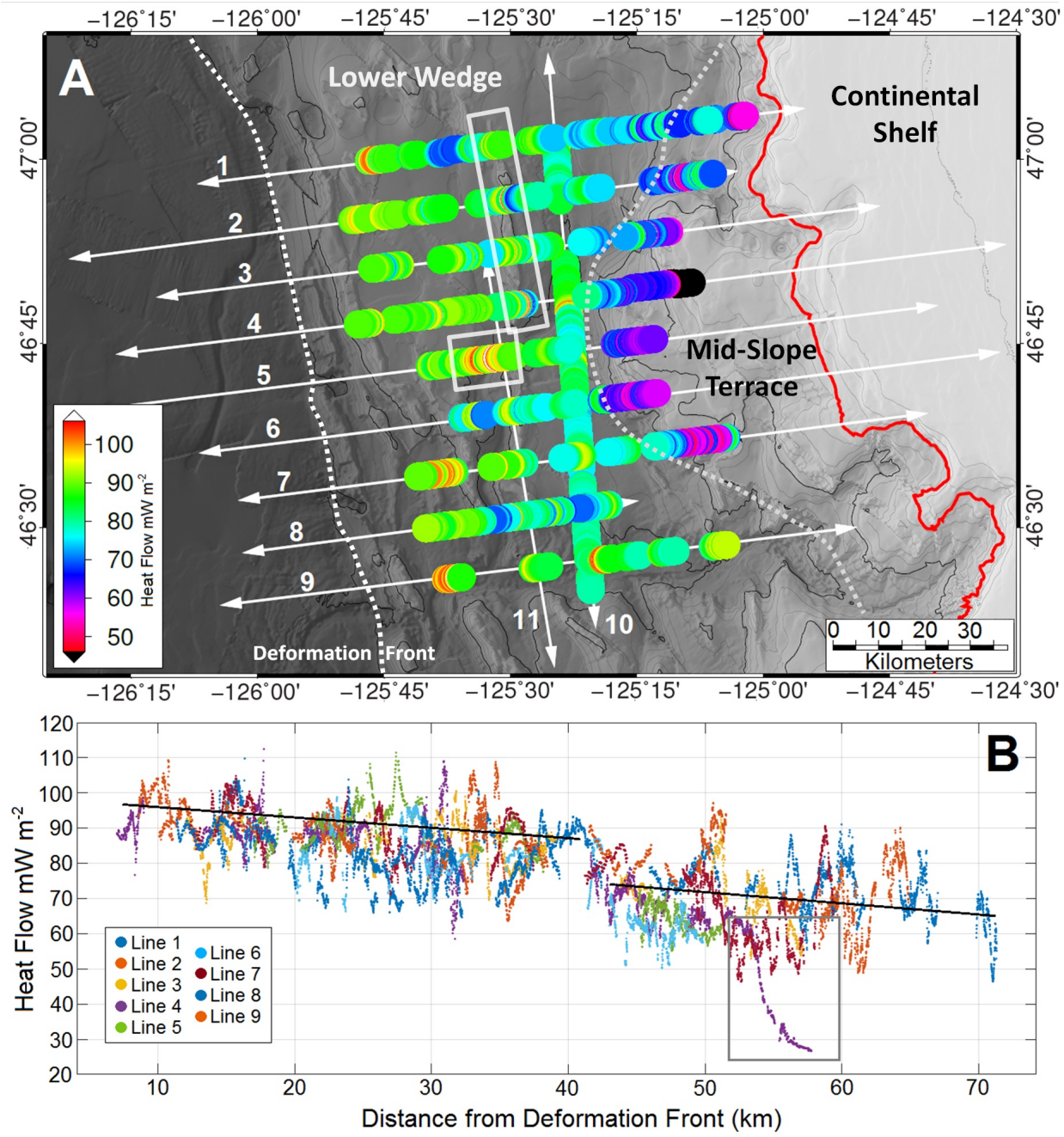

Figure 2.5: A) BSR heat flow measurements (circles) along the 11 MCS lines (white solid lines). Deformation front, lower and mid-slope defined by dashed grey lines. The 500 meter upper limit of hydrate stability is indicated by a solid red line. B) All heat flow profiles are indexed based on distance from the deformation front. General heat flow trends are traced by black lines. The grey box outlines the abnormally low heat flow values observed along Line 4.

profiles. This FEM produces surface heat flow values that can be compared with BSRs and continental heat flow values. We use the algorithm of Wang et al. (Wang et al., 1995) previously used in many subsequent heat flow studies (Harris and Wang, 2002; Harris et al., 2010; Cozzens and Spinelli, 2012). The FEM uses an 8-node construction with a corresponding thermal element defined by estimated thermal parameters governed by the following equation (Equation 2.5),

$$0 = \bigtriangledown \cdot (K_B \bigtriangledown T) - \rho c v \cdot \bigtriangledown T + Q_R \tag{2.5}$$

where c is volumetric thermal capacity, K_B is bulk material thermal conductivity, v is material velocity, T is modeled temperature, and Q_R is radiogenic heating. The thermal model was iterated until the thermal environment reached steady state.

The thermal model internal structure was determined by assigning zones corresponding to physical/geological units of the CSZ such as the depth and thickness of the downgoing Juan de Fuca plate (Flueh et al., 1998; Parsons et al., 1999) and the location and shape of the Siletz terrane; an oceanic basaltic complex accreted onto the North American plate (Blackwell et al., 1990; Parsons et al., 1999; Wong, 2015). Unfortunately, little is known of the *in-situ* state of the Siletz rock properties but data based on published laboratory, seismic velocities, and exhumed sections of subducted crust are used instead.

Subduction Zone Geometry

The geometry of the FEM (Figure 2.6) is defined through node location, providing the internal physical structure of the model. The young (8.5 Ma) lithosphere of the Juan de Fuca plate has not yet reached thermal equilibrium, therefore isotherms at the western boundary and lithosphere thickness are assigned a full theoretical thickness of 95 km (Stein and Stein, 1992). This assignment allows the plate and upper mantle geotherms to evolve with age based on a modified half space cooling model. MCS profiles collected from the Juan de Fuca Spreading Ridge to the Cascadia margin offshore Washington suggest a relatively constant

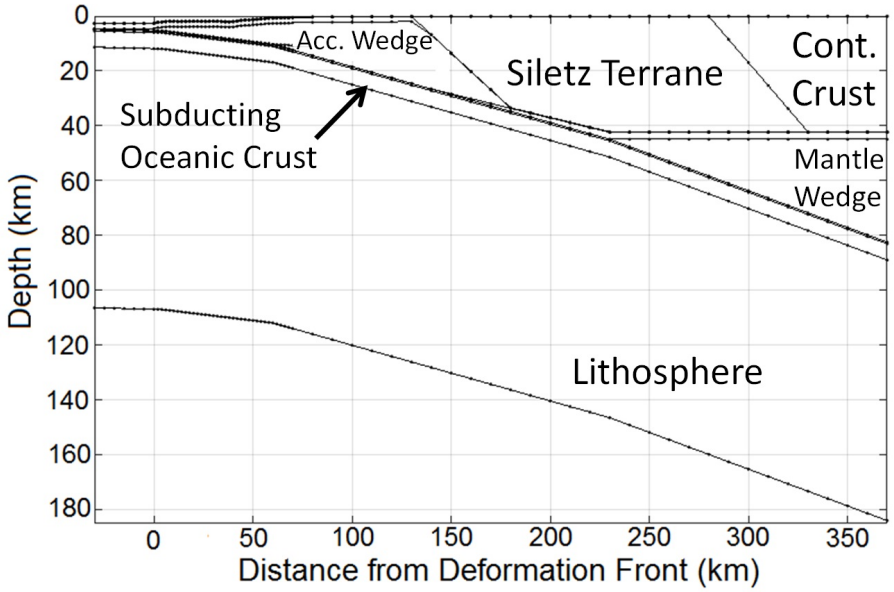

Figure 2.6: Thermo-physical units of the finite element model based on active and passive seismic profiles.

crustal thickness of 6.5 km (Han et al., 2016). The COAST *Langseth* seismic profiles indicate that the sediment thickness at the deformation front varies between 2.5 and 2.9 km (Table 2.4), values which were incorporated into the corresponding thermal models for each MCS line. We assigned a 1° slope for the incoming oceanic plate just west of the deformation front due to the pre-subduction bending of the incoming plate (Han et al., 2016). The plate continues to subduct at a shallow angle of 5° beneath the outer accretionary wedge, increasing to 10° at the mid-accretionary wedge 60 km from the deformation front, and continuing to increase to 15° as the oceanic plate separates from the continental plate (Flueh et al., 1998; Parsons et al., 1999; Han et al., 2016).

The western boundary of the Siletz terrain at the Washington Coast marks the transition from accretionary wedge sediments to the basaltic Siletz backstop which extends to the eastern edge of Puget Sound for this latitude (Parsons et al., 1999). Incorporated seafloor depths were estimated from bathymetry within the GMRT database (Ryan et al., 2009) and

Table 2.4: Sediment thickness on the incoming Juan de Fuca Plate prior to subduction and modeled plate temperature at the deformation front for the nine MCS profiles perpendicular to the deformation front.

Line Number	Sediment Thickness (meters)	Temperature (°C)
1	2288	175.3
2	2385	179.5
3	2382	179.2
4	2252	174.3
5	2077	166.3
6	2067	166.5
7	2015	164.3
8	2049	165.5
9	2162	171.0

extrapolated to a 2 km horizontal grid to fit the mesh resolution of the model. The incoming oceanic plate was assigned a horizontal velocity of 40 mm year^{-1} (Clague, 1997; McNeill et al., 1997) and adjusted as the plate subduction angle increased (Figure 2.7). Estimated mantle wedge circulation beneath Puget Sound was determined based on the subduction rate of the incoming oceanic crust (Figure 2.7). The North American continental plate has an estimated thickness of 42 ± 6 km (McCrory et al., 2014). Slight ambiguities in the assumed model geometry account for a potential heat flow variability of ±3.5 mW m^{-2} at the deformation front and ±1 mW m^{-2} in the Puget Sound Basin, corresponding to uncertainties of the plate interface of ±4.7°C and ±22°C respectively.

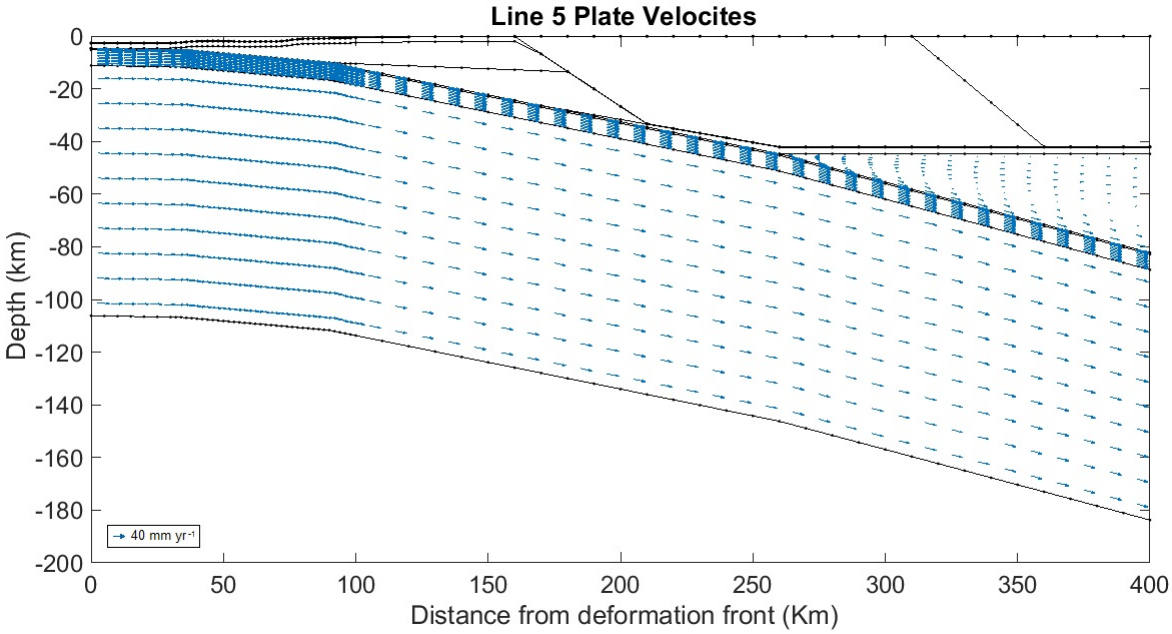

Figure 2.7: Thermal model geometric velocities for the downgoing plate and back-arc mantle. Incoming plate velocity is set to 40 mm yr^{-1}.

Boundary Conditions

Boundary conditions for the numerical model are calculated using the same thermal properties assigned to the thermal model (Table 2.5). The top (seafloor and land topography) and bottom boundaries are set to constant temperatures of 2°C and 1450°C, respectively (Stein and Stein, 1992). A 500 meter thick thermal zone, utilizing thermal parameters that match the average BSR variables (Table 2.5), was incorporated into the top of the model to calculate surface heat flow. The landward boundary conditions consist of a continental geothermal gradient parameterized with a heat flow of 60 mW m^{-2} and an adiabatic gradient of 0.3°C km^{-1} through the mantle wedge (Blackwell et al., 1990; Hyndman and Wang, 1993). The seaward boundary geotherm, located 30 km seaward of the deformation front, was calculated using the program SlugSed (Hutnak and Fisher, 2007). This finite element model simulates the thermal evolution of the oceanic plate in 2-D and includes the thermal impact of the rapid sediment accumulation as the oceanic plate ages. Thermal diffusivity

was adjusted within the SlugSed model to closely match heat flow values obtained using two thermal blankets deployed west of the deformation front (Salmi et al., 2014; Johnson et al., 2013). All other parameters within SlugSed were kept identical to the FEM. The plate is assumed to be 7.75 Ma old at the western edge of the model, with continuous spreading producing an oceanic plate age of 8.5 Ma at the deformation front (Wilson, 1993).

Thermal Parameters

Radioactive decay due to heat production (Q_R) within the sediments will increase surface heat flow. Estimates of radiogenic heating were assigned to each sub-surface structure using *in-situ* measurements and published models (Table 2.5). Radiogenic heat production for the Siletz terrain, composed largely of oceanic basalt, is assumed to be 0.02 μW m^{-3} (Wong, 2015). The assigned effective coefficient of friction of 0.03 along the subduction thrust is consistent with previous published values (Wang et al., 1995; Wada and Wang, 2009; Harris et al., 2010). Thermal conductivity was determined using a porosity model that varies both as a function of depth due to variable sediment compaction and across-strike to account for large porosity changes within the sediment column. Excluding the top two kilometers of accretionary wedge sediments, thermal conductivity values for each thermo-physical unit are reported in Table 2.5. A variation of 10% in model thermal conductivity values can offset offshore heat flow values near the deformation front by $\pm$12 mW m^{-2} and alter plate temperatures by $\pm$0.5°C at the deformation front increasing to $\pm$10°C near the mantle tip.

Seismic velocity analyses reveal a general across-strike variation in velocities that are attributed to porosity changes. The thermal conductivity values used in the model were assumed to be a direct function of these porosities. To capture the landward decrease in porosity within the thermal model, the nodes within the top 2 km of the accretionary wedge were assigned values of thermal conductivity based on their position within the margin. The 2 kilometer depth limit was based on the depths within the MCS shipboard profiles that had identifiable reflectors. Bulk thermal conductivity (K_B) for each node with the top

Table 2.5: Model Thermal Parameters.

Name	Thermal Conductivity (W $m^{-1}K^{-1}$)	Thermal Capacity (J $m^{-3}K^{-1}$)	Radiogenic Heat (μW m^{-3})
Heat flow zone	1.1[A]	2.6 x 10^6	0.6[H,I]
Continental Crust	2.50[B]	3.3 x 10^6 [G]	0.2
Siletz terrain	1.59[C,D]	3.3 x 10^6 [G]	0.02[D,G]
Upper Sediment	Range[*]	2.6 x 10^6	0.6[F,H,I]
Main Sediment	2	2.6 x 10^6	0.6[F,H,I]
Lower Sediment	2.3	3.0 x 10^6	0.6[F,H,I]
Transition	2.9[G]	3.3 x 10^6	0.02
Mantle	3.1[G]	3.3 x 10^6 [G]	0.02[G]
Oceanic Crust 2A	2.9[E,F,K]	3.3 x 10^6 [F,I,K] 2.6 x 10^6 [G]	0.01[J]
Oceanic Crust 2B+C	2.9[E,F,K]	3.3 x 10^6 [F,I,K]	0.01[J]
Lithosphere	3.25	3.3 x 10^6 [I,K]	0.02[G]

[*] Range of thermal conductivity determined based on depth for upper 2 km of the accretionary sediments using an assumed grain thermal conductivity of 2.5 W $m^{-1}K^{-1}$

[A] Davis et al. (1990)

[B] McKenzie et al. (2005)

[C] Blackwell et al. (1990)

[D] Wong (2015)

[E] Wang and Davis (1992)

[F] Hyndman and Wang (1993)

[G] Wada et al. (2008)

[H] Lewis et al. (1988)

[I] Wang et al. (1995)

[J] Oleskevich et al. (1999)

[K] Cozzens (2011)

2 km was calculated using the geometric mean of water (K_w) and sediment (K_s) thermal conductivities: $K_B = K_w^{\phi} K_s^{1-\phi}$ where porosity (ϕ) was defined using $\phi = \phi_o e^{-z/L}$, which accounts for porosity reduction with increasing sediment depth (z) due to sedimentation compaction (Athy, 1930; Kinoshita, 2012). The surface porosity ϕ_o is assigned a value of 0.55 and composite thermal conductivity is calculated based on a grain thermal conductivity of 2.5 W $m^{-1}K^{-1}$ (Grevemeyer and Villinger, 2001) and water thermal conductivity of 0.6 W $m^{-1}K^{-1}$. Previous studies of the porosity scaling parameter (L) have found variations in compaction lengths exists along the margin cross-strike, with a value of L = 1.5 for the incoming plate sediments, L = 1.0 for the lower margin and L = 2.5 for the mid-slope terrace (Hyndman et al., 1993).

In comparison to the Vancouver Island margin, the high resolution seismic velocity structure of COAST MCS Line 5 (Fortin, 2015) shows similar porosity length scales and a sharp transition from 1.3 to 2.7 km from the lower to middle/terrace portion of the wedge, but only a very slight +0.1 km change from the incoming sediments to the lower wedge (Figure 2.8). For our model calculations, we assigned L values of 1.3, 1.2, and 2.7 km to the incoming sediment, the lower wedge and the remaining continental margin, respectively.

Uncertainty in the thermal model due to geometry and thermal properties (see Section 2.3.2) show that surface heat flow variability ranges from ±8 to ±16 mW m^{-2} for the lower accretionary wedge surface heat flow, primarily due to the large unknowns in thermal conductivity. This leads to a maximum plate temperature uncertainty of ±7°C at the deformation front, which reaches ±32°C at the mantle tip located 230 km east of the deformation front at a depth of 41 km.

2.3.2 Thermal Model Uncertainty

Thermal model uncertainty can be derived using multiple variables, including uncertainty in the assumed geometry of the geological units and thermal properties. The thermal structure of the incoming Juan de Fuca plate is based on the general half-space cooling model of

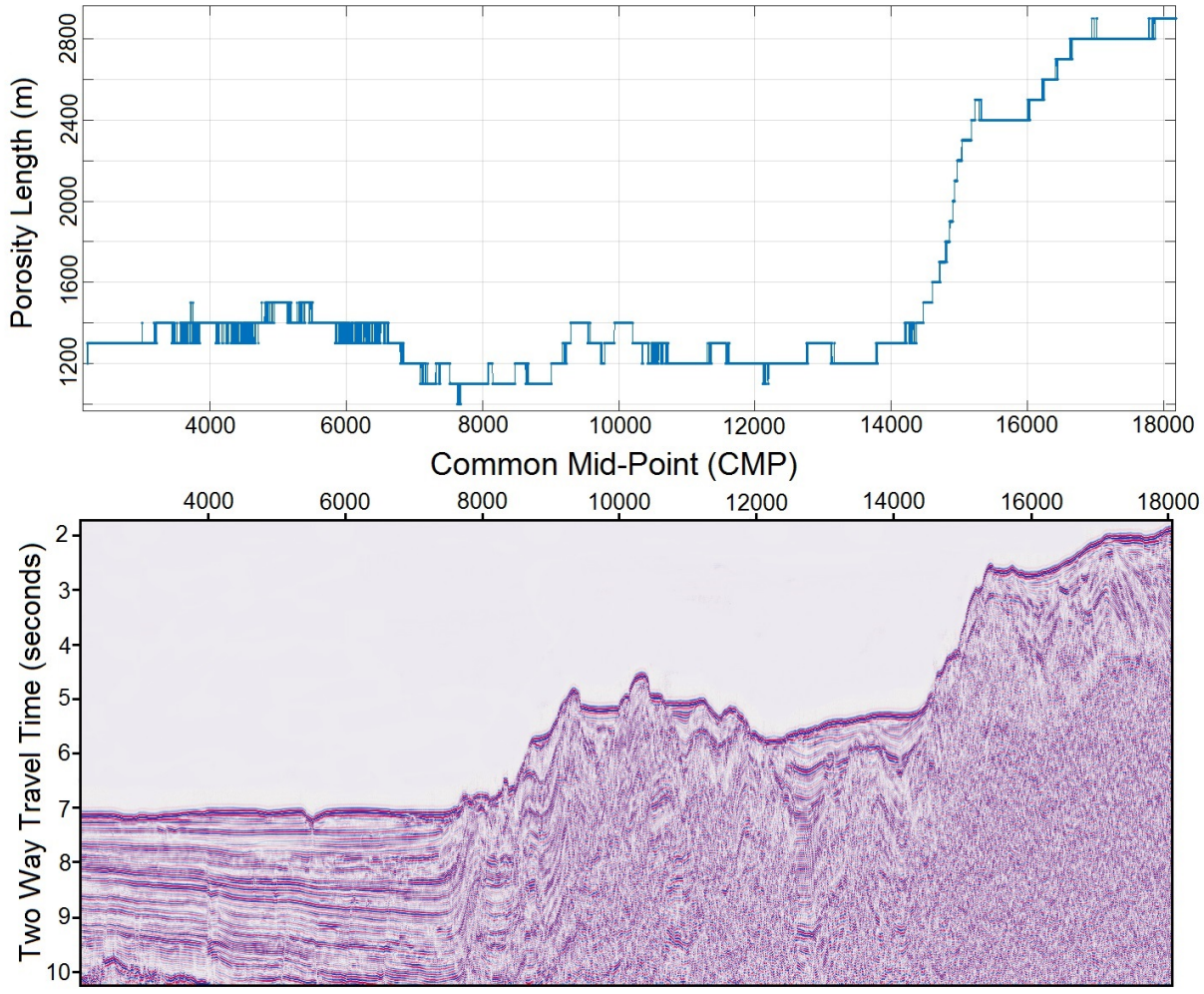

Figure 2.8: (top) Porosity scale length L (see text for equation) calculated for each common mid-point (x-axis) within the post stack depth migrated MCS Line 5 (bottom).

an oceanic plate (Stein and Stein, 1992), which has values and associated uncertainties of 1450° ± 60°C in temperature and 95 ±15 km in thickness (Stein and Stein, 1992; Herzberg et al., 2007). With a lithospheric basal temperature uncertainty of ±60°C, the temperature can have a plausible range of 1390° to 1510°C (Herzberg et al., 2007) that produces a maximum variation with the thermal model of 2.8% (9.4°C) for the plate interface at the deformation front. The impact of the lithospheric assumption on the surface heat flow has the most pronounced effect on the outer accretionary wedge where sediments are relatively thin in comparison to the accretionary wedge. The associated heat flow values change by ±3.5 mW m^{-2} at the deformation front, then decrease to ±1 mW m^{-2} at the coastline. The change in the lithospheric depth corresponding to the uncertainty of 95 ±15 km appears to have little effect on the thermal model, providing evidence that the 95 km depth limit is sufficient for the modeled upper mantle to cool appropriately as it ages.

Continental crustal thickness estimates have ranged from 38 km to 46 km for the southern Washington area (McCrory et al., 2014). Potential variations in continental crust thicknesses that depart from the average of 42 km produce no distinguishable variability in offshore plate interface temperatures and surface heat flow due to distance from continental crust. However, in the back-arc region, the plate temperature varies ±22°C within the mantle wedge tip. This temperature variation results in a ±2-4% variation in terrestrial surface heat flow at a distance of 150 to 250 km east of the deformation front. West of the deformation front, the incoming plate thickness was imaged using active source MCS and found to be roughly 6.5 km thick (Han et al., 2016). With variations in the plate thickness of ±500 m, plate temperatures could diverge as much as ±2 °C, a comparatively small (<0.5%) change in relation to the absolute plate temperatures.

Thermal Parameters

As described in Section 2.2.2, thermal conductivity is a relatively uncertain parameter that is often estimated to vary by ±10% and proves to be one of the largest sources of

uncertainty for heat flow studies (Grevemeyer and Villinger, 2001). Varying the thermal conductivity for the numerical model produced surface heat flow variations of ±12 mW m^{-2} offshore, as the oceanic plate approaches the deformation front, then drops to a low of ±1 mW m^{-2} within the Puget Sound Basin. This corresponds to an overall average plate boundary temperature variation of ±6°C (±1.25%) along the subducting plate boundary with a ∼±0.5°C variation at the deformation front. While surface heat flow has the largest percentage change offshore at the deformation front, the largest absolute variation in plate temperature of ±10°C is located beneath the Siletz terrane, located 130 to 230 km east of the deformation front.

The Siletz terrane is a unique geological feature as data derived from both onshore and offshore borehole measurements produces large variability in thermal conductivity and radiogenic heating. Thermal conductivity estimates have been reported as 1.69 W $m^{-1}K^{-1}$ (Blackwell et al., 1990; Wong, 2015), a value that is low in comparison to the continental crust with a traditional thermal conductivity of 2.5 W $m^{-1}K^{-1}$. Assuming a Siletz terrane thermal conductivity of 2.5 W $m^{-1}K^{-1}$ (McKenzie et al., 2005) produces a large spike in surface heat flow up to +11.6 mW m^{-2} (53%) over the Siletz terrane region which, in turn, corresponds to a plate interface temperature drop of 30°C within the Siletz and back-arc regions.

Radiogenic heating for the Siletz terrain is relatively unknown, with two reported values of 0.02 and 0.47 μW m^{-3} (McKenna and Blackwell, 2002; Wong, 2015). For the thermal model presented in this paper, 0.02 μW m^{-3} was used, although for comparison, a value of 0.47 μW m^{-3} would produce an increase in surface heat flow of +10 mW m^{-2} (+40%) and an increase of up to 45°C along the subducting plate boundary. While changes to the Siletz terrane thermal parameters produce large variability, most of this variability is confined to the onshore and back-arc basin areas, with little or no change in the offshore model parameters.

Overall Thermal Model Uncertainty

Accounting for all potential sources of uncertainty within the present study, the maximum possible surface heat flow variability ranges from ±8 to ±16 mW m^{-2} for the lower accretionary wedge surface heat flow, primarily due to the large uncertainties in the thermal conductivity. Maximum plate temperature uncertainties vary along-strike from ±7°C at the deformation front to ±32°C within the mantle tip located 230 km east of the deformation front at a depth of 42 km. This variance in estimated temperatures could shift the 350°C and 450°C isotherms by as much as ±17 and ±22 km, respectively, up-dip (west) and down-dip (east) along the subducting plate boundary. All thermal model uncertainty parameters are listed in Table 2.6.

Property	Listed Uncertainty	Magnitude of Accretionary Wedge Heat Flow Uncertainty
Model: Lithosphere Temperature	± 60°C	5.8%
Model: Lithosphere Depth	± 15 km	∼0%
Model: Continental Crust thickness	± 4 km	∼0%
Model: Thermal Conductivity	± 10%	8-14%
Overall Model Uncertainty	± 8-16 mW m^{-2}	10-20%

Table 2.6: Overview of Thermal Model uncertainties

2.3.3 Thermal Model Results

Individual thermal models for the accretionary wedge were constructed for all 9 MCS profiles oriented perpendicular to the subduction zone strike. Each model used distinct seafloor bathymetry and thermal conductivities, as described above, to emulate variations within each profile (Figure 2.9). The terraced shape of the Washington accretionary wedge has a pronounced effect on calculated heat flow values. Sediment thickness on the incoming plate ranged from 2540 meters on Line 7 to 2910 meters on Line 3 (Table 2.4) and was accounted for in the thermal models. The general north-south trend in sediment thicknesses arises from the regional distribution of Pleistocene sediment fans on the Juan de Fuca plate (Figure 2.1), which includes the Nitinat Fan to the north and the Astoria Fan to the south (Gutscher et al., 2001).

Modeled surface heat flow (Q_{model}) decreases systematically landward toward the Puget Sound Basin (Figure 2.9) due to the subduction of the relatively cooler oceanic plate that initially depresses isotherms within the overlying continental plate prior to reaching the warm back-arc mantle within the Puget Sound basin. Model values of seafloor heat flow on the incoming oceanic plate immediately west of the deformation front have an average value of 110 ± 1.1 mW m^{-2}. At approximately 75 km landward of the deformation front, most heat flow profiles have decreased to values near 53 mW m^{-2} coinciding with the seaward edge of the Washington continental shelf. Continuing eastward, heat flow decreases to 39 mW m^{-2} at the Washington coastline 135 km east of the deformation front, and falls to values near 21 mW m^{-2} beneath Olympia, Washington. Heat flow values from the FEM compare closely to onshore heat flow measurements from drilled wells located within 100 km north and south of the subducting plate dip profile (Blackwell et al., 1990)[Figure 2.9 and Figure 2.1- inset]. Heat flow values located within the lower margin, less than 20 km from the deformation front, display a pronounced trend where general heat flow values decrease faster in the northern lines compared to the southern lines (Figure 2.9). Line 9 is an exception to this trend within the first 5 km, due to the influence of a large isolated anticlinal ridge

located directly landward of the deformation front (Figure 2.1).

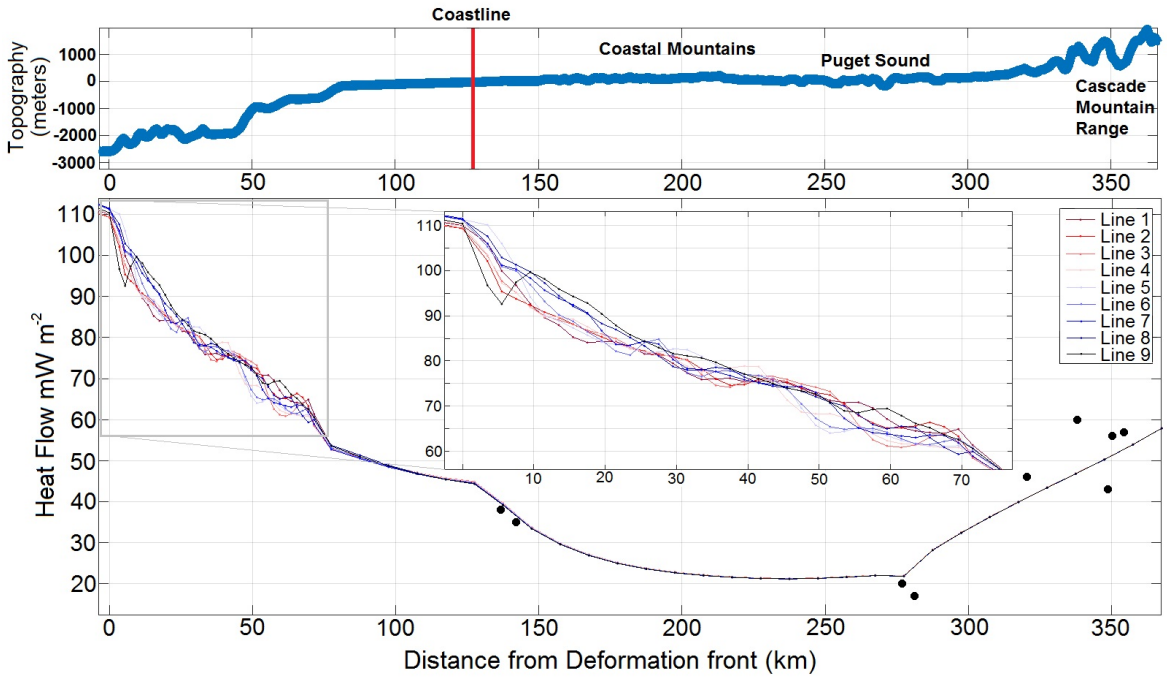

Figure 2.9: Large scale view of model derived surface heat flow profiles from the incoming Juan de Fuca plate to east of the Cascade Mountains. Topographic profile (top) indicates major geographical locations. Co-located black dots mark continental heat flow measurements (Blackwell et al., 1990).

2.4 Discussion

2.4.1 Localized Anomalously Low Heat Flow values

A recent slope failure produced by slumping of up-slope margin sediments appears to be the source of systematically low heat flow values along the landward portion of MCS Line 4 (Figure 2.5), but is not detected in the nearby seismic lines. Line 4 is parallel to an erosional turbidite channel at the outer edge of the mid-terrace plateau (Figure 2.10), although the heat flow anomaly remains after applying bathymetric corrections. This dramatic but localized decrease can be explained by slumping of the up-slope sediment which occurred too recently

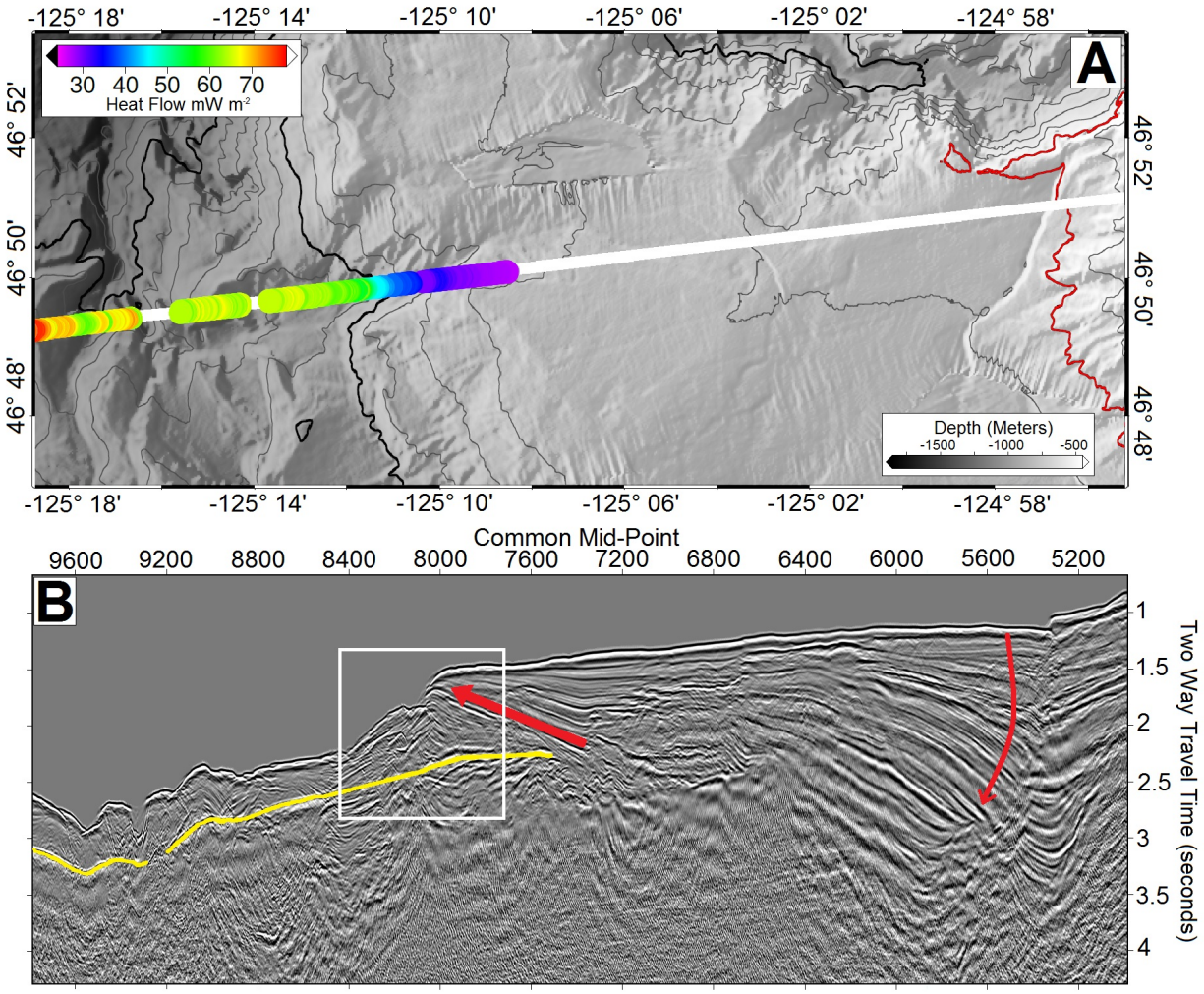

Figure 2.10: Swath bathymetry of the landward segment of Line 4 where the low heat flow anomaly occurs as shown in Figure 2.5B. Note: heat flow scale is different from Figure 2.5. A) The seafloor bathymetry with 500 meter contours shown as black lines and the 500 meter isobath indicated in red. The white line traces the MCS Line 4 trackline. B) COAST-based MCS profile co-registered with the bathymetry in Figure 2.5A. Red arrows show plausible sediment mass movement that could result in the observed abnormally low heat flow. The yellow line traces the BSR until it disappears at 7400 CMP.

to be in thermal equilibrium with the underlying sediments. If the BSR temperature has not had sufficient time to come into thermal equilibrium with the recently deposited sediments, it would still retain the isotherm distribution prior to the slope failure. Applying the pre-slump thermal parameters that include a BSR temperature of 14.1°C, heat flow of 61 mW m^{-2} and thermal conductivity of 1.17 W $m^{-1}K^{-1}$ to the post-slump environment requires an abrupt addition of 340 meters of extra sediment to produce the observed heat flow change, a change consistent with a structural interpretation of the MCS profile (Figure 2.10).

Previous studies have shown that the mid-slope terrace sediments of the Washington margin is an area presently undergoing east-west extension aided by the presence of the over-pressured underlying mélange and broken formation (McNeill et al., 1997; Adam et al., 2004). This collapse of the overlying surface sediments is confirmed by the COAST *Langseth* data where multiple extensional features include large listric faults (Figure 2.10B) visible in the MCS profiles and surface scarps produced by normal faulting imaged in seafloor bathymetry (Figure 2.10A). Rotation associated with listric faulting produces a corresponding upward shoaling toe along the thrust fault, providing the required 340 meters of displacement needed to reduce heat flow to the observed values. Although not conclusive, this rotational mechanism is the most plausible explanation for the systematically reduced heat flow at the eastern end of Line 4.

2.4.2 Comparison of Modeled to BSR derived Heat Flow

Comparison of observed BSR heat flow to predicted surface heat flow derived from the numerical model ($Q_{BSR}-Q_{model}$) reveals an overall average difference of +6.2 mW m^{-2} with a RMS of 10.2 mW m^{-2} (Figure 2.11). Areas of good agreement between the modeled surface heat flow and BSR derived heat flow include the western portion of the lines near the deformation front, including Lines 3-4 and 7-9 and the mid-slope terrace along Lines 4 through 7 (Figure 2.11). An anticlinal ridge located within the central portion of the lower wedge 25-35 km from the deformation front shows a large positive deviation in BSR heat

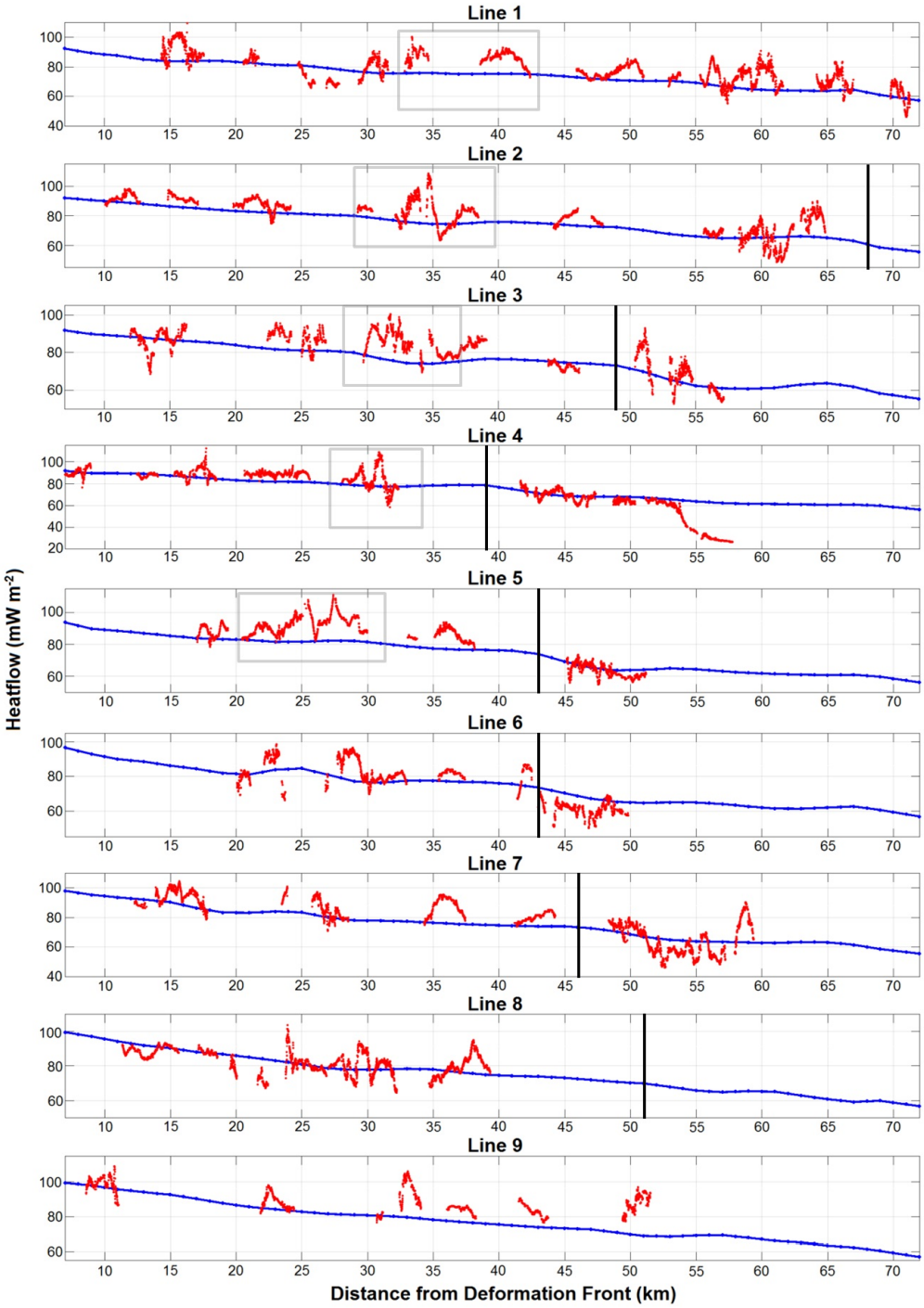

Figure 2.11: Comparison of modeled surface heat flow and BSR-derived heat flow. Individual profiles for MCS lines 1-9 visualize the offset where red dots are BSR heat flow and blue lines trace the model estimated heat flow. The vertical black lines indicate the onset of the mid-slope portion of the accretionary wedge and grey boxes outline elevated BSR heat low along a prominent anticlinal ridge.

flow from model values, attributed to localized upward fluid advection. The largest region of positive BSR/model heat flow difference along Lines 3-5 lies within the landward portion of the lower accretionary wedge located 20 to 45 km east of the deformation front. This departure is most notably along Line 5 where BSR heat flow values are 20 mW m^{-2} higher than modeled results (Figure 2.5 and Figure 2.11). Similar observations have been identified on the Vancouver Island margin (Davis et al., 1990; Hyndman et al., 1993)(Figure 2.11).

Modeled profile lines and BSR heat flow within Lines 3, 4 and 5 (Figures 2.9 and 2.11), both show a strong decrease in heat flow that begins approximately 45 km landward of the deformation front. Line 6 and 7 (Figure 2.11) also shows a similar systematic drop although the BSR heat flow drops roughly 10 mW m^{-2} lower than modeled surface heat flow. In this area, possible deep wedge thickening of the mid-slope terrace reduces the BSR heat flow, similar to that suggested for Vancouver Island (Wang et al., 1993). In contrast, areas without a bathymetrically defined lower margin, such as in Lines 1 or 9, show consistently decreasing heat flow values to the east. This observation strongly suggests that the presence of a lower margin terrace is a Cascadia accretionary wedge feature that strongly impacts the thermal environment.

2.4.3 Seismic Velocity Based Thermal Conductivity

The two *Langseth* MCS lines (Line 3 and Line 5) that were further processed post-cruise for sub-surface seismic velocities resulted in both more accurate and higher resolution velocity profiles. To determine how localized thermal conductivity varied at the spatial scale of anticlinal ridges (2 to 5 km), we constructed models for Line 3 and 5 with thermal conductivities determined using seismic velocities as a proxy. Sediment porosities were derived from the seismic velocity profiles using the following equations (Hoffman and Tobin, 2004),

$$V_p = A + B_\phi + \frac{0.305}{[(\phi + C)^2 + \frac{0.305}{(1.51 - A - B)} - C^2 - 2C - 1]} + 0.61(V_{sh} - 1.123)X_m \qquad (2.6)$$

$$X_m = tanh[40(\phi - \phi_c)] - |tanh[40(\phi - \phi_c)]| \tag{2.7}$$

Where the constants for this segment of Cascadia are V_{sh} = 1.057, A = 0.746, B = 0.532, C = 0.124, and ϕ_C = 0.295. This equation, compared to other velocity-porosity relations, also appears to have the best fit to ODP Site 808 located offshore Vancouver Island, which also provided some of the data used in the derivation.

Thermal conductivities derived from seismic velocities along Lines 5 and 3 showed elevated values beneath the pronounced anticlinal ridges present on the lower terrace and also a pronounced increase in porosity within the mid-slope terrace (Figure 2.8). These observations are similar to the porosity trends for these features reported for the Vancouver Island accretionary margin (Wang et al., 1993). Pronounced differences in surface heat flow in comparison to the standard sediment compaction model show an elevation of heat flow over the flanks and summit of the first anticlinal ridge (Figure 2.12). For example, Line 5 shows an increase in thermal conductivity approaching the deformation front that acts inversely to the reduction of heat flow due to deepening plate, producing a constant surface heat flow up to the deformation front. Areas over sharp, high amplitude ridges within the lower margin terrace have elevated heat flow values when compared to the standard compaction model, producing variations that are small (7%) but still significant.

2.4.4 Modeled Temperatures of the Plate Interface

The subducting Juan de Fuca plate has a poorly imaged decollement along the subducting plate fault plane and it is assumed for the purpose of this study that the sediment/ igneous crust interface is the plate boundary (Davis and Hyndman, 1989; Booth-Rea et al., 2008). Modeled temperatures along the crust/sediment interface at the deformation front for the nine closely spaced MCS lines range between 164°C to 179°C (Figure 2.13). It should be noted that the variations between modeled temperatures are within the range of uncertainty. Incoming plate boundary temperatures appear positively correlated with the thickness of the

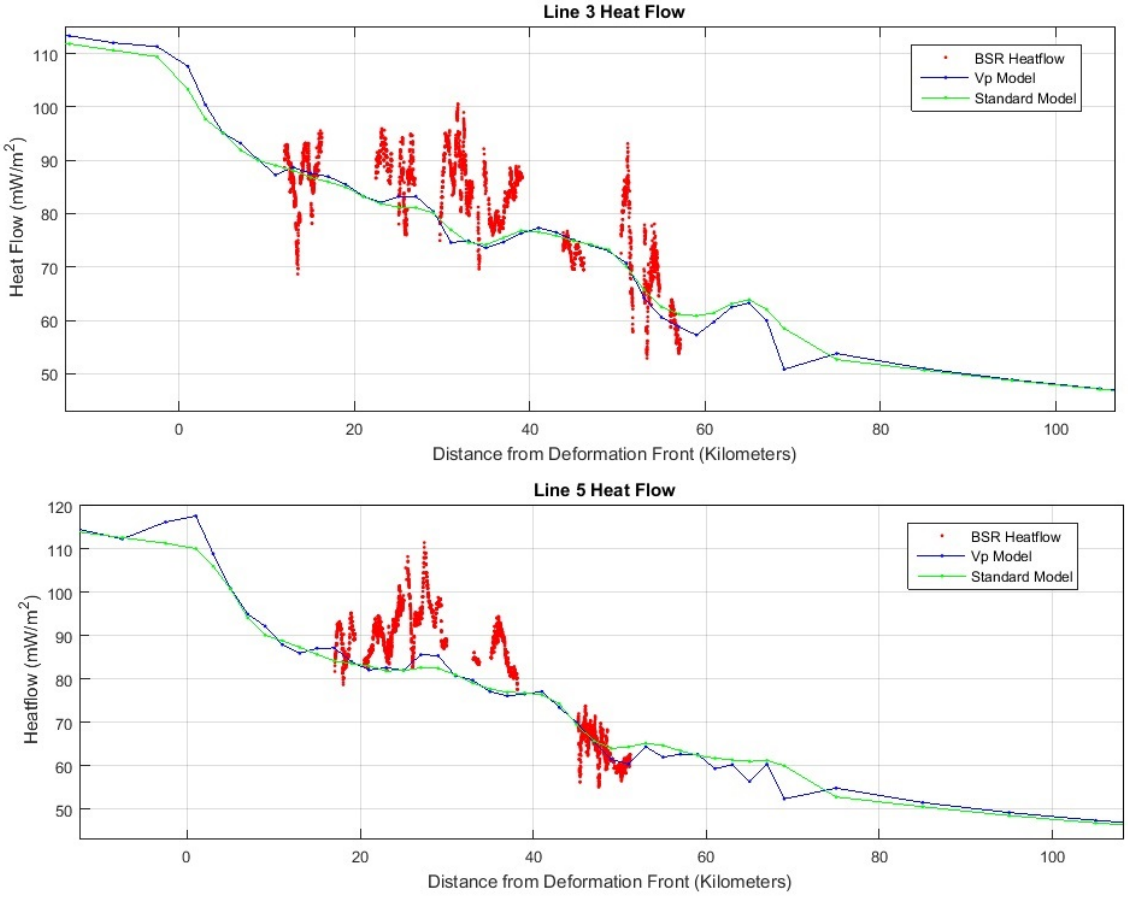

Figure 2.12: Modeled heat flow estimates of the lower accretionary margin for *Langseth* MCS Lines 3 and 5 utilizing bulk matrix thermal conductivity estimated using Athys Law and derived from seismic velocity. Red dots are the BSR heat flow associated with the individual MCS lines.

incoming sediment package (Figures 2.9 and 2.13; Table 2.4) and represent a source of along-strike thermal variability for the updip limit of the seismogenic zone. Our thermal models predict that the 350°C plate boundary temperature occurs 94 km east of the deformation front and the decollement temperature reaches 450°C at 155 km from the deformation front (Figure 2.13).

The location of the seismogenic zone, where tectonic stress is stored along the megathrust fault, depends, at least in large part, on thermally mediated processes (Hyndman et al., 1993; Cozzens and Spinelli, 2012). In older models, the updip limit of the seismogenic portion of the fault zone was determined by the smectite-illite transition temperatures between 100°-150°C (Hyndman and Wang, 1993; Moore and Saffer, 2001). However, recent studies have identified other chemical and physical processes such as porosity and diagenetic alterations that also alter the friction along the decollement in the temperature range of 60° to 150°C (Saffer and Marone, 2003; Lauer and Saffer, 2015). The development of chemical diagenesis along the downgoing plate interface and within the overlying sediments strongly depends on the temperature and pressure environment. Thermal modeling of the COAST dataset indicates a plate boundary temperature range of 164°C to 179°C at the deformation front. This isotherm distribution would place the smectite-illite thermal transition zone well within the overlying sediment column, rather than located at the sediment-igneous plate boundary. A smecitite-illite transition that lies within the overriding sediment package has implications with how the deformation front and accretionary wedge may deform and shift during a megathrust earthquake.

Based on chemical and physical properties of the relevant rock composition, the down-dip limit of the seismogenic zone has been suggested to correlate with the 350°C isotherm due to the brittle-ductile transition (Hyndman et al., 1993; Oleskevich et al., 1999; Hyndman, 2013). A higher temperature range of 350°C to 450°C for the fault interface has been assigned as a transition zone, where earthquakes will not originate but a megathrust fault can still slip if initiated further updip (Hyndman et al., 1997). It has been suggested the significant

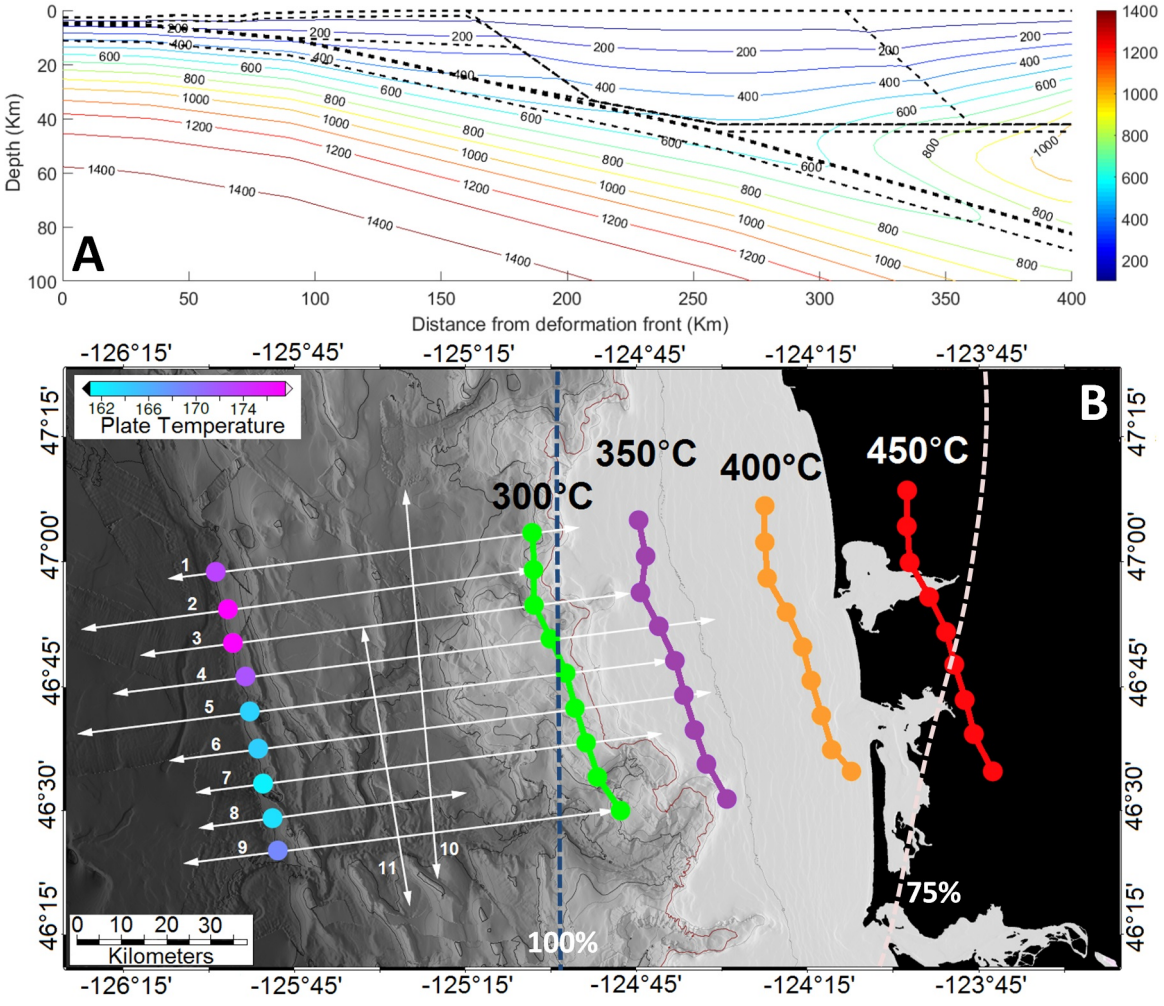

Figure 2.13: A) Modeled isotherm profile for MCS Line 5. B) Temperatures of Juan de Fuca plate sediment interface at the deformation front (circles) for all 9 profile lines, see color bar for scale. The 300°, 350°, 400°, and 450°C isotherms for the plate sediment interface are marked with connected circles. The COAST survey profiles are marked by white lines. Dashed line marks the fully locked (dark blue) and the 75% locked (white) plate interface based on geodetic modeling (Wang et al., 2003).

presence of quartz within the overlying oceanic derived Siletz terrane at the fault zone could elevate this transition zone temperature as high as 550°C (McCrory et al., 2014). Based on the assumed 150° to 350°C temperature bounds, the proposed fully-locked seismogenic zone is roughly 100 km wide along the southern Washington portion of the Cascadia Margin and we identify this location as fully offshore. This result compares well with the previous thermal model constructed by Hyndman and Wang, (Hyndman and Wang, 1995)[Figure 2.13], despite different lithostatic and incoming plate parameter assumptions.

Comparison of modeled thermal boundaries to the geodetic model locking zones from Wang et al., (Wang et al., 2003) shows that our thermally defined boundaries of 300°C and 450°C are located within the same regions as their zones of 100% and 75% locking. However, our thermal boundaries are slightly narrower in the northern section of the survey area (Lines 1 - 4) and diverge landward from the geodetic model further south (Lines 5 - 9 in Figure 2.13). Geodetic modeling by Schmalzle et al., (Schmalzle et al., 2014) that assume the outer portion of the accretionary wedge is fully locked show a similar locking distribution to Wang et al., (Wang et al., 2003) but appear more parallel to the coast, closer to our modeled isotherms. The general agreement between model-derived isotherms and geodetically determined locked percent argue for the importance of using both methods to determine seismogenic risk of subduction zones.

2.4.5 Fluid Advection

Upward fluid advection within the lower accretionary margin produced from sediment compaction or escape from within the igneous plate can explain the observed BSR heat flow departures from the models. Previous studies showing a similar overall increase in heat flow within the central portion of the lower wedge (Figure 2.5A) has been interpreted as evidence for substantial sub-surface diffuse fluid flow on the Vancouver Island margin based on Darcy fluid modeling of the accretionary wedge (Davis et al., 1990; Wang et al., 1993).

To estimate upward fluid advection, we first assume that most fluid is initially produced

from sources below the upper 500 meters of the sediment column and flows vertically into the near seafloor BSR zone (Le Pichon et al., 1991). Fluid movement can be estimated using Equations 2.8 and 2.9 below (Bredehoeft and Papadopulos, 1965; Hutnak and Fisher, 2007),

$$\frac{T_2 - T_1}{T_P - T_1} = \frac{e^{(\frac{\beta Z_{BSR}}{Z_p})} - 1}{(e^{\beta} - 1)} \tag{2.8}$$

$$\beta = \frac{v_z c_f \rho_f Z_P}{K_m} \tag{2.9}$$

using seafloor temperature (T_1), BSR temperature (T_2), matrix thermal conductivity (K_m), water volumetric thermal capacity ($c_f \rho_f$), the dimensionless parameter β, and modeled temperature (T_p) at ~500 meter sediment depth (Z_p). The resulting fluid flow estimates (v_z) ranged locally from weak down flow of fluid to a maximum fluid flow approaching +3.8 cm yr^{-1}. The median fluid flow for the study area was +0.53 cm yr^{-1}, based on the offset between BSR and model values (Figure 2.11). Comparison to previous estimates of fluid advection include +1.6 mm yr^{-1} based on standard porosity compaction (Le Pichon et al., 1991) and measured fluid advection within the Oregon coast of +3.2 cm yr^{-1} (Zwart et al., 1996), our estimates lie within the previous estimates of margin fluid flow.

2.4.6 Fluid Circulation within the underlying Crustal Aquifer

Recent models of subduction zones have examined active fluid circulation within the incoming oceanic Layer 2A aquifer at Costa Rica (Harris et al., 2010), Nankai, Japan (Yamano, 2003; Spinelli and Wang, 2008) and the Cascadia Subduction Zone (Cozzens and Spinelli, 2012; Gao et al., 2017). The rationale for incorporating hydrothermal circulation within the subducting oceanic crust provides an explanation for unusually high heat flow values identified seaward of the deformation front and lower than expected values landward within the accretionary margin that cannot be explained alone by the subduction of the oceanic plate (Yamano, 2003; Harris et al., 2010; Spinelli and Wang, 2009).

The possibility of active intra-crustal fluid circulation is closely linked to the permeability

of the crustal rocks. Crustal permeability within the incoming Juan de Fuca plate include estimates of 2 x 10^{-12} to 3 x 10^{-14} m^2 at the spreading ridge (Wilcock and McNabb, 1996), a range of 10^{-11} to 5 x 10^{-14} m^2 for the top 500 meters of 2 million years crust based on borehole packer tests (Fisher et al., 2008), to 0.7 x 10^{-12} to 2 x 10^{-12} m^2 (Fisher et al., 2008), and 10^{-10} m^2 for 3.5 Ma crust (Spinelli and Fisher, 2004). While there is clear evidence of fluid circulation within the eastern Juan de Fuca ridge flanks prior to reaching the deformation front (Spinelli and Fisher, 2004; Hutnak et al., 2006), a combination of increasing temperature, pressure, and alteration processes such as dehydration or quartz precipitation, are likely to dramatically reduce the subducting basaltic crust permeability (Fortin et al., 2011).

The high temperatures of the subducting oceanic plate can approach 400°C beneath the accretionary wedge (Davis et al., 1990), providing unique conditions that would reduce the permeability within the shallower crust in comparison to cooler subduction zone systems. Two chemical and physical processes that strongly reduce permeability within the igneous plate aquifer are alteration and subsequent quartz deposition within pore spaces. Theoretical models show a maximum quartz precipitation rate from silica rich pore fluid into the basalt occurs at around 295°C (Martin and Lowell, 2000; Breeding et al., 2003). In addition, increased lithostatic pressure in the temperature range present beneath the margin and causes a reduction in connected permeability (Fortin et al., 2011). To examine a range of possible reduced fluid circulation values, we tested permeabilities (k) for the Layer 2A of the subducting plate of 1 x 10^{-10}, 1 x 10^{-12}, and 1 x 10^{-14} m^2, which emulate high, medium, and low fluid circulation respectively. We also assumed that fluid circulation must cease above 400°C, where crustal permeability is theorized to dropped below 10^{-17} m^2 (Ingebritsen and Gleeson, 2015).

Using the methodology described in Cozzens and Spinelli, (Cozzens and Spinelli, 2012), we tested for fluid migration within oceanic crust by modifying the thermal conductivity of ocean crustal Layer 2A to simulate fluid circulation using the equation for the Rayleigh

number (Ra):

$$Ra = \frac{\alpha_v g k (Z_a)^2 \rho_f Q_c}{\mu \kappa K_m} \tag{2.10}$$

Where α_v is fluid volumetric expansion of 8 x 10^{-4} K^{-1}, Z_a (meters) is Layer 2A thickness, ρ_f (kg m^{-3}) is fluid density determined from salinity and temperature, μ is fluid viscosity of 1.89 x 10^{-4} kg m^{-1} s^{-1}, and κ is matrix thermal diffusivity of 1.75 x 10^{-7} m^2 s^{-1}. Q_c is conductive heat flow through the crustal layer, which was determined using a no-fluid-flow thermal model and the previous described range of permeability (k) steps. The revised thermal conductivity was calculated by multiplying the Nusselt number (Nu) by the original thermal conductivity for the Layer 2A (Table 2.5), determined using an empirical Rayleigh-Nusselt number relationship (Spinelli and Wang, 2008),

$$Nu = 0.08 Ra^{0.89} \tag{2.11}$$

Advection produces noticeably different heat flow results only for the highest permeability values (k = 10^{-10}). In this model run, elevated heat flow values appear landward for 10 km to the east of the deformation front and reduced heat flow appear throughout the rest of the profile until ∼130 km from the deformation front (Figure 2.14). Surface heat flow values produced for both medium and low tested permeabilities in the crustal aquifer show little change from the model with zero fluid flow. Based on the differences between the revised modeled heat flow with fluid circulation and measured surface heat flow values, we interpret these results as indicating the presence of either low or zero fluid flow within a low permeability ($< 10^{-12}$ m^2) Layer 2A. This result is in contrast with that of Cozzens and Spinelli, (Cozzens and Spinelli, 2012) based on different postulated high temperatures effects on the incoming Juan de Fuca plate.

With high temperatures occurring at shallow depths within Cascadia, temperature dependent sediment dehydration reactions will initiate further updip than on other subduction zone margins (Lauer and Saffer, 2015). The relatively shallow depth of these strongly

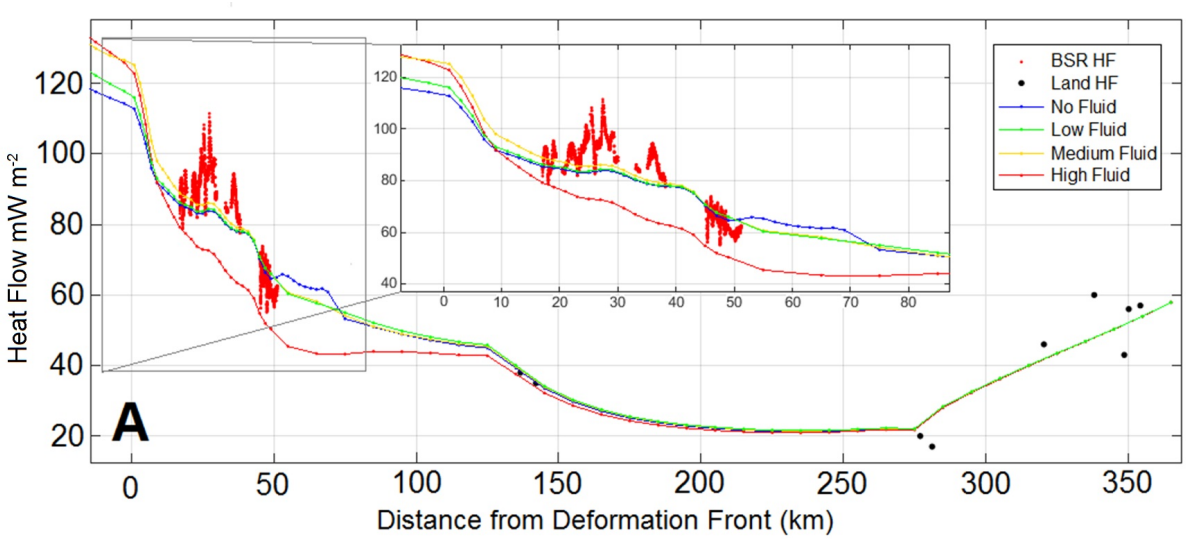

Figure 2.14: A two dimensional view of the various fluid circulation models for the subducted plate. Lines indicate surface heat flow for all crustal permeabilities ranging from no fluid flow (blue line) to high fluid flow (red line). Black dots mark the continental heat flow measurements and red dots are Line 5 BSR derived heat flow.

temperature-dependent reactions will result in the generation of unbound fluid within the accretionary sediments of the offshore section of the accretionary wedge. This is in contrast to models of fluid generation that occur further landward beneath the continental plate for subduction zones with lower accretionary wedge temperatures (Hyndman et al., 1997; Spinelli and Wang, 2008; Rotman and Spinelli, 2014). Supplemental fluid injection into the accretionary wedge could serve as a potential source of fluid, in addition to sediment compaction, that assists in the observed elevated BSR heat flow values when compared to modeled surface heat flow.

2.5 Conclusions

Bottom simulating reflectors derived from 11 multi-channel seismic profiles identify key variations in heat flow values within the southern Washington section of the Cascadia Subduction Zone. These new MCS profiles detected gas hydrate deposits extending across-strike,

ranging from 7 km east of the deformation front to the shallowest seafloor depth of 700 meters on the upper margin. After corrections for bathymetry and sedimentation, heat flow values follow a generally declining trend beginning approximately 95 mW m^{-2} and decreasing to near 60 mW m^{-2} at a 60 km distance from the deformation front. Abnormally low heat flow in the Line 4 MCS profile indicates recent large-scale slumping and listric fault rotation within an area permeated with abundant extensional normal fault zones visible in the COAST MCS profiles.

Thermal models corresponding to the nine across-strike MCS lines were constructed using variable accretionary wedge thermal conductivity values and thicknesses of the incoming sediment. Modeled decollement temperatures at the deformation front produced incoming oceanic plate interface temperatures ranging from 164°C to 179°C. These temperatures locate the updip limit of the seismogenic zone at the deformation front and identify a source of along-strike thermal variability. The downdip limit of the seismogenic zone at 350°C occurs west of the coastline at 94 km from the deformation front. These boundaries resolve a narrow 100 km wide seismogenic zone that is completely off-shore Washington State. Predicted plate sediment interface isotherms of 300°C and 450°C co-locate with the boundaries of 100% and 75% locking respectively based on geodetic models.

Comparison between measured and numerically modeled BSR heat flow identify localized but substantial departures that reflect vertical fluid advection occurring throughout the lower accretionary wedge terrace sediments. Differences between the BSR data and model estimates produce a fluid flow mean value of +0.53 cm yr^{-1} for the entire survey area, with localized fluid flow extremes approaching +3.8 cm yr^{-1}. Models derived for possible fluid advection within the underlying crustal Layer 2A produce a detectable deviation in surface heat flow for only the highest potential crustal permeability. However, surface heat flow matches well with lower crustal permeability values suggesting that substantial updip transport of crustal fluid is unlikely. The model results indicate that surface heat flow may not be an easily quantifiable means of determining permeabilities of 10^{-12} m^2 or lower, and

thus not a completely reliable test for detecting fluid circulation within crustal Layer 2A for this portion of the Cascadia Subduction Zone. An alternative path for fluid advection within the subduction zone is vertically through the sediments of the warm accretionary margin wedge that can explain the deviation between the observed BSR and modeled surface heat flow.

Chapter 3

DETAILED COMPARISON OF MULTIPLE SEAFLOOR HEAT FLOW INSTRUMENTS ACROSS AN ACCRETIONARY WEDGE

3.1 Introduction

Accurately determining near seafloor heat flow has wide ranging applications, from mapping of small scale fluid circulation, to large scale heat distribution resulting from tectonic movement. Direct seafloor heat flow data can be collected in areas independent of the hydrate stability zone, revealing fluid and thermal sediment/water column interactions. In addition, seafloor heat flow measurements allow for mapping of sub-seafloor localized fluid discharge/circulation features such as methane emission locations, faults, mud volcanoes (Eldholm et al., 1999; Krabbenhoeft et al., 2013), and salt diapirs (Hornbach et al., 2005; Macelloni et al., 2015). Where seafloor heat flow is collected over large (∼km) spatial scales, fluid reservoir residence times and basement temperatures can be determined (Langseth and Herman, 1981; Davis et al., 1992).

Surface heat flow is determined by the combination of two parameters, geothermal gradient and bulk sediment thermal conductivity. Instrument mounted thermistors placed at fixed intervals are used to estimate the geothermal gradient while thermal conductivity is estimated either *in-situ* or from recovered sediment cores. Understanding the ability of an instrument to accurately capture the local geothermal heat flow is a major concern when interpreting surface heat flow measurements. Such methodological uncertainty analysis has been an area of interest for previous studies in an attempt to improve the probe technique, primarily by reviewing the accuracy of the thermal conductivity measurements (Nagihara and Lister, 1993; Hartmann and Villinger, 2002). Overall heat flow uncertainty arises from

two general sources: 1) instrumental uncertainty and 2) external environmental uncertainties such as unaccounted variability in bulk sediment thermal conductivity and changes in ocean temperatures near the seafloor (Wang and Beck, 1987; Hamamoto et al., 2005; Harris et al., 2010).

The multi-penetration heat flow probe has become the standard heat flow instrument, widely used during the last four decades. Within the United States, variable 0.6 to 3.5 meter probe lengths are available for quick acquisition of the heat flow measurement utilizing *in-situ* thermal conductivity estimates (Lister, 1979; Wheat et al., 2004). The shorter 0.6 meter long probe can be deployed by an ROV or submersible, allowing for high spatial resolution heat flow surveys in areas of shallow sediment thickness such as on Baby Bare seamount (Wheat et al., 2004) and lightly sedimented off-axis spreading ridges (Johnson et al., 1993; Becker et al., 1996; Rona et al., 1996). The longer 3.5 meter Violin-bow Probe, deployed directly from a surface ship, can efficiently cover larger spatial areas such as oceanic plates (Moran and Lister, 1987; Villinger et al., 2017), active subduction accretionary wedges (Davis et al., 1990), and passive continental margins (Lucazeau et al., 2004).

Heat flow instruments also have nontraditional forms, where temperature sensors are attached to instruments initially designed for other purposes such as gravity cores (Gerard et al., 1962; Langseth, 1965; Kinoshita et al., 2008), piston sediment cores (Pfender and Villinger, 2002), along the core-liner of a Multi-coring system (Johnson et al., 2012), or short ROV sediment cores (Kinoshita et al., 2006). The standard sediment Multi-corer system is designed to simultaneously collect an array of 6 sediment samples over a small $\sim$1 m^2 area. It is primarily used to recover undisturbed geological samples for pore water analysis that can be collected in tandem with heat flow measurements (e.g., Haeckel et al., 2001; Murrell and Lehrter, 2011). The Thermal Blanket is an additional means of capturing heat flow that allows for the geothermal gradient to be captured within the instrument's foam. The Thermal Blanket is unique in that it does not require a soft seafloor sediment layer that other heat flow instruments depend upon and can be deployed in a multitude of hard seafloor

environments. These include heavily carbonated seafloor (this study), minimally sedimented exposed seamounts (Johnson and Hutnak, 1996), unsedimented mid-ocean ridge axial valleys (Johnson and Hutnak, 1997; Johnson et al., 2010; Salmi et al., 2014), and hydrothermally active lakes (Tivey et al., 2016).

While confidence in instrument performance has improved with evolving technology, data analysis methods have primarily concentrated on the accuracy of the temperature and thermal conductivity estimates, while environmental factors remain a persistent source of uncertainty. Conducting a heat flow study that incorporates more than one type of instrument allows for a quantitative comparison of how each instrument behaves in varying environmental conditions. The instruments determine the geothermal gradient over different sediment penetration depths, utilize different vertical sensor resolution and sampling time periods, and have different deployment methodologies. While earlier heat flow studies have included multiple types of heat flow instruments, there was no direct overlap between the measurement sites (Davis et al., 1992; Fisher et al., 2003; Wheat et al., 2004). The goal of this study is to highlight sources of uncertainty and to provide a framework for future work through a rigorous sensitivity analysis of 4 different types of surface heat flow instruments: the 3.5 meter Violin-bow Probe, 0.6 meter Alvin Probe, Thermal Blanket, and a modified sediment Multi-core Logger that includes attached thermistors (Figure 3.1). The measurements used within this study were collected during an *Atlantis* 2013 GeoPRISMS cruise across the Cascadia accretionary wedge. This setting includes various environments including carbonate crust in areas of diffuse fluid flux, active methane emissions, large range of seafloor depths, and strong seafloor temperature variability.

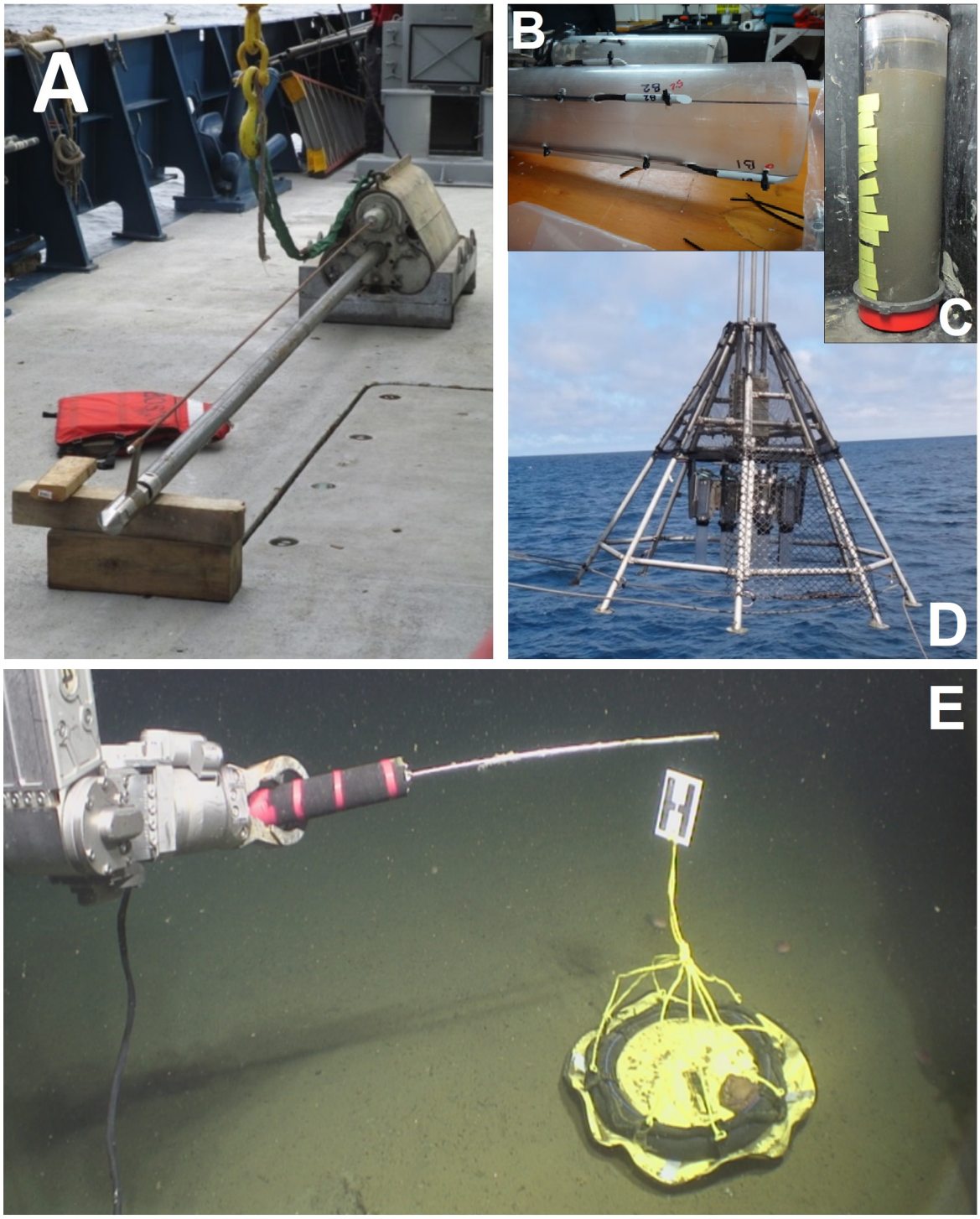

Figure 3.1: Images of the four heat flow instruments used for this study: A) Violin-bow Probe, B-D) Multi-core Logger, and E) Alvin Probe being held horizontal in the water for thermistor calibration by ROV *Jason* near deployed Thermal Blanket labeled H. Closer examination of the Multi-core Logger modifications include B) a Multi-core liner with thermistors attached to the outside and C) a filled second multi-core liner with yellow electrical tape covering predrilled holes prior to thermal conductivity measurements.

3.2 Instrumentation

3.2.1 Lister Violin-bow Probe

The Violin-bow Probe consists of a 3.5 meter strength member with an external instrument string that includes 11 thermal sensors spaced at 0.3 meter intervals. The probe was deployed from the ship in a pogo style deployment allowing for 5 to 7 heat flow measurements in quick succession. Thermistor *in-situ* water calibrations were determined by hanging the probe above the seafloor at the beginning of a series of pogo stations. Each deployment consisted of inserting the probe into the sediment, allowing the frictional heating to decay, followed by powering the heating wire at 30 watts for 20 seconds (Figure 3.2). *In-situ* thermal conductivity estimates were determined by a heat pulse from a resistance wire within the instrument string (Hyndman et al., 1979; Nagihara and Lister, 1993)(Figure 3.1A). See Hartmann and Villinger (2002) for a more detailed description of the probe construction and thermodynamic models of the measurement process.

The raw thermistor sensor data was processed using the Matlab program SlugHeat to determine the heat flow measurement. SlugHeat was designed by A. Cherkaoui and A. Fisher at the University of California, Santa Cruz, and is based on the HFRED algorithm developed by Hartmann and Villinger (2002). The HFRED algorithm provides a more accurate *in-situ* thermal conductivity estimate, in comparison to the previous heat flow methodology (Villinger and Davis, 1987), due to an updated modeled thermal response of the probe by accounting for probe configuration, the use of specific construction materials, and any seawater introduced from probe insertion (Hartmann and Villinger, 2002).

Violin-bow Probe heat flow data were collected primarily within the two major sediment ponds in the lower portion of the Cascadia accretionary wedge (Figure 3.3). A total of 14 Violin-bow Probe measurements were acquired over three pogo cycles between the seafloor depths of 1892 to 1958 meters (Appendix A.1). Due to the pogo style deployment, there were no duplicate measurements, which are defined as pairs of measurements taken within 10

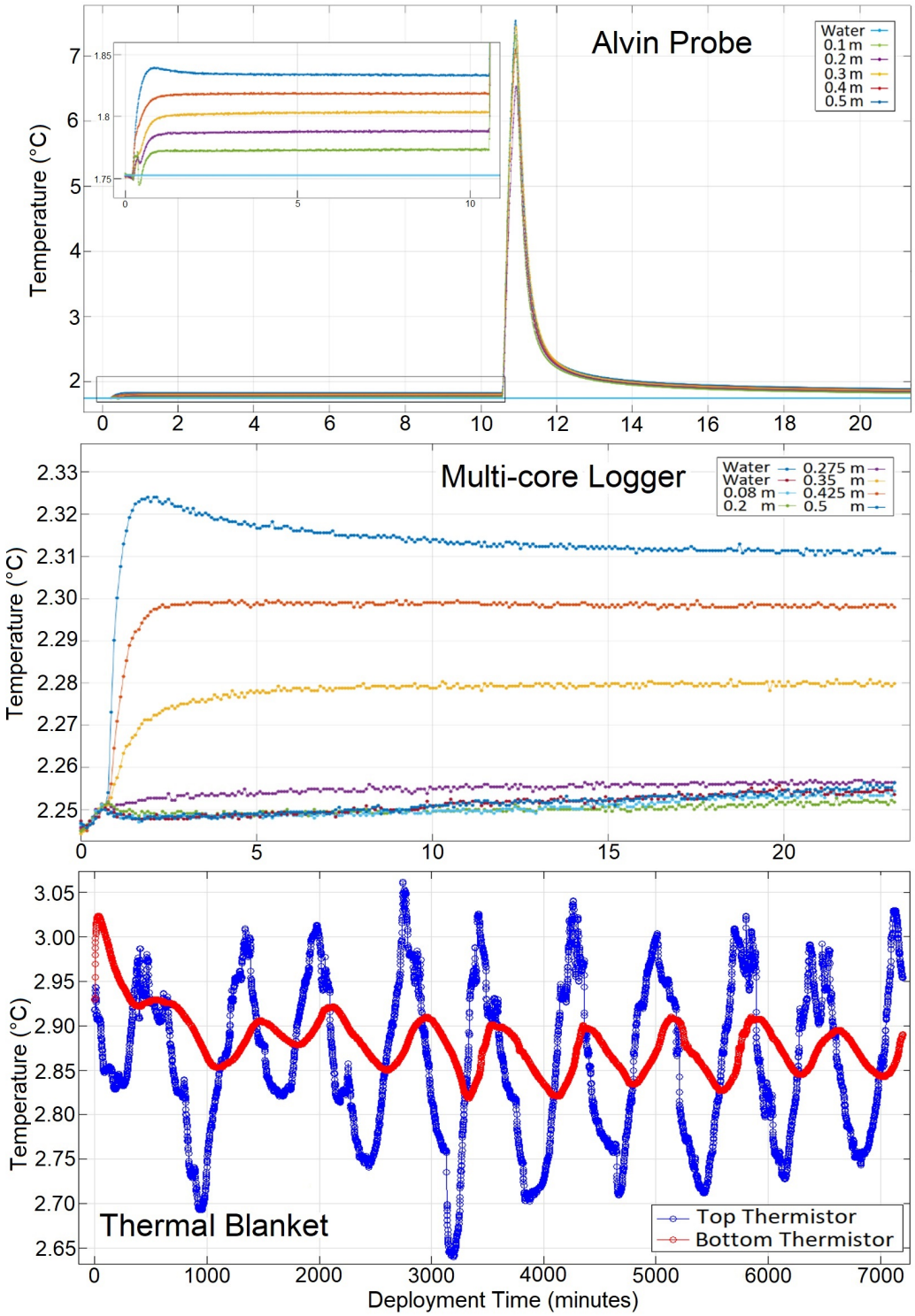

Figure 3.2: Temperature sensor data from each of the heat flow instruments during example deployments. From top to bottom are examples of deployment temperature records for the Alvin Probe (Violin-bow Probe time series is similar), Multi-core Logger, and Thermal Blanket. The Alvin Probe example includes an inset showing an expanded view of the first 10 minutes showing the frictional heating and decay.

meters of each other. No long probe measurements were removed from the data set as none had indicators of a low-quality estimate, where the criteria included unrealistic thermal conductivities or a non-linear Bullard plot (Figure 3.4). In addition, no individual temperature sensor derived measurements were removed during post-processing data analysis.

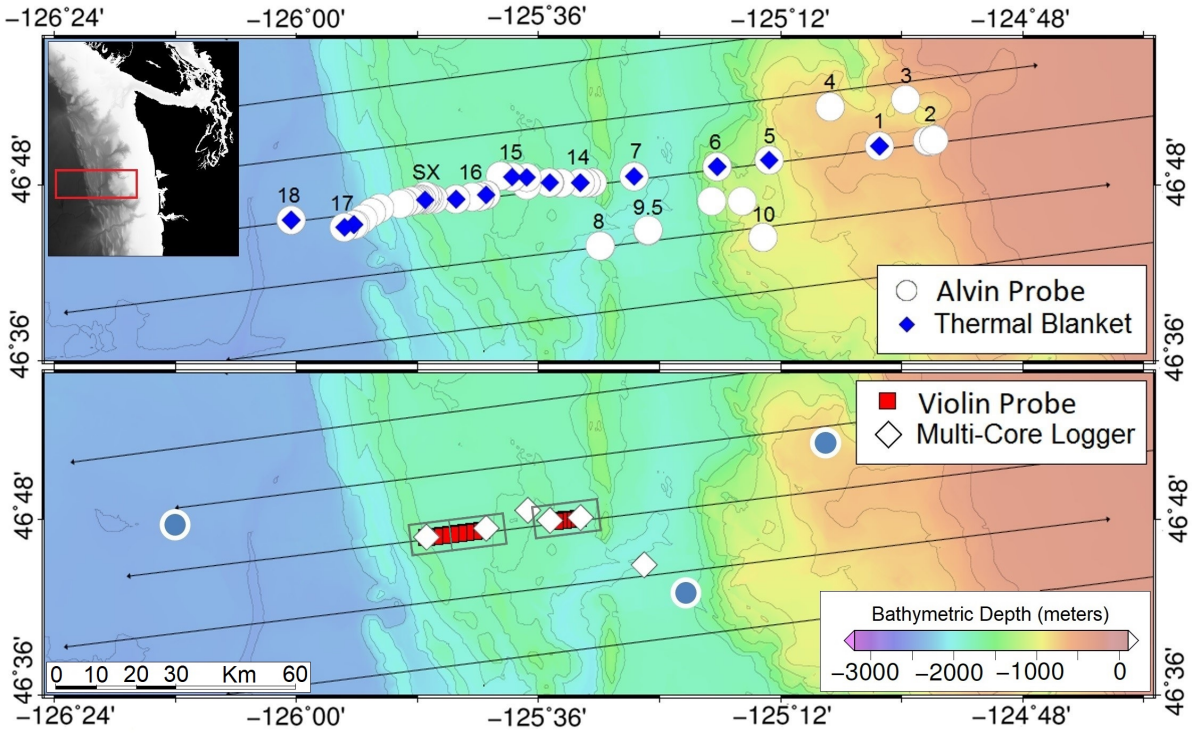

Figure 3.3: Map showing depth and spatial distribution of the deployment sites for the four different types of instruments. Station centers are labeled with associated numbers. Black lines mark the R/V *Langseth* (MGL1212) multi-channel seismic track lines. Blue circles with white outline in the lower panel marks the locations of Ocean Bottom Seismometers (OBSs) equipped with temperature sensors deployed in October 2011 and September 2013 for a 1-year time period.

3.2.2 Alvin Heat Flow Probe

The Alvin Probe is 0.6 meter long and contains five Yellow Spring (YS) 44032 NT thermistors spaced at 0.1 meter intervals, combined with a heating element that extends the full length of the probe (Figure 3.1C). For this survey, two 0.6 meter Alvin Probes were deployed using ROV *Jason II*. The first probe, designated A, was used for Alvin heat flow measurements during the first ROV dive (dive 719) only. A combination of both Alvin Probes, typically deployed simultaneously, were used on subsequent dives (720 to 723) until the A probe failed at a thick carbonate rich site on the accretionary wedge toe. After this failure, the secondary heat flow probe (B) was used for the remainder of the cruise. No obvious bias in either the heat flow or thermal conductivity measurements were detected between Alvin Probes A and B based on the duplicate deployments.

The measurement procedure consisted of holding the probe horizontal to the seafloor for ∼5 minutes in the water column while ROV *Jason* was resting on the seafloor in order to measure relative thermistor offsets in Alvin Probe thermistors *in-situ*, a function of water temperature. Each probe was inserted into the sediment and the ROV *Jason* manipulator would then release the probe handle to prevent ROV derived vibrations from affecting the measurement. In contrast to the Violin-bow Probe, the Alvin Probe did not have a tilt meter and instead the probe's angle of insertion was based on the ROV video observations. The probe thermistors would record the frictional insertion pulse and subsequent decay to near thermal equilibrium over a 10 minute time period (Figure 3.2). A heating pulse was then applied to the sediment for 20 seconds at 20 watts and the subsequent temperature decay for an additional 10 minutes provided the thermal conductivity estimate. As the Alvin Probe has a very similar construction and deployment procedure to the Violin-bow Probe, these data were also processed using the SlugHeat algorithm.

Each Alvin Probe temperature measurement required an accurate calibration of the thermistor offsets taken at different seafloor temperatures in order to capture the true geothermal gradient. Calculated thermistor sensor offsets had a well-behaved decrease with increasing

in-situ water temperatures. Of the 179 water calibration measurements, only 22 had offsets that exceeded one standard deviation of the second-order polynomial fit shown in Figure 3.5. An improper calibration can arise if the probe was still cooling from a previous measurement or if it was not held fully stationary in the water by the ROV manipulator. The 25 Alvin Probe measurements that were missing a water calibration, along with 22 with larger offsets (discussed previously), were provided with an estimated water calibration derived from the fitted curve and the measured *in-situ* water temperature (Figure 3.5).

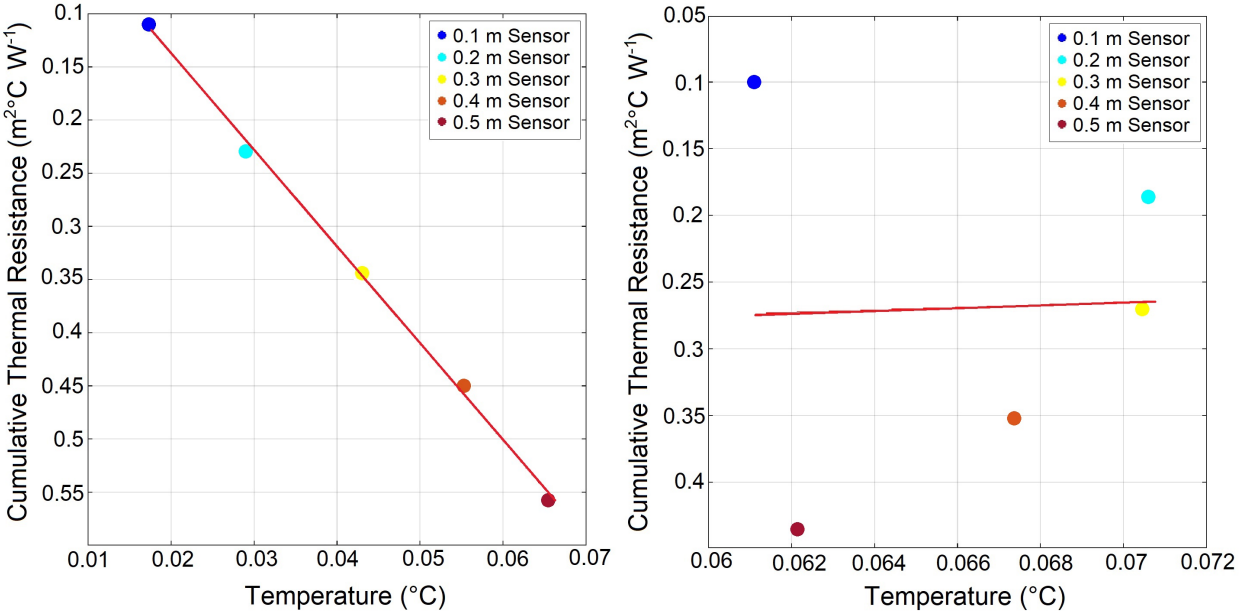

Figure 3.4: Example Bullard plots using data collected by the Alvin Probe. (Left) A well-behaved Bullard plot that is roughly linear with increasing (downward) cumulative thermal resistance with increasing temperature. (Right) A poor fit to a Bullard plot. Note that the linear regression line produces a highly unlikely heat flow (slope of the line).

Overall a total of 204 Alvin Probe measurements were collected throughout the study area, from 550 m water depth on the mid-accretionary shelf to 2588 m at the deformation front (Figure 3.3; Appendix A.2). As a quality control procedure, measurements were removed and excluded from interpretation based on the following criteria: 1) missing or in-

complete sensor data including both temperature and thermal conductivity estimates (such as no heating pulse data available), 2) negative heat flow value, and 3) non-linear Bullard plots due to a low signal/noise ratio arising from near seafloor water column temperature fluctuations. There were 12 Alvin Probe measurements with missing sensor or heating pulse data. A total of 75 measurements were excluded from further interpretation due to calculated negative heat flow values (25 measurements) or non-linear Bullard plots (68 measurements) which were identified by a correlation R^2 value of less than a 0.90 fit to a line (Figure 3.4).

3.2.3 Sediment Multicore Logger

To allow for heat flow determination using the Multi-core system (Figure 3.1D), two of the six core liners required physical modifications. These modifications included predrilling and covering holes into the first core liner that allowed for post-recovery sediment thermal conductivity measurements onboard the ship. A second core liner had eight YS 44031 Precision thermistors attached to the exterior of the liner at 0.075-0.01 meter intervals (see legend in Figure 3.2B). When deployed from the surface ship, the Multi-core system releases a weight stand that inserts all sediment core liners into the seafloor sediment simultaneously over a period of 90 seconds. During recovery from the seafloor, a mechanical cap automatically covers the bottom of the core liners to prevent sediment loss from the captured sediment cores. Due to core liner and instrument configuration, the thermistor equipped core liner was unable to have an auto-capping mechanism attached, which necessitated using the second sediment core for thermal conductivity measurements.

The deployment procedure consisted of lowering the Multi-core Logger from the ship, similar to the Violin-bow Probe, and hanging the system above the seafloor for 15 minutes to calibrate the thermistors at *in-situ* temperature conditions. After recovery, thermal conductivity was measured onboard using a Hukseflux thermal conductivity needle probe. The probe was inserted perpendicular into the core at a 2 cm depth through the tape covered pre-drilled holes, which reduced sediment disturbance and water drainage (Von Herzen and

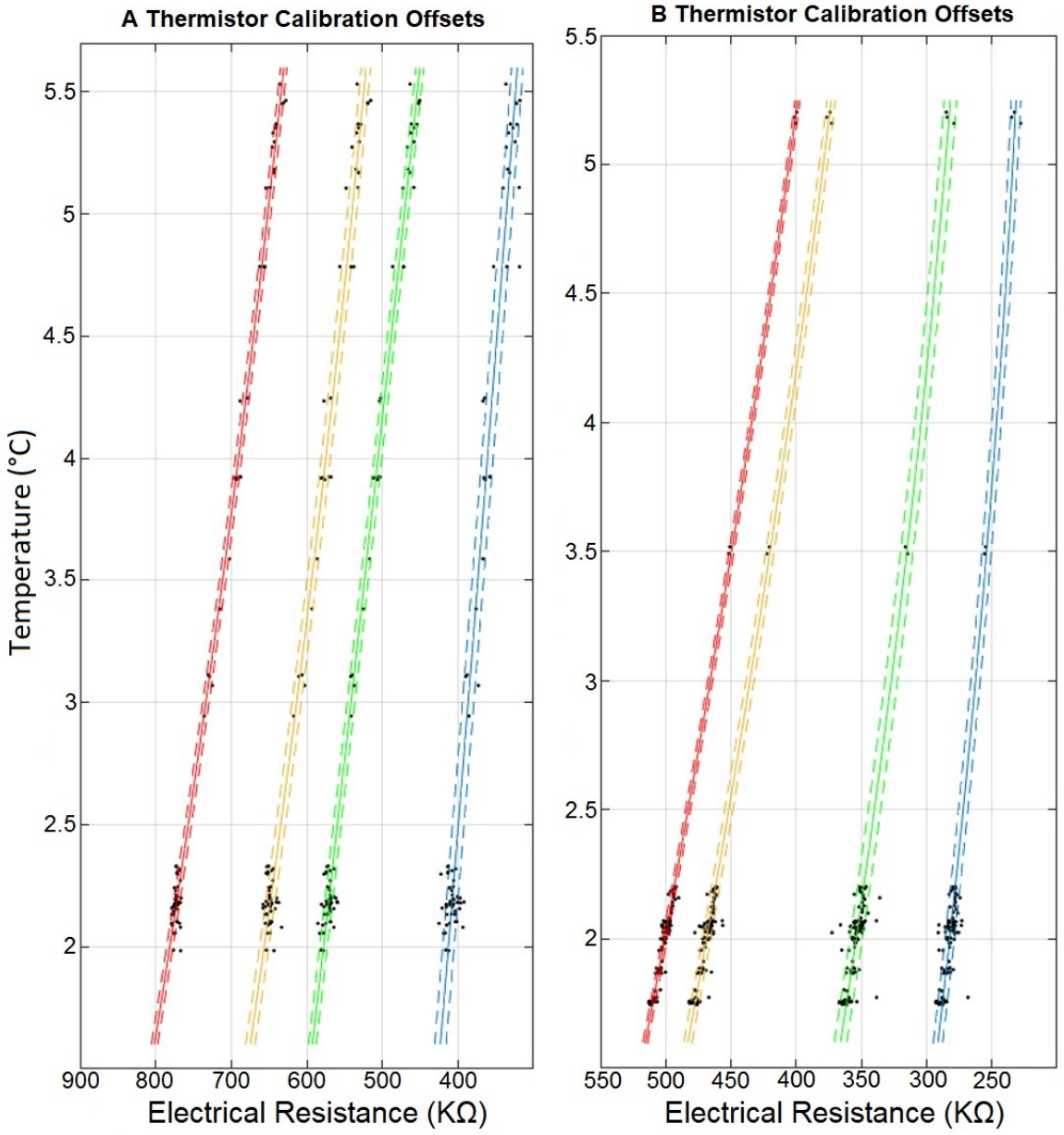

Figure 3.5: *In-situ* water column thermistor offset calibrations based on the raw electrical resistance from the A (left) and B (right) Alvin Probes. Offsets were determined in relation to the 5th thermistor probe representing the *in-situ* water temperature. Fitted polynomial lines to 135 individual calibration data (Black dots) and the dashed lines represent the 1 standard deviation.

Maxwell, 1959; Lister, 1979; Goto and Matsubayshi, 2008). The sediment core was kept capped and care was taken to keep the core from draining of water, a major component of the bulk thermal conductivity. Cores were stored onboard the ship at room temperature of approximately 20°C and it was assumed that the core warmed uniformly to thermal equilibrium. This temperature change would have a less than 5% effect on the thermal conductivity measurements, primarily based on the temperature-dependent thermal conductivity of the water that make up a larger percentage of the sediment.

To accurately measure the geothermal gradient, equilibrium temperatures were determined by plotting the temperature versus logarithmic inverse time and extrapolating to infinity using a linear fit and solving for the vertical intercept. Data from all temperature sensors that penetrated the sediment were used for the post-measurement analysis. The thermal gradient data was then resampled for ease of calculation to coincide with the depth of the thermal conductivity probe measurements, assuming both Multi-core liners penetrated the same sediment types. Heat flow values were calculated using a Bullard plot of thermal resistance (w; m^2 K W^{-1}) versus sediment temperature (T; °C) (Bullard, 1954),

$$T(z) = Qw - T_{SF} \tag{3.1}$$

$$w = \int_0^z \frac{1}{K(z)} dz \tag{3.2}$$

where Q is heat flow (W m^{-2}), z is depth (meters) below the seafloor, T_{SF} is the temperature (°C) at the seafloor, and K is sediment thermal conductivity (W $m^{-1}K^{-1}$). A linear least-squares fit to the Bullard plot provides an accurate estimate of heat flow that accounts for thermal conductivity variations with depth. The Bullard plot is also utilized for the Violin-bow and Alvin Probe heat flow calculations within the SlugHeat package.

The modified Multi-core Logger was deployed at 6 locations (Figure 3.3; Appendix A.3) arranged primarily across-strike along the lower portion of the accretionary prism, at depths

ranging from 1763 to 1994 meters. There were no duplicate heat flow measurements collected with this instrument.

3.2.4 Thermal Blanket

The Thermal Blanket instrument consists of a 0.16 m^2 foam circle encompassed by a canvas material and weighed down by a motorcycle inner-tube filled with super-saturated sodium chloride solution to help seal the foam to the seafloor, allowing for accurate determination of the seafloor geothermal gradient (Figure 3.1E) (Salmi et al., 2014). Antares miniaturized temperature data loggers are attached to the center of each side of the instrument, measuring the thermal gradient through the foam. Relative temperature offsets between each of the instruments' paired Antares loggers were determined by recording all thermistors in an ice water bath for several hours prior to deployment and were applied to the data during post-processing prior to the heat flow calculation.

Thermal Blanket deployments consisted of transferring the instrument to the seafloor from the ship either by ROV *Jason* or from an autonomous elevator. To minimize excess heat within the foam, the instruments were soaked in a cold ice bath prior to deployment from the surface ship. As an additional pre-deployment step, the autonomous elevators were released from the ship for upward of 24 hours prior to deployment to assist in acclimatization of the Blankets to the cold near-seafloor water. Individual deployment sites were selected for a smooth sediment surface without uneven rocks or fissures that would prevent the Thermal Blanket from fully sealing to the seafloor. The Thermal Blankets were deployed for a minimum duration of 5 days allowing the instruments to come into thermal equilibrium with the underlying sediments. This period was longer than previous deployments that have successfully produced heat flow measurements through modeling and extrapolating the cooling curve to a steady state (Salmi et al., 2014) and proved to be a suitable time period as determined by the estimation of a stable temperature difference (ΔT) between the two thermistors following the removal of near-bottom water variability from the temperature

record.

Heat flow (Q) is determined with the solution to the 1-D heat flow equation,

$$Q = -K\Big(\frac{T_2 - T_1}{z_2 - z_1}\Big) \tag{3.3}$$

where T_1 and T_2 (°C) are temperatures at associated depths z_1 and z_2 (meters) into the sediment. In the case of the Thermal Blankets, T_1 and T_2 correspond to the top and bottom thermistors while z_2 - z_1 is the thickness of the foam. The foam matrix thermal conductivity (K; W $m^{-1}K^{-1}$) is close to the water thermal conductivity due to the fluid soaked open cell foam. However, it is dependent on ΔT due to susceptibility to minor amounts of fluid circulation occurring within the foam based on the following relationship:

$$K = 0.0348 \ln (T_2 - T_1) + 0.7339, \tag{3.4}$$

determined by fitting a quadratic curve to model-derived thermal conductivity of well-behaved Thermal Blankets placed in the Juan de Fuca axial valley (Salmi et al., 2014).

The downward propagation of the water temperature variations from the top to the bottom thermistor provides a method to successfully remove the thermal signal from the Blanket record originating from near seafloor temperature changes. The bottom thermistor was assumed to be affected by the heat transfer through the foam of near-bottom water variability (as recorded by the top thermistor), assuming the foam is purely conductive and homogeneous (Carslaw and Jaeger, 1959; Hamamoto et al., 2005), by the equation,

$$T(z,t) = T_0 + (Gz) + \sum_i \Big[A_i e^{-\sqrt{\frac{\pi z}{\kappa_B P_i}}} \cos\Big(\frac{2\pi t}{P_i} - \phi_i - \sqrt{\frac{\pi z}{\kappa_B P_i}}\Big)\Big] \tag{3.5}$$

where T(z,t) is the Blanket bottom temperature (°C) at z Blanket thickness (meters) and t time (seconds), T_o is the temperature at time zero seconds and at zero meters depth (top of the Blanket), G is the linear thermal gradient (°C m^{-1}) through the Blanket, and κ_B

is thermal diffusivity (m^2 s^{-1}) of the water soaked foam. A, P, Φ and are the amplitude, frequency, and phase respectively of the temperature time series over i terms.

Variations in seawater temperatures recorded by the top thermistor were propagated through the instruments' body and iterated through various foam thicknesses in order to determine the best model fit to the bottom thermistor record. This approach accounts for small shifts in thermistor vertical spacing during deployment due to the thermistors being attached to a non-rigid canvas lining and subsequently placed on a variety of seafloor types ranging from soft sediments to hard rock.

The Thermal Blankets were placed by ROV *Jason* throughout the survey area (Figure 3.3) and were generally co-located with Alvin Probe stations at deployment depths that ranged from 586 to 2559 meters, with emphasis on the lower accretionary wedge sediment pond sites and potential areas of fluid emissions. A total of 27 Thermal Blanket measurements were made during the cruise (Appendix A.4). Two instruments failed to seal to the seafloor at Station 1 located at a depth of 586 meters, and thus did not produce usable data. Two additional measurements using Thermal Blanket S were removed due to a thermistor offset calibration that appeared inaccurate.

3.2.5 Seafloor Temperature Mooring

In addition to the heat flow instruments, a small mooring was deployed by ROV *Jason* at Station 10 at a depth of 956 meters (Figure 3.3) in 2012 and recovered during the *Atlantis* 2013 cruise, recording 12.8 months of data. The mooring consisted of two Antares thermistors positioned approximately 1 meter above the seafloor. The goal was to record the near-seafloor water temperature variability for the previous year at one location prior to measuring the sediment geothermal gradient. These data (Figure 3.6) showed a general seasonal variation in temperature from 3.6° in winter to 3.75°C in summer, with excursions as low as 3.4°C and as high as 3.9°C and two strong positive thermal anomalies in the spring.

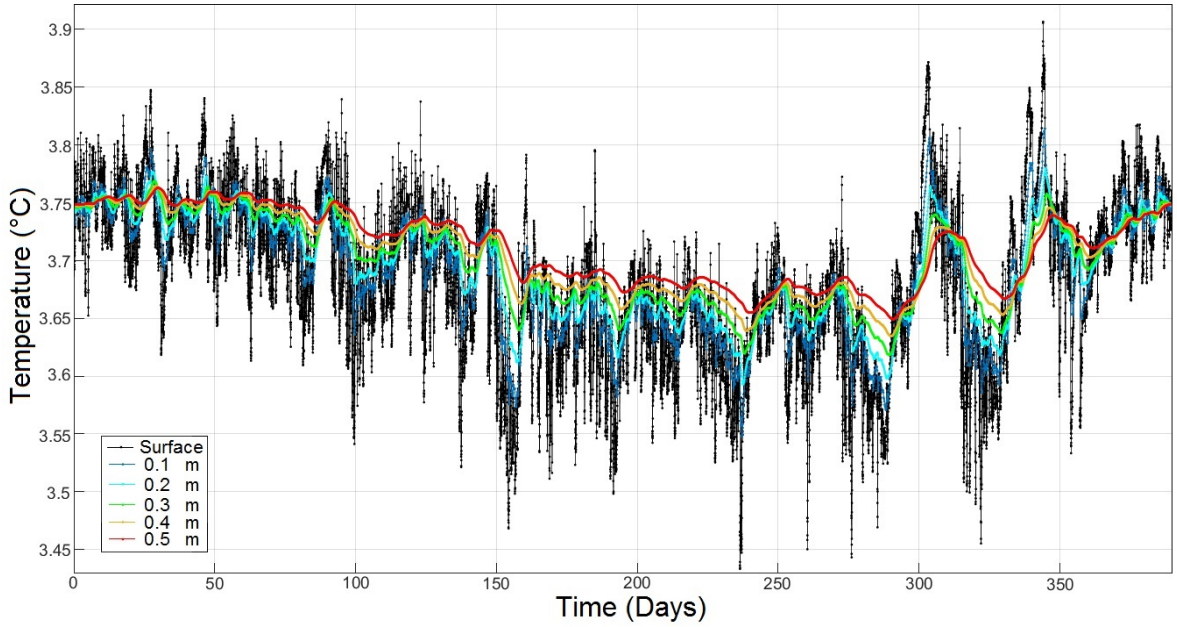

Figure 3.6: Observed near-bottom water temperature record of the year-long mooring (Black) located at Station 10 (Shown in Figure 3.3) at a seafloor depth of 956 meters. The mooring temperature record began on 7/8/2012 (day 0). This surface record was propagated using Equation 3.5 at 0.1 meter intervals into sediment depths representative of the Alvin heat flow probe thermal sensors including an imposed background heat flow of 60 mW m^{-2}. Propagation of the near-bottom water temperatures illustrates the dampening of seafloor variability with increasing sediment depth.

3.3 Instrumental Uncertainty

Total instrumental uncertainty is derived from the combined uncertainties associated with the instrument tilt, sensor depth within the sediment, temperature sensor, and thermal conductivity. All of the heat flow instruments were examined using a Monte Carlo simulation analysis, which is a reliable probabilistic approach for complicated uncertainty analysis (Doubilet et al., 1985; Papadopoulos and Yeung, 2001). This sensitivity analysis considers the effects of individual components of the heat flow equation (Equation 3.3) by randomly selecting the temperature, depth, and thermal conductivity values within their assigned individual uncertainties, whether it is a normal distribution standard deviation or instrument

resolution (Table 3.1). The heat flow analysis was performed using 10,000 random simulations to produce a stabilized result (Figure 3.7). The aggregated simulation results produced a normalized distribution and the uncertainty was determined as one standard deviation from the mean.

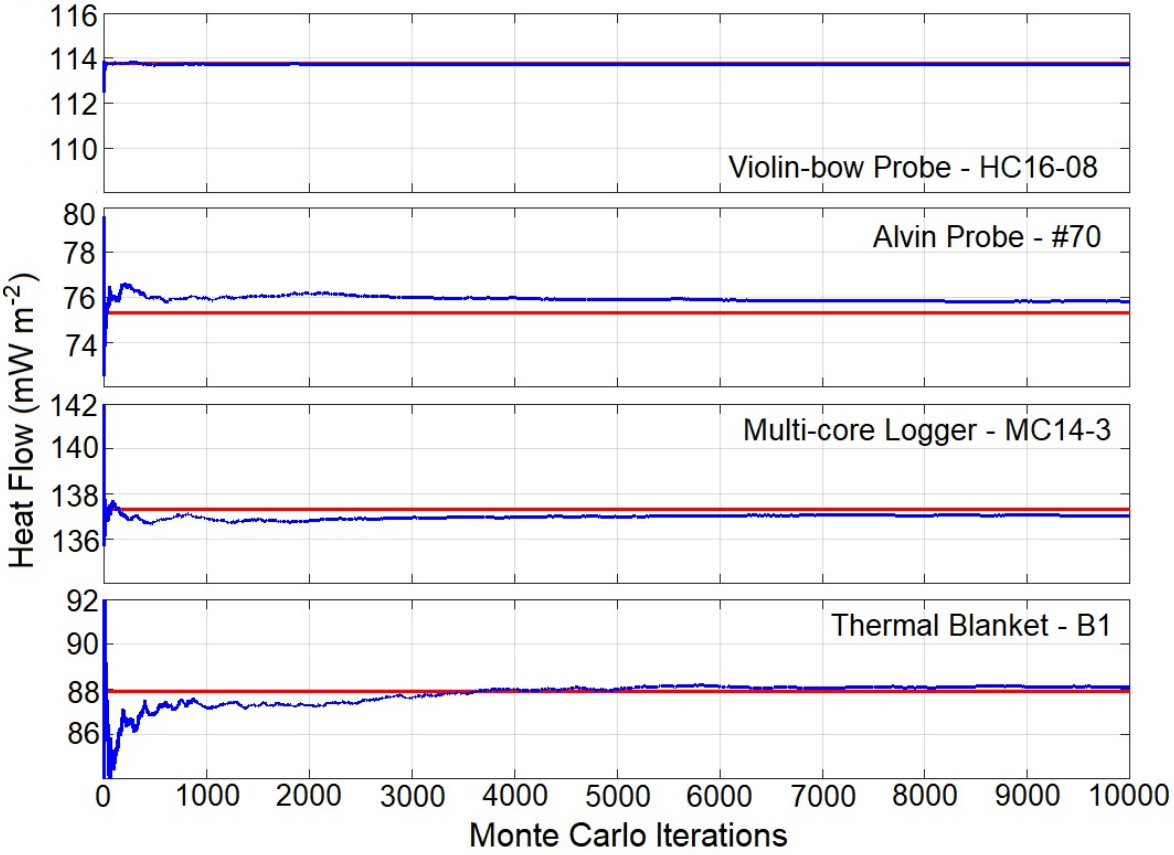

Figure 3.7: Examples of heat flow stabilizing over the 10000 iterations (blue line) throughout the Monte Carlo uncertainty analysis for each of the heat flow instruments. The red line indicates the measured heat flow.

Table 3.1: Bounds used for Monte Carlo instrumental sensitivity analysis based on one standard deviation or the resolution (marked as *, based on manufacturer specifications).

Parameters	Violin-bow Probe	Alvin Probe	Multicore Logger	Thermal Blanket
Instrument Tilt	0.05°	26.50°	5.00°	5.00°
Temperature Sensor*	±1mK	±1mK	±1mK	±1mK
Sediment Steady State Temperature	$\pm 3.5 \times 10^{-4}$ to 0.003 K	$\pm 5.1 \times 10^{-4}$ to 0.009 K	$\pm 3.5 \times 10^{-4}$ to 0.003 K	$\pm 1.1 \times 10^{-4}$ to 0.005 K
Temperature Sensor Depth	±0.5cm	±0.5cm	±1cm	±0.5cm
Thermal Conductivity	±0.014 to 0.114 W $m^{-1}K^{-1}$	±0.002 to 0.281 W $m^{-1}K^{-1}$	±0.002 to 0.027 W $m^{-1}K^{-1}$	±0.026 to 0.03 W $m^{-1}K^{-1}$

3.3.1 Instrument Tilt

For the probe-type instruments to capture the true heat flow, the instruments need to be placed vertically into the sediment. Departures from vertical will impact the estimated depths of both the temperature and thermal conductivity components of the heat flow measurement. This relatively common problem will noticeably reduce the measured heat flow since both the temperature and the *in-situ* thermal conductivity are being measured at different depths than assumed. As a hypothetical example, a 25° tilt from vertical would produce a 10% decrease in heat flow (Figure 3.8).

Due to the varying construction of each instrument, different tilt assumptions were used for the uncertainty analysis. The Violin-bow Probe is equipped with a tilt sensor and the instrument tilt angle was accounted for during the heat flow calculation producing a tilt sensitivity of 0.05° based on the tiltmeter resolution of 0.1° (Table 3.1). Both the Thermal Blanket and Multi-core Logger had no tilt sensor and it was assumed that both instruments had a tilt from vertical of 5° based on the average seafloor slope around the measurement locations (Table 3.1).

No tilt sensor data was available for the Alvin Probe and the instrument insertion angle

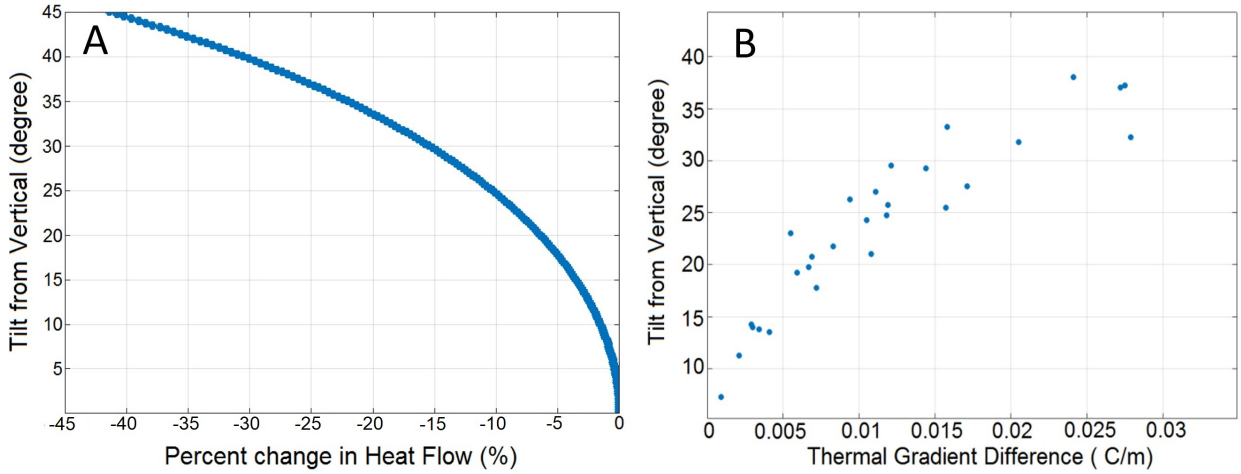

Figure 3.8: Impact of instrument probe tilt from vertical (90° from the seafloor) on a hypothetical Alvin Probe based heat flow measurement. A) Percent reduction in heat flow values based on instrumental degree of tilt from vertical. B) Duplicate sets of Alvin heat flow probe thermal gradient differences and the equivalent theoretical tilt assuming that one probe was exactly vertical. The duplicate Alvin probes were taken within 1 meter from each other at roughly the same time.

was based on visual inspection using the ROV cameras, therefore the tilt uncertainty has the potential to be considerably larger than the other seafloor heat flow instruments. A total of 34 duplicate Alvin Probe measurements were collected where both probes were deployed almost simultaneously by ROV *Jason*'s two manipulators with less than 1 m separation, provide a means of exploring the impact of instrument tilt uncertainty. Of the 34 total Alvin duplicate sets, 29 were considered reliable with indicators such as a positive heat flow and near-linear Bullard plot. Assuming the full mean differences of 11.2 mW m^{-2} between the duplicate sensors are due to tilt alone and ignoring any local heat flow variations, the resulting analysis of these 29 Alvin Probe duplicates produces a mean tilt of 23.2 ± 8.2 degrees offset with a maximum estimate of 39° from vertical (Figure 3.8B). Although this is a rough estimate, a tilt uncertainty of 26.5°, which encompasses 68% of the duplicate tilt calculation, was used for the Monte Carlo analysis (Table 3.1).

3.3.2 Temperature Calibrations

All heat flow measurements require calibration of the thermistors due to changes caused by the *in-situ* cold (2 to 6°C) temperatures of the near-seafloor water in comparison to the lab or ship environment. The Violin-bow, Alvin, and Multi-core temperatures were calibrated *in-situ* by allowing the instruments to equilibrate to the near seafloor environment prior to deployment. The calibration offsets were applied to the temperature measurements during the heat flow calculations. Calibration offsets were captured for almost every Alvin Probe deployment over a range of temperatures and seafloor depths and used to determine the dependence of both A and B Alvin probes offset on seafloor temperature (Figure 3.5) that was used to process measurements missing this calibration.

For the Thermal Blanket, calibrations were determined in a laboratory setting by immersing the Antares data loggers in an ice water bath for two hours, emulating the temperatures on the seafloor. Measured offsets were calculated by taking the average of all temperature measurements and determining the difference from the mean value. These calibrations were carried out after applying the factory conversion from electrical resistance to temperature calculations. The average laboratory offset between two Antares temperature readings was 0.025°C, although the offset could be as large as 0.1°C. Without a method of determining Thermal Blanket thermistor *in-situ* offset accurately, distinguishing poorly determined calibrations is difficult and inaccurately estimated offsets can have potentially profound effects on the heat flow measurement. As an example, with an average ΔT (T_2 - T_1) of 0.0106°C for the Thermal Blanket heat flow measurements, a change of 2 mK that represents the resolution of both of the thermistors, can produce an uncertainty of ± 23.6 mW m^{-2} for an average heat flow of 125.2 mW m^{-2} obtained in this study. Exploring and detecting poorly determined thermistor offset calibration requires additional information including laboratory calibration tests or independent verifications from *in-situ* calibrations.

The Antares logger instrumental response to *in-situ* temperature changes, during both short and long deployments periods, and instrumental drift can have a big impact on the

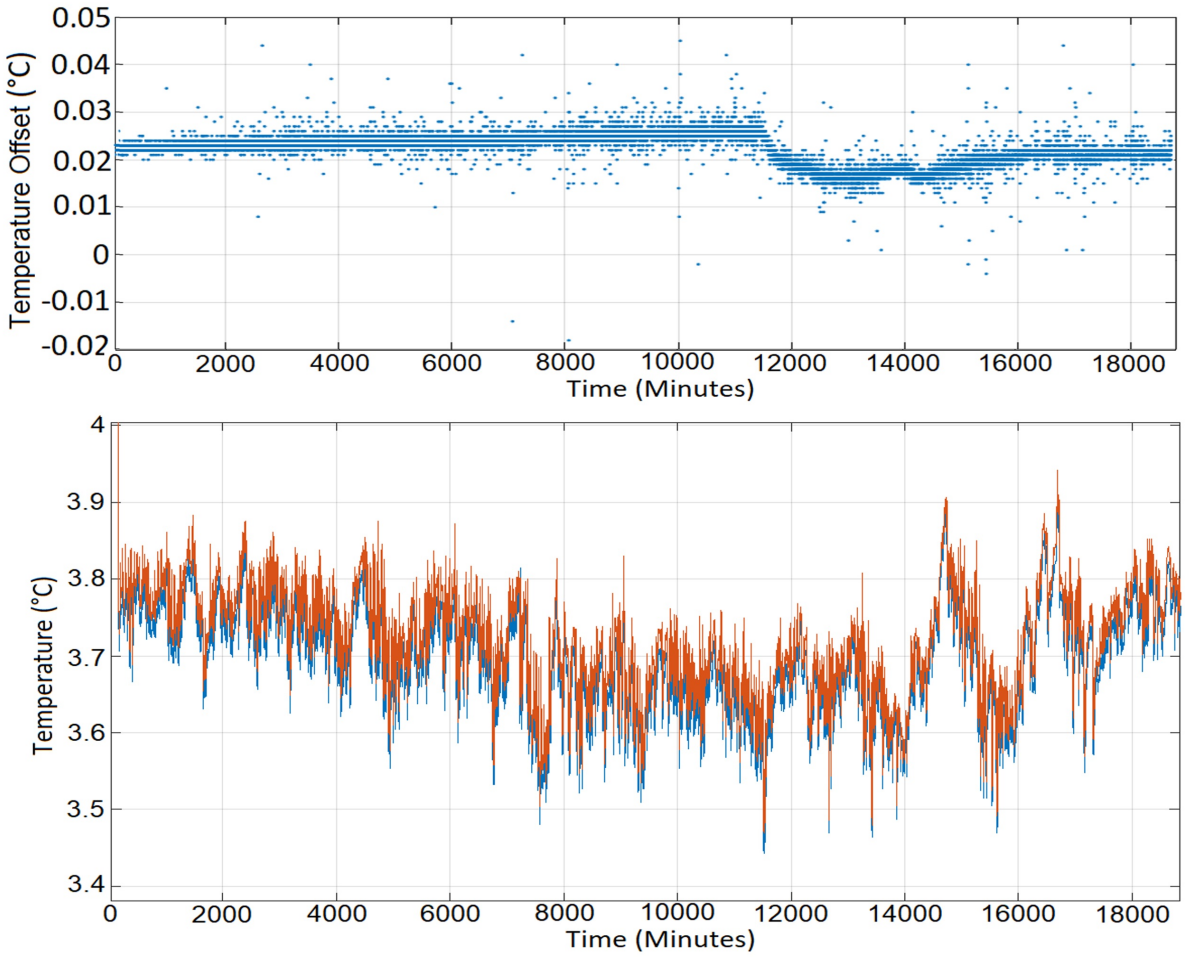

Figure 3.9: Year-long thermal record of the small mooring located at Station 10 at a seafloor depth of 956 meters. The mooring temperature record began on 7/8/2012 (minute 0). Top) the ΔT between the two mooring Antares. Bottom) detailed thermal record of the year-long mooring of the two distinct (Red and Blue) Antares 1 meter above the seafloor.

ΔT component of heat flow estimates. The seafloor temperature mooring provided a long calibration time-series between two Antares thermistors that demonstrated a small trend in offset between the two sensors of 0.0005°C per month and an unexplained temperature instability midway through the record that changed the offset by 0.01°C (Figure 3.9). Ice bath tests from 2011 provide additional information on long-term calibration stability, that when compared to the 2013 offsets show a systematic shift of +0.0008 $\pm$ 0.0051°C (Figure

3.10).

In principle, the water column near the seafloor provides a more representative experimental environment for Antares temperature offset calculations, with a more representative *in-situ* temperature in comparison to the ice water bath derived calibrations. Opportunistic *in-situ* water temperature calibrations were determined for 18 of the 27 Thermal Blanket deployments that had the necessary environment. Comparisons of these *in-situ* calibrations to the laboratory ice bath calibration demonstrate the effectiveness and reliability of the ice bath calibrations, which differ from other heat flow methods that preferentially utilize hanging temperature offset calibrations (Figure 3.10). Problems with obtaining reliable *in-situ* calibrations for the Thermal Blanket include not immersing the Blanket in the near seafloor water for an adequate time period to allow for thermal equilibrium, not knowing with certainty that the thermistors are completely exposed to the water, and the high foam heat capacity of roughly 4000 J kg^{-1} K^{-1} that affects thermistors even if they are not in contact with the seafloor.

3.3.3 Thermal Gradient

The thermal gradient uncertainty results from the combined uncertainties of the change in temperature (T_2 - T_1) and change in depth (z_2 - z_1). The thermistors for all four instruments have a nominal temperature accuracy of ± 0.1°C, although since these measurements are calibrated relative to each other, the relative temperature uncertainty is reduced to ± 1 mK (Hartmann and Villinger, 2002; Fisher and Harris, 2010)(Table 3.1).

A third component of the temperature estimate is how accurately the instrument captured the steady state heat flux. As the instrument is placed on or inserted into the seafloor environment, the instrument will disturb the local thermal environment. The Thermal Blanket was placed on the seafloor for multiple days until the instrument's material came into equilibrium with the seafloor sediments. In order to capture a rapid heat flow measurement using the Alvin and Violin-bow Probes, the steady state equilibrium was determined based

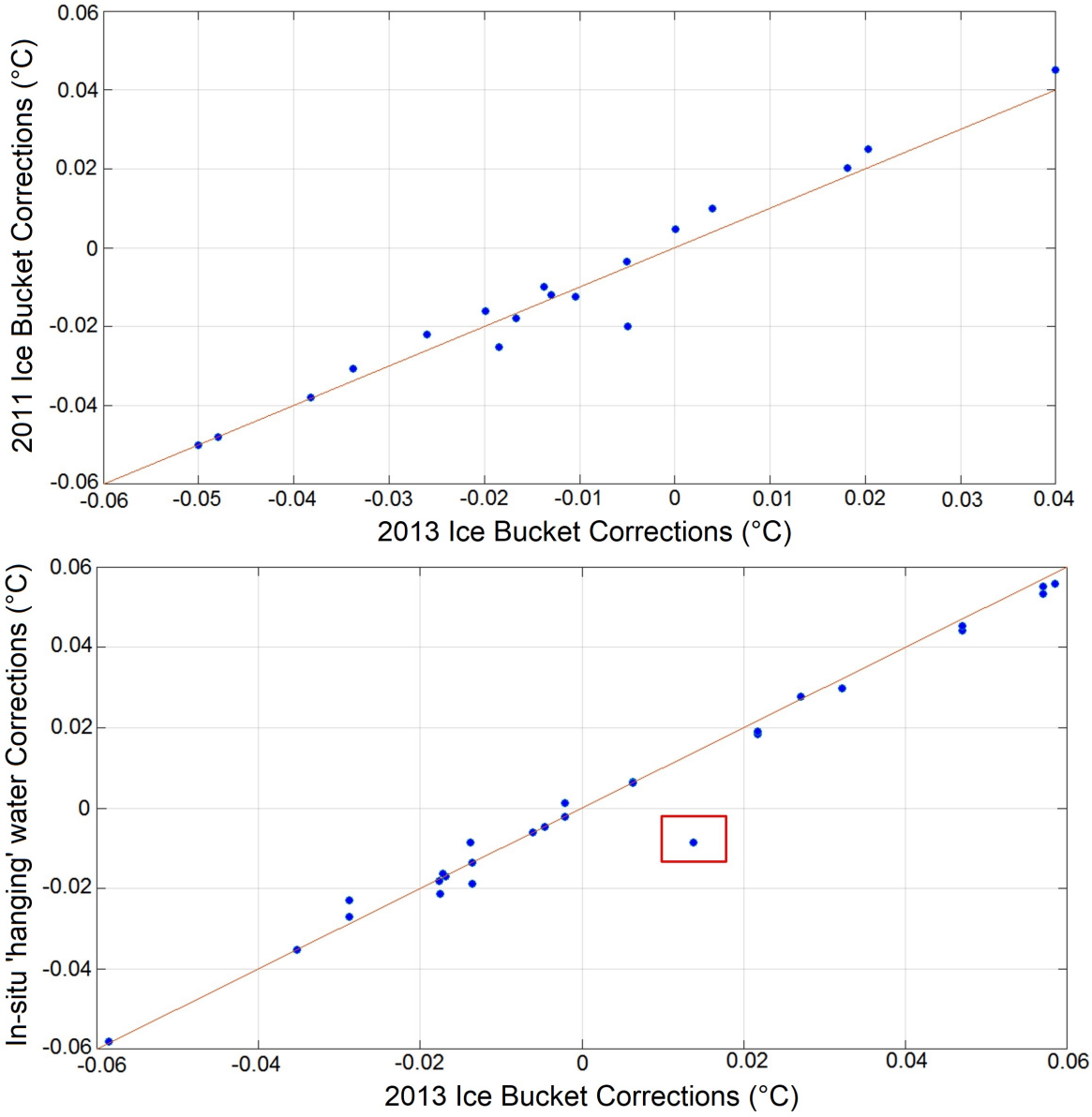

Figure 3.10: Comparison of the different methods used to determine the Thermal Blanket Antares thermistor water calibration offsets, of which the 2013 ice bucket calibration was used for the primary heat flow calculations for most of this study. For each scenario, individual data points represent the same Antares Logger pairing offset and a linear fit (orange line) is included to highlight any unusual deviations. Top) 2011 ice bucket Antares offset calibrations compared to 2013 ice bucket offset calibrations. Bottom) Antares calibrations ice bucket compared to opportunistic seafloor hanging temperature calibrations. The offset calibration for Blanket S Antares, which was removed from analysis is highlighted by a red box showing a strong deviation from the linear fit.

on the calculated root mean standard deviation from a theoretical cooling rates derived using the known thermal properties of the probe materials and calculated within the SlugHeat algorithm (Hartmann and Villinger, 2002). For this study, the equilibrium steady state temperature measurement uncertainties were on average within a standard deviation of ±0.5% for the Violin-bow and Alvin Probes (Table 3.1).

The sensor position uncertainty does vary between instruments based on differences in construction. The Violin-bow and Alvin Probe sensor position uncertainty along the probe length is assumed to be ±0.5 cm due to any potential shifting of the sensor position within the instrument housing. For the Multi-core logger, the sensor spacing uncertainty of the thermistors position along the core barrel is assumed to be ±1 cm, due to possible movement of the mounted thermal sensors within the exposed core liner during deployment and retrieval from the seafloor. For the Thermal Blanket, uncertainty in foam thickness can arise from compression of the bottom thermistor into the foam and the overlying pressure that the inner-tube exerts on the Blanket edges, which is dependent on seafloor sediment type. The standard deviation uncertainty in the distance between the two Antares thermistors on either side of the Thermal Blanket was set at 5 mm, a 10% variation from the nominal 0.0508 meter Blanket thickness, determined based on the variations in thermistor depth required for accurate propagation and removal of near-bottom water temperature variability.

3.3.4 Thermal Conductivity

For the Violin-bow Probe, Alvin Probe, and Multi-core Logger, the thermal conductivity uncertainty is based on the instruments' ability to estimate the sediment thermal conductivity of the *in-situ* or collected sediments. For the Violin-bow and Alvin Probes, the uncertainty for each sediment thermal conductivity measurement was calculated as the root mean standard deviation fit to the idealized cooling rate (Table 3.1). For the Thermal Blanket, a standard deviation of 5% of the estimated values was assumed and was determined based on the variations in thermal conductivity values used to remove near-bottom

water variability from the Blanket temperature record. Thermal conductivity measurements are also impacted by the sensor depth uncertainty (Table 3.1) because it affects thermal resistance, i.e., the thermal conductivity integration over depth.

The thermal conductivity values for the Multi-core Logger were measured independently on a separate sediment core and had its own independent depth uncertainties of ±1 mm. In addition, the Multi-core Logger measurement accuracy is affected by any unaccounted loss of core material or fluid during core recovery. Core material loss from the base would cause an offset between the thermal gradient and the thermal conductivity measurements, while fluid drainage produces an unexplained increase in thermal conductivity near the top of the core; a phenomenon not observed in the core data. A loss of up to a few centimeters of the core was noted for some of the sediment cores, although quantifying the exact amount is difficult.

3.3.5 Overall Instrumental Heat Flow Uncertainty

Overall, the Violin-bow Probe had the lowest total instrumental uncertainty, followed by the Multi-core Logger, Alvin Probe, and finally the Thermal Blanket. The Thermal Blanket and Alvin Probe had the higher percent measurement uncertainties associated with lower heat flow measurements, implying that these instruments are more accurate in higher heat flow environments. The Violin-bow Probe heat flow measurements range from 84 mW m^{-2} to 117 mW m^{-2} have a corresponding average Monte Carlo derived uncertainty heat flow value of ±1.21 mW m^{-2} or 1.25% of the mean heat flow value (Figure 3.11; Table 3.2). The total uncertainties were less than 3.2% for all of the Violin-bow Probe heat flow data with the dominant source of uncertainty derived from the thermal conductivity measurement (Figure 3.12). The shorter Alvin Probe had a mean uncertainty of ±14.8 mW m^{-2} or 14% of the mean heat flow measurement of 104.0 mW m^{-2}. The larger uncertainty of the Alvin Probe thermal gradient components is apparent, especially when compared to the Violin-bow Probe, and is due to the larger tilt uncertainty that accounts for a majority (∼95%) of the

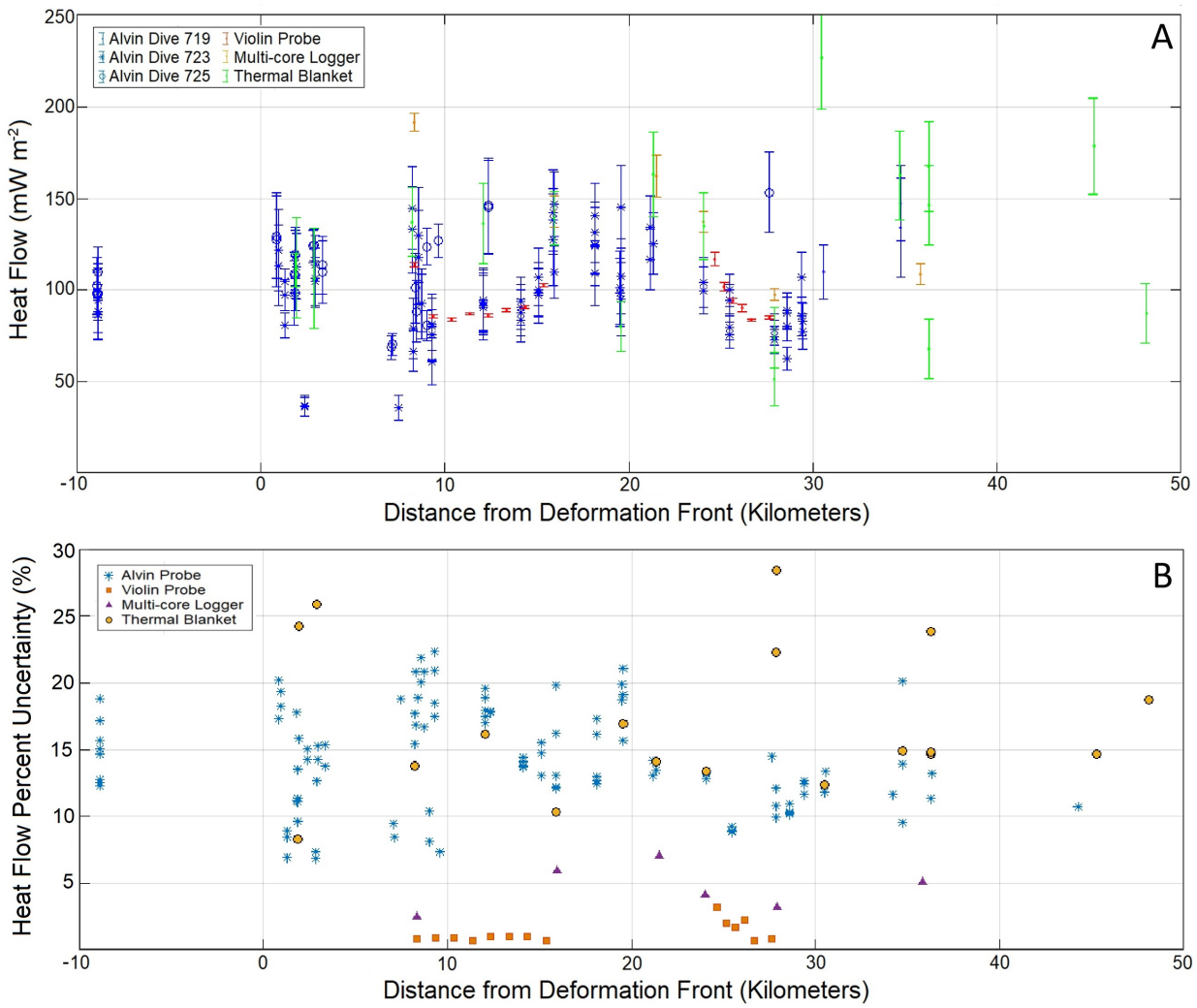

Figure 3.11: Summary of heat flow data and associated uncertainties for all four instrument types. A) All reliable heat flow measurements (symbols) and individual uncertainties (vertical bars) based on distance from the deformation front eastward towards the Washington coast. B) The individual percent uncertainties of the heat flow measurement by instrument type.

total instrument uncertainty (Figure 3.12). Five of the six Multi-core Logger measurements produced near-linear Bullard plots with heat flow measurements that varied from 108 mW m^{-2} to 180 mW m^{-2} with an average of 140 mW m^{-2}. The Multi-core Logger mean heat flow uncertainty was ±6.96 mW m^{-2} with thermal gradient (temperature and depth) uncertainty accounting for a majority of the total. Reliable Thermal Blanket heat flow measurements ranged from 51.7 mW m^{-2} to 228 mW m^{-2} with an average of 128.6 mW m^{-2} and a mean heat flow uncertainty of ±19.6 mW m^{-2} (16.1%). Uncertainties associated with the Thermal Blanket thermal conductivity, which are less well known in comparison to the other three instruments, disproportionately affect the heat flow uncertainty by 5% in comparison to less than 1.2% for the three other instruments (Table 3.2, Figure 3.12).

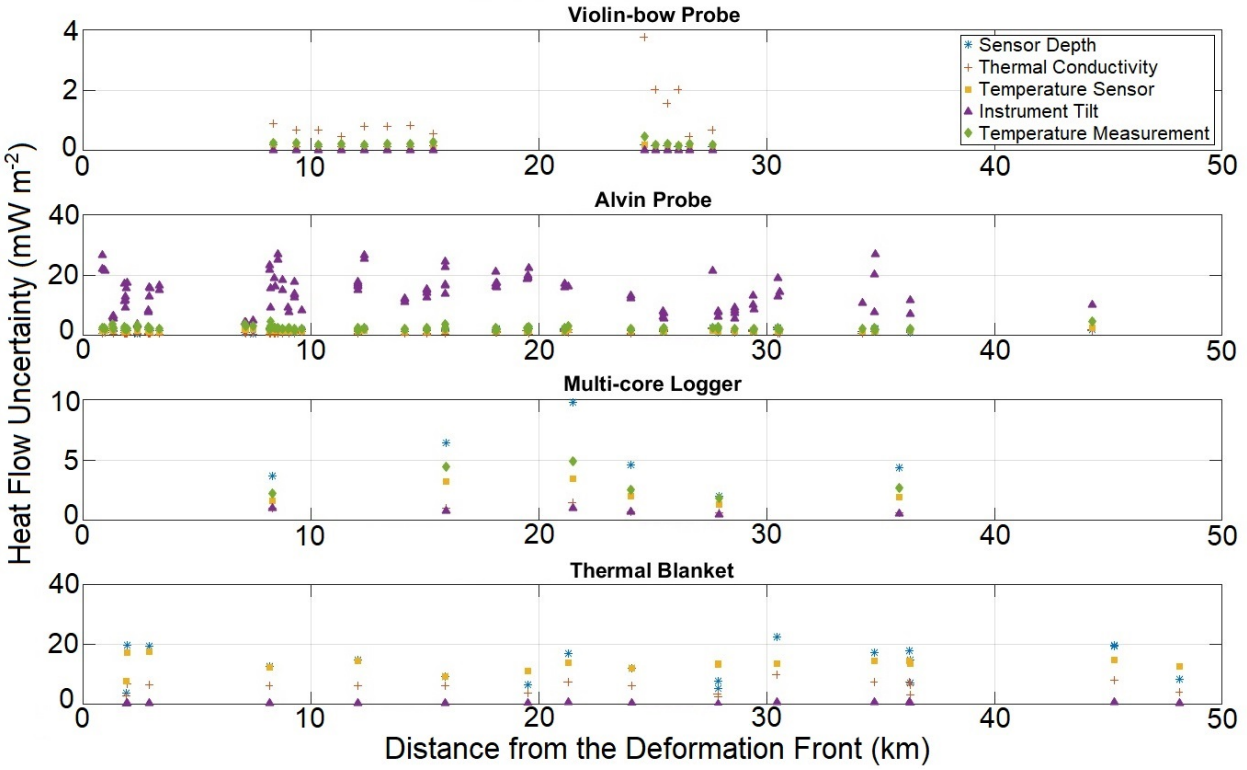

Figure 3.12: Breakdown of the sources of the uncertainty in terms of standard deviation for reliable heat flow measurements from the four instrument types. Note that the y-axis is different for each subpanel.

Table 3.2: The mean heat flow uncertainty (mW m^{-2}) and percent of the heat flow in parenthesis produced by the various components of the measurement (Table 3.1). Thermal Blanket uncertainty was calculated based on just the instrumental uncertainty.

Parameters	Violin-bow Probe	Alvin Probe	Multi-core Logger	Thermal Blanket
Instrument Tilt	$2.8x10^{-5}$ ($3.0x10^{-5}$%)	14.1 (13.3%)	0.79 (0.57%)	0.46 (0.29%)
Temperature Sensor	0.17 (0.18%)	1.64 (1.86%)	2.26 (1.63%)	12.9 (5.03%)
Sediment Steady State Temperature	0.24 (0.25%)	2.48 (2.75%)	3.10 (2.25%)	10.2 (3.58%)
Temperature Sensor Depth	0.15 (0.17%)	1.58 (1.60%)	5.13 (3.63%)	12.0 (7.32%)
Thermal Conductivity	1.16 (1.19%)	1.10 (1.19%)	0.93 (0.67%)	5.46 (3.47%)
Total Heat Flow Uncertainty	1.21 (1.25%)	14.8 (14.0%)	6.4 (5.0%)	19.7 (16.5%)
Monte Carlo Heat Flow Bias	0.17 (0.16%)	2.11 (2.6%)	0.26 (0.18%)	1.3 (1.0%)

The offset from the estimated Monte Carlo heat flow to the measured heat flow (Figure 3.7) is another statistical indicator of how well the Monte Carlo simulations mimicked the measurement. Measurement bias had a positive linear correlation with the uncertainty and was low (<0.2%) for the Violin-bow Probe and Multi-core Logger. The Alvin Probe had the highest heat flow bias, averaging 2.6%, a symptom of the high tilt uncertainty, a parameter that only lowers the heat flow and does not produce a normal heat flow distribution.

3.3.6 Measurement Geographic Location

Accurate knowledge of the geographical location of the heat flow measurement is another experimental design consideration that is vital to the interpretation of measured heat flow, especially in high resolution heat flow studies. Of the four types of instruments presented in this study, the Violin-bow Probe and Multi-core Logger were deployed directly from the ship with their measurement location based on ship Global Positioning System (GPS). Horizontal offsets of the instrument location compared to the ship, due to oceanic current or ship movement, may cause a total location uncertainty on the seafloor of up to ±150 to 200 meters (Kaul et al., 2000). The Thermal Blanket and Alvin Probe were deployed using ROV *Jason* that utilized an Ultra-Short Base-Line (USBL) for navigation with a smaller potential location uncertainty of ±1.5 to 8 meters (Sonardyne, 2009).

Due to the pogo-style deployment, the Violin-bow Probe required time to swing from the previous station to the new location beneath the ship. If there was inadequate time to allow the probe to swing directly under the ship, the Violin-bow Probe would have an additional location uncertainty in comparison to the Multi-core Logger. Assuming that an increasing deployment tilt from vertical is a qualitative indication of wire angle and horizontal offset from the ship location, the measured Violin-bow Probe tilts implied the probe navigational uncertainty was increasing throughout the pogo cycle.

3.4 Environmental Uncertainty

External environmental factors add additional sources of variability to uncertainties inherent to the instrument and that are difficult to quantify due to limited knowledge about the sediment and thermal environment. These factors include localized oceanic bottom water temperature variability, fluid advection, and variations in thermal conductivity present between adjacent thermistors.

3.4.1 Bottom Water Variability

Large-scale near-bottom water temperature variations can produce a non-linear or altered geothermal gradient. One clear indicator of strong environmental influences on a heat flow measurement is a non-linear Bullard plot (Equation 3.1 and 3.2, Figure 3.4). In the presence of long-term temperature trends or substantial near-bottom water variability, there are time periods where the instantaneous Bullard plot is linear. Thus, the observation of a non-linear Bullard plot provides a minimal criterion for rejecting heat flow measurements. The Violin-bow Probe average coefficient of determination (R^2) value for linear regression of the Bullard plot is 0.9986 ± 0.0030, indicating that a near linear heat flow profile was consistently measured with that instrument, a possible consequence of measuring heat flow in only the deeper section of the accretionary wedge. The majority (63%) of all of the Alvin Probe heat flow measurements have an R^2 value above 0.90, the criteria limit used for measurement rejection. For the Multi-core Logger, all measurements had an R^2 value above 0.90, with three of the six measurements rising above an R^2 of 0.98. A visible curve in the theoretically linear Bullard Plot provides strong evidence for an environmental influence on the sediment temperature profile at this site.

All of the 25 negative Alvin Probe heat flow values (13% of all measurements) that were deemed unsuitable for analysis, had a poor average R^2 fit of 0.73 ± 0.26 indicative of highly non-linear geothermal profiles. These heat flow probes were all deployed in water depths shallower than 1300 meters, seafloor depths associated with larger seasonal cycle in temperature, suggesting that bottom water temperature variability is a major environmental source of uncertainty for the Alvin Probe.

The Thermal Blanket top thermistor recorded 5 to 6 days of the near seafloor temperature throughout the survey area that can be used to understand the impact of water column thermal variations on the heat flow within the shallow sediments. Propagating these temperatures into the sediment over the duration of the deployment (Equation 3.5), and assuming a homogeneous thermal diffusivity of 1.15×10^{-7} m^2 s^{-1} (Homola et al., 2015), produces a

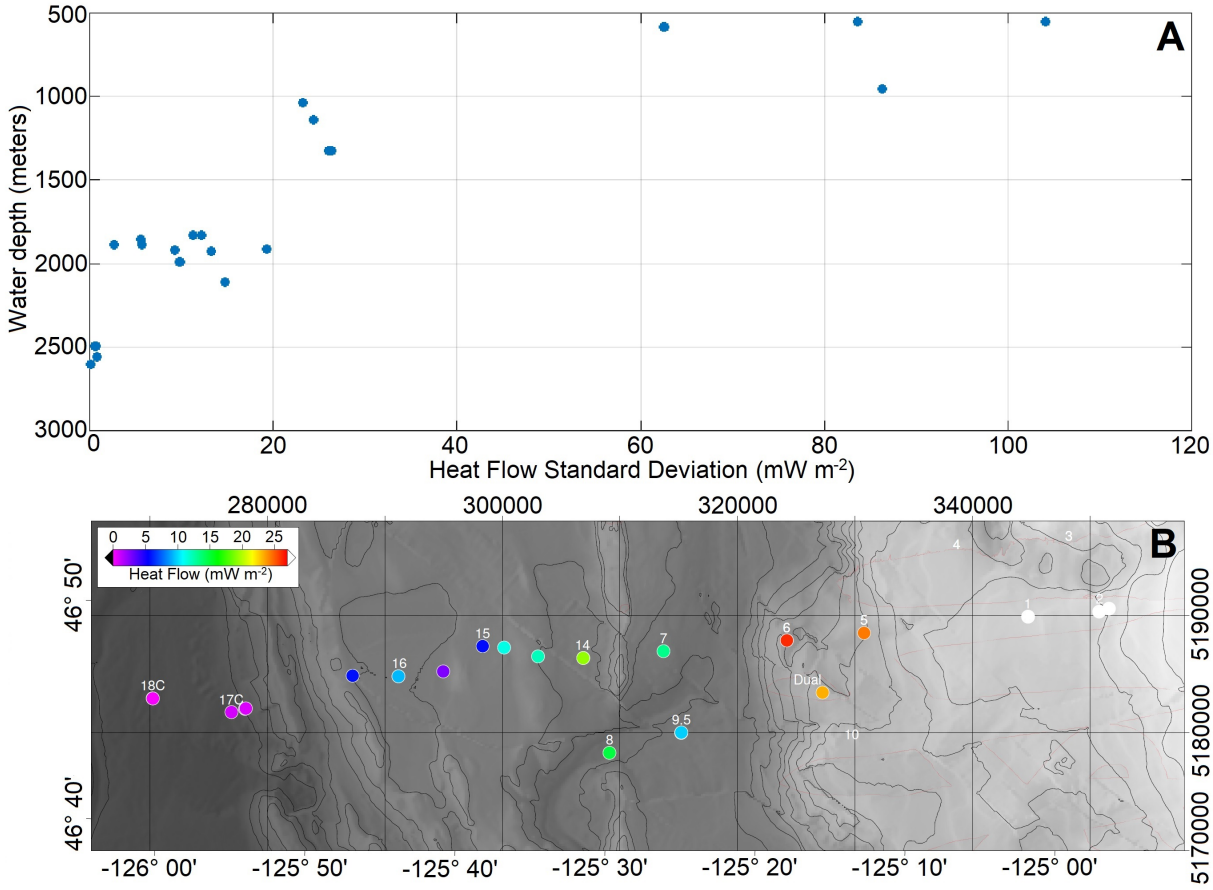

Figure 3.13: Heat flow variations in the top 0.6 meters of the sediment column due to bottom water temperature changes. Calculations are based on Thermal Blanket top thermistor data obtained over a 5 to 6 day period that were propagated to the Alvin probe sensor depths. The heat flow variations are presented from two perspectives: A) versus seafloor depth, and B) map view of the margin that includes showing variations in seafloor bathymetry.

modeled sediment thermal variability at the individual depths of the Alvin Probe thermistors. A time-series of sediment heat flow at each individual Thermal Blanket deployment can then be calculated from the modeled sediment thermal variability. The heat flow standard deviation from this calculation can be as high as 104 mW m^{-2} at a shallow depth of 550 meters (Figure 3.13), supporting the previously noted association of shallower water and negative heat flow values from the Alvin Probe. In general, the standard deviation of

inferred heat flow decreases with increasing water depth. However, the decrease is not solely dependent on water depth. The lower accretionary margin, a wide relatively flat terrace at roughly 1800 meters water depth, exhibits a heat flow standard deviation as low as ∼3 mW m^{-2} and as high as 20 mW m^{-2} during the survey time period (Figure 3.13). These partially depth-dependent heat flow variations highlight the major roles that near seafloor currents and regional bathymetry play in seafloor temperature variability. As oceanic conditions change based on the locations of eddies and currents, the near-seafloor temperature derived heat flow standard deviation across the lower terrace is expected to change with time.

Thermistor data from the seafloor temperature mooring, located at 956 meters water depth, recorded the previous year's thermal variability of the near-bottom water column (Figure 3.6, Figure 3.9). Using the same Equation 3.5 and the parameters and assumptions listed above to propagate the year-long temperature record into the sediment produces a standard deviation of 246.0 mW m^{-2}, for the Alvin Probe, a higher heat flow variability than the 23 to 25 mW m^{-2} estimated nearby for the 5 to 6 day study period. It should be noted that the year-long near seafloor variability is strong enough to disturb the longer Violin-bow Probe measurement by as much as ±20 mW m^{-2} over a year, indicative of how instrument penetration depth can reduce the environment uncertainty of the heat flow measurement. As the intensity of the near-seafloor temperatures can change throughout the year, depending on when the 6-day period of measurement was taken, standard deviation ranged from 9.0 mW m^{-2} to 136.4 mW m^{-2} based on the seafloor mooring record.

Long-term near seafloor temperature records can be used for correcting heat flow measurements. The assumed background heat flow for this area is 60 mW m^{-2} based on a thermal model of the subduction zone (Chapter 2). The modeled surface heat flow, in combination with propagating the year-long temperature record into the sediments using Equation 3.5, can produce a very similar non-linear upward curved thermal gradient as measured by the Alvin Probes at Station 10 (Figure 3.14). Thus, bottom water temperature variability

can explain the non-linear upper sediment temperature profiles observed at shallower water depths on the accretionary wedge.

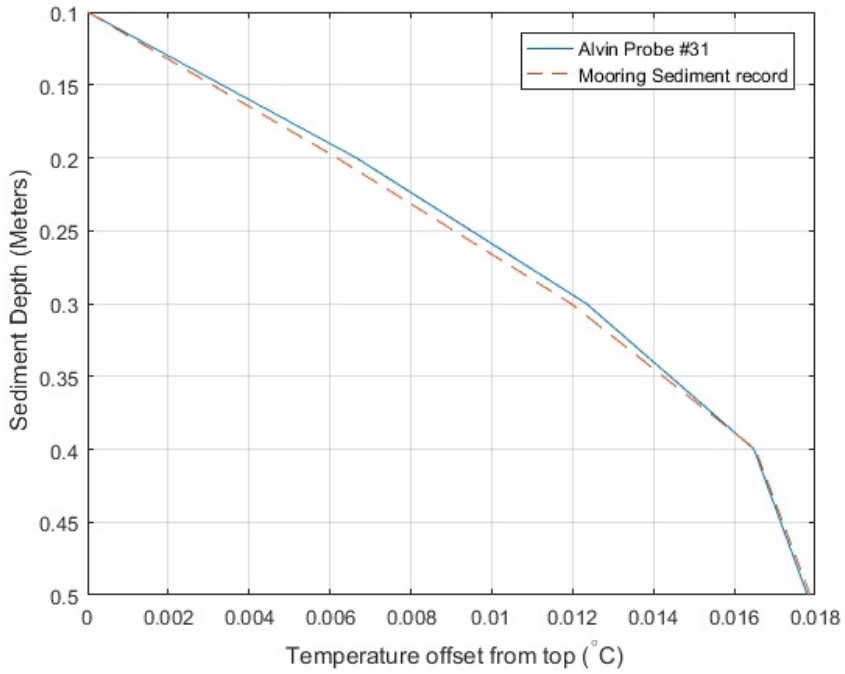

Figure 3.14: Overlay of the temperature profiles with depth for the Alvin Probe measurement 31 at Station 10 (Blue line) and the sediment derived using the mooring thermal record (Red Line). The mooring record was determined by propagation of the seafloor thermal record determined by using the year-long mooring (Figure 3.6; 3.9) into the sediment and an assumed heat flow of 60 mW m^{-2}.

The Thermal Blanket does not completely isolate the underlying sediment from bottom water temperature variability, instead the thermal signals are only attenuated by the Blanket material. The larger modeled uncertainties in the overall heat flow were found at shallower water depths, where the apparent root mean standard deviation of the model fit to the bottom thermistor data is higher (Figure 3.15). Thus, the thermal gradient measured by the Blanket can vary over the deployment time period, which was experimentally observed. If these temperature variations are sufficiently large and transferred to the underlying sedi-

ment thermal gradients, then the Thermal Blanket data analyses will also record variable geothermal gradients due to bottom water variability. A good example is the pair of Thermal Blankets deployed at 554 meters that recorded an average negative heat flow of -137 ± 10 mW m^{-2}.

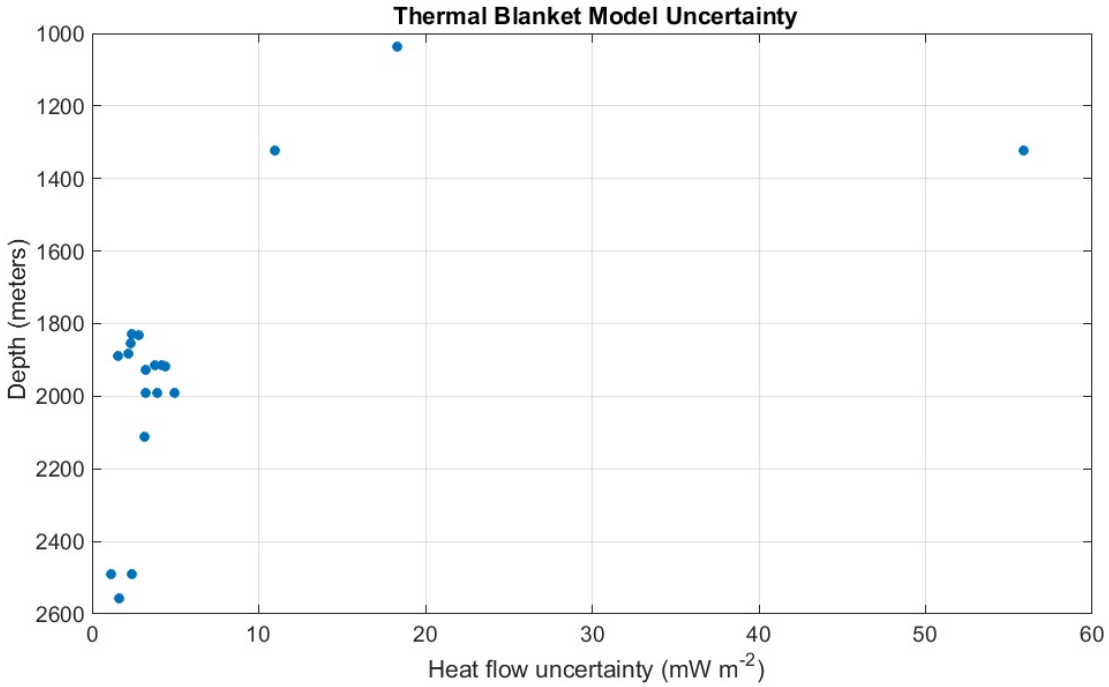

Figure 3.15: The Thermal Blanket Root Mean Standard Deviation (RMSD) of the bottom thermistor fit to the modeled conductive thermal propagations converted to changes in the Blanket's heat flow estimates. The RMSD based heat flow uncertainty plotted against seafloor depth shows potential correlation with near seafloor temperature changes.

3.4.2 Other Environmental Factors

Environmental factors such as variations in sediment thermal conductivity and fluid advection provide additional uncertainties that are difficult to fully quantify using only a heat flow instrument and may require co-registered sediment cores or fluid flux meters to resolve. Small resolution, high thermal conductivity variations could be present between the sensor

spacing such as thin highly permeable turbidite layers (Harris et al., 2010), an unmeasured variation that could alter heat flow. Longer instrument probes and high-resolution thermal conductivity measurements, such as with the Violin-bow probe and Multi-core logger, reduce the heat flow measurement sensitivity to unknown small sediment lenses of different thermal conductivity.

Fluid advection can produce a local elevation in the geothermal gradient by transporting warmer fluids through the sedimentary environment (Bredehoeft and Papadopulos, 1965). Fluid transport up highly permeable layers, such as faults, or as *in-situ* vertical diffuse fluid flow can also elevate heat flow and in cases of high flow rates, will produce measurably curved geothermal gradients. Distinguishing fluid flow derived elevated heat flow requires additional information about the sediment chemistry profile, *in-situ* fluid flow, and the near bottom water temperature variability to rule out other causes of non-linear temperature profiles.

3.5 Discussion

3.5.1 Intra- and Inter-instrument Comparison

Due to the difference in deployment methodology and survey design, only two of the four types of heat flow instruments, the Thermal Blanket and Alvin Probe, had duplicate measurements that allowed for measurement comparison between the same type of instrument under similar environmental conditions. There were 3 sets of duplicate measurements where two Thermal Blankets were placed within 3 meters of each other. The first set, L1 (Instrument number/Deployment number; see Appendix A.4) and T1, both failed to seal to seafloor. The second set (T2/S2) used the S Thermal Blanket which was removed due to poor thermistor calibration. A third set of Thermal Blankets (P1/G1) at Station 6 and a water depth of 1324 meters, had a 3 meter separation and measured heat flow values of 178.4 $\pm$ 26.1 m Wm^{-2} and 179.0 $\pm$ 26.2 mW m^{-2}, a 0.6 mW m^{-2} difference. A pair of Thermal Blankets, deployed at Station 2 and located within 17.5 meters of each other, both produced a significantly negative average heat flow value of -137.4 mW m^{-2} at a shallow water depth

of 553 meters. The Alvin Probe had 29 reliable duplicates within 10 meters of each other, of which 25 were consistent and within their individual heat flow uncertainties, implying that the estimated uncertainties for the Alvin Probe are reasonable.

Comparison of heat flow values from multiple instrument types in relatively close proximity provides a gauge for how well each instrument performs under similar environmental conditions. Since the Thermal Blankets were deployed in conjunction with the Alvin Probe and recovered 5 to 6 days later, an inter-instrument measurement comparison that includes the different responses to short-term water temporal variability can be explored. A combination of 22 Thermal Blanket and Alvin Probe measurement site pairings were deployed using ROV *Jason* (Table 3.3), where the ROV's USBL navigation system lead to a high confidence in the distances between sites. Almost all of these measurements were taken within 10 meters of each other, with the exception of one pair with a separation of 24 meters, deployed on two separate *Jason* dives. Most Alvin Probe measurements were made during ROV *Jason* dives where Thermal Blankets were also being deployed on the seafloor. This chronology resulted in the Alvin Probe capturing the near-instantaneous thermal gradient while the nearby Thermal Blanket was still cooling and coming into equilibrium with the seafloor, resulting in measurements outside their determined uncertainties. Only a single Alvin Probe (#49) was deployed during the dive that recovered the Thermal Blankets from the middle margin site measured a value within 5.5 mW m^{-2} (3.1%) of the nearby Blanket G1 heat flow located 24 meters away (Table 3.3).

As the Multi-core system was primarily used for pore water chemical studies, it was deployed relatively distant from the other instrument sites, with an average separation of 220 meters from the nearest measurement. The pairings between the Multi-core Logger and other heat flow instruments had an average offset of 21% and only half had values that were within their heat flow uncertainties from each other. Because the Multi-core Logger was deployed from the surface ship, the precise measurement location was less well known than for the instruments deployed by the ROV, and it is difficult to tell if the larger offsets are

Table 3.3: Comparisons between Thermal Blanket and Alvin heat flow Probe measurement duplicates. Each measurement pairing was captured within 10 meters of each other with the exception of G1 and Probe 49.

Seafloor Depth (meters)	Blanket Name	Blanket Uncertainty (mW m^{-1})	Alvin Name	Alvin Heat Flow (mW m^{-1})	R^2	Distance between (meters)	Within Uncertainty?
1323.6	G1	178.4 ± 26.1	20	58.0 ± 61.9	0.7420	3	No
1323.6	G1	178.4 ± 26.1	21	74.4 ± 7.9	0.8790	3	No
1323.6	G1	178.4 ± 26.1	19	75.8 ± 27.2	0.8488	8	No
1323.6	G1	178.4 ± 26.1	49	172.9 ± 64.6	0.3709	24[1]	**Yes**
1323.6	P1	179.0 ± 26.2	20	58.0 ± 61.9	0.7420	6	No
1323.6	P1	179.0 ± 26.3	21	74.4 ± 7.9	0.8790	1	No
1828.6	N2	163.2 ± 22.9	82	125.4 ± 16.9	0.9454	2	**Yes**
1853.0	P2	80.1 ± 13.5	84	107.5 ± 20.8	0.9071	6	**Yes**
1853.0	P2	80.1 ± 13.5	85	94.9 ± 19.8	0.9005	6	**Yes**
1887.6	D1	139.2 ± 14.4	96	109.6 ± 14.5	0.9624	5	No
1887.6	D1	139.2 ± 14.4	97	146.9 ± 17.5	0.9614	5	**Yes**
1913.1	O2	51.3 ± 14.5	65	78.3 ± 8.5	0.9569	3	No
1913.1	Q2	73.8 ± 16.4	66	72.7 ± 7.2	0.9406	7	**Yes**
1926.3	N1	162.7 ± 24.2	24	144.9 ± 19.9	0.9334	5	**Yes**
1926.3	N1	162.7 ± 24.2	23	147.2 ± 20.7	0.9425	9	**Yes**
1991.0	I1	167.5 ± 24.5	28	246.9 ± 40.0	0.8199	1	No[2]
1991.1	O1	67.9 ± 16.2	29	127.3 ± 18.5	0.9491	2	No[2]
2111.0	R1	226.9 ± 28.1	53	116.4 ± 13.6	0.9540	4 [1]	No[2]
2111.0	R1	226.9 ± 28.1	54	156.3 ± 19.3	0.9666	4 [1]	No[2]
2491.3	H2	112.1 ± 27.2	157	112.8 ± 18.2	0.9435	7	**Yes**
2490.7	I2	111.0 ± 9.2	154	118.5 ± 16.3	0.9574	8	**Yes**

[1] Alvin Probe Deployed during the retrieval of the Thermal Blanket.

[2] Station 8 and 9.5 - potential fluid and methane emissions sites.

due to environmental causes or location uncertainties.

The Violin-bow Probe was also generally deployed at larger separation distances from other instruments, with an average spacing of approximately 400 meters from the next adjacent measurement. Only one Multi-core Logger measurement was within approximately 30 meters of a Violin-bow Probe measurement and it recorded a heat flow that was 77.6 mW m^{-2} higher. There is no obvious reason for the large difference in heat flow values as both measurements appear reliable, with high R^2 Bullard plots and comparative thermal conductivity measurements. However, given the larger location uncertainty associated with measurements made from the surface ship, it is possible they were much further apart than 30 m. Alternatively, the Multi-core Logger may have sampled a high heat flow value within a localized area of elevated heat flow related to fluid advection, or the measurements were disturbed by bottom water variability that did not appear to alter the Bullard plots.

3.5.2 Bottom Water Variability and Deployment Chronology

The dominant environmental impact on heat flow uncertainty is the near-seafloor water temperature variations, a well-known issue discussed in previous studies (Ruppel et al., 1995; Hamamoto et al., 2005). It should be assumed that near bottom water temperatures and therefore the geothermal gradient within the shallow sediments will not remain constant during subsequent heat flow measurements, especially on the shallow continental shelf and slope. Within this dataset, temporal variability in heat flow measurements, non-linear geothermal profiles, and measured near seafloor water temperature records are distinctly evident within the shallow portion of the accretionary margin. Surface heat flow measurements in close spatial proximity but separated temporally, such as those deployed at similar locations but on different ROV *Jason* dives (Table 3.3), revealed significant shifts in near-seafloor geothermal gradient that would otherwise remain undetected. This is notably true for the lower accretionary margin where it was assumed that there would be a largely reduced bottom water temperature variations at the greater seafloor depths of 1800 to 2000 meters.

Table 3.4: Thermal Blanket and Alvin Probe heat flow measurement offsets categorized by middle terrace (seafloor depths less than 1800 meters, see the upper portion of the table) and lower terrace (seafloor depths greater than 1800 meters, see the lower portion of the table). Measurement uncertainties can be found in Table 3.3. Deployments that occurred at potential methane and fluid emission sites, such as Station 8 and 9.5, have been removed from the analysis.

Dive	Seafloor Depth (meters)	Alvin Name	Alvin Heat Flow (mW m^{-1})	Blanket Name	Blanket Heat Flow (mW m^{-1})	Distance between (meters)	Heat Flow Difference
719	1323.6	20	58.0	G1	178.4	3	120.4
719	1323.6	21	74.4	G1	178.4	3	104.0
719	1323.6	19	75.8	G1	178.4	8	102.6
719	1323.6	20	58.0	P1	179.0	6	121.0
719	1323.6	21	74.4	P1	179.0	1	104.6
721	1323.6	49	172.9	G1	178.4	24*	5.5
						Mean	110.5
719	1926.3	24	144.9	N1	162.7	5	17.8
719	1926.3	23	147.2	N1	162.7	9	15.5
723	1828.6	82	125.4	N2	163.2	2	37.7
723	1853.0	84	107.5	P2	80.1	6	27.4
723	1853.0	85	94.9	P2	80.1	6	14.8
723	1887.6	96	109.6	D1	139.2	5	29.6
723	1887.6	97	146.9	D1	139.2	5	7.7
723	1913.1	65	78.3	O2	51.3	3	27.0
723	1913.1	66	72.7	Q2	73.8	7	1.1
723	2491.3	157	112.8	H2	112.1	7	0.7
723	2490.7	154	118.5	I2	111.0	8	7.5
						Mean	17.0

[1] Alvin Probe deployed during the retrieval of Thermal Blanket G1.

With no repeat visits to Alvin Probe sites within the lower margin on different ROV dives, comparison to nearby Thermal Blankets provided the only means to quantify the effect of water temperature variations within the lower accretionary terrace. On the upper portion of the study area, in water as shallow as 550 meters and in an area associated with relatively high seawater temperature variations, five individual Alvin Probes had an average difference of 110.5 mW m^{-2} from their nearest Thermal Blankets (Table 3.4). In contrast, the relatively thermally quiescent lower margin sites had an average offset of only 17 mW m^{-2} for 11 instrument pairings. However, although the offsets decrease with increasing water depth as expected, both instrument types appear to be heavily impacted by bottom water temperature variations.

Based on observed difficulties measuring the geothermal gradient at numerous shallow sites, the Alvin Probe 0.6 meter length appears insufficient for work in depths shallower than 1800 meters along the mid-slope terrace offshore Washington State. Using the year-long mooring data at 956 meters water depth, a probe longer than 4 meters would be required to avoid a $\pm$10 mW m^{-2} uncertainty caused by the near-bottom temperature variations (Figure 3.16). In comparison, the shorter Alvin probe length and sensor resolution would produce uncertainty of over 60 mW m^{-2}. It appears the probe length is a more important consideration than temperature sensor density along the probe.

Reliable heat flow measurements in shallower water depths require using a probe with sufficient length paired with a multiple-year near-bottom water temperature record deployed at the same location (e.g. Hamamoto et al. 2011). Using Equation 3.5 and a knowledge of the dominant seawater temperature variation frequency and amplitude, along the sediment thermal diffusivity, the depth of near-seafloor temperature propagation can be assessed. As a case study, the depth of a 0.001°C seawater-related temperature change was determined for a sediment thermal diffusivity of 1.15 x 10^{-7} m^2 s^{-1} over a range of temperature frequencies and periods (Figure 3.17), demonstrating that with increasing temperature amplitude and, more notably, increasing period, the near-bottom water temperature will have a deeper reaching

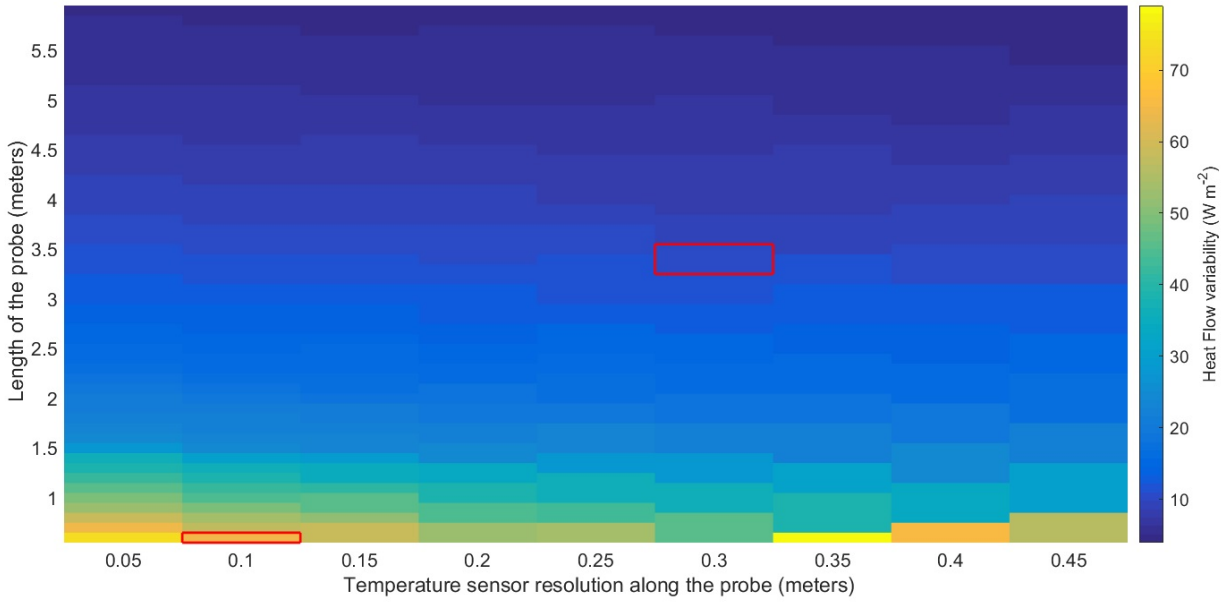

Figure 3.16: Sensitivity to near-bottom water variability based on the length of the probe (y-axis) and sensor resolution (x-axis). The data was generated by utilizing the year-long temperature record collected at Station 10 (Figure 3.6), propagating the record into the sediment using Equation 3.5, and determining the magnitude of change in the heat flow measurement. The Alvin and Violin-bow probe configurations are outlined in red.

impact on the sediment column.

3.5.3 Ideal Instrumentation Use and Suggested Improvements

Major aspects for any heat flow study to consider are 1) instrument deployment logistics that include surface ship or ROV availability, 2) accuracy of instrument deployment location and measurement, and 3) the impact of sediment lithology and geological structure where instruments with varying penetration depths can be deployed, including the presence of authigenic carbonate deposition or turbiditic sand deposits. Deployment directly from the surface ship provides an easier means of covering large areas for geological studies, while instrument deployment by an ROV allows for higher spatial resolution of measurements and higher location accuracy necessary for detecting fluid advection. Thermal Blankets

are uniquely able to measure heat flow where the seafloor consists of hard rock, either of igneous or carbonate composition. Determining thermal conductivity *in-situ* provides a more accurate and quicker measurement than post-recovery laboratory measurements, without the risk of losing water or sediment material during recovery, while laboratory measurements can capture a higher resolution thermal conductivity profile.

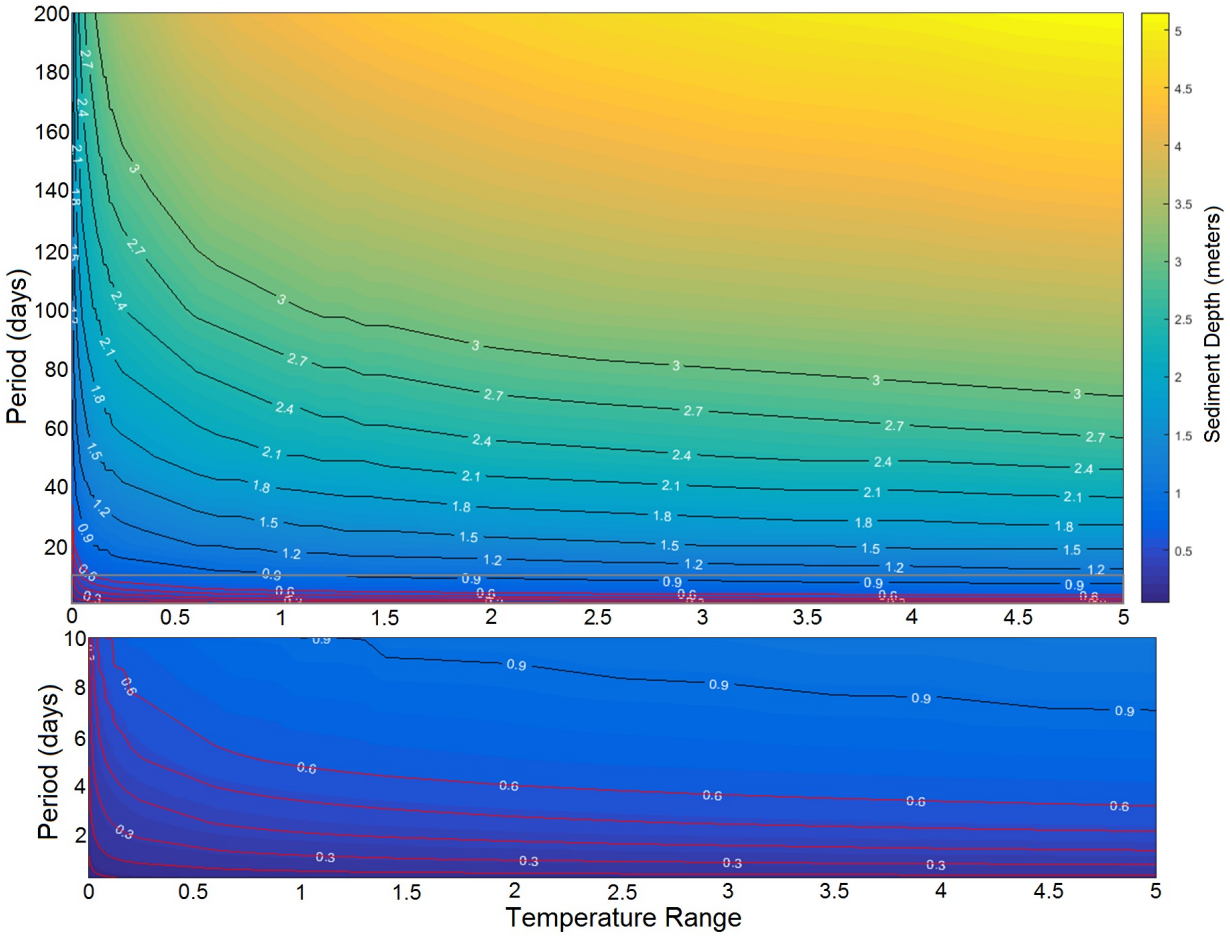

Figure 3.17: Propagation depths (meters) of the 0.001°C thermal disturbance for various temperature period lengths and ranges determined using Equation 3.5. Black contours (labels are in units of meters) mark the Violin-bow Probe thermistor depths and Red contours indicate Alvin heat flow Probe thermistor depths.

Data from additional instrument types and external bottom water moorings recorded prior to, and during, heat flow campaigns can add an assessment of near-bottom water variability into heat flow studies. For example, the use of temperature sensors attached to Ocean Bottom Seismometers (OBSs), as deployed by the Cascadia Initiative (Toomey et al., 2014; Johnson et al., 2017a), and temperature loggers attached to cabled networks such as Ocean Networks Canada (Barnes et al., 2011) and Ocean Observatories Initiative (Cowles et al., 2010), could provide essential long-term multi-year water temperature records for heat flow stations located in close proximity. While temperature records longer than a year did not exist in the Southern Washington Cascadia study area, multi-year near seafloor temperature trends are known to be present and can alter the thermal regime of the near seafloor sediments (Hautala et al., 2014). Deployment of heat flow instruments with corresponding water column temperature records can also provide a means of correcting for near seafloor thermal variations, as shown in studies off the Nankai margin (Hamamoto et al., 2005, 2011) in addition to offering insight into local fluid flow regimes (Goto et al., 2005). A method that appears quite promising is the continued development in regional scale oceanographic fluid dynamic models (MacCready and Giddings, 2016) which offers a numerical approach to determining near-bottom temperature variability.

There is clearly room for technical improvement in the acquisition of heat flow data. For any inter-instrument comparison, improving the accuracy of the measurement location would be a significant advantage. The use of positioning beacons, such as USBL, directly on the instrument package would provide an increased location accuracy for surface ship deployments. A tilt sensor on all probe type measurements, including those deployed by ROV manipulators is essential, since tilt can produce large artificial reductions in measured heat flow, as reflected in the Alvin Probe uncertainty calculations. For near bottom water variability, consistently capturing *in-situ* Antares thermistor calibrations at the deployment depth for the Thermal Blankets appears essential and would provide a better insight into the accuracy of laboratory ice bath calibrations.

3.6 Conclusions

An analysis of marine heat flow measurements from four different instruments can provide valuable insight into the thermal environment, quantifying fluid advection, detecting recent mass sediment movement, and other key geological processes. It is therefore vital to understand the accuracy of these measurements. In an attempt to understand uncertainties associated with each instrument, we compared heat flow measured using four different heat flow instruments. A total of 251 measurements were collected during a single cruise on Cascadia margin, over a depth range from 550 to 2600 meters that encompassed a wide range of bathymetric and oceanographic environments. An analysis of the variables that affect individual instruments reveals that each instrument type is uniquely impacted by a range of prevailing factors that include instrument tilt, method of deployment, bottom water temperature variations, and penetration depth. The Thermal Blanket and Alvin Probes were deployed over a wide range of sediment environments and in higher spatial density compared to the Violin-bow Probe and Multi-core Logger, but produced data with a larger degree of uncertainty due to both environmental stressors and instrument construction. The Multi-core Logger provided robust heat flow measurements owing to the stable frame and deployments in the thermally quiet lower margin. The Violin-bow Probe that can sample sedimented location similar to the Multi-core Logger, captured the most accurate heat flow measurements due to its extended probe length.

Based on the quantitative comparison of multiple heat flow instruments, and including incorporation of near-seafloor temperature records, the variability of the seafloor water temperatures along the accretionary wedge has a profound impact on the absolute accuracy of the heat flow measurements. While it is generally assumed that near-seafloor water temperature variations systematically decrease with increasing depth offshore Cascadia Subduction zone, both bathymetry and contact with variable oceanographic currents can have a strong local impact. Heat flow measurements made at deployment sites at similar depths but at different time periods were exposed to dissimilar seafloor thermal conditions. In shallow

water, obtaining long term records of near-bottom water temperature variations prior to the heat flow study is essential to understanding the local thermal environment. These data can be obtained through sources that include temperature moorings, OBS deployments with temperature sensors, ocean dynamic modeling where boundary conditions are well known, or cabled instrumentation located near the heat flow measurement sites.

Chapter 4

SEAFLOOR FLUID EMISSIONS AND SHALLOW CIRCULATION WITHIN THE SOUTHERN WASHINGTON ACCRETIONARY MARGIN

4.1 Introduction

Accretionary wedge sediments form an environment that supports a multitude of fluid-driven processes integral to ocean-earth interactions. Within the accretionary prism, sediment deformation interacts with fluids filling the pore space, driving fluid movement and producing an increase in pore fluid pressure relative to the sediment on the incoming plate. The resulting fluid flux transports solutes, hydrocarbons, and thermal energy from deep within the sediments through the accretionary wedge into the overlying ocean. Knowledge of the accretionary fluid budget can address questions about fluid pressure and rates of dewatering, parameters associated with fault strength and wedge mechanics (Saffer and Bekins, 2002). Fluid budgets are typically either numerically modeled based on general wedge parameters such as prism geometry and sediment porosity (Le Pichon et al., 1991; Moore and Vrolijk, 1992; Ellis et al., 2015) or inferred by locating and quantifying surface fluid discharge locations (Carson et al., 1990).

Fluid discharge locations on accretionary prisms can be detected directly with fluid flow meters (Tryon et al., 1999), or indirectly via their associated chemosynthetic biological communities, methane emissions, and carbonates. Authigenic carbonate precipitates, mostly in the form of aragonite or calcite minerals, provide superficial evidence for the venting of methane laden fluids (Suess and Bohrmann, 1997; Sample and Reid, 1998; Luff and Wallmann, 2003). Carbonate precipitation distribution also provides superficial evidence for faults that transport warm fluids sourced from a depth of several kilometers in the sedimen-

tary prism (Westbrook et al., 1994; Dumke et al., 2014).

Without distinct indicators of methane, gas-free fluid discharge sites are challenging to identify based on video and acoustic surveys, although vent locations can be distinguished by their impact on surface and Bottom Simulating Reflector (BSR) heat flux (e.g., Zwart et al. 1996). Previous approaches to detecting fluid venting include identifying elevated heat flow measurements due to warmer fluids migrating through the sediments (Foucher, 1990; Feseker et al., 2008) and vertical geochemical sediment pore fluid profiles (Torres et al., 2002). In addition, comparisons of thermal model results to BSR derived heat flow measurements have allowed for the quantification of deeply-sourced diffuse fluid emissions through the accretionary wedge (Wang et al., 1993; Ganguly et al., 2000)(Chapter 2).

4.1.1 Survey Location – Cascadia Subduction Zone

The Cascadia Subduction Zone extends roughly 1000 km from Vancouver Island, Canada to Mendocino, California, USA and is formed by subduction of the Juan de Fuca plate beneath the North American plate at a rate of roughly 40 mm yr^{-1} offshore Washington State (Wilson, 1993)(Figure 4.1). The incoming plate is relatively young at 6 to 8 Myr and represents the high temperature end member for an incoming subduction zone sediment-plate interface with estimated modeled temperatures in the 160°C to 250°C range (Hyndman and Wang, 1995; Johnson et al., 2012)(Chapter 2; Figure 4.2). The accretionary wedge structure off southern Washington State has an atypical two-tiered bathymetric profile. The lower portion of the margin consists of folded and faulted sediments, with clear indications of compressional strain (Adam et al., 2004; Booth-Rea et al., 2008), while the middle to upper portion of the wedge is an area of horizontal extension, characterized by prominent listric faults formed due to over-pressurization within the underlying sediments (McNeill et al., 1997).

Multiple localized methane emission sites have been observed within the Cascadia accretionary wedge offshore Oregon (Luff and Wallmann, 2003; Torres et al., 2009), Washington

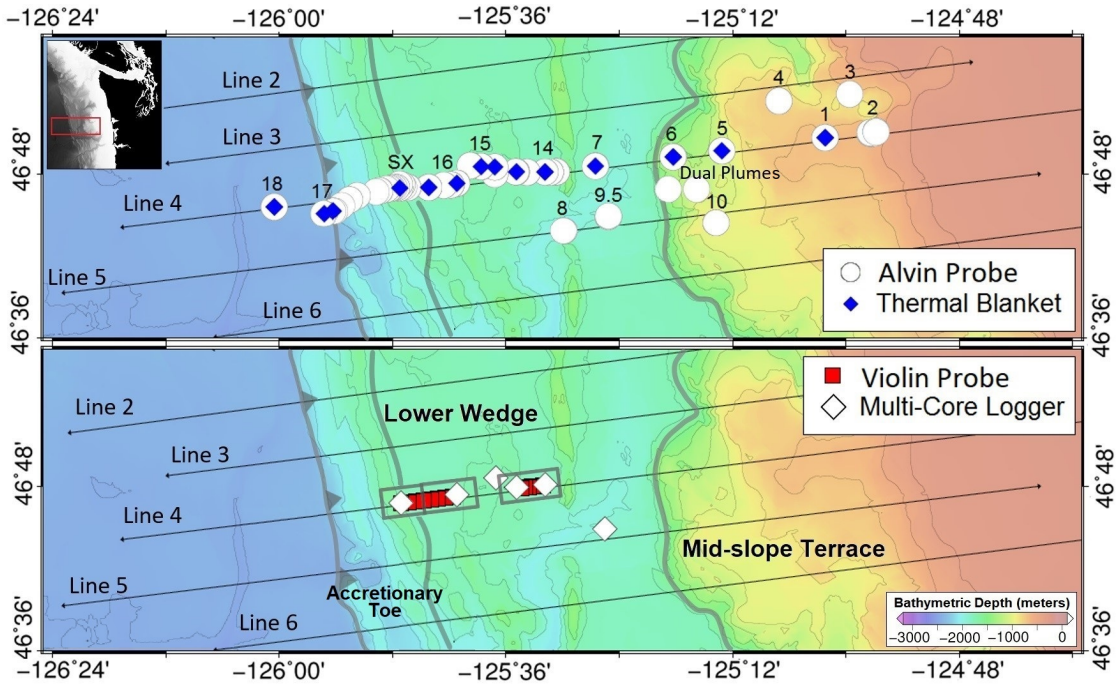

Figure 4.1: Location of the four types of heat flow measurements. Black lines mark the R/V *Langseth* (MGL1212) multi-channel seismic track lines 2 through 6. Station centers are labeled with their associated numbers. The deformation front and transition from the lower accretionary wedge to mid-slope terrace are marked by a gray line.

(Salmi et al., 2011), and Vancouver Island, Canada (Zuhlsdorff et al., 2000; Riedel et al., 2010). Carbonate deposits have been inferred from side-scan sonar surveys along large portions of the Cascadia margin (Carson et al., 1994) indicating substantial diffuse methane-rich fluid discharge. Previous surface heat flow study locations using the Violin-bow Probe on the Cascadia accretionary wedge include offshore Vancouver Island (Davis et al., 1990), Washington State on the accretionary toe (Shi et al., 1988), and Oregon State (Cozzens and Spinelli, 2012). Fluid emission from the Cascadia accretionary prism has either been modeled as a general diffuse flux through the wedge sediments with rates up to 45 mm yr^{-1} (Wang et al., 1993), with estimated substantial flow rates at methane emission locations within the accretionary toe of 105 m yr^{-1} to 115 m yr^{-1} (Carson et al., 1990), or as point sources where faults provide permeable pathways (Zwart et al., 1996; Tryon et al., 2002). Direct measurement of

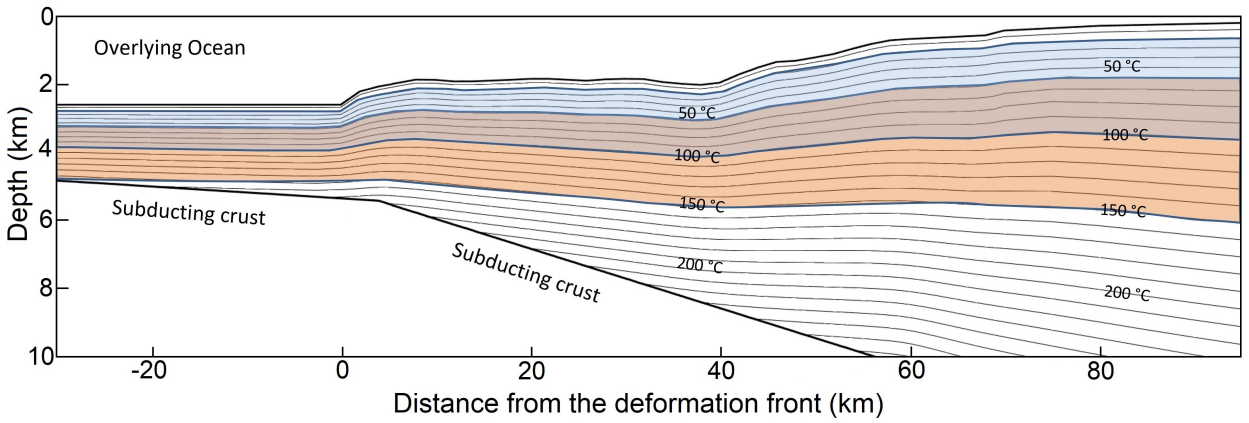

Figure 4.2: Modeled isotherm map of the accretionary wedge along the MGL1212 Line 4 profile from Chapter 2. Contours are at 10°C interval. Shading mark the temperatures associated with the dehydration reactions that include smectite to illite (60° to 150°C, blue) and Opal A to quartz (20° to 100°C, orange).

fluid discharge has occurred on the Oregon margin near the active Hydrate Ridge methane seep site, with values of up to 1 m yr^{-1} (Linke et al., 1994; Tryon et al., 1999).

This study presents the results obtained using four different heat flow instruments that measure the geothermal heat flow over varying seafloor depths and deployment time periods along a transect that spans most of the Cascadia accretionary prism off southern Washington State (Figure 4.1). The survey extends from the abyssal plain at 2600 m depth to 75 km landward of the deformation front at a water depth of 550 m, including a high resolution survey over the accretionary toe. The use of four different instruments provides multiple methodological approaches to increase confidence in the background heat flow estimates (Chapter 3). Geological and structural context are derived from co-located 2012 R/V *Langseth* Cascade Open Access Seismic Transects (COAST) multi-channel seismic profiles Lines 3, 4, and 5 (Holbrook et al., 2012)(Chapter 2) and auxiliary environmental data such as sediment thermal conductivity measurements, multibeam-derived acoustic backscatter, and ROV-derived seafloor video observations. Through combining these diverse data sources, this study aims to both pinpoint fluid discharge locations, and link the observed heat flow

distribution to larger thermal and fluid distributions associated with wedge mechanics.

4.2 Methods

4.2.1 Surface Heat Flow

Violin-bow Probe

The Violin-bow Probe consists of a 3.5 meter weighted strength member equipped with an external string of 11 thermistors at 0.3 meter spacing. An electrical resistance wire within the external string provides heating for *in-situ* thermal conductivity measurements. The instrument was deployed from the ship in the pogo style that allows for more efficient use of ship time (Moran and Lister, 1987). Each pogo series of measurements had an average station spacing of 829 meters (±250 meters), with a 9.3 kilometer distance between two separate deployment regions that were chosen to deliberately avoid buried or exposed anticlinal ridges. Heat flow was calculated using the Matlab program SlugHeat, based on the HFRED algorithm (Villinger and Davis, 1987).

Alvin Heat Flow Probe

The Alvin heat flow Probe consists of a shorter 0.6 meter length strength member that houses the heating coil with 5 thermistors spaced at 0.1 meter intervals. The ROV *Jason II* manipulator arm was used to hold the probe in the water for an *in-situ* thermistor calibration prior to inserting the probe into the sediment and releasing the manipulator. After ten minutes capturing the *in-situ* thermal gradient, a heat pulse was fired to determine thermal conductivity. As with the Violin-bow Probe, data was processed using the Matlab program SlugHeat, with parameters appropriate for the Alvin Probe.

Multi-core Logger

The Multi-core Logger consists of a frame and piston system that can collect multiple short cores within a localized area simultaneously and is typically used for near-surface

geochemistry studies. The Multi-core system was modified to record the geothermal gradient by attaching thermistors to a core liner at intervals ranging from 0.075 to 0.01 meters. A second adjacent core liner with pre-drilled 2 cm spacings collected sediments for onboard thermal conductivity measurements using a needle probe (Von Herzen and Maxwell, 1959; Lister, 1979; Goto and Matsubayshi, 2008). The first step in processing was to calibrate the temperature sensors based on the *in-situ* near-seafloor temperature record. Next, the thermal gradient was determined by extrapolating the measured sub-surface temperatures to steady state. The geothermal gradient was resampled at a 2 cm interval to match the thermal conductivity measurement depths. Finally, heat flow was determined from the slope of the Bullard Plot (Bullard, 1939), a graph of temperature versus sediment thermal resistance.

Thermal Blanket

The Thermal Blanket is a roughly 0.16 m^2 foam pad covered in a heavy canvas. A rubber tube filled with super-saturated sodium chloride provides negative buoyancy to help seal the Thermal Blanket to the seafloor. Two Antares temperature sensors were fixed to the top and bottom of the instrument body to capture the thermal environment surrounding the Thermal Blanket. The Thermal Blanket was deployed by ROV *Jason* for periods of 5 to 6 days on the seafloor in order for the instrument to reach equilibrium with the seafloor environment. To accurately capture the geothermal gradient, water column temperature variations detected by the top thermistor were propagated through the Blanket assuming the instrument foam body responded as a purely conductive medium (Carslaw and Jaeger, 1959; Hamamoto et al., 2005). The thickness between the two thermistors is also assumed to vary slightly due to changes in the seafloor medium and the sensors shifting within their cloth housing affixed to the blanket canvas cover. With thermal behavior due to near-bottom water temperature variations removed, the remaining temperature offset provides the geothermal gradient derived from the underlying sediments. More details are available in Salmi et al. (2014) and Chapter 3.

Data Filtering Criteria

Conditions for rejecting individual heat flow measurements include 1) a non-linear Bullard plot, attributed to large near-seafloor temperature variability or other environmental factors, 2) poor thermistor offset calibrations, 3) negative heat flow value, 4) both thermistors on the Thermal Blanket detecting temperature trends simultaneously, an indicator that the Blanket did not have a full seal to the seafloor, or 5) missing data, such as thermal conductivity or a heating pulse. In many cases, if an instrument did not capture reliable heat flow data, other components of the heat flow measurement, such as thermal conductivity and seawater temperatures, still provided useful information.

Non-linear Bullard plots indicate a non-steady state thermal environment potentially due to bottom water temperature variations or fluid flux through the sediment (Bredehoeft and Papadopulos, 1965; Hamamoto et al., 2005). Unreliable thermal conductivity measurements were evident by a poorly behaved or non-conductive cooling rate, resulting in the inability to estimate a value or an abnormally high calculated uncertainty of greater than ∼20% (Hartmann and Villinger, 2002), and these data points were not included in the analysis. For the Thermal Blankets, calibrations between specific Antares thermistor pairs were checked against their laboratory calibrations performed for a previous study (Salmi et al., 2014) and to opportunistic *in-situ* calibrations for 18 of the 27 Thermal Blankets. If any Blanket calibrations shifted significantly over time, data from these instruments were discarded.

Uncertainties in heat flow differ for each instrument type and were estimated for each individual measurement using known errors associated with temperature measurement, thermal conductivity estimate, and sensor depth (Chapter 3). Due to the deployment length of several days, the Thermal Blanket data allow for some assessment of environmental uncertainty derived from changes in the near-bottom water temperature. By numerically propagating the frequency components of the near-seafloor temperature records into the sediment column, assuming the foam has homogeneous thermal diffusivity and is fully conductive, environmental uncertainty in the thermal gradient and heat flow can also be estimated for the shorter

sediment penetration depths of the Multi-core Logger and Alvin Probe (Hamamoto et al., 2005)(Chapter 3).

4.2.2 Seafloor Video Observations

During Thermal Blanket and Alvin Probe deployments and transits between stations, ROV *Jason* photographed the seafloor environment, and unusual seafloor geological characteristics associated with fluid flow were spatially located using the ROV Ultra Short Base Line (USBL) navigation. Such seafloor features included carbonate deposits, clam fields, and bioherms (large carbonate mounds covered with biological communities). While the ROV-mounted camera system provided an opportunistic view of the seafloor, it had limitations that include imperfect 3D visualization and depth perception, reduced color contrast, and incomplete areal coverage.

4.2.3 Backscatter Data

R/V *Atlantis* was equipped with a Kongsberg EM122 12 kHz hull mounted multibeam echo sounder system that mapped the seafloor during the 2013 heat flow study, primarily co-located with the 2012 COAST R/V *Langseth* Lines 4 and 5 (Holbrook et al., 2012)(Chapter 2), covering 118 km along-strike across the accretionary wedge. Data was processed with CARIS HIPS, accounting for variations in sound velocity and gridded at a resolution of 50 x 50 meters. Seafloor backscatter consists of the integration of the highest amplitude acoustic returns. These returns are sensitive to the seafloor morphology and sediment acoustic density gradient within the top 2.6 to 6.5 meters of the sediment column for a 15° beam angle (Johnson and Helferty, 1990; Mitchell, 1993). Backscatter intensity was corrected for incident ray angle and bathymetric slope using the co-registered swath bathymetry. One of the benefits of multibeam backscatter is its ability to detect rough seafloor bathymetry and different sediment characteristics such as large grain size, and moderate carbonate content, which produces high intensity acoustic returns when compared to the lower amplitude

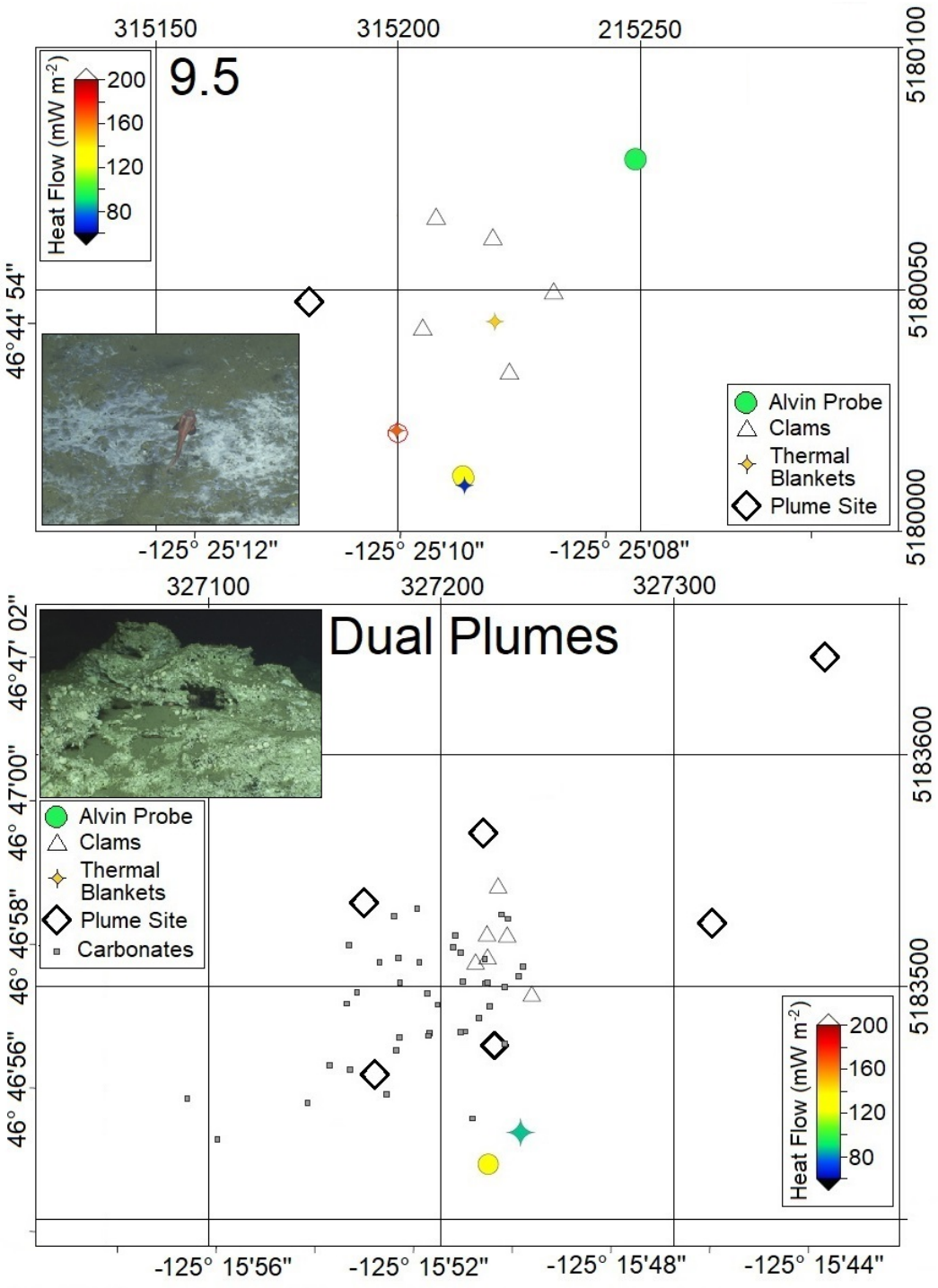

Figure 4.3: Close up visualization of two active bubble plumes emission sites detected using the multibeam system: Dual Plumes and Station 9.5, at seafloor depths of 1039 and 1991 meters, respectively (see Figure 4.1). Additional contextual data in the form of ROV *Jason* video observations and heat flow measurements. Inset images provide an example of seafloor environment for each site. The left and bottom axes labels are in latitude and longitude while the top and right axes labels are UTM Zone 10 (meters).

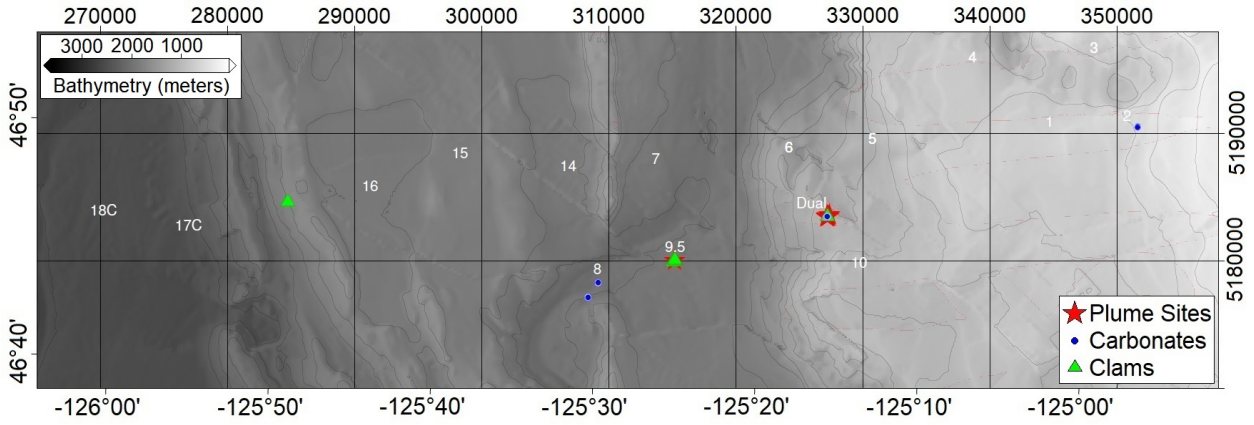

Figure 4.4: Map view of *Jason* video derived observations showing locations of clam beds and carbonate plates, as well as acoustically detected methane emission sites detected by surface ship multibeam system. Underlay is swath derived bathymetry shown in gray scale with lighter shades representing shallower depths and contours at 200 meter intervals. The left and bottom axes labels are in latitude and longitude while the top and right axes labels are UTM Zone 10 (meters).

reflections from soft carbonate-free sediments (Carson et al., 1994).

4.3 Observations and Results

4.3.1 Seafloor and Subseafloor Observations

Active bubble emissions were detected using the hull-based multibeam system at two different stations within our survey area; Dual Plumes and Site 9.5 (Figure 4.1). At Station 9.5, ROV *Jason* video mapped the presence of clams and active gas bubbles emitted from the sediment, but did not detect carbonate deposits on the seafloor (Figure 4.3). In contrast, the Dual Plumes station is characterized by large (1+ meters long) visible carbonate mounds and clam beds on the seafloor (Figure 4.3). While Station 8 did not have any bubble emissions detected within the water column by either the multibeam system or imaged by ROV *Jason*, it did have visibly exposed carbonate protruding from the sediment (Figure 4.4).

General acoustic backscatter distribution within the lower accretionary wedge includes

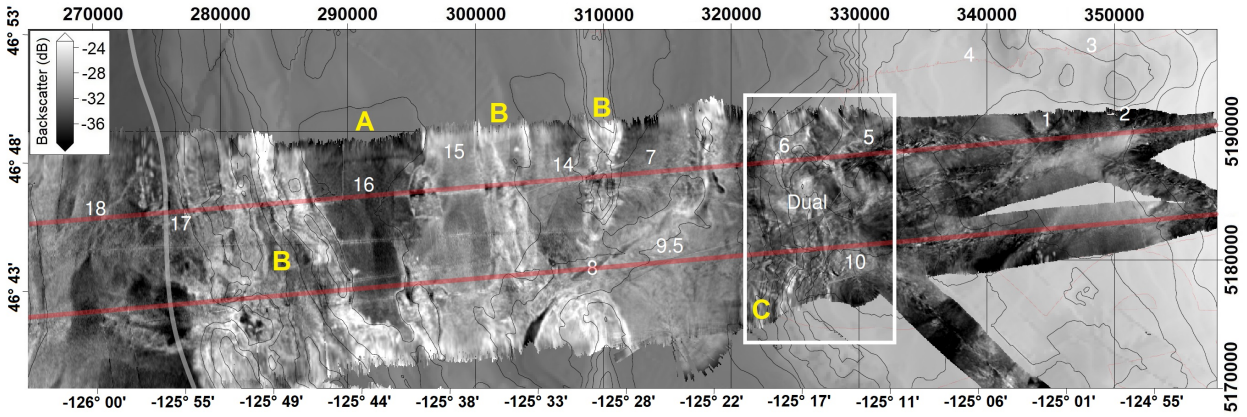

Figure 4.5: Multibeam derived acoustic backscatter along the *Langseth* MCS Line 4 and 5 Profile (red lines). Polarity shown is light color as hard backscatter returns. Dominate features include A) sediment pond with very low backscatter, B) primarily north-south high backscatter features, and a C) patchy high backscatter pattern.

high amplitude seafloor returns located primarily within the first anticlinal ridge/accretionary toe and within a large portion of the lower margin (Figure 4.5). However, a sediment pond to the east of the first anticlinal ridge showed only low amplitude backscatter (A on Figure 4.5). Narrow bands of high amplitude backscatter are oriented primarily north-south and appear correlated with the bathymetry within the first anticlinal ridge, and along the transitions from exposed ridges to nearby sediment ponds within the lower wedge (B on Figure 4.5). Landward from the lower wedge and onto the mid-slope terrace, the higher relatively uniform background backscatter transitions to a patchy nature and then progressively evolves farther up-slope into an area of uniformly lower backscatter (C on Figure 4.5).

The heat flow survey area was primarily co-located with Line 4, and to a lesser extent Lines 3 and 5 of the 2012 R/V *Langseth* multi-channel seismic profiles to take advantage of the information on the subseafloor structure (Figure 4.1, Figure 4.6). The R/V *Langseth* Line 4 profile near the accretionary toe indicates that over 2 km of sediment has been deposited on the incoming Juan de Fuca plate west of the deformation front and that the incoming deformed sediment package includes areas with a combination of west and east

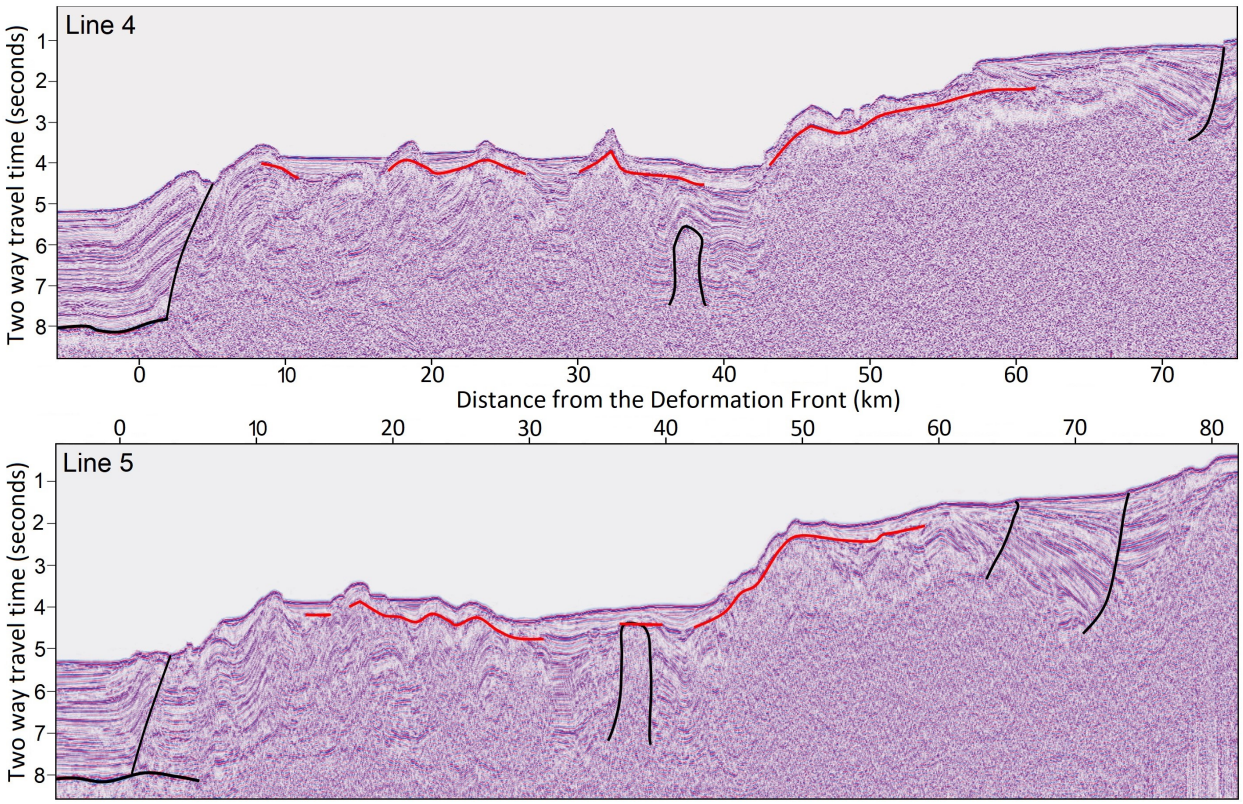

Figure 4.6: R/V *Langseth* multi-channel seismic profile Line 4 (top) and Line 5 (bottom) of the Cascadia accretionary wedge from deformation from to mid-slope. Red lines indicate BSRs within the upper sediments while black lines highlight diapirs, listric and normal faults, and trace the incoming plate.

dipping faults near the deformation front (Figure 4.7). A large thrust fault was imaged that originates near the plate interface and that surfaces within the depression west of main anticlinal ridge (Figure 4.7D). The first anticlinal ridge encompasses small faults that dip inward toward the ridge on both the seaward and landward sides, a sign of strong horizontal compression from the incoming Juan de Fuca plate motion. The lower accretionary wedge consists primarily of deformed sediments from the incoming plate with hemi-pelagic and minor turbidite infill between the exposed ridges. BSRs, an indicator of the transition from solid methane hydrate phase to gas with increasing depth into the sediments, evolve landward to become well-established acoustic reflectors within the eastern portion of the lower wedge

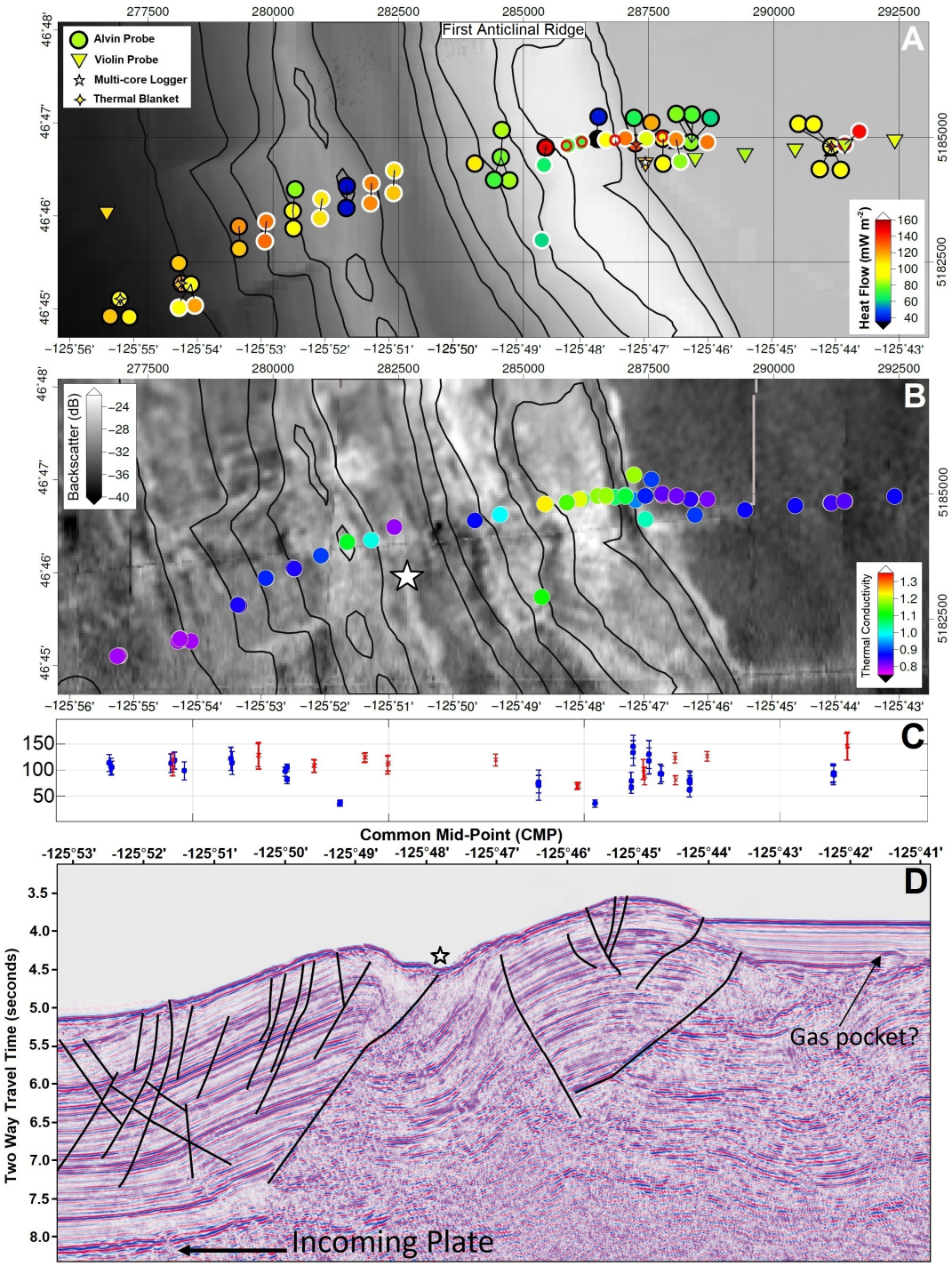

Figure 4.7: The Accretionary toe along MCS Line 4. A) Heat flow Measurements taken at roughly the same location are connected by black lines. Black outlined symbols for heat flow measurements correspond to Dive 723 while white outlined symbols correspond to Dive 725, where data were acquired 5.5 days later. B) Acoustic backscatter with symbols representing mean thermal conductivity measurements from the Alvin and Violin Probes. The seafloor location of the large normal fault is marked by a white star. C) Alvin Probe data as a function of distance from the deformation front. The colored symbols show Dive 723 (Blue) and Dive 725 (Red). D) *Langseth* MCS with prominent imaged faults highlighted with traced black lines. Note: the reflector interpreted as a pocket of free gas in right hand portion of the image.

and onto the mid-slope terrace (Figure 4.6). Within the bathymetric valley west of the mid-slope area, large diapiric structures emanating from deeper within the wedge were imaged within the sediment column.

4.3.2 Heat Flow Measurements

Heat flow data were collected across the Cascadia accretionary margin from the abyssal plain west of the deformation front to the mid-slope terrace (Figure 4.1; Figure 4.8), a water depth range of 2589 to 550 meters. All Violin-bow Probe and Multi-core Logger measurements collected within the lower margin and all but one Multi-core measurement at Station 9.5 were considered reliable measurements. While the percentage of good quality Thermal Blanket and Alvin Probe heat flow measurements is high within the lower accretionary wedge, the percentage dropped within the mid-slope terrace section. In this shallower part of the margin, near-bottom water temperature variations generated significant thermal noise in the upper sediment (Chapter 3) that masked the basal geothermal gradient captured by these instruments.

Alvin Probe heat flow measurements were collected by ROV *Jason* over the accretionary toe at a higher spatial resolution compared to the rest of the survey, with an average horizontal distance of 450 meters between stations (Figure 4.7A). While the heat flow measurements were predominately within the 60 to 100 mW m^{-2} range, a subset of the measurements had anomalous values as low as 30 to 40 mW m^{-2}, with standard deviations of 5 to 9 mW m^{-2}, and as high as 130 $\pm$ 22 mW m^{-2} over the two localized bathymetric highs (Figure 4.7; 4.9). Large variations were observed at closely spaced sites over the 5-day interval between repeat ROV *Jason* dives, indicative of temporal or small-scale spatial variability in the accretionary toe environment. As an example, Alvin Probe heat flow values varied from 27 $\pm$ 7.4 mW m^{-2} to 70 $\pm$ 5.9 mW m^{-2} over the main first anticlinal ridge, where station locations were separated by a horizontal distance of only 17 meters (Figure 4.7; Figure 4.9).

The mid-slope terrace, comprising Stations 1 through 6, 10, and Dual Plumes (Figure 4.1),

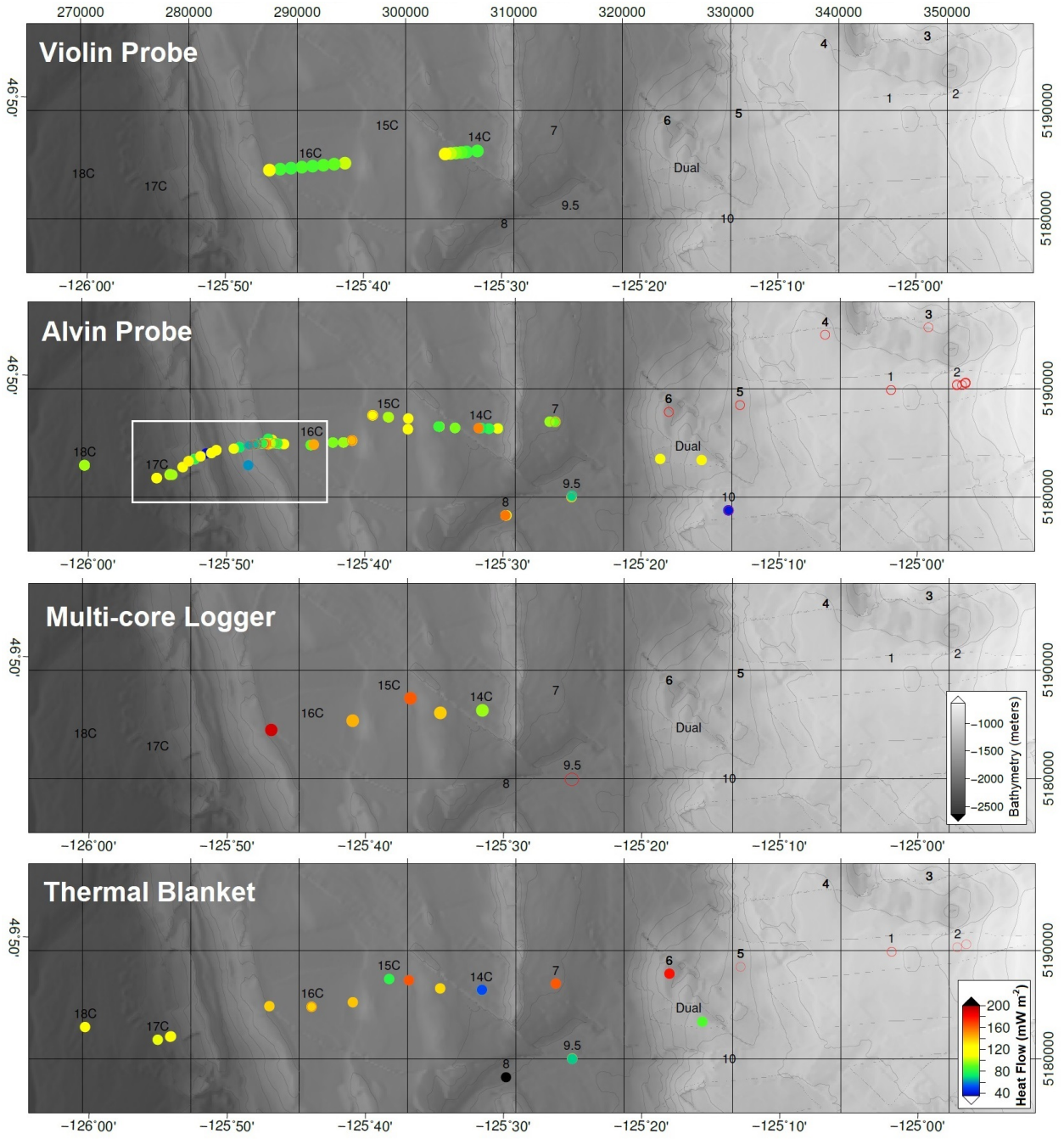

Figure 4.8: Locations of heat flow measurements for the four different types of heat flow instruments; Violin Probe, Alvin Probe, Multi-core Logger, and Thermal Blanket from the abyssal plain to mid-slope terrace. Heat flow value at each measurement location is shown as circles with color scale on lower right. Empty red circles indicate a categorized bad measurement based on the criterial listed in the text. Swath bathymetry indicated in gray scale with lighter shades indicating shallower depths. The white box within the Alvin Probe panel shows the area of the expanded Figure 4.7.

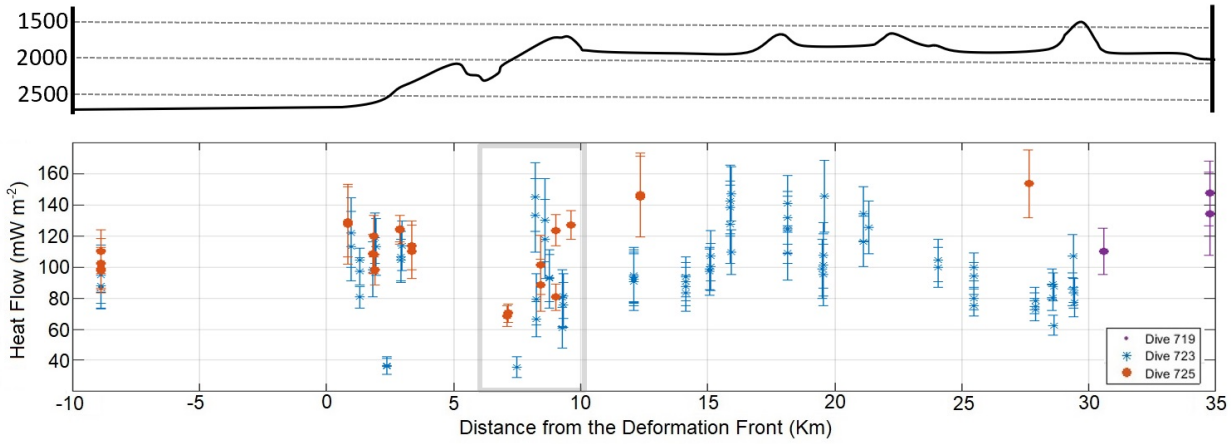

Figure 4.9: Alvin Probe heat flow data as a function of distance from the deformation front. The colored symbols correspond to the ROV *Jason* dive in which the measurement was taken demonstrating a temporal component to the heat flow measurements. The heat flow variations discussed in the text at the first anticlinal ridge are enclosed in the gray box.

is an area that is subject to large oceanic thermal variations due the relatively shallow seafloor depths, as shallow as 550 meters. Most Alvin Probe and Thermal Blanket measurements failed to produce useable data at depths shallower than 800 meters in this area (Figure 4.8; Chapter 3). Closer inspection reveals predominately negative heat flow measurements, for both the Thermal Blanket and Alvin Probe, and very non-linear Bullard plots for the Alvin Probe at Stations 1 through 6. Station 6, a localized topographic high on the transition from mid-slope to lower accretionary wedge has abnormally high Thermal Blanket heat flow values of 178.4 $\pm$ 26.1 and 179 $\pm$ 26.2 mW m^{-2}. Unfortunately, the Alvin Probes at this location did not produce good quality heat flow estimates.

The two active bubble emission stations, Dual Plumes and 9.5, presented localized areas of highly variable subseafloor thermal environments. One of the two Alvin Probe measurements collected in the Dual Plumes area had a value of 128 $\pm$ 11.3 mW m^{-2} while the other had a Bullard plot with a non-linear profile (Figure 4.3). Heat flow measurements at Station 9.5 were determined using 3 different types of instruments. The Thermal Blankets and Alvin Probes were placed near each other and within 50 meters of the plume site. These

instruments recorded heat flow that varied from 70 ± 16.2 to 168 ± 24.5 mW m^{-2} within the area near the methane/fluid emission site (Figure 4.3). The Multi-core was deployed at a later date from the ship at a distance of 900 meters from the plume site and recorded a heat flow of 108 ± 6 mW m^{-2}, but with a prominently curved temperature profile. Station 8, with signs of past methane venting but no detectable gas bubbles, had a total of five heat flow measurements. Four Alvin Probes measured similar heat flow values averaging 111 ± 16 mW m^{-2}, while one thermal blanket deployment had much higher average heat flow of 226.9 ± 19.7 mW m^{-2}.

4.3.3 Thermal Conductivity

At each location, the average value was determined for each set of thermal conductivity measurements collected by the Violin-bow Probe, Alvin Probe and Multi-core Logger (Figure 4.10). Abnormal top sensor measurements, defined as outside 3 standard deviations, were excluded to avoid bias due to outliers. General background thermal conductivity values within the survey area ranged from 0.8 to 0.85 W $m^{-1}K^{-1}$ for those areas located just landward of the deformation front and within the lower accretionary wedge sediment ponds. Higher thermal conductivity values were recorded predominantly near the edges of the sediment ponds and at a location east of Site 15 (within gray box, Figure 4.10B) with an average thermal conductivity over 1.0 W $m^{-1}K^{-1}$, significantly larger than measurement from surrounding locations. The first anticlinal ridge also had a consistently high average thermal conductivity of approximately 1.3 W $m^{-1}K^{-1}$. For most measurements on the mid-slope terrace, thermal conductivity values determined from the Alvin Probes produced average values in the 1.0 to 1.5 W $m^{-1}K^{-1}$ range, except for lower measured values at Station 3 (0.7 to 0.8 W $m^{-1}K^{-1}$) and Station 5 and 10 in the 0.8 to 0.9 W $m^{-1}K^{-1}$ range (Figure 4.10).

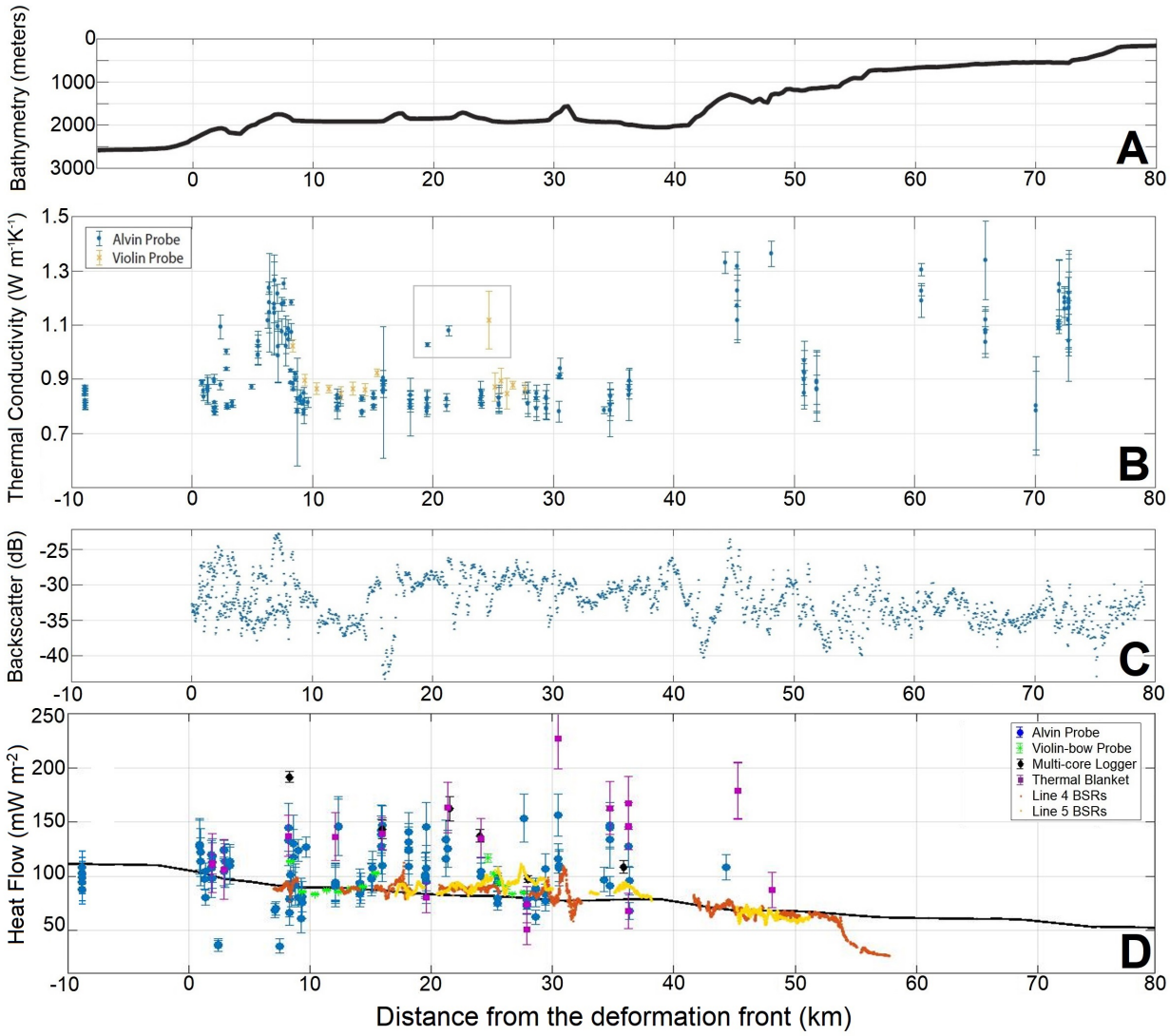

Figure 4.10: Comparisons of various accretionary wedge parameters. A) Line 4 bathymetric profile. B) Average thermal conductivity measurements as a function of distance from the deformation front. C) Multi-beam derived acoustic backscatter along the *Langseth* MCS Line 4 profile D) Comparison of the surface heat flow values (symbols; this study) to Bottom Simulating Reflector heat flow (dots, Chapter 2) from R/V *Langseth* MCS lines 4 (Red) and 5 (Green) and thermal model derived surface heat flow (black line)

4.4 Discussion

4.4.1 Sediment Carbonate Distribution

Elevated acoustic seafloor backscatter can indicate large areas of authigenic carbonate precipitation on and within the seafloor sediments, due to the sharp acoustic contrast of the rough, dense carbonate precipitation in comparison to the surrounding fine grain sediments, producing a typical amplification of ∼10 to 18 dB (Holland et al., 2006; Naudts et al., 2008). This method has been utilized along numerous subduction zones to indicate locations of fluid and methane flux within the shallow (<10 meters) seafloor sediments (e.g, Naudts et al. 2008, Dumke et al. 2014), including the Cascadia Subduction zone (Carson et al., 1994; Johnson et al., 2003). Independent verification of carbonate precipitation within the sediments has been achieved through visual inspection of the seafloor using a submersible or through collection and chemical analysis of seafloor sediment samples (Carson et al., 1994; Bohrmann et al., 1998; Torres et al., 2009).

High amplitude backscatter along the Washington margin is associated with both exposed and shallowly buried anticlinal ridges within the lower accretionary wedge (Figure 4.5). This relationship has been suggested to represent vertical pore fluid migration through the more permeable deformed and fractured anticlinal ridges, with only limited flow possible through the lower permeability sedimented ponds (Ritger et al., 1987; Carson et al., 1994; Johnson et al., 2003). The backscatter displays a patchier distribution in a subset of locations, such as the western edge of the mid-slope terrace, that may reflect locations of geologically recent methane venting not visually identified by ROV *Jason* or detected using the multibeam system. The location of the highest backscatter amplitudes recorded within the survey, the accretionary toe, differs from previous studies offshore Oregon that placed the highest backscatter on the second anticlinal ridge, 20 km from the deformation front (Carson et al., 1994). This change indicates along-strike variability in the fault derived network of predominate fluid pathways within the outer wedge and possible morphological differences between the two segments.

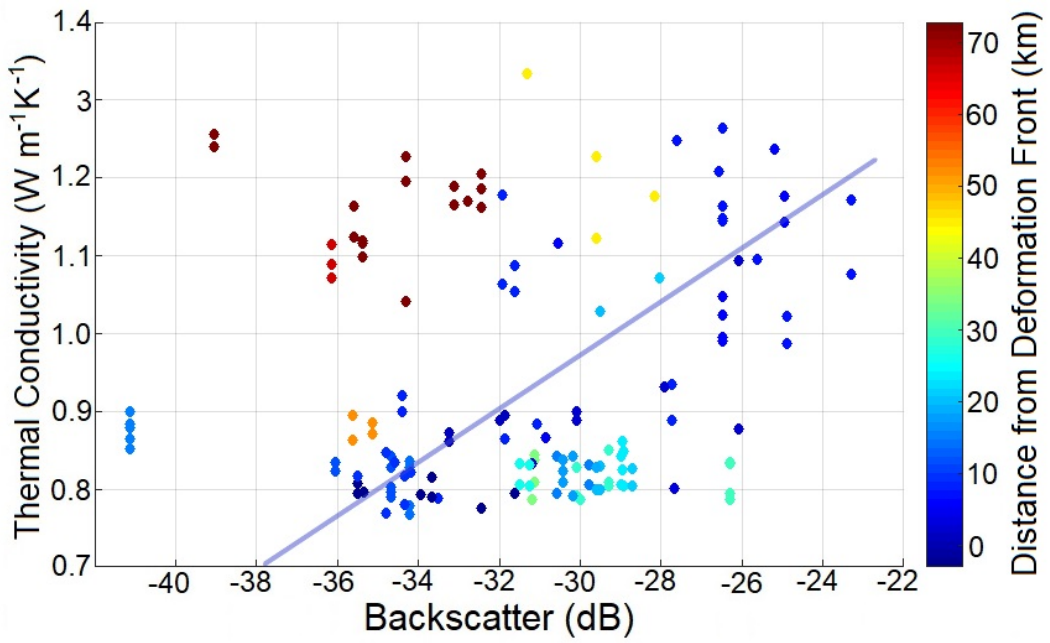

Figure 4.11: Acoustic backscatter intensities (X-axis) from surface ship multibeam and average thermal conductivity measurements (Y-axis) based on the distance from the deformation front (color bar). Thermal conductivity values are based on Alvin Probe measurements within the top 0.6 meters of the sediment column. Blue line marks the linear regression fit of the data between 0 and 10 km from the deformation front.

The across-strike *in-situ* thermal conductivity measurements may indicate the presence of authigenic carbonate within the shallow margin sediments. Due to the spatial scaling difference between the 50 x 50 meter backscatter cells and the highly localized seafloor probe measurements, backscatter will only be affected by carbonate formation that occurs extensively throughout the regions of interest. Comparison of backscatter intensity to sediment thermal conductivity measurements from the survey area reveals three relationship types (Figure 4.11). These include A) a positive correlation with an R^2 of 0.48 over the first anticlinal ridge (within 0 to 10 km of the deformation front), B) a general range of backscatter values in the lower wedge associated with steady lower thermal conductivity of 0.8 to 0.85 W $m^{-1}K^{-1}$ (10 to 40 km from the deformation front) and C) regions of lower backscatter but higher thermal conductivity within the mid-slope terrace area (40 to 75 km from the

deformation front). The correlation between backscatter and thermal conductivity within the 0 to 10 km region, over the accretionary toe, occurs in an area associated with strong upward fluid flow corresponding with sediment wedge compaction (Moore and Vrolijk, 1992; Wang et al., 1993). This compressional process, producing excess pore pressure, is expected to increase carbonate precipitation within the pores of the shallow sediments (Han and Suess, 1989; Carson et al., 1991). The lack of correlation between seafloor backscatter and sediment thermal conductivity within the lower and middle wedge argues for other processes dictating the relationship, including coarse grain/rough seafloor, a potential source of higher grain thermal conductivities, or processes that could inhibit carbonate formation such as lower fluid flux rates and high sedimentation. For example, sediment lithologies, such as high quartz sands (Harris et al., 2011) with a thermal conductivity of 6.2 to 11.4 W $m^{-1}K^{-1}$ (Clauser and Huenges, 1995), could produce a similar increase in thermal conductivity results with no corresponding increase in backscatter (Figure 4.12).

The observed correlation over the accretionary toe suggests that in this region acoustic backscatter intensity may be used as a proxy for authigenic carbonate precipitation. Carbonate formation will increase the thermal conductivity both by precipitating primarily within the sediment voids, effectively reducing porosity, and by providing a higher thermal conductivity material within the sediment matrix. The primary control on shallow sediment bulk thermal conductivity is typically the porosity, which for this survey area is 0.5 to 0.85 for surficial margin sediments (Solomon, E, per. comm., 2018). The bulk thermal conductivity (K_B) can be determined using the geometric mean $K_B = K_W^{\phi} K_S^S K_C^C$, knowing the sediment porosity (ϕ), fractions of carbonate (C) and sediment (S), and grain (K_S), water (K_W), and carbonate (K_C) thermal conductivities. With a thermal conductivity value near 0.6 W $m^{-1}K^{-1}$ for water, any substantial reduction in porosity within the sediment matrix would noticeably increase the bulk thermal conductivity. For example, with a background grain thermal conductivity of 2.5 W $m^{-1}K^{-1}$, a porosity reduction of 10% results in a 14% increase in matrix thermal conductivity.

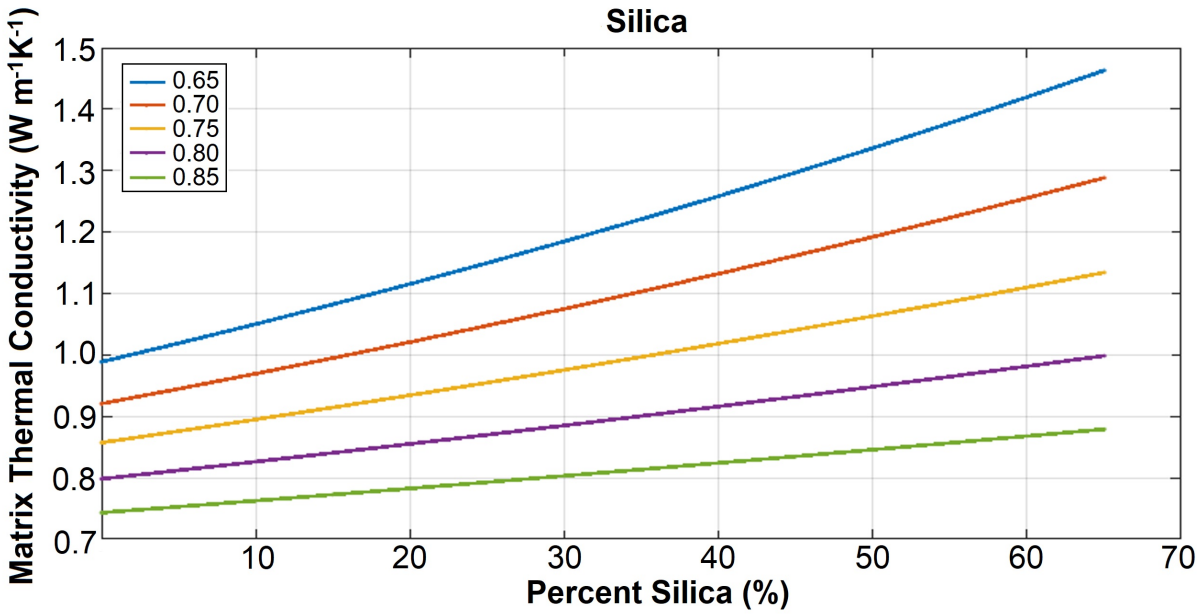

Figure 4.12: Bulk sediment thermal conductivity based on varying percent of silica and sediment porosity (colored lines). Bulk thermal conductivity is dictated by geometric mixing mean. Background sediment thermal conductivity is assumed to be 2.5 W $m^{-1}K^{-1}$ and silica thermal conductivity of 14 W $m^{-1}K^{-1}$ (Clauser and Huenges, 1995).

Matrix grain lithology provides the secondary control on bulk thermal conductivity. Based on chemical analysis of authigenic carbonates collected from methane venting sites, such as at Hydrate Ridge on the Oregon accretionary wedge, the dominant forms of carbonate mineralogy are aragonite, and in small quantities magnesium calcite ($MgCO_3$), for areas of strong fluid venting such as methane venting sites, and calcite in more diffuse flow regions (Bohrmann et al., 1998; Luff and Wallmann, 2003). The thermal conductivity of aragonite is roughly 2.37 W $m^{-1}K^{-1}$, calcite is 3.5 to 5.0 W $m^{-1}K^{-1}$, and magnesium calcite is 7.3 to 8.2 W $m^{-1}K^{-1}$ (Clauser and Huenges, 1995). A composition including the carbonate phases would noticeably increase the non-carbonate seafloor sediment thermal conductivity of 85 W $m^{-1}K^{-1}$ (Figure 4.13).

For authigenic carbonate precipitation to increase the bulk thermal conductivity measurements, it must be present in sufficient concentrations to alter the bulk sediments but

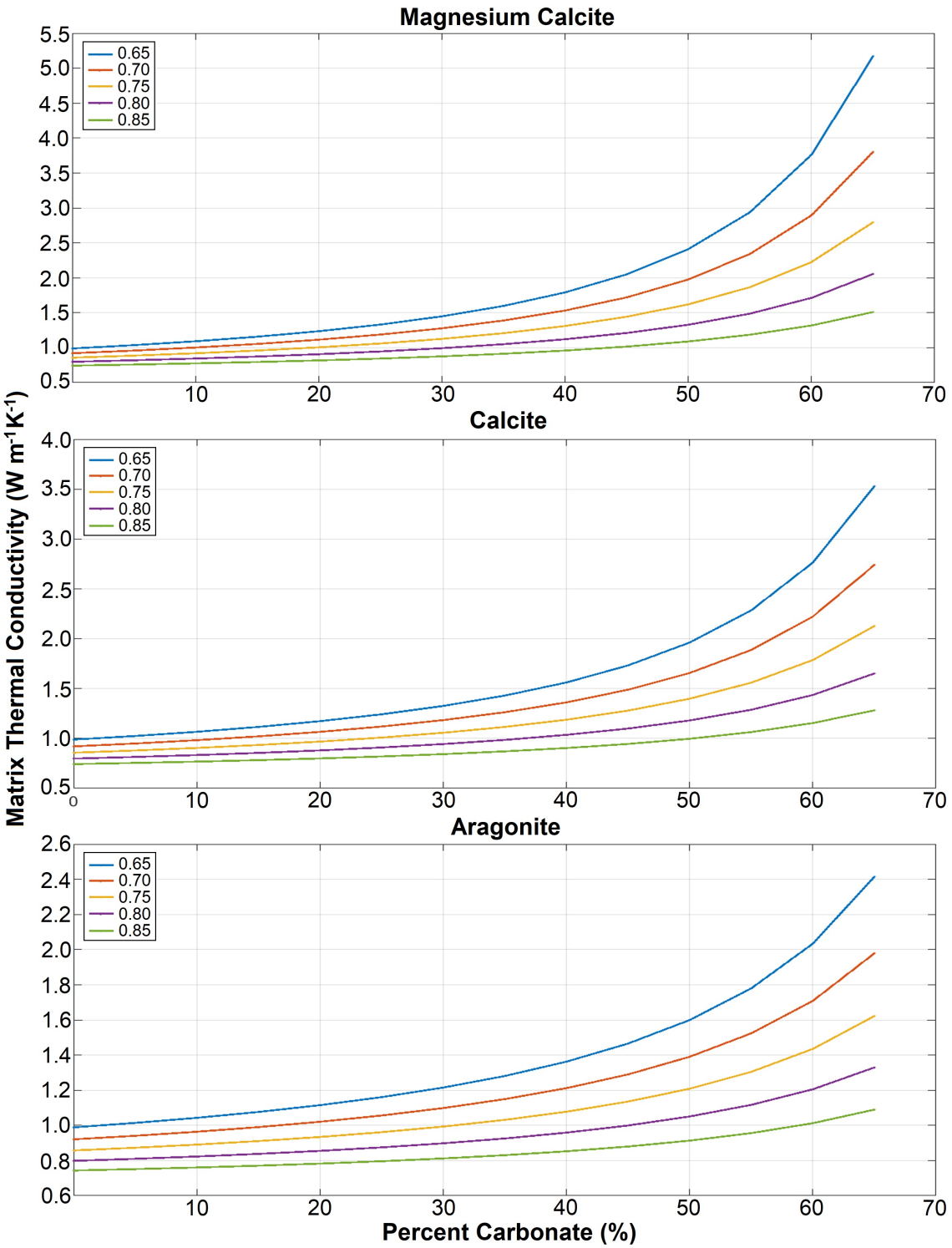

Figure 4.13: Bulk sediment thermal conductivity based on varying initial sediment porosity (colored lines) and percent of three types of carbonates and their associated thermal conductivities: magnesium calcite (7.65 W $m^{-1}K^{-1}$), calcite (4.25 W $m^{-1}K^{-1}$), and aragonite (2.37 W $m^{-1}K^{-1}$) (Clauser and Huenges, 1995). Bulk thermal conductivity is dictated by geometric mixing mean and background sediment thermal conductivity is assumed to be 2.5 W $m^{-1}K^{-1}$.

remain at a stage where it has not formed a continuous carbonate crust, which would prevent a heat flow probe insertion into the sediment. Carbonate precipitate distributed within the sediments has been observed along Cascadia (Carson, 1977; Luff and Wallmann, 2003) in concentrations as high as 71% to 80% by weight within surficial sediments (Carson, 1977; Scamman, 1981). Assuming a direct reduction in porosity with an increase in carbonate content, a 30% CaCO3 content by weight (Luff et al., 2004), initial porosity of 80%, and a calcite thermal conductivity of 4.25 W $m^{-1}K^{-1}$, the estimated bulk thermal conductivity would be 1.3 W $m^{-1}K^{-1}$, similar to values observed in this study. Seafloor or borehole samples will be required to confirm the relationship suggested by the backscatter/thermal conductivity correlation.

4.4.2 Across-strike Fluid Venting Distribution

The across-strike survey coverage, ranging from seaward of the toe of the prism to 75 km west of the deformation front within the Cascadia accretionary wedge, provides valuable across-strike information about the evolution of wedge scale fluid emission. Three regions of the accretionary wedge appear to have different fluid venting behaviors (Figure 4.14), 1) strong diffuse and fault channelized fluid flow through the accretionary toe, 2) diffuse fluid and methane movement within the central portion of the lower accretionary wedge, and 3) long-lived and deeply sourced methane emission within 30 to 50 km of the deformation front.

Compression and Deformation at the Prism Toe

The accretionary toe, defined here as the section of the prism from the deformation front to 10 km landward and east of the first anticlinal ridge (Figure 4.1; Figure 4.7), contains an evolving thermal environment and high fluid flux, a result of the dynamic geological deformation and dehydration of the 2 to 3 km thick incoming sediments (Wang et al., 1993; Saffer et al., 2008). A few localized high heat flow sites appear to correlate with imaged faults within the deforming sediments on the primary anticlinal ridge (Figure 4.7), potentially signifying that warm fluids are being transported along these faults. Also, the large westward

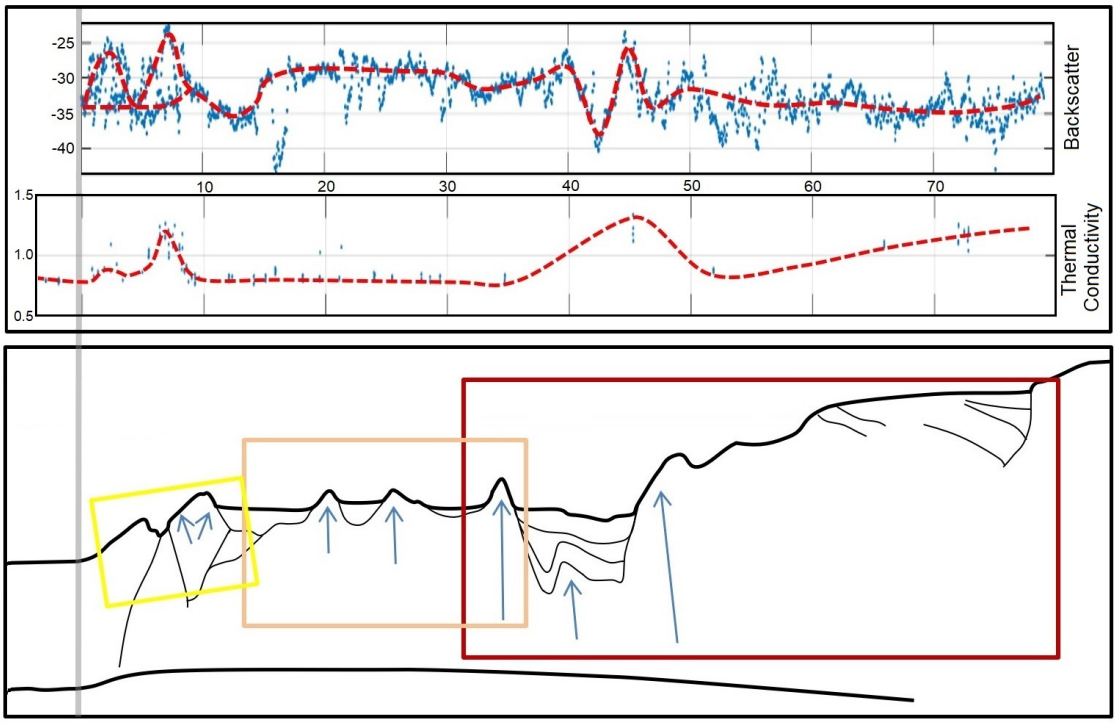

Figure 4.14: Overview cartoon of the different types of fluid/methane venting behaviors within the survey area and general margin trends. Top) Co-located backscatter and thermal conductivity general trend line (red dashed line) along R/V *Langseth* Line 4. Bottom) Trends include vigorous fluid venting within the accretionary toe (yellow box), evolving to deeper sourced diffuse and channelized fluids within the lower margin (Orange box). By the mid-slope, fluid flow pathways are restricted to primarily localized point source fluids that are transported along faults and up through diapirs (Red Box).

dipping fault that surfaces within the basin west of the first anticlinal ridge corresponds to a narrow band of high acoustic backscatter and an area of hard carbonates, indicative of a possible conduit for fluid from deeper within the sediment toe near the decollement. Similar faulting and a measured local fluid flow of 410 - 490 m^3 yr^{-1} m^{-1} has been observed on the Oregon accretionary wedge margin in combination with evidence of abundant fluid and methane that is able to support an active chemosynthetic community (Carson et al., 1994; Kastner et al., 2014).

The high resolution and replicated heat flow measurements along the first anticlinal ridge

reveal small-scale spatial and temporal changes in the shallow thermal gradient (Figure 4.7, Figure 4.9). Large variations in heat flow on the order of 40 - 60 mW m^{-2} occurring near the apex of both localized bathymetric highs appear associated with a region of high *in-situ* thermal conductivity and high backscatter. One possible interpretation is that a combination of diffuse and channelized methane rich fluid is moving up faults imaged along the MCS profiles (Figure 4.7D) to produce an elevated concentration of authigenic carbonates within the top several meters of the sediments over a broad area (Figure 4.7B). The large amplitude differences in heat flow measurements occurring within a very localized spatial scale provide thermal evidence of shallow, near seafloor fluid circulation pathways that are present and partially channelized by the dominant along-strike faulting found within the accretionary toe. However, as the survey was designed primarily to determine 2-D across-strike variability, it is not possible to resolve any along-strike component to fluid circulation within the accretionary toe.

There does not appear to be a single obvious explanation for the significant changes in heat flow observed over the relatively short period of time of 5 to 6 days between ROV *Jason* dives (Figure 4.9). Instrumental sources of uncertainty are primarily derived from probe tilt from vertical and have an average uncertainty of 14 mW m^{-2} for reliable measurements within the accretionary toe area. Some of the environmental sources that could impact the geothermal gradient over rapid time scales include sediment slumping, dramatic increases in fluid flux, and/or changes in the near-bottom temperatures (Martin and Lowell, 2000; Hamamoto et al., 2011). While it is likely that tidal forces modulate the sub-surface sediments and fluid flux (Wang et al., 1999; Torres et al., 2002), when the heat flow measurements were compared to variable tidal heights for the same time windows, little correlation was found.

Two additional mechanisms for short term geothermal variations are prominent bottom water temperature fluctuations or rapid fluid flux reversal within the sediments, where either process could produce a non-linear geothermal gradient. Seafloor temperature variations

derived from the Thermal Blankets top thermistor at Stations 16FFW and 16C on the nearby sediment pond next to the ridge suggest variable bottom water temperatures impact heat flow by 10 to 20 mW m^{-2}, values that are much smaller than the observed differences. However, without neither time series measurement of near-seafloor temperature variations, or direct records of fluid flux changes at the measurement sites on the accretionary toe, it is difficult to rule out either mechanism as a source of the observed heat flow differences.

Fluid and Methane Movement within the Central Margin

The lower accretionary margin transitions from a highly dynamic fluid and heat flow environment within the accretionary toe area to a region thought to have more uniform upward diffuse fluid flow. This region is still producing compression-derived fluids that are expelled from the wedge sediments while increasingly sourcing fluids from higher-temperature dehydration reactions at depth (Kastner et al., 2014). Indicators of methane start as gas pockets within the sediments just landward of the first anticlinal ridge (Figure 4.6D) and moving east become more prominent and are associated with BSRs. The use of multiple detection methodologies within this survey such as higher backscatter, heat flow measurements, and seismic imaging of the prism also argue for a general upward flux through the wedge near the boundaries of the sediment ponds, although isolated fluid movement along faults and conduits still occurs. Evidence for upward fluid flow and methane include strong BSR reflections (Hyndman et al., 1992; Haacke et al., 2008) and a large area of generally higher amplitude backscatter, possibly linked to carbonate precipitation within the sediments with indicators of fluid preferentially transported along the sediment-anticlinal ridge interface. BSRs derived from the 2012 R/V *Langseth* (Figure 4.10D) provides additional context, with associated heat flow measurements at distinctly higher values than the predicted conductive background, yielding a broadly diffuse fluid flux of up to 4 cm yr^{-1} (Chapter 2).

Several heat flow stations, such as Station 16C (Figure 4.8), displayed a strong thermal signature of localized upward fluid flow based on the heat flow measurements, but had

no visual or acoustic signs of methane. These sites may be examples of warmer fluids sourced from deep within the wedge lacking the corresponding methane component at high concentrations. The absence of visual confirmation of methane is not a completely conclusive indicator since methane may still be present in small quantities as gas within the sediment, but not migrating to the seafloor surface at the time of the observations. Station 16C may fall into this category, located above a feature, imaged within the MCS profile, that appears to be a sub-surface gas pocket roughly 600 meters directly beneath the seafloor (Figure 4.7D).

Long-lived Methane Emission Sites

Several stations, namely Dual Plumes, Site 8, and Site 9.5, show convincing evidence for long-lived methane venting (Figure 4.11), although only Dual Plumes and Site 9.5 had acoustically- and visually-imaged methane bubble emissions. Many of these long-lived venting sites were detected within the central portion of the wedge, generally 30 to 50 km landward of the deformation front and located within a transitional area between the lower accretionary wedge and the mid-slope terrace. At several of these sites, ROV *Jason* provided visual confirmation of cold seep bioherms and the active methane vent communities commonly associated with both methane emission and upward fluid flow. These sites showed the presence of highly variable surface heat flow measurements that ranged both substantially above and below the expected conductive background heat flow of 75 to 80 mW m^{-2} for this segment of the accretionary wedge, as determined from thermal modeling (Figure 4.8; Figure 4.10; Chapter 2). These observations are consistent with both active upward fluid flow and localized fluid circulation paths that are typical of methane vent sites (Grevemeyer et al., 2004; Feseker et al., 2008)(Figure 4.7).

Warm vertical fluid flow through the sediments produces an upward bend in the geothermal gradient profile and fluid flux can be quantified from the temperature profile curvature (Bredehoeft and Papadopulos, 1965). The theoretical temperature profile is derived as a solution to the 1-D steady-state vertical advection/diffusion equation with boundary conditions

$T(z = 0) = T_0$ and $T(z = L) = T_L$ (Bredehoeft and Papadopulos, 1965):

$$\frac{(T_L - T_o)}{(T_z - T_o)} = \frac{e^{(\frac{\beta L}{Z})} - 1}{(e^{\beta} - 1)} \tag{4.1}$$

$$\beta = \frac{v_z c_o \rho_o Z}{K_m} \tag{4.2}$$

where z = 0 is at the seafloor and z = L is taken to be the bottom of the measured temperature profile. T_z is the temperature (°C) at any depth where z = Z between 0 and L. It is assumed that the geothermal profile has not been influenced by either rapid erosion and/or near bottom water temperature variability, and that a vertical steady-state, depth-independent fluid flux originates below the measured temperature profile and is traveling through a homogenous fully saturated medium. It is additionally assumed that there is no compaction and reduction of the sediment porosity. Under these conditions, upward fluid flow (v_z) is determined as a best fit of the temperature profile data to this solution, assuming sediment matrix heat capacity (c_o) of 4.19 J $kg^{-1}K^{-1}$, thermal conductivity (K) of 0.83 W $m^{-1}K^{-1}$ and water density (ρ_o) of 999.2 kg m^{-3}.

Near Station 9.5, the Multi-core Logger measurement displayed a distinct upward curve in the geothermal gradient (Figure 4.15) within a thermally-quiescent seawater environment (i.e., < 10 mW m^{-2} sediment thermal gradient disturbance based on the 6-day temperature record near the seafloor captured by a nearby Thermal Blanket). By modeling the thermal profile with Equations 4.1 and 4.2, an exceptionally high upward fluid velocity of 43 m yr^{-1} was estimated for this site with the profile fitting the idealized upward fluid flow thermal gradient well, with a root mean standard deviation of 1.7 x 10^{-4}. Concurrently collected sediment cores did not show any evidence of upward fluid flux within the pore water chemistry (Solomon, E. pers. comm., 2018) suggesting that a general diffuse flux through the sediments was not present and that the modified core liner may have picked up a channelized transient event. Alternatively, the highly altered temperature profile could have been produced by erosion, bioturbation, a shifting of the fluid rich sediments due to the Multi-core system

landing on the seafloor or during core liner insertion, or other unaccounted environmental sources of heat.

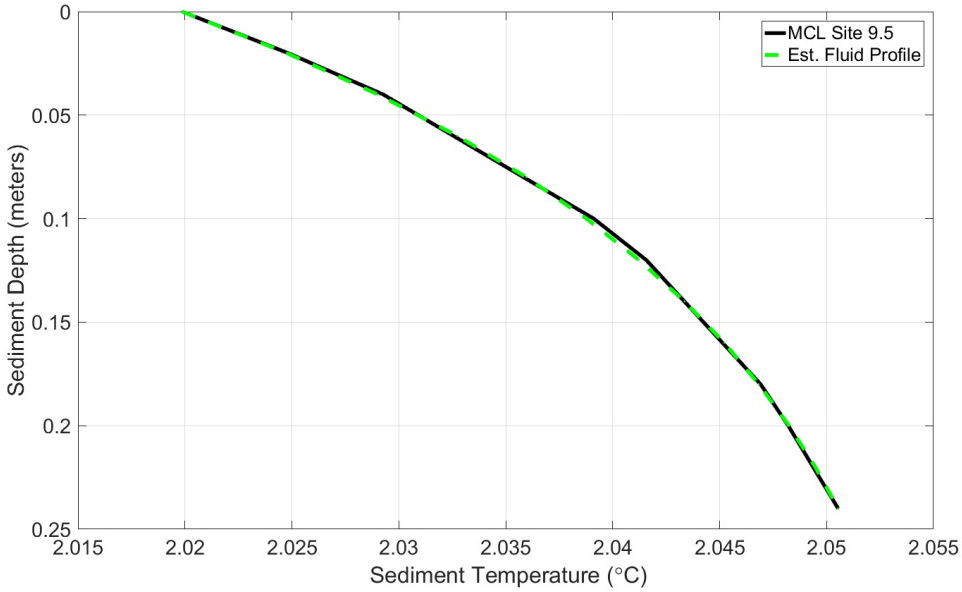

Figure 4.15: Comparison between a theoretical thermal gradient (Green dashed line) produced by an upward fluid flux of 43 m yr^{-1} to the thermal gradient (Black line) acquired by the Multi-core Logger thermal at Station 9.5. The theoretical thermal gradient was determined by solving for the best fit fluid velocity using the equations from Bredehoeft and Papadopulos (1965).

Station 8 was characterized by the presence of large surficial carbonate slabs but no currently active methane venting (Figure 4.4), suggesting that this site was in an inactive portion of its venting cycle (Torres et al., 2003). This particular station is located at the confluence of a large prominent and higher permeable anticlinal ridge and the main across-strike turbidite channel (Figure 4.1). The region of interaction between these two major geological features may be preferentially utilized by fluids due to lower permeability and may provide an explanation for the high methane fluid production within this area. While the connection between the two structural features cannot be conclusively established because of the limited coverage of the ROV *Jason* seafloor video survey, the observations at this

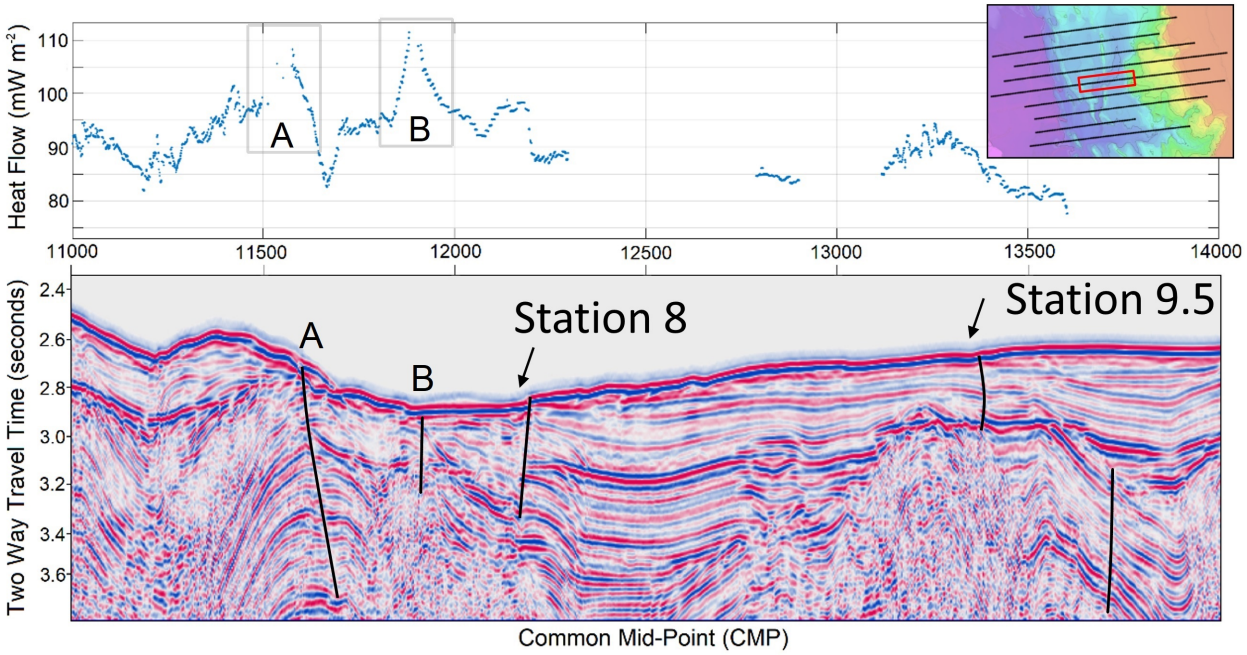

Figure 4.16: (Top) High resolution distribution of heat flow values from Bottom Simulating Reflectors (Chapter 2) along (Bottom) magnified section of the *Langseth* MCS Line profile 5. Horizontal scales for the top and bottom profiles are co-registered, showing heat flow anomalies associated with sub-surface faulting and indicative of active fluid flow. Calculated heat flow is 1.9 cm yr^{-1} for section A and 2.0 cm yr^{-1} for section B. Figure 4.15 displays curved geotherm due to upward fluid flow at station 9.5. Inset indicates the location of the zoomed in profile (red box) along the *Langseth* MCS survey lines.

station are consistent with the hypothetical increase in areal density of methane and fluid emission sites that would occur along the exposed anticlinal ridge, most notably within the large turbidite channel.

Multiple vent sites associated with sub-surface structures and faults advocates for the emission of deeply sourced fluids within the central portion of the accretionary wedge. Examples are found within our survey at the long-lived emission sites near and over diapiric features, such as at Station 9.5 and Dual Plumes (Figure 4.1). In addition, MCS survey Lines 4 and 5 reveals multiple sub-surface faulted zones and buried diapirs, where many of the features appear correlated with fluid emission sites observed on the seafloor. Warm sub-

surface fluids vigorously moving up faults appear in the MCS *Langseth* profiles as upward bending BSR heat flow measurements located on both sides of faults (Zwart et al., 1996). As examples, multiple prominent faults along Line 5 (Figure 4.16) show signs of elevated heat flow heat flow west of Station 8, a location of high heat flow and seafloor carbonate crust. The elevated BSRs produced a local 0.014 °C km^{-1} increase in the thermal gradient that, using Equations 4.1 and 4.2, translates to a fluid flow of 1.9 and 2.0 cm yr^{-1} for the elevated BSRs around faults A and B respectively (Figure 4.16). A fault exists beneath Station 8 although no arched BSR appears to be present, supporting the idea that this particular system is in an inactive phase or extinct. This complex subsurface structure provides plausible evidence for channelized pathways of fluid migration from deep within the accretionary wedge likely formed due to over-pressurization from depth and extend several kilometers into the prism structure. These deeper sources are important mechanisms for the relatively efficient transport of fluids and materials originating within subducting sediments via dehydration reactions (Lauer and Saffer, 2015).

4.5 Conclusions

A heat flow survey of the southern Washington segment of the Cascadia margin encompassed the mid-margin to the accretionary toe with the goal of mapping both diffuse and point source seafloor fluid emissions. Heat flow measurements included 4 different types of surface instrumentation, the Alvin Probe, Multi-core Logger, Violin-bow Probe, and Thermal Blanket, that were co-located with ROV *Jason* video imaging capturing seafloor expressions of potential methane emissions, along with geological structures determined from the 2012 COAST multichannel seismic profiles. A strong correlation between the multibeam backscatter intensity and near-surface thermal conductivity over the first anticlinal ridge was attributed to an increase in authigenic carbonate precipitation within the near surface sediments.

An across-strike fluid pattern emerged when analyzing the heat flow and auxiliary data

over the accretionary wide survey area. Moving landward across the accretionary wedge from the deep abyssal plain, the accretionary toe provides abundant evidence of extensive faulting and high backscatter reflectivity, related to the intense deformation of this sediment section and with abundant methane-rich fluid expulsion. Farther landward, the fluid flow pattern evolves to a general diffuse fluid flux throughout the lower accretionary wedge. The fluid flow within the transitional section of the accretionary wedge between the lower and mid-slope wedge is associated with faulted pathways and supplied by fluid and methane from deep within the sediment prism. The preferential location within the turbidite canyon of several long-lived emission sites with substantial carbonate deposits indicates a potential link between processes that shape the seafloor and the upward fluid migration pathways from deep within accretionary wedge.

While detecting fluid emission sites using shipboard multibeam systems is very efficient in covering large survey areas, localized heat flow measurements can identify areas of fluid emission that may be missing direct visual or acoustic evidence of fluid or methane venting. Combining a multitude of different fluid venting detection methods, including anomalies detected in seafloor thermal measurements, provides a more complete assessment, allowing for the identification of both past and present regions of emissions and quantification of the important flux rates.

Chapter 5
SUMMARY

The overarching goal of this thesis was to understand the thermal and fluid environments within the Cascadia Subduction zone offshore southern Washington State. Exploring the intertwined nature of these two properties demonstrates the importance of both in understanding subduction zone processes. While the nature of the survey data led to a detailed analysis of across-strike features, because of multiple closely-spaced survey lines, smaller scale along-strike patterns were revealed for seafloor morphology, fluid venting, and the thermal regime at depth within the sediments and along the subduction plate.

Marine heat flow data was heavily utilized within this thesis because of its ability to provide valuable insight into the sub-seafloor thermal environment, allowing for a quantification of fluid advection, detection of recent mass sediment movement, and insights into other key geological processes associated with the evolution of an accretionary wedge. Heat flow can be estimated from Bottom Simulating Reflectors (BSRs) imaged in seismic profiles within hydrate rich environments, and measured on the seafloor with several kinds of instruments. It was vital to understand the accuracy of each of these approaches in order to differentiate geological signal from thermal noise derived from external processes, such as near-seafloor temperature changes within the overlying seawater. BSR heat flow estimates are dependent on not just sediment geochemistry but also *in-situ* pressure, long term oceanic temperature trends, seafloor sediment accumulation rates, and local bathymetry (Chapter 2). By delving into each of these subcomponents that affected the BSR heat flow calculations, the uncertainty determined matched well with previously reported values of roughly $\pm 10\%$.

In Chapter 2, finite element thermal models were constructed accounting for the thermal structure of the incoming plate, subducting plate angle, and thickness of the overlying

continental plate. The thermal models also included variable accretionary wedge thermal conductivity values, high-resolution seafloor bathymetry, and the thicknesses of the incoming sediment derived from the Cascade Open Access Seismic Transects (COAST) Multi-Channel Seismic (MCS) profiles. Modeled plate surface temperatures place the thermally-defined seismogenic zone, the region that will produce a large mega-thrust earthquake, by placing the up-dip limit at the deformation front and the downdip limit 90-100 km from the deformation front, 30 km west of the coastline. These boundaries resolve a narrow 100 km wide seismogenic zone that is completely offshore Washington State. In addition, BSRs traced within the 11 R/V *Langseth* COAST MCS profiles were compared to numerically modeled heat flow values derived from thermal models. BSR heat flow measurements were determined to be elevated which likely reflects vertical fluid advection occurring throughout the lower accretionary wedge terrace sediments. Differences between the BSR measurements and thermal model estimates produce an estimated mean fluid flow value of 0.53 cm yr^{-1} for the entire survey area, with localized fluid flow extremes approaching 3.8 cm yr^{-1}.

The subduction zone thermal models also allow for an examination of fluid advection within the underlying crustal Layer 2A. A detectable deviation in modeled surface heat flow, in comparison to thermal models without fluid transport up through Layer 2A, is produced for only the highest potential crustal permeability of 10^{-10} m^2. The BSR heat flow agrees well with surface heat flow modeled with reduced or no fluid flow within Layer 2A, and lower crustal permeability values suggest that substantial up-dip transport of crustal fluid is unlikely. Seafloor heatflow may not be a means to easily quantifying fluid advection through crustal permeabilities of 10^{-12} m^2 or lower, and thus not a completely reliable test for detecting lower volume fluid migration within crustal Layer 2A for this portion of the Cascadia Subduction Zone. As fluids are still being produced and released *in-situ* at depth within the crust and sediment, an alternative path for fluid advection within the subduction zone may be vertically through the sediments of the accretionary margin wedge, producing the widespread elevation of the observed BSR heat flow values.

A comparison of direct measurements of seafloor heat flow acquired by different types of instruments, shows that there are several highly versatile methodologies that can be deployed in a region of significantly varied environments. A total of 251 surface heat flow measurements were collected over a wide range of bathymetric and oceanographic environments across the accretionary wedge. A combination of four different types of heat flow instruments, the Alvin Probe, Multi-Core Logger, Violin-bow Probe, and Thermal Blanket, allowed for an exploration of each instrument's strengths and weaknesses in addition to inter-instrument comparison. In Chapter 3, an analysis of the parameters affecting the different instrument types revealed that each instrument is uniquely impacted by a range of prevailing factors including bottom water temperature variations, penetration depth into the sediment, instrument tilt, and deployment method. While it is assumed that near-seafloor water temperature variations systematically decrease with increasing seafloor depth, it appears both local bathymetry and the effects of variable oceanographic currents have a strong impact on near seafloor temperatures. Although high variability in near-seafloor temperatures is a known problem for shallow heat flow measurements (<1800 meters seafloor depth for offshore Washington State), this is the first example of heat flow measurements in deeper water depths that are generally assumed to be semi-quiescent, that shows them to be highly disrupted, up to a standard deviation of 20 mW $^{-2}$. Repeat Alvin Probe measurements taken over a 5- to 6-day period, combined with seafloor temperature records measured by the Thermal Blankets, demonstrated that measurements can be influenced by ocean temperatures even when a measurement appears to be of high quality.

In contrast to the subduction-scale processes discussed in Chapter 2, the focus of Chapter 4 was point-source fluid emissions inferred from these seafloor heat flow observations and how their characteristics change across the subduction zone. An across-strike survey utilized all four different types of surface heat flow instruments in combination with co-located multi-beam, MCS profiles from the 2012 COAST experiment, and ROV *Jason II* video capturing seafloor evidence of methane emissions such as clam beds and carbonate deposits. While

detecting fluid emissions using a shipboard multibeam system is an efficient technique for covering large survey areas, localized seafloor heat flow measurements can more accurately identify areas of fluid emission that lack direct visual or acoustic evidence associated with active venting of fluid or methane. Combining different fluid venting detection methods provides a more complete coverage, allowing identification of both past and present regions of emissions and the quantification of flux rates.

Exploring these diverse data types reveals three different regions of fluid venting in the across-strike direction over the accretionary prism. The accretionary toe provides evidence of active fluid venting and small-scale fluid circulation in the form of highly variable heat flow data and high backscatter reflectivity, linked to extensive faulting and deformation of the sediment section and methane-rich fluid expulsion. Based on the elevated BSR-derived heat flow and regions of high backscatter, the central, broad lower terrace exhibits evidence for extensive areas of diffuse fluid venting channelized primarily through buried and exposed anticlinal ridges. Several long-lived emission sites within the eastern portion of the lower terrace, with associated imaged faults and arched BSRs, indicate locations of upward fluid venting pathways from deep within accretionary wedge.

As the survey area incorporated multiple MCS profiles separated by an average of 12 km, along-strike thermal variability and features distinct to individual profile lines were apparent on this local scale. The thermal models produced incoming décollement temperatures at the deformation front ranging from 164°C to 179°C, that were controlled by sediment thickness along the incoming plate. The seafloor fluid and thermal environment appear driven by underlying features including locations of dominant faults, diapirs, and exposed ridge material that varied along-strike. For example, comparison between the adjacent MCS Lines 4 and 5 shows that a larger percentage of diffuse fluids is venting along Line 5. Structurally similar along-strike locations to Line 5, outside the survey area but within the lower accretionary wedge, could facilitate fluid migration from depth. In addition, abnormally low BSR derived heat flow values in the Line 4 MCS profile indicate a recent large-scale slumping and listric

fault rotation within an area permeated with abundant extensional normal fault zones visible in the COAST MCS profiles.

In summary, this thesis presents a unique high-resolution view of the Cascadia Subduction zone that demonstrates a multitude of fluid transport pathways and changes in the temperature distribution. Understanding the venting patterns on these smaller scales provides greater insight into the larger scale fluid budgets of the evolving and dynamic subduction zone accretionary wedge.

BIBLIOGRAPHY

Adam, J., Klaeschen, D., Kukowski, N., and Flueh, E. (2004). Upward delamination of Cascadia Basin sediment infill with landward frontal accretion thrusting caused by rapid glacial age material flux. *Tectonics*, 23(3):TC3009.

Athy, L. (1930). Density, Porosity, and Compaction of Sedimentary Rocks. *Am. Assoc. Petrol. Geol. Bull.*, 14(1):1 – 24.

Atwater, B. F. (2010). Evidence for Great Holocene Earthquakes along the Outer Coast of Washington State. *Science*, 236(4804):942 – 944.

Atwater, B. F. and Hemphill-Haley, E. (1997). Recurrence intervals for great earthquakes of the past 3,500 years at northwest Willapa Bay, Washington. *Prof. Paper 1576*.

Barnard, W. D. (1978). The Washington Continental Slope: Quaternary Tectonics and Sedimentation. *Mar. Geol.*, 27:79 – 114.

Barnes, C., Best, M. M., Pautet, L., and Pirenne, B. (2011). Understanding Earth–Ocean processes using real-time data from NEPTUNE, Canadas widely distributed sensor networks, northeast Pacific. *Geoscience Canada*, 38(1).

Becker, K., Herzen, R. V., Kirklin, J., Evans, R., Kadko, D., Kinoshita, M., Matsubayashi, O., Mills, R., Schultz, and A., Rona, P. (1996). Conductive heat flow at the TAG active hydrothermal mound: Results from 1993-1995 submersible surveys. *Geophysical Research Letters*, 23:3463 – 3466.

Blackwell, D. D., Steele, J. L., Kelley, S., and Korosec, M. A. (1990). Heat flow in the State of Washington and Thermal Conditions in the Cascade Range. *J. Geophys. Res*, 95(B12):19495 – 19516.

Bohrmann, G., Greinert, J., Suess, E., and Torres, M. (1998). Authigenic carbonates from the Cascadia subduction zone and their relation to gas hydrate stability. *Geology*, 26:647 – 650.

Booth-Rea, G., Klaeschen, D., Grevemeyer, I., and Reston, T. (2008). Heterogeneous deformation in the Cascadia convergent margin and its relation to thermal gradient (Washington, NW USA). *Tectonics*, 27(4):TC4005.

Bredehoeft, J. D. and Papadopulos, I. S. (1965). Rates of Vertical Groundwater Movement Estimated from the Earths Thermal Profile. *Water Resources Res.*, 1:325 –328.

Breeding, C. M., Ague, J. J., Brocker, M., and Bolton, E. W. (2003). Blueschist preservation in a retrograded, high-pressure, low-temperature metamorphic terrane, Tinos, Greece: Implications for fluid flow paths in subduction zones. *Geochem., Geophys., Geosys.*, 4(1).

Bullard, E. C. (1939). Heat Flow in South Africa. *Proc. R. Soc. London, Ser. A*, 173:474 – 502.

Bullard, E. C. (1954). The flow of heat through the floor of the Atlantic Ocean. *Proc. R. Soc. London*, 222:408 – 429.

Calkins, J. A., Abers, G. A., Ekström, G., Creager, K. C., and Rondenay, S. (2011). Shallow structure of the Cascadia subduction zone beneath western Washington from spectral ambient noise correlation. *J. Geophys. Res.*, 116(B7):B07302.

Carslaw, H. S. and Jaeger, J. C. (1959). *Conduction of Heat Through Solids, 2nd ed.* Oxford at the Carleton Press, London, U. K.

Carson, B. (1977). Tectonically induced deformation of deep-sea sediments off Washington and Northern Oregon: Mechanical Consolidation. *Marine Geology*, 24:289 – 307.

Carson, B., Holmes, M. L., Umstattd, K., Strasser, J. C., and Johnson, H. P. (1991). Fluid expulsion from the Cascadia accretionary prism: evidence from porosity distribution, di-

rect measurements, and GLORIA imagery. *Philosophical Transactions: Physical Sciences and Engineering*, 335(1638):331–340.

Carson, B., Seke, E., Paskevich, V., and Holmes, M. L. (1994). Fluid expulsion sites on the Cascadia accretionary prism: mapping diagenitic deposits with processed GLORIA imagery. *Geophysical Research Letters*, 99(94):11959–11969.

Carson, B., Suess, E., and Strasser, J. C. (1990). Fluid Flow and Mass Flux Determinations Margin Accretionary Prism. *Journal of Geophysical Research*, 95(B6):8891–8897.

Clague, J. J. (1997). Evidence for large earthquakes at the Cascadia Subduction Zone. *Reviews of Geophysics*, 35(4):439 – 460.

Clauser, C. and Huenges, E. (1995). Thermal conductivity of rocks and minerals, in Rock Physics and Phase Relations: A handbook of Physical Constants. In Ahrens, T. J., editor, *Rock physics and phase relations: a handbook of physical constants*, pages 105 – 126. AGU, Washington, D. C.

Cowles, T., Delaney, J., Orcutt, J., and Weller, R. (2010). The Ocean Observatories Initiative: Sustained Ocean Observing Across a Range of Spatial Scales. *Marine Technology Society Journal*, 44(6):54–64.

Cozzens, B. D. (2011). A wider seismogenic zone at Cascadia due to hydrothermal circulation in subducting ocean crust. Master's thesis, New Mexico Institute of Mining and Technology, Socorro, New Mexico, USA.

Cozzens, B. D. and Spinelli, G. A. (2012). Awider seismogenic zone at Cascadia due to fluid circulation in subducting oceanic crust. *Geology*, 40(10):899–902.

Cubas, N., Souloumiac, P., and Singh, S. C. (2016). Relationship link between landward vergence in accretionary prisms and tsunami generation. *Geology*, 44(10):787–790.

Daigle, H. and Screaton, E. J. (2015). Evolution of sediment permeability during burial and subduction. *Geofluids*, 15:84 – 105.

Davis, E. E., Chapman, D. S., Mottl, M. J., Bentkowski, W. J., Dadey, K., Forster, C., Harris, R., Nagihara, S., Rohr, K., Wheat, G., and Whiticar, M. (1992). FlankFlux: an experiment to study the nature of hydrothermal circulation in young oceanic crust. *Can. J. Earth Sci.*, 29:925 – 952.

Davis, E. E. and Hyndman, R. D. (1989). Accretion and recent deformation of sediments along the northern Cascadia subduction zone. *Geol. Soc. Am. Bull*, 101:1465–1480.

Davis, E. E., Hyndman, R. D., and Villinger, H. (1990). Rates of Fluid Expulsion Across the Northern Cascadia Accretionary Prism: Constraints From New Heat Flow and Multichannel Seismic Reflection Data. *J. Geophys. Res.*, 95:8869 – 8889.

Davis, E. E., Wang, K., Becker, K., Thomson, R. E., and Yashayaev, I. (2003). Deep-ocean temperature variations and implications for errors in seafloor heat flow determinations. *J. Geophys. Res.*, 108(B1):20 – 34.

Doubilet, P., Begg, C. B., Weinstein, M. C., Braun, P., and McNeil, B. J. (1985). Probablistic Sensitivity Analysis Using Monte Carlo Simulation - A Practical Approach. *Medical decision making*, 5(2):157–177.

Dumke, I., Klaucke, I., Berndt, C., and Bialas, J. (2014). Sidescan backscatter variations of cold seeps on the Hikurangi Margin (New Zealand): Indications for different stages in seep development. *Geo-Marine Letters*, 34(2-3):169–184.

Eldholm, O., Sundvor, E., Vogt, P., Hjelstuen, B., Crane, K., Nilsen, A., and Gladczenko, T. (1999). SW Barents Sea continental margin heat flow and Hakon Mosby Mud Volcano. *Geo-Mar. Lett.*, 19:29–37.

Ellis, S., Fagereng, A., Barker, D., Henrys, S., Saffer, D., Wallace, L., Williams, C., and Harris, R. (2015). Fluid budgets along the northern Hikurangi subduction margin, New

Zealand: the effect of a subducting seamount on fluid pressure. *Geophys. J. Int.*, 2002:277–297.

Feseker, T., Foucher, J.-P., and Harmegnies, F. (2008). Fluid flow or mud eruptions? Sediment temperature distributions on Hakon Mosby mud volcano, SW Barents Sea slope. *Marine Geology*, 247(3 - 4):194–207.

Fildani, A., Normark, W. R., Kostic, S., and Parker, G. (2006). Channel formation by flow stripping: large-scale scour features along the Monterey East Channel and their relation to sediment waves. *Sedimentology*, pages 1–23.

Fisher, A., Davis, E., Hutnak, M., Speiss, V., Zuhlsdorff, L., Cherkaoui, A., Christiansen, L., Edwards, K., Macdonald, R., Villinger, H., Mottl, M., Wheat, C., and Becker, K. (2003). Hydrothermal recharge and discharge across 50 km guided by seamounts on a young ridge flank. *Nature*, 421:618–621.

Fisher, A. T., Davis, E. E., and Becker, K. (2008). Borehole-to-borehole hydrologic response across 2.4 km in the upper oceanic crust: Implications for crustal-scale properties. *J. Geophys. Res.*, 113(B7):B07106.

Fisher, A. T. and Harris, R. N. (2010). Using seafloor heat flow as a tracer to map subseafloor fluid flow in the ocean crust. *Geofluids*, 10:142 – 160.

Flueh, E. R., Fisher, M. A., Bialas, J., Childs, J. R., Klaeschen, D., Kukowski, N., Parsons, T., Scholl, D. W., ten Brink, U., Tréhu, A. M., and Vidal, N. (1998). New seismic images of the Cascadia subduction zone from cruise SO108 – ORWELL. *Tectonophysics*, 293:69–84.

Fortin, J., Stanchits, S., Vinciguerra, S., and Guegun, Y. (2011). Influence of thermal and mechanical cracks on permeability and elastic wave velocities in a basalt from Mt. Etna volcano subjected to elevated pressure. *Tectonophysics*, 503:60 – 74.

Fortin, W. F. J. (2015). *Extracting physical parameters from marine seismic data: New methods in seismic oceanography and velocity inversion*. PhD thesis, University of Wyoming, Laramine, Wyoming, USA.

Foucher, J. P. (1990). Heat flow, tectonics, and fluid circulation at the toe of the Barbados Ridge accretionary prism. *Journal of Geophysical Research*, 95(B6):8859–8867.

Ganguly, N., Spence, G. D., Chapman, N. R., and Hyndman, R. D. (2000). Heat flow variations from bottom simulating reflectors on the Cascadia margin. *Mar. Geol.*, 164:53–68.

Gao, D., Wang, K., Davis, E. E., Jiang, Y., Insua, T. L., and He, J. (2017). Thermal state of the Explorer segment of the Cascadia subduction zone: Implications for seismic and tsunami hazards. *Geochemistry, Geophysics, Geosystems*, 18(4):1569–1579.

Gerard, R., Langseth, M., and Ewing, M. (1962). Thermal gradient measurements in the water and bottom sediment of the western Atlantic. *J. Geophys. Res.*, 67(2):785–803.

Goldfinger, C., Nelson, C. H., Morey, A. E., Johnson, J. E., Patton, J. R., Karabanov, E., Gutierrez-Pastor, J., Eriksson, A. T., Gracia, E., Dunhill, G., Enkin, R. J., Dallimore, A., and Vallier, T. (2012). Turbidite Event History - Methods and Implications for Holocene Paleoseismicity of the Cascadia Subduction Zone. *U. S. Geol. Surv. Prof. Pap. 1661-F*, page 170.

Golmshtok, A. Y., Duchkov, A. D., Hutchinson, D. R., and Khanukaev, S. B. (2000). Heat flow and gas hydrates of the Baikal Rift zone. *Int. J. Earth Sci*, 89:193–211.

Goto, S. and Matsubayshi, O. (2008). Inversion of needle-probe data for sediment thermal properties of the eastern flank of the Juan de Fuca Ridge. *J. Geophys. Res.*, 113(B8):B08105.

Goto, S., Yamoano, M., and Kinoshita, M. (2005). Thermal response of sediment with vertical fluid flow to periodic temperature variation at the surface. *Journal of Geophysical Research: Solid Earth*, 110(B1).

Grevemeyer, I., Kopf, A. J., Fekete, N., Kaul, N., Villinger, H. W., Heesemann, M., Wallmann, K., Spieb, V., Gennerich, H.-H., Muller, M., and Weinrebe, W. (2004). Fluid flow through active mud dome Mound Culebra offshore Nicoya Peninsula, Costa Rica: Evidence from heat flow surveying. *Mar. Geol.*, 207:145 – 157.

Grevemeyer, I. and Villinger, H. (2001). Gas hydrate stability and the assessment of heat flow through continental margins. *Geophys. J. Int*, 145:647–660.

Gutscher, M., Klaeschen, D., Flueh, E., and Malavieille, J. (2001). Non-Coulomb wedges, wrong-way thrusting, and natural hazards in Cascadia. *Geology*, 29:379–382.

Haacke, R. R., Westbrook, G. K., and Riley, M. S. (2008). Controls on the formation and stability of gas hydrate-related bottom-simulating reflectors (BSRs): A case study from the west Svalbard continental slope. *J. Geophys. Res.*, 113(B5):B05104.

Hacker, B. R., Abers, G. A., and Peacock, S. M. (2003). Subduction factory 1. Theoretical mineralogy, densities, seismic wave speeds, and H_2O contents. *J. Geophys. Res.*, 108:126.

Haeckel, M., I., K., Riech, V., Weber, M., and Suess, E. (2001). Pore water profiles and numerical modelling of biogeochemical processes in Peru Basin deep-sea sediments. *Deep Sea Research Part II*, 48(17):3713 – 3736.

Hamamoto, H., Yamano, M., and Goto, S. (2005). Heat flow measurement in shallow seas through long-term temperature monitoring. *Geophys. Res. Lett.*, 32(21).

Hamamoto, H., Yamano, M., Goto, S., Kinoshita, M., Fujino, K., and Wang, K. (2011). Heat flow distribution and thermal structure of the Nankai subduction zone off the Ki-I Peninsula. *Geochem. Geophys. Geosyst.*, 12(10):Q0AD20.

Han, M. W. and Suess, E. (1989). Subduction-induced pore fluid venting and the formation of authigenic carbonates along the cascadia continental margin: Implications for the global Ca-cycle. *Palaeogeography, Palaeoclimatology, Palaeoecology*, 71:97–118.

Han, S., Carbotte, S. M., Canales, J. P., Nedimovi, M. R., Carton, H., Gibson, J. C., and Horning, G. W. (2016). Seismic reflection imaging of the Juan de Fuca plate from ridge to trench: new constraints on the distribution of faulting and evolution of the crust prior to subduction. *Journal of Geophysical Research: Solid Earth*, 121(3):1849–1872.

Harris, R. N., Conder, J. A., and Heuret, A. (2014). The thermal structure of the subduction thrust within accretionary and erosive margins. *Tectonophysics*, 633:221 –231.

Harris, R. N., Grevemeyer, I., Ranero, C. R., Villinger, H., Barckhausen, U., Henke, T., Mueller, C., and Neben, S. (2011). Thermal regime of the Costa Rican convergent margin: 1. Along-strike variations in heat flow from probe measurements and estimated from bottom-simulating reflectors. *Geochemistry, Geophysics, Geosystems*, 11(12).

Harris, R. N., Spinelli, G. A., Ranero, C. R., Grevemeyer, I., Villinger, H., and Barckhausen, U. (2010). Thermal regime of the Costa Rican convergent margin: 2. Thermal model of the shallow Middle America subduction zone offshore Costa Rica. *Geochemistry Geophys. Geosystems*, 11(12):Q12S29.

Harris, R. N. and Wang, K. (2002). Thermal models of the Middle America trench at the Nicoya Peninsula, Costa Rica. *Geophys. Res. Lett.*, 29(21).

Hartmann, A. and Villinger, H. (2002). Inversion of marine heat flow measurements by expansion of the temperature decay function. *Geophys. J. Int.*, 148:628 – 636.

Hautala, S. L., Solomon, E. A., Johnson, H. P., Harris, R. N., and Miller, U. K. (2014). Dissociation of Cascadia margin gas hydrates in Response To Contemporary Ocean Warming. *Geophysical Research Letters*, 41:8486–8494.

He, T., Spence, G. D., Riedel, M., Hyndman, R. D., and Chapman, N. R. (2007). Fluid flow and origin of a carbonate mound offshore Vancouver Island: Seismic and heat flow constraints. *Mar. Geol.*, 239(1 - 2):83 – 98.

Heaton, T. H. and Hartzell, S. H. (1987). Earthquake hazards on the Cascadia subduction zone. *Sci. New Ser.*, 236(4798):162 – 168.

Hedges, J. I., Hu, F. S., Devol, A. H., Hartnett, H. E., Tsamakis, E., and Keil, R. G. (1999). Sedimentary Organic Matter Preservation: A Test for Selective Degradation Under Oxic Conditions. *American Journal of Science*, 299:529–555.

Henry, P. and Clennell, M. B. (1999). Formation of natural gas hydrates in marine sediments 2. Thermodynamic calculations of stability conditions in porous sediments. *J. Geophys. Res.*, 104:23005 – 23022.

Herzberg, C., Asimow, P. D., Arndt, N., Niu, Y., Lesher, C. M., Fitton, J. G., Cheadle, M. J., and Saunders, A. D. (2007). Temperatures in ambient mantle and plumes: Constraints from basalts, picrites, and komatiites. *Geochem. Geophys. Geosys.*, 8(2).

Hoffman, N. W. and Tobin, H. J. (2004). An Empirical Relationship between Velocity and Porosity for Underthrust Sediments in the Nankai Trough Accretionary Prism. *Proceedings of the Ocean Drilling Program, Scientific Results, Volume 190/196*, 190/196.

Holbrook, W., Kent, G., Keranen, K., Johnson, P., Tréhu, A., Tobin, H., Caplan-Auerbach, J., and Beeson, J. (2012). Cascadia fore arc seismic survey: Open– access data available. *Eos (Transactions, American Geophysical Union)*, 93.

Holland, C. W., Weber, T. C., and Etiope, G. (2006). Acoustic scattering from mud volcanoes and carbonate mounds. *The Journal of the Acoustical Society of America*, 120(6):3553–3565.

Homola, K., Johnson, H. P., and Hearn, C. (2015). *In-situ* measurements of thermal diffusivity in sediments of the methane-rich zone of cascadia margin, ne pacific ocean. *Elem. Sci. Anthr.*, 3.

Hornbach, M., Holbrook, W., Gorman, A., Hackwith, K., Lizarralde, D., and Pecher, I. (2003). Direct seismic detection of methane hydrate on the Blake Ridge. *Geophysics*, 68:92–100.

Hornbach, M., Ruppel, C., Saffer, D., Van Dover, C., and Holbrook, W. (2005). Coupled geophysical constraints on heat flow and fluid flux at a salt diapir. *Geophysical Research Letters*, 32(24).

Hutchison, I. (1985). The effects of sedimentation and compaction on oceanic heat flow. *Geophys. J. R. Astron. Soc.*, 82:439–459.

Hutnak, M. and Fisher, A. T. (2007). Influence of sedimentation, local and regional hydrothermal circulation, and thermal rebound on measurements of seafloor heat flux. *J. Geophys. Res.*, 112(B12):B12101.

Hutnak, M., Fisher, A. T., Zuhlsdorff, L., Spiess, V., Stauffer, P. H., and Gable, C. W. (2006). Hydrothermal recharge and discharge guided by basement outcrops on 0.7-3.6 Ma seafloor east of the Juan de Fuca Ridge: Observations and numerical models. *Geochemistry, Geophys. Geosystems*, 7(6923):Q07O02.

Hyndman, R. D. (2013). Downdip landward limit of Cascadia great earthquake rupture. *J. Geophys. Res. Solid Earth*, 118:5530–5549.

Hyndman, R. D., Davis, E. E., and Wright, J. A. (1979). The measurement of marine geothermal heat flow by a multi-penetration probe with digital acoustic telemetry and in situ thermal conductivity. *Mar. geophys. Res.*, 4:181 – 205.

Hyndman, R. D., Foucher, J. P., Yamano, M., and Fisher, A. (1992). Deep sea bottom-simulating-reflectors: calibration of the base of the hydrate stability field as used for heat flow estimates. *Earth Planet. Sci. Lett.*, 109:289–301.

Hyndman, R. D. and Wang, K. (1993). Thermal Constraints on the Zone of Major thrust earthquake failure: The Cascadia Subduction Zone. *J. Geophys. Res.*, 98:2039 – 2060.

Hyndman, R. D. and Wang, K. (1995). The rupture zone of Cascadia great earthquakes from current deformation and the thermal regime. *J. Geophys. Res.*, 100:22133–22154.

Hyndman, R. D., Wang, K., Yuan, T., and Spence, G. D. (1993). Tectonic Sediment Thickening, Fluid Expulsion, and the Thermal Regime of Subduction Zone Accretionary Prisms: The Cascadia Margin off Vancouver Island. *J. Geophys. Res.*, 98:21865–21876.

Hyndman, R. D., Yamano, M., and Oleskevich, D. A. (1997). The seismogenic zone of subduction thrust faults. *Isl. Arc*, 6(3):244–260.

Ingebritsen, S. E. and Gleeson, T. (2015). Crustal permeability: Introduction to the special issue. *Geofluids*, 15:1–10.

Johnson, H., Gomberg, J., Hautala, S., and Salmi, M. (2017a). Sediment Gravity Flows Triggered by Remotelygenerated Earthquake Waves. *Journal of Geophysical Research: Solid Earth*.

Johnson, H., Solomon, E., Harris, R., and Salmi, M. (2017b). Processed heat flow data acquired at the Cascadia Subduction Zone during the 2013 R/V Atlantis expedition AT26-04. Interdisciplinary Earth Data Alliance (IEDA).

Johnson, H. P., Becker, K., and Herzen, R. V. (1993). Near-axis heat flow measurements on the northern Juan de Fuca Ridge: Implications for fluid circulation in oceanic crust. *Geophysical Research Letters*, pages 1875–1878.

Johnson, H. P., Hautala, S. L., and Bjorklund, T. A. (2012). The thermal environment of Cascadia Basin. *Geochemistry, Geophysics, Geosystems*, 13(7).

Johnson, H. P. and Helferty, M. (1990). The geological interpretation of side-scan sonar, 2, Processing and analysis of images. *Rev. Geophys.*, 28:357–380.

Johnson, H. P. and Hutnak, M. (1996). Conductive heat flow measured in unsedimented regions of the seafloor. *Eos*, 77:321–324.

Johnson, H. P. and Hutnak, M. (1997). Conductive heat loss in recent eruptions at midocean ridges. *Geophysical research letters*, 24(23):3089 – 3092.

Johnson, H. P., Miller, U. K., Salmi, M. S., and Solomon, E. A. (2015). Analysis of bubble plume distributions to evaluate methane hydrate decomposition on the continental slope. *Geochem. Geophys. Geosyst.*, 16(11):3825–3839.

Johnson, H. P., Solomon, E. A., Harris, R. N., Salmi, M. S., and Berg, R. D. (2013). Heat Flow and Fluid Flux in Cascadia's Seismogenic Zone. *Eos, Transactions American Geophysical Union*, 94(48):457 – 458.

Johnson, H. P., Tivey, M. A., Bjorklund, T. A., and Salmi, M. S. (2010). Hydrothermal Circulation within the Endeavour Segment; Juan de Fuca Ridge. *Geochemistry Geophys. Geosystems*, 11(5):Q05002.

Johnson, J. E., Goldfinger, C., and Suess, E. (2003). Geophysical constraints on the surface distribution of authigenic carbonates across the Hydrate Ridge region, Cascadia margin. *Marine Geology*, 202(1-2):79–120.

Judd, A. G., Hovland, M., Dimitrov, L. I., Garci, S. G., and Jukes, V. (2002). The geological methane budget at Continental Margins and its influence on climate change. *Geofluids*, 2:109–126.

Kastner, M., Kvenvolden, K. A., Whiticar, M. J., Camerlenghi, A., and Lorenson, T. D. (1995). 10. Relation between Pore Fluid Chemistry and Gas Hydrates Associated with Bottom-Simulating Reflectors at the Cascadia Margin, Site 889 and 892. *Proc. Ocean Drill. Program Sci. Results*, 146:175–187.

Kastner, M., Solomon, E. A., Harris, R. N., and Torres, M. E. (2014). *Fluid Origins, Thermal Regimes, and Fluid and Solute Fluxes in the Forearc of Subduction Zones*, volume 7. Elsevier.

Kaul, N., Rosenberger, A., and Villinger, H. (2000). Comparison of measured and BSR-derived heat flow values, Makran accretionary prism, Pakistan. *Mar. Geol.*, 164:37–51.

Kinoshita, M. (2012). Estimation of grain thermal conductivity in the turbidite sediment of the Juan de Fuca Ridge. *Proc. ODP, Sci. Results*, 139:553–558.

Kinoshita, M., Kanamatsu, T., Kawamura, K., Shibata, T., Hamamoto, H., and Fujino, K. (2008). Heat flow distribution on the floor of Nankai Trough off Kumano and implications for the geothermal regime of subducting sediments. *JAMSTEC Report of Research and Development*, 8:13–28.

Kinoshita, M., Kawada, Y., Tanaka, A., and Urabe, T. (2006). Recharge/discharge interface of a secondary hydrothermal circulation in the Suiyo Seamount of the Izu-Bonin arc, identified by submersible-operated heat flow measurements. *Earth and Planetary Science Letters*, 245(3):498–508.

Kirby, S. H., Wang, K. L., and Dunlop, S. (2002). The Cascadia Subduction Zone and related subduction systems: Seismic Structure, Intraslab Earthquakes and Processes, and Earthquake Hazards. Technical Report August, U.S. Geological Survey.

Krabbenhoeft, A., Bialas, J., Klaucke, I., Crutchley, G., Papenberg, C., and Netzeband, G. L. (2013). Patterns of subsurface fluid-flow at cold seeps: The Hikurangi Margin, offshore New Zealand. *Marine and Petroleum Geology*, 39(1):59–73.

Kvenvolden, K. A. (1993). Gas hydrate–Geological perspective and global change. *Reviews of Geophysics*, 31:173–187.

Langseth, M. G. (1965). Techniques of measuring heat flow through the ocean floor. In Lee, W. H. K., editor, *Terrestrial Heat Flow*, volume 8 of *Geophys. Monogr. Ser.*, pages 58 – 77. AGU, Washington, D. C.

Langseth, M. G. and Herman, B. M. (1981). Heat transfer in the oceanic crust of the Brazil Basin. *Journal of Geophysical Research*, 86(B11):10805–10819.

Lauer, R. M. and Saffer, D. M. (2015). The impact of splay faults on fluid flow, solute transport, and pore pressure distribution in subduction zones: A case study offshore the Nicoya Peninsula, Costa Rica. *Geochemistry Geophys. Geosystems*, 16:1089–1104.

Le Pichon, X., Henry, P., and Crew, K.-N. S. (1991). Water budgets in accretionary wedges: a comparison. *Phil. Trans. R. Soc.*, 335:315–330.

Lewis, T. J., Bentkowski, W. H., Davis, E. E., Hyndman, R. D., Souther, J. G., and Wright, J. A. (1988). Subduction of the Juan de Fuca Plate: Thermal consequences. *J. Geophys. Res.*, 93:15207 – 15225.

Li, H., He, T., and Spence, G. D. (2013). North Cascadia heat flux and fluid flow from gas hydrates: Modeling 3-D topographic effects. *J. Geophys. Res. Solid Earth*, 119:99 –115.

Linke, P., Suesss, E., Torres, M., Martens, V., Rugh, W., Siebis, W., and Kulm, L. (1994). In situ measurements of fluid flow from cold seeps at active continental margins. *Deep Sea Research Part I: Oceanographic Research Papers*, 41(4):721–739.

Lister, C. (1979). The pulse-probe method of conductivity measurement. *Geophys. J. R. astr. Soc.*, 57:451–461.

Liu, X. and Flemings, P. B. (2006). Passing gas through the hydrate stability zone at southern Hydrate Ridge, offshore Oregon. *Earth Planet. Sci. Lett.*, 241:211–226.

Lucazeau, F., Brigaud, F., and Bouroullec, J. (2004). High–resolution heat flow density in the lower Congo basin. *Geochemistry, Geophysics, Geosystems*, 5(3).

Luff, R. and Wallmann, K. (2003). Fluid flow, methane fluxes, carbonate precipitation and biogeochemical turnover in gas hydrate-bearing sediments at Hydrate Ridge, Cascadia Margin: numerical modeling and mass balances. *Geochimica et Cosmochimica Acta*, 67(18):3403 – 3421.

Luff, R., Wallmann, K., and Aloisi, G. (2004). Numerical modeling of carbonate crust formation at cold vent sites: significance for fluid and methane budgets and chemosynthetic biological communities. *Earth and Planetary Science Letters*, 221(1-4):337–353.

MacCready, P. and Giddings, S. (2016). The Mechanical Energy Budget of a Regional Ocean Model. *Journal of Physical Oceanography*, 46(9):2719–2733.

Macelloni, L., Lutken, C., Garg, S., Simonetti, A., D'Emidio, M., Wilson, R., Sleeper, K., Lapham, L., Lewis, T., Pizzi, M., and Knapp, J. (2015). Heat-flow regimes and the hydrate stability zone of a transient, thermogenic, fault-controlled hydrate system (Woolsey Mound northern Gulf of Mexico). *Marine and Petroleum Geology*, 59:491–504.

Malinverno, A., Kastner, M., Torres, M. E., and Wortmann, U. G. (2008). Gas hydrate occurrence from pore water chlorinity and downhole logs in a transect across the northern Cascadia margin. *Integrated Ocean Drilling Program Expedition 311*, 113:1 – 18.

Marcaillou, B., Spence, G., Collot, J., and Wang, K. (2006). Thermal regime from bottom simulating reflectors along the north Ecuador south Colombia margin: Relation to margin segmentation and great subduction earthquakes. *Journal of Geophysical Research*, 111:1–16.

Martin, J. T. and Lowell, R. P. (2000). Precipitation of quartz during high-temperature, fracture-controlled hydrothermal upflow at ocean ridges: Equilibrium versus linear kinetics. *Journal of Geophysical Research*, 105(B1):869 – 882.

Martin, V., Henry, P., Nouz, H., Noble, M., Ashi, J., and Pascal, G. (2004). Erosion and sedimentation as processes controlling the BSR - derived heat flow on the Eastern Nankai margin. *Earth Planet. Sci. Lett.*, 222:131 – 144.

McCrory, P. A., Hyndman, R. D., Blair, and Blair, J. L. (2014). Relationship between the Cascadia forearc mantle wedge, nonvolcanic tremor, and the downdip limit of seismogenic rupture. *Geochemistry, Geophys. Geosystems*, 15:1071 – 1095.

McKenna, J. R. and Blackwell, D. D. (2002). Shallow Thermal Conditions in the Central and Southern Cascadia Subduction Zone. Text can be found at `http://cascadiageo.org/documentation/literature/cascadia_papers/cszthermal.pdf`.

McKenzie, D., Jackson, J., and Priestley, K. (2005). Thermal structure of oceanic and continental lithosphere. *Earth Planet. Sci. Lett.*, 233:337 – 349.

McNeill, C., Piper, A., Goldfinger, C., Kulm, L. D., and Yeats, S. (1997). Listric normal faulting on the Cascadia continental margin Coast Range. *J. Geophys. Res.*, 102:12123 – 12138.

Mitchell, N. (1993). A model for attenuation of backscatter due to sediment acumulations and its application to determine sediment thicknesses with GLORIA sidescan sonar. *J. Geophys. Res. Solid Earth*, 98(B12):22477 – 22493.

Moore, J. C. and Saffer, D. (2001). Updip limit of the seismogenic zone beneath the accretionary prism of southwest Japan: An effect of diagenetic to low-grade metamorphic processes and increasing effective stress. *Geology*, 29:183–186.

Moore, J. C. and Vrolijk, P. (1992). Fluids in Accretionary Prisms. *Reviews of Geophysics*, 30(2):113–135.

Moran, J. E. and Lister, C. R. B. (1987). Heat flow across Cascadia Basin near 47°N, 128°W. *J. Geophys. Res.*, 92:11416 – 11432.

Morton, E. A. and Bilek, S. L. (2015). Preliminary Event Detection of Earthquakes Using the Cascadia Initiative Data. *Seismological Research Letters*, 86(5).

Murrell, M. C. and Lehrter, J. C. (2011). Sediment and lower water column oxygen consumption in the seasonally hypoxic region of the Louisiana continental shelf. *Estuaries and Coasts*, 34(5):912–924.

Nagihara, S. and Lister, C. R. B. (1993). Accuracy of marine heat-flow instrumentation: numerical studies on the effects of probe construction and the data reduction scheme. *Geophs. J. Int.*, 112:161 – 177.

Naudts, L., Greinert, J., Artemov, Y., Beaubien, S. E., Borowski, C., and Batist, M. D. (2008). Anomalous sea-floor backscatter patterns in methane venting areas, Dnepr paleodelta, NW Black Sea. *Marine Geology*, 251(3):253 – 267.

Nayar, K., Sharqawy, M., Banchik, L., and V, J. L. (2016). Thermophysical properties of seawater: A review and new correlations that include pressure dependence. *Desalination*, 390:1 – 24.

Oleskevich, D. A., Hyndman, R. D., and Wang, K. (1999). The updip and downdip limits to great subduction earthquakes: Thermal and structural models of Cascadia, south Alaska, SW Japan, and Chile. *J. Geophys. Res.*, 104:14965–14991.

Papadopoulos, C. and Yeung, H. (2001). Uncertainty estimation and Monte Carlo simulation method. *Flow Measurement and Instrumentation*, 12:291–298.

Parsons, T., Wells, R. E., Fisher, M. A., Flueh, E., and ten Brink, U. S. (1999). Three-dimensional velocity structure of Siletzia and other accreted terranes in the Cascadia forearc of Washington. *J. Geophys. Res*, 104:18015 – 18039.

Pfender, M. and Villinger, H. (2002). Miniaturized data loggers for deep sea sediment temperature gradient measurements. *Marine Geology*, 186:557–570.

Riedel, M. and Shankar, U. (2012). Combining impedance inversion and seismic similarity for robust gas hydrate concentration assessments - A case study from the Krishna-Godavari basin, East Coast of India. *Mar. Pet. Geol.*, 36:35 – 49.

Riedel, M., Tréhu, A. M., and Spence, G. D. (2010). Characterizing the thermal regime of cold vents at the northern Cascadia margin from bottom-simulating reflector distributions, heat-probe measurements and borehole temperature data. *Mar. Geophys. Res.*, 31:1–16.

Riedel, M., Willoughby, E. C., Chen, M. A., He, T., Novosel, I., Schwalenberg, K., Hyndman, R. D., Spence, G. D., Chapman, N. R., and Edwards, R. N. (2006). Gas hydrate on the northern Cascadia Margin: regional geophysics and structural framework. *Proc. Ocean Drill. Program Sci. Results*, 311:1 – 28.

Ritger, S., Carson, B., and Suess, E. (1987). Methane-derived authigenic carbonates formed by subduction- induced pore-water expulsion along the Oregon/ Washington margin. *Geological Society of America Bulletin*, 98(2):147–156.

Rogers, A. (1996). Assessing Earthquake Hazards and reducing Risk in the Pacific Northwest. *Professional Paper 1560*.

Rogers, G. and Dragert, H. (2003). Episodic Tremor and Slip on the Cascadia Subduction Zone: The chatter of Silent Slip. *Science*, 300(5627):1942–1943.

Rona, P., Petersen, S., Becker, K., Herzen, R. V., Hannington, M., Herzig, P., J. Naka, C. L., and Thompson, G. (1996). Heat flow and mineralogy of TAG relict high temperature hydrothermal Mid Atlantic zones: Ridge 26°N, 45°W. *Geophys. Res. Lett.*, 23:3311 – 3514.

Rotman, H. M. M. and Spinelli, G. A. (2014). Remarkably consistent thermal state of the south central Chile subduction zone from 36°S to 45°S. *Journal of Geophysical Research: Solid Earth*, 119(4):3503 – 3516.

Ruppel, C., Herzen, R. V., and Bonneville, A. (1995). Heat flux through an old (175 Ma) passive margin: Offshore southeastern United States. *Journal of Geophysical Research*, 100(B10):20037 – 20057.

Ryan, W. B. F., Carbotte, S., Coplan, J. O., S.OHara, Melkonian, A., Ferrini, V., Goodwillie, A., Nitsche, F., Bonczkowski, J., and Zemsky, R. (2009). Global multi-resolution topography synthesis. *Geochem. Geophys. Geosyst.*, 10(Q03014).

Saffer, D. M. (2015). The permeability of active subduction plate boundary faults. *Geofluids*, 15(193 - 215).

Saffer, D. M. and Bekins, B. A. (2002). Hydrologic controls on the morphology and mechanics of accretionary wedges. *Geology*, 30:271–274.

Saffer, D. M. and Marone, C. (2003). Comparison of smectite- and illite-rich gouge frictional properties: application to the updip limit of the seismogenic zone along subduction megathrusts. *Earth Planet. Sci. Lett.*, 215:219–235.

Saffer, D. M. and Tobin, H. J. (2011). Hydrogeology and Mechanics of Subduction Zone Forearcs: Fluid Flow and Pore Pressure. *Annu. Rev. Earth Planet. Sci.*, 39:157–186.

Saffer, D. M., Underwood, M. B., and McKiernan, A. W. (2008). Evaluation of factors controlling smectite transformation and fluid production in subduction zones: Application to the Nankai Trough. *Island Arc*, 17(2).

Salmi, M. S., Johnson, H. P., and Harris, R. N. (2017). Thermal environment of the Southern Washington region of the Cascadia subduction zone. *J. Geophys. Res. Solid Earth*, 122.

Salmi, M. S., Johnson, H. P., Leifer, I., and Keister, J. E. (2011). Behavior of methane seep bubbles over a pockmark on the Cascadia continental margin. *Geosphere*, 7(6):1273 – 1283.

Salmi, M. S., Johnson, H. P., Tivey, M. A., and Hutnak, M. (2014). Quantitative estimate of heat flow from a mid-ocean ridge axial valley, Raven Field, Juan de Fuca Ridge: Observations and Inferences. *J. Geophys. Res. Solid Earth*, 119.

Sample, J. and Reid, M. (1998). Contrasting hydrogeologic regimes along strike-slip and thrust faults in the Oregon convergent margin: Evidence from the chemistry of syntectonic carbonate cements and veins. *Geol. Soc. Am. Bull.*, 110:48–59.

Scamman, R. L. (1981). Diagenetic Carbonate Cementation of Clastic Sediments near the Sediment-water interface on the lower Continental Slope off Washington and Oregon. Master's thesis, Lehigh University.

Schmalzle, G. M., McCaffrey, R., and Creager, K. C. (2014). Central Cascadia subduction zone creep. *Geochem. Geophys. Geosyst.*, 15:1515 – 1532.

Screaton, E., Saffer, D., Henry, P., and Hunze, S. (2002). Porosity loss within the under thrust sediments of the Nankai accretionary complex: Implications for overpressures. *Geology*, 30:19–22.

Sharqawy, M. H., Lienhard, J. H., and Zubair, S. M. (2010). Thermophysical properties of seawater: A review of existing correlations and data. *Desalination and Water Treatment*, 16:354 – 380.

Shi, Y., Wang, C., Langseth, M. G., Hobart, M. A., and Huene, R. V. (1988). Heat Flow and Thermal Structure of the Washington-Oregon accretionary prism - A study of lower slope. *Geophys. Lett.*, 15:1113 – 1116.

Sonardyne (2009). Ranger usbl acoustic position system for dp and survey. `www.sonardyne.com`, Date accessed: 7/23/2018.

Spinelli, G. A. and Fisher, A. T. (2004). Hydrothermal circulation within topographically rough basaltic basement on the Juan de Fuca Ridge flank. *Geochemistry Geophys. Geosystems*, 5(Q02001).

Spinelli, G. A. and Wang, K. (2008). Effects of fluid circulation in subducting crust on Nankai margin seismogenic zone temperatures. *Geology*, 36:887.

Spinelli, G. A. and Wang, K. (2009). Links between fluid circulation, temperature, and metamorphism in subducting slabs. *Geophys. Res. Lett.*, 36(L13302).

Stein, C. A. and Stein, S. (1992). A model for the global variation in oceanic depth and heat flow with lithospheric age. *Nature*, 359.

Suess, E. and Bohrmann, G. (1997). FS SONNE, Cruise Report SO110:SO-RO (SONNE-ROPOS). Technical report, GEOMAR Research Center for Marine Geosciences, Kiel, Germany.

Tishchenko, P., Hensen, C., Wallmann, K., and Shing, C. (2005). Calculation of the stability and solubility of methane hydrate in seawater. *Chemical Geology*, 219.

Tivey, M., de Ronde, C., Tontini, F., Walker, S., and Fornari, D. (2016). A novel heat flux study of a geothermally active lakeLake Rotomahana, New Zealand. *Journal of Volcanology and Geothermal Research*, 314:95 – 109.

Tobin, H. J. and Saffer, D. M. (2009). Elevated fluid pressure and extreme mechanical weakness of a plate boundary thrust, Nankai Trough subduction zone. *Geology*, 37:679682.

Toomey, D. R., Allen, R. M., Barclay, A. H., Bell, S., Bromirski, P. D., Carlson, R. L., Chen, X., Collins, J. A., Dziak, R. P., and B. Evers, e. a. (2014). The Cascadia Initiative: A sea change in seismological studies of subduction zones. *Oceanography*, 27:138 – 150.

Torres, M., Mix, A., Kinports, K., Haley, B., Klinkhammer, G., McManus, J., and de Angelis, M. (2003). Is methane venting at the seafloor recorded by δ13C of benthic foraminifera shells? *Paleoceanography*, 18(3).

Torres, M. E., Embley, R. W., Merle, S. G., Tréhu, A. M., Collier, R. W., Suess, E., and

Heeschen, K. U. (2009). Methane sources feeding cold seeps on the shelf and upper continental slope off central Oregon, USA. *Geochemistry Geophysics Geosystems*, 10(11):1–21.

Torres, M. E., Mcmanus, J., Hammond, D. E., Angelis, M. A. D., Heeschen, K. U., Colbert, S. L., Tryon, M. D., Brown, K. M., and Suess, E. (2002). Fluid and chemical fluxes in and out of sediments hosting methane hydrate deposits on Hydrate Ridge, OR, I: Hydrological provinces. *Earth and Planetary Science Letters*, 201.

Tréhu, A. M., Braunmiller, J., and Davis, E. (2015). Seismicity of the Central Cascadia Continental Seismicity of the Central Cascadia Continental Margin near 44.5 °N: A Decadal View. *Seismol. Res. Lett.*, 86(3):819 – 829.

Tréhu, A. M., Braunmiller, J., and Nabelek, J. L. (2008). Probable low-angle thrust earthquakes on the Juan de Fuca - North America plate boundary. *Geology*, 36:127–130.

Tréhu, A. M., Lin, G., Maxwell, E., and Goldfinger, C. (1995). A seismic reflection profile across the Cascadia subduction zone offshore central Oregon: New constraints on methane distribution and crustal structure. *J. Geophys. Res. Solid Earth*, 100:15101 – 15116.

Tryon, M., Brown, K., Torres, M., Trehu, A., McManus, J., and Collier, R. (1999). Measurements of transience and downward fluid flow near episodic methane gas vents, Hydrate Ridge, Cascadia. *Geology*, 27:1075 – 1078.

Tryon, M. D., Brown, K. M., and Torres, M. E. (2002). Fluid and chemical flux in and out of sediments hosting methane hydrate deposits on Hydrate Ridge, OR, II: Hydrological processes. *Earth and Planetary Science Letters*, 201:541–557.

Villinger, H. and Davis, E. E. (1987). A new reduction Algorithm for Marine Heat Flow Measurements. *Journal of Geophysical Research*, 92(B12):12846 – 12856.

Villinger, H. W., Pichler, T., Kaul, N., Stephan, S., Palike, H., and Stephan, F. (2017). Formation of hydrothermal pits and the role of seamounts in the Guatemala Basin (Equa-

torial East Pacific) from heat flow, seismic, and core studies. *Geochemistry, Geophysics, Geosystems*, 18.

Von Herzen, R. and Maxwell, A. (1959). The Measurement of Thermal Conductivity of Deep-sea sediments by a Needle-Probe Method. *Journal of Geophysical Research*, 64(10):1557 – 1563.

Wada, I. and Wang, K. (2009). Common depth of slab-mantle decoupling: reconciling diversity and uniformity of subduction zones. *Geochemistry, Geophysics, Geosystems*, 10(Q10009).

Wada, I., Wang, K., He, J., and Hyndman, R. D. (2008). Weakening of the subduction interface and its effects on surface heat flow, slab dehydration, and mantle wedge serpentinization. *J. Geophys. Res.*, 113(B04402).

Wang, K. and Beck, A. E. (1987). Heat Flow Measurement in Lacustrine or Oceanic Sediments without Recording Bottom Temperature Variations. *J. Geophys. Res.*, 92(12):837 – 12845.

Wang, K. and Davis, E. E. (1992). Thermal effects of marine sedimentation in hydrothermally active areas. *Geophys. J. Int.*, 110:7078.

Wang, K. and Hu, Y. (2006). Accretionary prisms in subduction earthquake cycles: The theory of dynamic Coulomb wedge. *J. Geophys. Res.*, 111(B06410).

Wang, K., Hyndman, R. D., and Davis, E. E. (1993). Thermal Effects of Sediment Thickening and Fluid Expulsion in Accretionary Prisms: Model and Parameter Analysis. *J. Geophys. Res.*, 98:9975 – 9984.

Wang, K., Van Der Kamp, G. D., and Davis, E. E. (1999). Limits of tidal energy dissipation by fluid flow in subsea formations. *Geophysical Journal International*, 139(3):763–768.

Wang, K., Wells, R., Mazzotti, S., Hyndman, R. D., and Sagiya, T. (2003). A revised dislocation model of interseismic deformation of the Cascadia subduction zone. *J. Geophys. Res.*, 108:1 – 13.

Wang, K. L., Mulder, T., Rogers, G. C., and Hyndman, R. D. (1995). Case for very low coupling stress on the Cascadia subduction fault. *J. Geophys. Res.*, 100:12907 – 12918.

Westbrook, G. K., Carson, B., and Musgrave, R. J. (1994). ODP Leg 146 Scientific Party. *Proc. ODP, Init. Repts., 146 (Pt. 1)*.

Wheat, C. G., Mottl, M. J., Fisher, A. T., Kadko, D., Davis, E. E., Baker, E., and Baker (2004). Heat flow through a basaltic outcrop on a sedimented young ridge flank. *Geochemistry Geophys. Geosystems*, 5(12).

Wilcock, W. S. D. and McNabb, A. (1996). Estimates of crustal permeability on the Endeavour segment of the Juan de Fuca mid-ocean ridge. *Earth Planet. Sci. Lett.*, 138:83 – 91.

Wilson, D. S. (1993). Confidence intervals for motion and deformation of the Juan de Fuca Plate. *J. Geophys. Res.*, 98:16053 – 16071.

Wong, I. G. (2015). Low Potential for Large Intraslab Earthquakes in the Central Cascadia Subduction Zone Low Potential for Large Intraslab Earthquakes in the Central Cascadia Subduction Zone. *Bull. Seismol. Soc. Am.*, 95:1880 – 1902.

Yamano, M. (2003). Extremely high heat flow anomaly in the middle part of the Nankai Trough. *Phys. Chem. Earth*, 28:487 – 497.

Yuan, T., Hyndman, R. D., Spence, G. D., and Desmons, B. (1996). Seismic velocity increase and deep-sea gas hydrate concentration above a bottom-simulating reflector on the northern Cascadia continental slope. *J. Geophys. Res.*, 101:13655 – 13671.

Yuan, T., Spence, G. D., Hyndman, R. D., Minshull, T. A., and Singh, S. C. (1999). Seismic velocity studies of a gas hydrate bottom-simulating reflector on the northern Cascadia continental margin: Amplitude modeling and full waveform inversion. *J. Geophys. Res.*, 104:1179 – 1191.

Zuhlsdorff, L., Spieß, V., Hubscher, C., Villinger, H. W., and Rosenberger, A. (2000). Implications for focused fluid transport at the northern Cascadia accretionary prism from a correlation between BSR occurrence and near-sea-floor reflectivity anomalies imaged in a multi-frequency seismic data set. *International Journal of Earth Sciences*, 88(4):655–667.

Zwart, G., Moore, J. C., and Cochrane, G. R. (1996). Variations in temperature gradients identify active faults in the Oregon accretionary prism. *Earth Planet. Sci. Lett.*, 139:485 – 495.

Appendix A

SURFACE HEAT FLOW DATA

Surface heat flow data collected during the AT26-04 R/V *Atlantis* research cruise offshore Southern Washington State during the dates of 7/31/2013 to 8/26/2013. The surface heat flow data has been uploaded as ASCII text files to the Marine Geoscience Data System (MGDS), which can be found at the following website: `http://www.marine-geo.org/`. The surface heat flow is located under the dataset numbers: 21838 (Thermal Blanket), 24241 (Alvin Heat Flow Probe), 24240 (Multi-core Logger) (Johnson et al., 2017b). The Bottom Simulating Reflector heat flow data can also be found on the same database under the dataset number: 24242. Funding was provided by NSF grants OCE11-44164 and OCE12-49552. Investigators were: H. Paul Johnson, Evan Solomon, and Robert Harris.

A.1 Violin-bow Heat Flow Probe

Heat flow measurements, uncertainty in the form of standard deviation (σ_Q), and meta-data for the 3.5 meter Violin-bow Probe. The Violin-bow Probe is a multi-penetration lister type probe equipped with 11 thermistors on an external string. Heat flow data and associated uncertainties were calculated using the Matlab program SlugHeat, based on the HFRED algorithm (Villinger and Davis, 1987). Uncertainty was determined through Monte Carlo simulations and included the correlation coefficient (R^2) of the linear fit to the Bullard Plot. All measurements were considered of good quality and none were flagged as bad.

Probe Name	Date (GMT)	Date	Latitude	Longitude	Depth (meters)	Heat Flow (mW m^{-2})	σ_Q (mW m^{-2})	r^2
HC14-01	8/8/2013	09:12	N 46° 48.107'	W 125° 32.042'	1922	84.9	0.73	0.9996
HC14-02	8/8/2013	10:36	N 46° 48.041'	W 125° 32.822'	1957	83.8	0.56	0.9997
HC14-03	8/8/2013	11:44	N 46° 48.008'	W 125° 33.205'	1958	90.3	2.03	0.9979
HC14-04	8/8/2013	12:38	N 46° 47.975'	W 125° 33.598'	1929	94.1	1.57	0.9985
HC14-05	8/8/2013	13:41	N 46° 47.942'	W 125° 33.982'	1919	101.8	2.06	0.9980
HC14-06	8/8/2013	14:40	N 46° 47.908'	W 125° 34.373'	1892	116.5	3.73	0.9885
HC16-01	8/9/2013	09:04	N 46° 47.282'	W 125° 41.619'	1908	102.8	0.69	0.9997
HC16-02	8/9/2013	10:09	N 46° 47.214'	W 125° 42.398'	1916	90.7	0.89	0.9995
HC16-03	8/9/2013	11:18	N 46° 47.146'	W 125° 43.179'	1913	88.8	0.85	0.9995
HC16-04	8/9/2013	12:28	N 46° 47.078'	W 125° 43.959'	1917	86.1	0.84	0.9995
HC16-05	8/9/2013	13:35	N 46° 47.011'	W 125° 44.737'	1916	87.2	0.56	0.9998
HC16-06	8/14/2013	09:31	N 46° 46.941'	W 125° 45.520'	1913	83.7	0.75	0.9996
HC16-07	8/14/2013	10:30	N 46° 46.874'	W 125° 46.300'	1908	85.6	0.75	0.9995
HC16-08	8/14/2013	11:31	N 46° 46.806'	W 125° 47.077'	1896	113.8	0.96	0.9994

A.2 Alvin Heat Flow Probe

Heat flow measurements, uncertainty in the form of standard deviation (σ_Q), and meta-data for the 0.6 meter Alvin Probe. The Alvin Probe is equipped with 5 thermistors at a 0.1 meter spacing. The surface heat flow measurements were assigned quality flags of Good or Bad. Good signifies a relatively straight Bullard plot ($R^2 < 0.9$), good thermal conductivity measurements, etc. Bad indicates poor quality data that should not be used. Heat flow data and associated uncertainties were calculated using the Matlab program SlugHeat, based on the HFRED algorithm (Villinger and Davis, 1987). The uncertainties were determined through Monte Carlo simulations and included the correlation coefficient (R^2) of the linear fit to the Bullard plot.

Probe #	Dive	Probe	Station	Date	Time (GMT)	Latitude	Longitude	Depth (meters)	Heat Flow (mW m^{-2})	σ_Q (mW m^{-2})	r^2	Flag
1	719	A	1	8/3/2013	17:54	N 46.8444°	W 125.0367°	586.4	-189.7	34.5	0.7380	Bad
2	719	A	1	8/3/2013	18:24	N 46.8444°	W 125.0367°	586.4	-80.6	1786.6	0.6284	Bad
3	719	A	1	8/3/2013	18:45	N 46.8444°	W 125.0367°	586.4	-97.3	126.1	0.6899	Bad
4	719	A	2	8/4/2013	01:36	N 46.8496°	W 124.9572°	557.1	-220.8	52.6	0.8815	Bad
5	719	A	2	8/4/2013	02:31	N 46.8497°	W 124.9572°	554.2	-210.4	57.7	0.8661	Bad
6	719	A	2	8/4/2013	02:52	N 46.8498°	W 124.9572°	554.2	-208.3	59.7	0.8653	Bad
7	719	A	2.25	8/4/2013	04:25	N 46.8499°	W 124.9508°	559.6	-451.9	56.6	0.8566	Bad
8	719	A	2.25	8/4/2013	04:46	N 46.8499°	W 124.9508°	559.6	-216.9	1000.9	0.6998	Bad
9	719	A	2.25	8/4/2013	05:07	N 46.8499°	W 124.9508°	559.6	-280.0	94.9	0.7722	Bad
10	719	A	2.75	8/4/2013	07:20	N 46.8522°	W 124.9466°	558.5	-610.0	61.0	0.8596	Bad
11	719	A	3	8/4/2013	17:55	N 46.8972°	W 124.9933°	808.8	110.2	4825.1	0.4078	Bad
12	719	A	3	8/4/2013	18:20	N 46.8972°	W 124.9933°	808.8	86.4	4820.3	0.5126	Bad
13	719	A	4	8/5/2013	03:00	N 46.8888°	W 125.1182°	681.8	-99.0	8.5	0.8730	Bad
14	719	A	4	8/5/2013	03:22	N 46.8888°	W 125.1182°	681.8	-137.4	10.0	0.9717	Bad
15	719	A	4	8/5/2013	03:43	N 46.8888°	W 125.1183°	681.8	-122.6	9.5	0.9782	Bad
16	719	A	5	8/5/2013	12:02	N 46.8285°	W 125.2189°	1149.0	-92.0	1949.4	0.5373	Bad
17	719	A	5	8/5/2013	12:24	N 46.8285°	W 125.2189°	1149.0	-87.5	800.7	0.6218	Bad
18	719	A	5	8/5/2013	12:48	N 46.8285°	W 125.2189°	1149.0	-80.2	1304.1	0.6103	Bad
19	719	A	6	8/5/2013	20:08	N 46.8211°	W 125.3046°	1330.8	75.8	27.2	0.7526	Bad
20	719	A	6	8/5/2013	20:36	N 46.8211°	W 125.3047°	1330.8	58.0	61.9	0.7420	Bad
21	719	A	6	8/5/2013	21:04	N 46.8211°	W 125.3048°	1330.8	74.4	7.9	0.8790	Bad

22	719	A	7	8/6/2013	05:08	N 46.8101°	W 125.4416°	1927.1	134.1	26.8	0.9055	Good
23	719	A	7	8/6/2013	05:33	N 46.8101°	W 125.4417°	1927.1	147.2	20.7	0.9425	Good
24	719	A	7	8/6/2013	05:58	N 46.8101°	W 125.4419°	1927.1	144.9	19.9	0.9334	Good
25	719	A	8	8/6/2013	14:28	N 46.7312°	W 125.4972°	2095.5	107.2	15.8	0.9204	Good
26	719	A	8	8/6/2013	14:51	N 46.7312°	W 125.4972°	2095.5	109.9	14.8	0.9543	Good
27	719	A	8	8/6/2013	15:47	N 46.7311°	W 125.4984°	2115.3	Failed	Failed	Failed	Bad
28	719	A	9.5	8/7/2013	02:01	N 46.7482°	W 125.4195°	1992.6	246.9	39.0	0.8200	Bad
29	719	A	9.5	8/7/2013	07:19	N 46.7481°	W 125.4193°	1992.6	127.3	18.5	0.9491	Good
30	719	A	10	8/7/2013	16:37	N 46.7410°	W 125.2294°	956.1	50.9	257.7	0.7571	Bad
31	719	A	10	8/7/2013	17:07	N 46.7409°	W 125.2293°	956.1	43.1	905.7	0.7216	Bad
32	719	A	10	8/7/2013	17:30	N 46.7409°	W 125.2293°	956.1	47.2	26.9	0.7858	Bad
33	719	A	10	8/7/2013	17:53	N 46.7408°	W 125.2292°	956.1	40.2	15.7	0.8263	Bad
34	719	A	10	8/7/2013	18:19	N 46.7408°	W 125.2289°	954.8	37.0	100.8	0.6156	Bad
35	720	B	2.25	8/9/2013	18:47	N 46.8518°	W 124.9473°	564.8	-50.1	1217.7	0.4704	Bad
36	720	A	2.25	8/9/2013	19:45	N 46.8518°	W 124.9473°	564.8	91.1	1261.6	0.5045	Bad
37	720	B	2.25	8/9/2013	21:21	N 46.8518°	W 124.9466°	560.6	-1045.7	49292	0.0230	Bad
38	720	A	2.25	8/9/2013	21:22	N 46.8518°	W 124.9466°	560.6	-44.4	4627.1	0.4405	Bad
39	720	A	2.25	8/9/2013	21:56	N 46.8520°	W 124.9464°	560.6	Failed	Failed	Failed	Bad
40	720	B	2.25	8/9/2013	22:08	N 46.8505°	W 124.9569°	554.6	220.5	30.7	0.5236	Bad
41	720	A	2.25	8/9/2013	22:34	N 46.8505°	W 124.9569°	554.6	-199.7	20.0	0.7044	Bad
42	720	A	2.25	8/10/2013	00:06	N 46.8521°	W 124.9466°	560.6	-3431	23163	0.0289	Bad
43	720	A	2.25	8/10/2013	00:33	N 46.8521°	W 124.9466°	560.6	172.6	11432	0.0535	Bad
44	720	A	2.25	8/10/2013	01:20	N 46.8662°	W 124.9466°	500.3	Failed	Failed	Failed	Bad
45	720	A	2.25	8/10/2013	02:01	N 46.8512°	W 124.9466°	562.1	39.5	17.6	0.4249	Bad
46	721	A	1	8/10/2013	18:33	N 46.8444°	W 125.0366°	586.4	-62.8	5023	0.3181	Bad
47	721	A	1	8/10/2013	18:59	N 46.8444°	W 125.0366°	586.4	-83.5	11.0	0.9323	Bad
48	721	A	5	8/11/2013	07:22	N 46.8285°	W 125.2188°	1141.6	69.9	3467.2	0.4815	Bad
49	721	A	6	8/11/2013	14:19	N 46.8209°	W 125.3049°	1330.8	172.9	64.6	0.3709	Bad
50	721	B	7	8/11/2013	23:03	N 46.8099°	W 125.4422°	1927.0	91.0	8.8	0.9650	Good
51	721	B	7	8/11/2013	23:26	N 46.8098°	W 125.4422°	1927.0	-31.9	6.8	0.8134	Bad
52	721	B	7W	8/12/2013	03:30	N 46.8100°	W 125.4486°	1927.9	96.9	11.1	0.9684	Good

53	721	B	8	8/12/2013	11:40	N 46.7311°	W 125.4984°	2115.3	116.3	13.6	0.9541	Good
54	721	B	8	8/12/2013	12:01	N 46.7311°	W 125.4984°	2115.3	156.3	19.3	0.9666	Good
55	721	A	9.5	8/13/2013	01:46	N 46.7487°	W 125.4188°	1990.3	95.7	12.9	0.9297	Good
56	721	A	9.5	8/13/2013	02:26	N 46.7492°	W 125.4190°	1993.3	68.1	7.8	0.9576	Good
57	723	A	14FE	8/16/2013	02:50	N 46.8031°	W 125.5106°	1886.0	83.2	9.6	0.9337	Good
58	723	B	14FE	8/16/2013	02:56	N 46.8031°	W 125.5106°	1886.0	77.2	9.5	0.9509	Good
59	723	B	14FE	8/16/2013	03:20	N 46.8030°	W 125.5110°	1888.6	85.6	10.7	0.9498	Good
60	723	A	14FE	8/16/2013	03:21	N 46.8030°	W 125.5110°	1888.6	106.8	13.8	0.9562	Good
61	723	B	14E	8/16/2013	05:02	N 46.8027°	W 125.5214°	1904.3	62.3	6.4	0.9562	Good
62	723	A	14E	8/16/2013	05:03	N 46.8027°	W 125.5214°	1904.3	87.3	8.9	0.9657	Good
63	723	B	14E	8/16/2013	05:27	N 46.8027°	W 125.5217°	1904.6	88.9	9.7	0.9631	Good
64	723	A	14E	8/16/2013	05:30	N 46.8027°	W 125.5217°	1904.6	80.3	8.1	0.9663	Good
65	723	B	14C	8/16/2013	07:34	N 46.8030°	W 125.5309°	1914.1	78.3	8.5	0.9569	Good
66	723	B	14C	8/16/2013	08:43	N 46.8028°	W 125.5310°	1914.1	72.7	7.2	0.9506	Good
67	723	A	14C	8/16/2013	09:17	N 46.8030°	W 125.5311°	1913.7	74.4	9.2	0.9494	Good
68	723	A	14W	8/16/2013	13:40	N 46.8023°	W 125.5628°	1921.8	79.8	7.1	0.9658	Good
69	723	B	14W	8/16/2013	13:42	N 46.8023°	W 125.5628°	1921.8	99.9	9.0	0.9695	Good
70	723	A	14W	8/16/2013	14:12	N 46.8025°	W 125.5626°	1921.8	75.3	6.8	0.9521	Good
71	723	B	14W	8/16/2013	14:13	N 46.8025°	W 125.5626°	1921.8	94.3	8.6	0.9725	Good
72	723	B	14FW	8/16/2013	16:23	N 46.8031°	W 125.5816°	1833.3	99.7	12.7	0.9621	Good
73	723	A	14FW	8/16/2013	16:24	N 46.8031°	W 125.5816°	1833.3	104.2	13.6	0.9604	Good
74	723	B	14FW	8/16/2013	16:48	N 46.8031°	W 125.5820°	1833.3	95.7	23.7	0.8873	Bad
75	723	A	14FW	8/16/2013	16:49	N 46.8031°	W 125.5820°	1833.3	89.8	24.7	0.8745	Bad
76	723	B	14FW	8/16/2013	17:18	N 46.8031°	W 125.5827°	1832.6	86.9	26.3	0.8655	Bad
77	723	A	14FW	8/16/2013	17:19	N 46.8031°	W 125.5827°	1832.6	83.6	25.4	0.8649	Bad
78	723	A	15E	8/16/2013	20:51	N 46.8000°	W 125.6196°	1836.9	134.1	17.5	0.9528	Good
79	723	B	15E	8/16/2013	20:53	N 46.8000°	W 125.6196°	1836.9	116.4	16.3	0.9464	Good
80	723	B	15E	8/16/2013	21:20	N 46.8093°	W 125.6431°	1855.7	Failed	Failed	Failed	Failed
81	723	A	15E	8/16/2013	21:21	N 46.8093°	W 125.6431°	1855.7	145.4	22.9	0.9411	Good
82	723	B	15E	8/16/2013	21:50	N 46.8089°	W 125.6196°	1824.3	125.4	16.9	0.9454	Good
83	723	A	15E	8/16/2013	21:54	N 46.8089°	W 125.6196°	1824.3	Failed	Failed	Failed	Failed

84	723	A	15C	8/17/2013	02:47	N 46.8094°	W 125.6435°	1855.1	107.5	20.8	0.9071	Good
85	723	B	15C	8/17/2013	02:48	N 46.8094°	W 125.6435°	1855.1	94.9	19.9	0.9005	Good
86	723	A	15C	8/17/2013	03:15	N 46.8095°	W 125.6438°	1855.1	Failed	Failed	Failed	Failed
87	723	B	15c	8/17/2013	03:16	N 46.8095°	W 125.6438°	1855.1	101.3	20.1	0.9120	Good
88	723	B	15C	8/17/2013	03:40	N 46.8095°	W 125.6441°	1854.6	95.9	22.3	0.8935	Bad
89	723	A	15C	8/17/2013	03:41	N 46.8095°	W 125.6441°	1854.6	98.6	18.9	0.9065	Good
90	723	B	15W	8/17/2013	05:30	N 46.8106°	W 125.6627°	1872.4	124.6	16.0	0.9569	Good
91	723	A	15W	8/17/2013	05:32	N 46.8106°	W 125.6627°	1872.4	140.7	18.2	0.9572	Good
92	723	B	15W	8/17/2013	05:54	N 46.8106°	W 125.6629°	1872.4	123.8	21.5	0.9293	Good
93	723	A	15W	8/17/2013	05:55	N 46.8106°	W 125.6629°	1872.4	131.5	16.8	0.9565	Good
94	723	B	15W	8/17/2013	06:22	N 46.8106°	W 125.6630°	1872.4	-115.5	10.9	0.8442	Bad
95	723	A	15W	8/17/2013	06:22	N 46.8106°	W 125.6630°	1872.4	109.2	17.4	0.9353	Good
96	723	A	16FFE	8/17/2013	12:59	N 46.7890°	W 125.6865°	1888.6	109.6	14.5	0.9624	Good
97	723	B	16FFE	8/17/2013	13:00	N 46.7890°	W 125.6865°	1888.6	146.9	17.5	0.9614	Good
98	723	A	16FFE	8/17/2013	13:25	N 46.7891°	W 125.6867°	1886.8	127.5	25.2	0.9102	Good
99	723	B	16FFE	8/17/2013	13:28	N 46.7891°	W 125.6867°	1886.8	138.3	16.8	0.9579	Good
100	723	A	16FFE	8/17/2013	13:57	N 46.7892°	W 125.6870°	1902.0	142.5	23.0	0.9264	Good
101	723	B	16FFE	8/17/2013	14:00	N 46.7892°	W 125.6870°	1902.0	139.3	578.1	0.1158	Bad
102	723	B	16FE	8/17/2013	15:24	N 46.7872°	W 125.6969°	1916.8	100.0	14.9	0.9503	Good
103	723	A	16FE	8/17/2013	15:25	N 46.7872°	W 125.6969°	1916.8	107.2	15.9	0.9498	Good
104	723	B	16FE	8/17/2013	15:48	N 46.7872°	W 125.6971°	1916.8	98.5	13.1	0.9614	Good
105	723	A	16FE	8/17/2013	15:49	N 46.7872°	W 125.6971°	1916.8	97.1	15.3	0.9451	Good
106	723	B	16E	8/17/2013	17:16	N 46.7869°	W 125.7096°	1916.9	87.5	12.3	0.9545	Good
107	723	A	16E	8/17/2013	17:17	N 46.7869°	W 125.7096°	1916.9	90.6	12.3	0.9558	Good
108	723	B	16E	8/17/2013	17:41	N 46.7868°	W 125.7099°	1917.2	83.3	11.6	0.9572	Good
109	723	A	16E	8/17/2013	17:42	N 46.7868°	W 125.7099°	1917.2	93.7	12.8	0.9576	Good
110	723	B	16E	8/17/2013	19:54	N 46.78416°	W 125.7363°	1917.6	94.5	18.0	0.9258	Good
111	723	A	16E	8/17/2013	19:57	N 46.7841°	W 125.7363°	1917.6	91.8	16.7	0.9252	Good
112	723	A	16C	8/17/2013	20:32	N 46.7842°	W 125.7363°	1917.6	Failed	Failed	Failed	Failed
113	723	B	16C	8/17/2013	20:34	N 46.7842°	W 125.7363°	1917.6	93.4	16.1	0.9211	Good
114	723	B	16C	8/17/2013	21:01	N 46.7842°	W 125.7362°	1917.6	94.5	16.7	0.9300	Good

115	723	A	16C	8/17/2013	21:02	N 46.7842°	W 125.7362°	1917.6	90.4	18.1	0.9061	Good
116	723	B	16W	8/18/2013	00:31	N 46.7840°	W 125.7729°	1907.2	81.3	14.2	0.9348	Good
117	723	A	16W	8/18/2013	00:32	N 46.7840°	W 125.7729°	1907.2	75.5	14.3	0.9218	Good
118	723	B	16W	8/18/2013	00:56	N 46.7840°	W 125.7731°	1907.2	60.9	13.0	0.9015	Good
119	723	A	16W	8/18/2013	00:57	N 46.7840°	W 125.7731°	1907.2	80.0	18.2	0.9036	Good
120	723	B	16FW	8/18/2013	02:19	N 46.7845°	W 125.7803°	1903.3	92.9	15.1	0.9400	Good
121	723	A	16FW	8/18/2013	02:21	N 46.7845°	W 125.7803°	1903.3	Failed	Failed	Failed	Failed
122	723	B	16FW	8/18/2013	02:45	N 46.7848°	W 125.7805°	1903.2	60.9	23.0	0.4450	Bad
123	723	A	16FW	8/18/2013	02:46	N 46.7848°	W 125.7805°	1903.2	92.4	18.8	0.9175	Good
124	723	A	16FFW	8/18/2013	08:51	N 46.7873°	W 125.7834°	1903.2	117.7	25.4	0.9083	Good
125	723	B	16FFW	8/18/2013	09:00	N 46.7873°	W 125.7834°	1903.2	130.0	26.6	0.9179	Good
126	723	B	16FFW	8/18/2013	10:01	N 46.7835°	W 125.7874°	1892.3	133.1	23.5	0.9366	Good
127	723	A	16FFW	8/18/2013	10:04	N 46.7835°	W 125.7874°	1892.3	144.9	22.2	0.9468	Good
128	723	B	16FFW	8/18/2013	10:34	N 46.7880°	W 125.7880°	1898.9	66.5	11.3	0.9169	Good
129	723	A	16FFW	8/18/2013	10:36	N 46.7880°	W 125.7880°	1898.9	79.1	16.5	0.9111	Good
130	723	B	Sup1	8/18/2013	11:35	N 46.7839°	W 125.7928°	1898.8	39.6	16.2	0.7489	Bad
131	723	A	Sup1	8/18/2013	11:37	N 46.7839°	W 125.7928°	1802.5	47.8	16.5	0.7631	Bad
132	723	B	Sup2	8/18/2013	12:36	N 46.7840°	W 125.7973°	1765.4	22.5	9.0	0.7735	Bad
133	723	A	Sup2	8/18/2013	12:38	N 46.7840°	W 125.7973°	1765.4	35.8	6.7	0.9122	Good
134	723	B	Sup2.5	8/18/2013	13:36	N 46.7834°	W 125.8014°	1747.9	26.9	7.4	0.5919	Bad
135	723	A	Sup2.5	8/18/2013	13:39	N 46.7834°	W 125.8014°	1747.9	28.4	5.0	0.7644	Bad
136	723	B	Sup3	8/18/2013	14:32	N 46.7826°	W 125.8054°	1751.5	58.0	943.6	0.1907	Bad
137	723	A	Sup3	8/18/2013	14:33	N 46.7826°	W 125.8054°	1751.5	98.6	8788	0.0868	Bad
138	723	B	Sup3.5	8/18/2013	15:47	N 46.7822°	W 125.8108°	1776.7	42.3	8.7	0.7960	Bad
139	723	A	Sup3.5	8/18/2013	15:48	N 46.7822°	W 125.8108°	1776.7	156.6	19135	0.0499	Bad
140	723	B	Sup4.5	8/18/2013	17:56	N 46.7801°	W 125.8225°	1911.1	79.2	886.5	0.6526	Bad
141	723	A	Sup4.5	8/18/2013	17:57	N 46.7801°	W 125.8225°	1911.1	84.4	304.8	0.7449	Bad
142	723	B	Sup4.5	8/18/2013	18:20	N 46.7800°	W 125.8227°	1911.1	82.7	2225.8	0.5815	Bad
143	723	A	Sup4.5	8/18/2013	18:21	N 46.7800°	W 125.8227°	1911.1	71.8	3286.6	0.5324	Bad
144	723	B	Sup5	8/18/2013	19:36	N 46.7788°	W 125.8292°	1968.8	107.5	31.0	0.8797	Bad
145	723	A	Sup5	8/18/2013	19:37	N 46.7788°	W 125.8292°	1968.8	Failed	Failed	Failed	Failed

146	723	B	Sup5	8/18/2013	20:04	N 46.7789°	W 125.8295°	1968.9	Failed	Failed	Failed	Failed
147	723	B	Sup8	8/18/2013	23:07	N 46.7740°	W 125.8624°	2063.4	36.1	5.2	0.9486	Good
148	723	B	Sup8	8/18/2013	23:34	N 46.7741°	W 125.8623°	2063.0	36.8	5.6	0.9029	Good
149	723	B	Sup9	8/19/2013	01:58	N 46.7691°	W 125.8763°	2176.5	97.1	8.7	0.9394	Good
150	723	B	Sup9	8/19/2013	02:23	N 46.7689°	W 125.8759°	2177.8	104.5	7.4	0.9915	Good
151	723	B	Sup9	8/19/2013	02:36	N 46.7690°	W 125.8759°	2177.8	80.5	6.8	0.9494	Good
152	723	B	Sup10	8/19/2013	04:24	N 46.7620°	W 125.8899°	2360.8	113.3	22.3	0.9171	Good
153	723	B	Sup10	8/19/2013	04:48	N 46.7621°	W 125.8903°	2365.0	121.9	22.4	0.9223	Good
154	723	B	17B	8/19/2013	07:54	N 46.7554°	W 125.9046°	2490.5	118.5	16.3	0.9574	Good
155	723	B	17FE	8/19/2013	09:03	N 46.7553°	W 125.9022°	2468.0	98.3	17.7	0.9301	Good
156	723	B	17FE	8/19/2013	10:01	N 46.7554°	W 125.9040°	2486.9	Failed	Failed	Failed	Failed
157	723	B	17E	8/19/2013	12:51	N 46.7552°	W 125.9056°	2490.3	112.8	18.2	0.9435	Good
158	723	B	17C	8/19/2013	14:59	N 46.7522°	W 125.9207°	2557.2	104.5	13.3	0.9624	Good
159	723	B	17C	8/19/2013	15:23	N 46.7522°	W 125.9209°	2559.3	106.4	16.4	0.9480	Good
160	723	B	17C	8/19/2013	15:46	N 46.7521°	W 125.9213°	2559.3	113.8	15.9	0.9566	Good
161	723	B	18C	8/19/2013	20:54	N 46.7604°	W 126.0086°	2588.1	88.1	14.4	0.9343	Good
162	723	B	18C	8/19/2013	21:26	N 46.7605°	W 126.0086°	2588.2	86.2	12.9	0.9513	Good
163	723	B	18C	8/19/2013	21:59	N 46.7605°	W 126.0086°	2588.2	94.4	18.0	0.9258	Good
164	723	B	18C	8/19/2013	20:24	N 46.7605°	W 126.0086°	2588.2	99.0	15.2	0.9448	Good
165	724	B	Dual Plume	8/21/2013	17:13	N 46.7820°	W 125.2635°	1099.8	128.3	11.3	0.8977	Bad
166	724	B	Dual Plume	8/21/2013	17:37	N 46.7819°	W 125.3135°	1463.8	108.5	11.6	0.9133	Good
167	725	B	14C	8/21/2013	03:39	N 46.8028°	W 125.5341°	1916.5	Failed	Failed	Failed	Failed
168	725	B	14C	8/22/2013	04:03	N 46.8028°	W 125.5342°	1916.5	153.4	22.0	0.9395	Good
169	725	B	Sup 16C	8/23/2013	02:49	N 46.7846°	W 125.7327°	1918.8	146.2	26.7	0.9214	Good
170	725	B	Sup 16C	8/23/2013	03:12	N 46.7846°	W 125.7328°	1918.8	145.1	25.9	0.9178	Bad
171	725	B	HR1	8/23/2013	06:23	N 46.7841°	W 125.7686°	1909.9	126.9	9.4	0.9855	Good
172	725	B	HR1	8/23/2013	06:45	Failed	Failed	Failed	Failed	Failed	Failed	Failed
173	725	B	HR1	8/23/2013	07:01	N 46.7844°	W 125.7768°	1905.1	123.5	10.0	0.9757	Good
174	725	B	HR2	8/23/2013	08:16	N 46.7845°	W 125.7767°	1905.1	80.6	8.5	0.9749	Good
175	725	B	HR2	8/23/2013	08:42	Failed	Failed	Failed	Failed	Failed	Failed	Failed
176	725	B	HR3	8/23/2013	09:50	N 46.7843°	W 125.7846°	1900.3	88.4	16.7	0.9260	Good

177	725	B	HR3	8/23/2013	10:21	N 46.7843°	W 125.7849°	1900.3	101.2	19.0	0.9239	Good
178	725	B	HR4	8/23/2013	15:05	N 46.7843°	W 125.7901°	1844.9	126.5	447.0	0.6870	Bad
179	725	B	HR4	8/23/2013	15:30	N 46.7841°	W 125.7901°	1844.9	145.4	2509.1	0.7076	Bad
180	725	B	HR5	8/23/2013	16:40	N 46.7839°	W 125.7951°	1774.2	96.5	954.1	0.6476	Bad
181	725	B	HR5	8/23/2013	17:06	N 46.7841°	W 125.7951°	1774.2	79.1	17.6	0.8986	Bad
182	725	B	HR6	8/23/2013	18:38	N 46.7833°	W 125.8016°	1747.9	70.3	5.9	0.9767	Good
183	725	B	HR6	8/23/2013	19:02	N 46.7833°	W 125.8020°	1747.9	68.6	6.6	0.9397	Good
184	725	B	Sup 3	8/23/2013	20:03	N 46.7826°	W 125.8051°	1750.2	72.1	23.3	0.8509	Bad
185	725	B	Sup 3	8/23/2013	20:27	N 46.7826°	W 125.8053°	1751.5	65.7	40.4	0.7949	Bad
186	725	B	Sup 7	8/23/2013	21:42	N 46.7655°	W 125.8110°	1886.4	61.0	399.1	0.6480	Bad
187	725	B	Sup 7	8/23/2013	22:06	N 46.7822°	W 125.8111°	1783.0	64.4	3849.1	0.6060	Bad
188	725	B	HR8	8/24/2013	00:59	N 46.7770°	W 125.8502°	2175.4	109.8	17.2	0.9442	Good
189	725	B	HR8	8/24/2013	01:23	N 46.7771°	W 125.8501°	2175.4	113.8	15.7	0.9560	Good
190	725	B	HR9	8/24/2013	02:39	N 46.7746°	W 125.8560°	2144.0	124.6	8.5	0.9914	Good
191	725	B	HR9	8/24/2013	03:01	N 46.7745°	W 125.8561°	2144.8	123.8	9.1	0.9861	Good
192	725	B	HR10	8/24/2013	05:00	N 46.7715°	W 125.8689°	2098.8	107.9	12.2	0.9685	Good
193	725	B	HR10	8/24/2013	05:23	N 46.7715°	W 125.8691°	2099.8	108.6	12.3	0.9639	Good
194	725	B	HR11	8/24/2013	07:30	N 46.7671°	W 125.8831°	2262.4	Failed	Failed	Failed	Failed
195	725	B	HR11	8/24/2013	07:51	N 46.7671°	W 125.8831°	2262.4	127.4	25.6	0.9191	Good
196	725	B	HR11	8/24/2013	08:16	N 46.7671°	W 125.8833°	2262.4	129.0	22.7	0.9359	Good
197	725	B	17E	8/24/2013	Failed	Failed	Failed	Failed	Failed	Failed	Failed	Failed
198	725	B	3-17	8/24/2013	11:03	N 46.7557°	W 125.9051°	2490.5	119.6	13.3	0.9713	Good
199	725	B	3-17	8/24/2013	11:28	N 46.7556°	W 125.9051°	2490.5	98.3	9.6	0.9785	Good
200	725	B	17C	8/25/2013	00:03	N 46.7603°	W 126.0089°	2589.0	109.8	14.0	0.9627	Good
201	725	B	17C	8/25/2013	00:25	N 46.7603°	W 126.0089°	2589.0	97.9	14.5	0.9521	Good
202	725	B	18C	8/25/2013	00:49	N 46.7606°	W 126.0088°	2589.0	102.3	15.7	0.9477	Good
203	725	B	18C	8/25/2013	01:12	N 46.7606°	W 126.0088°	2589.0	98.7	12.3	0.9647	Good
204	725	B	18C	8/25/2013	01:40	N 46.7605°	W 126.0090°	2589.7	97.6	12.4	0.9627	Good

A.3 Multicore Logger Heat Flow

Heat flow measurement, uncertainty in the form of standard deviation (σ_Q), and meta-data for the Multi-core Logger. The Multi-Core system was modified to record the tempearture profile by attaching thermistors to a core liner at intervals ranging from 0.075 to 0.01 meters. A second adjacent core liner with pre-drilled 2 cm spacing collected sediments for onboard thermal conductivity measurements using a needle probe (Von Herzen and Maxwell, 1959; Lister, 1979; Goto and Matsubayshi, 2008). Uncertainty was determined through Monte Carlo simulations and included the correlation coefficient (R^2) of the Linear fit to the Bullard Plot.

Probe #	Date (GMT)	Time	Latitude	Longitude	Depth (meters)	Heat Flow (mW m^{-2})	σ_Q (mW m^{-2})	r^2	Flag
MC14-2	8/13/2013	17:35	N 46.8023°	W 125.530°	1916	97.4	3.1	0.9787	Good
MC14-3	8/13/2013	20:45	N 46.7991°	W 125.581°	1848	137.3	5.7	0.9927	Good
Site 9.5	8/14/2013	05:41	N 46.7486°	W 125.420°	1994	108.6	11.4	0.9900	Bad
MC16-1	8/14/2013	22:09	N 46.7801°	W 125.785°	1900	191.4	4.8	0.9969	Good
MC16-FFE	8/20/2013	02:56	N 46.7902°	W 125.687°	1882	143.0	8.4	0.9938	Good
MC15-E	8/20/2013	18:43	N 46.8104°	W 125.618°	1763	162.2	5.5	0.9536	Good

A.4 Thermal Blanket

Heat flow measurement, uncertainty in the form of standard deviation (σ_Q), and meta-data for the Thermal Blanket. The Thermal Blanket is a roughly 0.16 m^2 foam pad covered in a heavy canvas with two Antares temperature sensors fixed to the top and bottom of the pad to capture the surrounding thermal environment. Uncertainty was determined through Monte Carlo simulation. The surface heat flow measurements were assigned Good or Bad quality flags where Good signifies a good quality measurement while bad indicates a failure to seal to the seafloor or inaccurate Antares temperature offset calibrations.

Probe #	Dive	Deployment Date (GMT)	Deployment Time	Latitude	Longitude	Depth (meters)	Thermal Conductivity (W $m^{-1}K^{-1}$)	Blanket Thickness (meters)	Heat Flow (mW m^{-2})	σ_Q (mW m^{-2})	Flag
L1	719	8/3/2013	17:41	N 46.8444°	W 125.0366°	586.4	Failed	Failed	Failed	Failed	Bad
T1	719	8/3/2013	17:43	N 46.8444°	W 125.0366°	586.4	Failed	Failed	Failed	Failed	Bad
E1	719	8/4/2013	00:56	N 46.8496°	W 124.9575°	553.5	0.57	0.0504	-127.4	19.35	Good
H1	719	8/4/2013	08:11	N 46.8522°	W 124.9466°	553.3	0.57	0.0472	-147.9	22.5	Good
S1	719	8/5/2013	13:32	N 46.8285°	W 125.2190°	1143.0	0.57	0.0465	Failed	Failed	Bad
P1	719	8/5/2013	21:51	N 46.8211°	W 125.3048°	1323.6	0.585	0.0459	179.0	26.2	Good
G1	719	8/5/2013	22:05	N 46.8211°	W 125.3048°	1323.6	0.585	0.0461	178.4	26.2	Good
N1	719	8/6/2013	06:37	N 46.8101°	W 125.4419°	1926.3	0.583	0.0469	162.7	24.2	Good
R1	719	8/6/2013	16:37	N 46.7311°	W 125.4985°	2110.9	0.596	0.0504	226.9	28.1	Good
I1	719	8/7/2013	02:32	N 46.7482°	W 125.4195°	1991.0	0.584	0.0466	167.5	24.5	Good
Q1	719	8/7/2013	06:39	N 46.7484°	W 125.4192°	1991.0	0.581	0.0493	146.3	21.7	Good
O1	719	8/7/2013	07:46	N 46.7481°	W 125.4193°	1991.1	0.57	0.0470	67.9	16.2	Good
B1	722	8/15/2013	21:38	N 46.7821°	W 125.2633°	1038.0	0.57	0.0511	87.2	16.3	Good
Q2	723	8/16/2013	07:19	N 46.8029°	W 125.5311°	1913.1	0.57	0.0470	73.8	16.4	Good
O2	723	8/16/2013	08:02	N 46.8030°	W 125.5309°	1913.1	0.57	0.0476	51.3	14.5	Good
R2	723	8/16/2013	16:14	N 46.8030°	W 125.5815°	1832.6	0.582	0.0553	134.9	18.1	Good
N2	723	8/16/2013	22:27	N 46.8089°	W 125.6196°	1828.6	0.584	0.0487	163.2	22.9	Good
P2	723	8/17/2013	02:38	N 46.8094°	W 125.6435°	1853.0	0.57	0.0588	80.1	13.5	Good
D1	723	8/17/2013	12:48	N 46.7891°	W 125.6865°	1887.6	0.593	0.0732	139.2	14.4	Good

T2	723	8/17/2013	21:32	N 46.7842°	W 125.7362°	1917.4	0.576	0.0458	136.3	22.0	Good
S2	723	8/17/2013	21:36	N 46.7842°	W 125.7362°	1917.4	0.57	0.05	Failed	Failed	Bad
L2	723	8/18/2013	09:42	N 46.7834°	W 125.7872°	1884.2	0.582	0.0540	137.0	18.9	Good
I2	723	8/19/2013	08:24	N 46.7554°	W 125.9047°	2490.7	0.573	0.0506	111.0	9.2	Good
H2	723	8/19/2013	12:42	N 46.7551°	W 125.9056°	2491.3	0.573	0.0506	112.1	27.2	Good
G2	723	8/19/2013	14:53	N 46.7522°	W 125.9205°	2556.7	0.572	0.0506	106.2	27.5	Good
E2	723	8/19/2013	20:49	N 46.7604°	W 126.0086°	2589.0	0.593	0.0506	202.7	14.8	Good
C1	723	8/19/2013	21:57	N 46.7605°	W 126.0088°	2590.0	0.572	0.0506	108.5	9.2	Good